STIFFENING THE POSTERIOR RAT SCLERA TO PROVIDE NEUROPROTECTION IN GLAUCOMA

A Dissertation
Presented to
The Academic Faculty

by

Bailey G. Hannon

In Partial Fulfillment
of the Requirements for the Degree
Doctor of Philosophy in Bioengineering in the
George W. Woodruff School of Mechanical Engineering

Georgia Institute of Technology
August 2020

STIFFENING THE POSTERIOR RAT SCLERA TO PROVIDE NEUROPROTECTION IN GLAUCOMA

Approved by:

Dr. C. Ross Ethier, Co-Advisor
Wallace H. Coulter Department of Biomedical Engineering
Georgia Institute of Technology and Emory University

Dr. J. Brandon Dixon
George W. Woodruff School of Mechanical Engineering
Georgia Institute of Technology

Dr. Machelle T. Pardue, Co-Advisor
Wallace H. Coulter Department of Biomedical Engineering
Georgia Institute of Technology and Emory University

Dr. Brian C. Samuels
Department of Ophthalmology and Visual Sciences
University of Alabama at Birmingham

Dr. Mark R. Prausnitz
School of Chemical and Biomolecular Engineering
Georgia Institute of Technology

Date Approved:

To my Dad, Mom, Emerson, and Walker

ACKNOWLEDGEMENTS

Without the support, guidance, and mentorship of many individuals, this dissertation would not have been possible. I would like to recognize the invaluable assistance that you all have provided during my study.

First, I would like to acknowledge and thank my two thesis advisors, Dr. Ross Ethier and Dr. Machelle Pardue. I have grown a lot over these past five years, both as a scientist and as a person, much of which is due to my advisors' outstanding mentorship and guidance throughout my Georgia Tech journey. Dr. Ethier has dramatically sharpened my maturity as a researcher, not only by guiding me to improved presentation and writing skills, but more importantly by pushing me to think critically and in far broader terms. Dr. Pardue is both an ocular biology and laboratory technique genius and, at key times, a doctoral candidate life coach. I'm thankful for learning essential skills from her while being the beneficiary of her upbeat enthusiasm and motivating conversations. Together, my co-advisors' wisdom and assistance has been vital to the completion of this project. I cannot begin to express how thankful I am for their unwavering and holistic support throughout this process, without which this dissertation would not have been possible.

I am grateful for my other thesis committee members: Dr. Mark Prausnitz, Dr. Brian Samuels, and Dr. Brandon Dixon. Dr. Prausnitz' expertise in chemistry and ocular drug delivery provided essential guidance in the development and analysis of the in vivo glaucoma study. Dr. Samuels provided important suggestions for improvements in the microbead model from a clinical perspective, which was uniquely useful. Dr. Dixon was a

pleasure to TA for in Biosolid Mechanics, and his expertise on the subject has been key to the analysis of my inflation experiments.

I would like to thank Dr. Andrew Feola and Dr. Ian Campbell who are both past post-doctoral fellows in the Ethier Lab and Career Development Awardees in the Pardue Lab. Dr. Feola provided support, knowledge, and mentorship throughout our struggles with the microbead model and motivated me to persevere through these difficulties. Dr. Campbell provided much of the groundwork necessary to make this thesis possible, especially in developing the software and hardware necessary for the *supposed* 'turn-key' DIC experimental set-up.

I would like to give a special thanks to Dr. Brandon Gerberich who has worked closely with me throughout my PhD journey. From taking Biology of the Eye together my first year at Georgia Tech to our often-absurd glaucoma study schedule, Dr. Gerberich has dispensed vast knowledge of statistical analysis and chemistry that were key to this dissertation.

I am blessed to have had the opportunity to work with two undergraduate Petit Scholars: Matthew Ritch and R. Kijoon Kim. Matthew's sharp mind created the machine-learning axon counting software that was crucial to the completion of Chapters 5-7. As much as I love manually counting axons, this automated a very tedious process. Kijoon provided essential support in the development of molecular assays and the microbead model, while sharing an appreciation with me for both nighttime IOP measurements and Northern Ireland.

Additionally, I would like to thank the other past and present Ethier and Pardue Lab members who have been generous with their encouragement and experimental ideas throughout my time at Georgia Tech. Specifically, I would like to acknowledge Dr. Thomas Read, who was instrumental in my early DIC inflation tests, sectioned countless optic nerves, and taught me an appreciation for the beauty in histology. Additionally, I would like to acknowledge Dr. Stephen Schwaner for helping me navigate through the PhD process, providing professional development advice, and for taking the time to create the MATLAB GUI used for analysis of our inflation tests.

I would also like to acknowledge Laura Paige, for her unmatched knack for coming up with a solution to every problem (no matter how obscure) and having the compassion to drop everything to solve it. Laura has done a wonderful job as an administrator and made my time as a BioE student unforgettable.

Finally, I cannot begin to express my heartfelt gratitude to my family, friends, and puppies who supplied endless love and support during my PhD journey. My family, in particular, has supported me immensely by providing the enthusiasm, advice, and perspective necessary to keep me motivated and emotionally well during this trying quest. Without this underpinning support this dissertation would simply not be.

TABLE OF CONTENTS

LIST OF TABLES

LIST OF FIGURES

LIST OF SYMBOLS AND ABBREVIATIONS

ANCOVA	Analysis of Covariance
ANOVA	Analysis of Variance
CEI	Controlled Elevation of Intraocular Pressure
DIC	Digital Image Correlation
ERG	Electroretinogram
GP	Genipin
HBSS	Hank's Balanced Salt Solution
MB	Methylene Blue
nSTR	Negative Scotopic Threshold
IOP	Intraocular Pressure
OCT	Optical Coherence Tomography
OHT	Ocular Hypertension
OMR	Optomotor Response
ONH	Optic Nerve Head
PBS	Phosphate Buffered Saline
PhNR	Photopic Negative Response
pSTR	Positive Scotopic Threshold
RGC	Retinal Ganglion Cell
RT-PCR	Reverse Transcription Polymerase Chain Reaction

Summary

Glaucoma is the leading cause of irreversible blindness in the world, affecting approximately 80 million people in the year 2020. This degenerative optic neuropathy is characterized by retinal ganglion cell (RGC) death, optic nerve damage, and progressive vision loss. While the exact etiology remains elusive, elevated intraocular pressure (IOP) is a known risk factor and lowering IOP remains the only effective treatment. Elevated IOP causes deformation and remodeling of the optic nerve head (ONH) tissues, which in turn is thought to promote localized neurodegeneration. Computational and *ex vivo* studies have shown that scleral stiffness strongly influences deformation of the ONH, and that increasing the stiffness of the sclera surrounding the ONH (the peripapillary sclera) can significantly reduce these excessive strains. **We hypothesize that by crosslinking the collagenous peripapillary sclera, we will reduce mechanical deformation in the ONH, which will in turn mitigate glaucomatous vision loss.**

To investigate this hypothesis, we developed a safe and efficacious scleral stiffening treatment using the collagen crosslinking agent genipin, assayed through *ex vivo* and *in vivo* experiments in healthy rat eyes. We then evaluated our treatment's efficacy to prevent glaucomatous damage in a microbead rat model of ocular hypertension. **Our results indicate that scleral stiffening protected against retinal thinning but did not show protective effects on visual or retinal function, nor preservation of RGC axons.** Overall, these results demonstrate the feasibility of using genipin for a scleral stiffening treatment. The absence of a strong protective effect of genipin-induced scleral stiffening on RGC function and structure may be due to limitations in the glaucomatous rat model,

in that our model does not mirror the slow progression, nor the moderate IOP elevation characteristic of clinical glaucoma.

CHAPTER 1. **Introduction**

1.1 **Glaucoma**

1.1.1 *Pathophysiology of Glaucoma*

Glaucoma is the leading cause of irreversible blindness and affects roughly 80 million people worldwide (Cook and Foster 2012; Quigley and Broman 2006). This degenerative optic neuropathy is characterized by retinal ganglion cell (RGC) dysfunction and death, which leads to progressive and irreversible vision loss. RGC axons transmit visual information from the retina to the brain and thus are critical to visual function. Although the exact etiology of glaucomatous damage to RGCs is unknown, several risk factors have been associated with glaucoma, including: African American descent, family history of glaucoma, older age, corticosteroid use, and elevated intraocular pressure (IOP) (Weinreb, Aung, and Medeiros 2014; Sommer et al. 1991; Mc, Gordon, and Koteen 1951; Tielsch et al. 1994).

1.1.2 *Regulation of Intraocular Pressure*

The intraocular pressure (IOP) within the globe helps maintain the shape of the eye and is determined by the circulation of aqueous humor. Aqueous humor is a transparent fluid secreted by the ciliary processes, which flows into the anterior chamber and exits the eye through one of two pathways (Figure 1). In the main outflow pathway, known as the conventional outflow pathway, aqueous humor flows through the trabecular meshwork, into Schlemm's canal, and then exits the eye through the episcleral vasculature (Goel et al. 2010; Ashton 1952; Tripathi 1972). The second pathway is known as the unconventional,

or uveoscleral, pathway, in which aqueous humor flows out of the eye through the ciliary muscle into the suprachoroidal space, and then exits through the sclera, among other routes (Tripathi 1977).

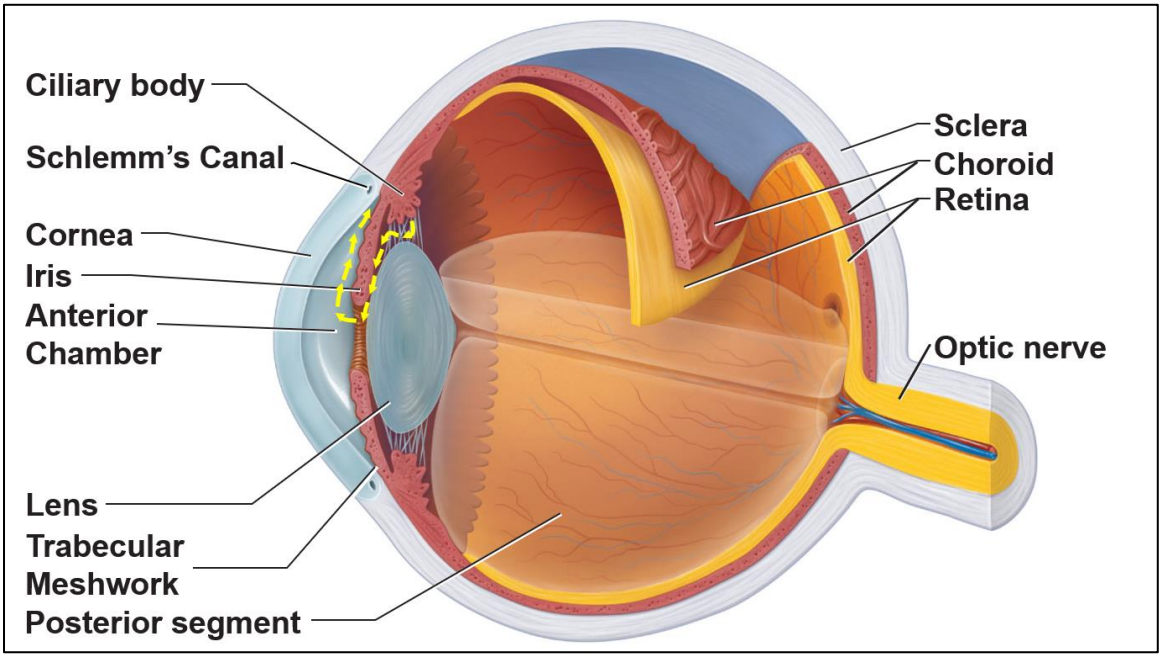

Figure 1: Ocular cross section with anatomical features labelled. Yellow arrows denote flow patterns of aqueous humor. Adapted from Martini 2010 (Martini 2010).

Since IOP is major risk factor for glaucoma, a great deal of glaucoma research is focused on development of IOP-lowering techniques that utilize pharmacology or surgery. Commonly used pharmaceuticals aim to lower IOP by increasing unconventional (prostaglandin analogs) or conventional (cholinergic agonists or rho kinase inhibitors) aqueous humor outflow, or by reducing aqueous humor production (beta-adrenergic blockers and carbonic anhydrase inhibitors, and alpha-adrenergic agonists) (Weinreb, Aung, and Medeiros 2014; Tanna and Johnson 2018; Goh et al. 1988; Kerstetter et al. 1988; Elliot, Cullen, and Phillips 1975; Becker 1955). IOP-lowering drugs have been shown to slow or prevent the progression of vision loss in glaucoma patients (Bron 2002; Becker

1954). Unfortunately, IOP-lowering drugs have notably poor patient compliance and in some cases do not lower IOP sufficiently (Robin and Grover 2011). In such cases, surgically-based methods of lowering IOP are required. These include laser trabeculoplasty, shunts, trabeculotomy, and more recently, minimally-invasive glaucoma surgical techniques (Mori et al. 2020; Bovee and Pasquale 2017; Hu, Ang, and Yip 2020), which all aim to increase aqueous humor outflow without the need for daily patient intervention. While these approaches are useful, studies have shown that as many as 45% of patients continue to progress even with use of IOP-lowering therapies (Heijl et al. 2002). Thus, there is a significant need to develop a treatment for glaucoma that is not solely aimed at lowering IOP.

1.2 Biomechanics in Glaucoma

With the goal of developing other treatments for glaucoma, research has focused on understanding the relationship between ocular biomechanics and glaucomatous damage. To better understand this relationship, I will first describe the anatomical features of the posterior eye (Figure 2) that are thought to be important in glaucoma.

1.2.1 *Posterior Ocular Anatomy*

RGCs are retinal neurons which transmit visual information from the retina to the brain via axons which make up the optic nerve. The sclera is the opaque, collagenous, connective tissue that comprises five-sixths of the outer layer of the eye and provides structural support for the globe (Figure 2A). The optic nerve head (ONH) is a region within the posterior sclera where RGC axons converge and exit the eye through a canal known as

the scleral canal (Figure 2B). The posterior scleral region immediately surrounding the ONH is known as the peripapillary sclera.

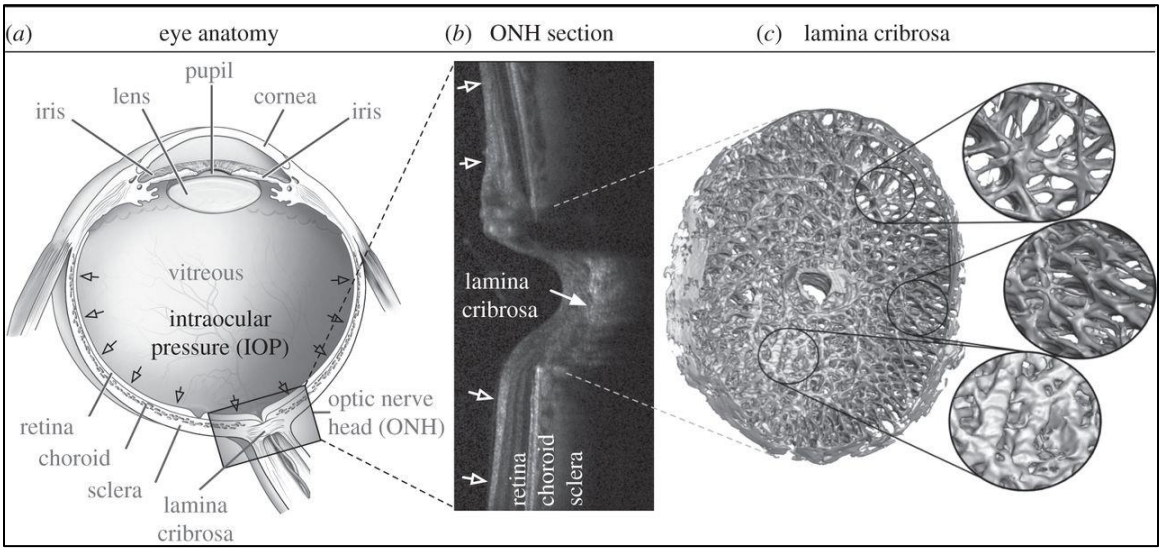

Figure 2: A) Overview of eye anatomy. Arrows denote IOP. B) OCT image showing a cross-section of the optic nerve head region and demonstrating the characteristic cupping in glaucoma. The lamina cribrosa and other structures are identified. C) 3D representation of a monkey lamina cribrosa showing its beautifully intricate structure. RGC axons pass through these pores to form the optic nerve (Girard et al. 2013).

1.2.1.1 Scleral Structure

The sclera consists of lamellar layers containing mainly crosslinked type I collagen fibers (90% by weight) and elastin surrounded by a proteoglycan-rich matrix (Rada, Shelton, and Norton 2006). These collagen lamellae are oriented in a heterogeneous manner; for example, in the peripapillary sclera the collagen preferentially aligns in a circumferential orientation to resist expansion of the scleral canal (Coudrillier et al. 2013; Pijanka et al. 2012; Gogola et al. 2018). In contrast, collagen lamellae are less aligned in the peripheral sclera, but have a preferred radial orientation (Gogola et al. 2018; Pijanka et al. 2012).

1.2.1.2 Optic Nerve Head and Lamina Cribrosa Structure

Along with RGC axons, the ONH contains support cells (astrocytes and glial cells) and, in humans, a collagenous, sieve-like structure called the lamina cribrosa (Figure 2C). The lamina cribrosa is composed of types I and III collagen, elastin, and proteoglycans (Hernandez et al. 1987) and provides the main structural and functional support to the RGC axon bundles that pass through its pores (Girard et al. 2013; Burgoyne et al. 2005).

1.2.2 *Biomechanical Damage in Glaucoma*

It is well accepted that elevated IOP leads to biomechanical insult to the ONH, which in turn likely contributes to RGC loss (Burgoyne 2011) via several different mechanisms. In glaucoma, elevated IOP causes the ONH to undergo a significant amount of tissue remodeling, including posterior bowing of the lamina cribrosa. One of the hallmarks of glaucoma is an early thickening of the lamina followed by a thinning and posterior bowing, which contributes to the phenomenon observed clinically as 'cupping' (Figure 2B) (Agoumi et al. 2011; Girard et al. 2013; Yang, Downs, and Burgoyne 2009). Since the lamina cribrosa provides structural and functional support for RGC axons, this remodeling of the lamina is believed to contribute to RGC axonal death in glaucoma (Sigal et al. 2007; Coudrillier et al. 2012; Quigley et al. 1985). Additionally, mechanosensitive astrocytes become reactive and form glial scars, which promotes RGC apoptosis (Alqawlaq, Flanagan, and Sivak 2019; Nickells 1996; Hayreh 1976; Hernandez 2000; Pena et al. 2001). RGC death can also in part be attributed to ischemia caused by mechanically obstructed blood flow in ONH capillaries (Burgoyne 2011; Hamard et al. 1994). Together, these mechanisms of RGC damage can each be linked back to excessive ONH strains.

Thus, if there was a way to mitigate such strains, we could presumably decrease RGC dysfunction, and thereby preserve vision in patients with glaucoma.

1.2.3 *Scleral Biomechanics in Glaucoma*

Motivated by a desire to understand the causes of excessive ONH strain in eyes with elevated IOP, a computational study determined which biomechanical properties of posterior eye tissues most influenced ONH strain (Sigal, Flanagan, and Ethier 2005). This study revealed that the stiffness of the peripapillary sclera had a major influence on strain in the ONH. Several other computational studies have further demonstrated similar conclusions, i.e. that these excessive strains could be alleviated by increasing the peripapillary scleral stiffness (Figure 3) (Eilaghi et al. 2010; Sigal et al. 2004). **Therefore, it is hypothesized that scleral stiffening may confer protection against IOP-induced glaucomatous damage (Campbell, Coudrillier, and Ethier 2014).**

This hypothesis was further evaluated in an *ex vivo* study which showed that increasing peripapillary scleral stiffness by approximately 100%, i.e. a doubling in scleral stiffness, provided a significant reduction in ONH strain (Coudrillier, Campbell, et al. 2016) Additionally, preliminary *in vivo* data has revealed a neuroprotective effect in rats with ocular hypertension (OHT) when increasing the scleral stiffness by 75% via overexpression of bone morphogenetic protein 2 using a viral vector delivered to the posterior eye (Ethier 2015).

Currently, one study has considered the effect of scleral stiffening in an animal model of glaucoma, specifically analyzing the effect of glyceraldehyde *in vivo* in mice (Kimball et al. 2014). Contrary to our hypothesis, this study reported that stiffening the posterior

sclera caused *increased*, rather than decreased, RGC damage in an OHT model of glaucoma, rather than acting as a neuroprotectant. I will discuss this in more detail in section 1.3.1.2 and Chapter 7.

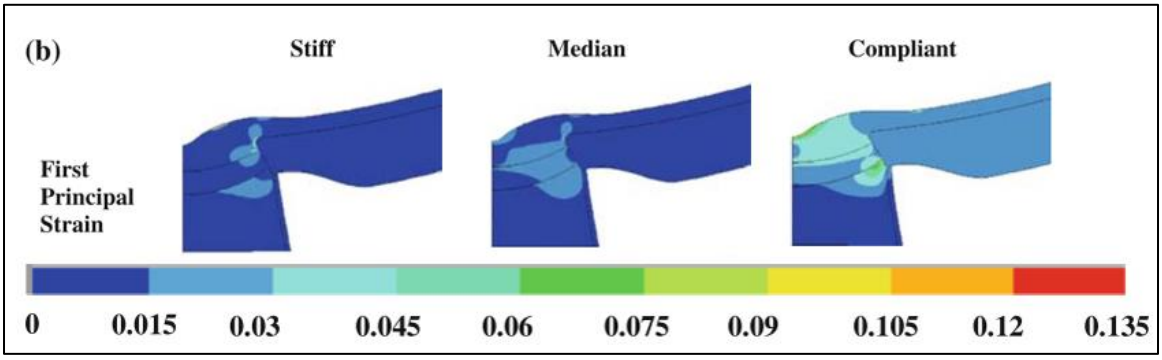

Figure 3: Finite element model of the ONH and peripapillary sclera depicting the first principal strains when considering a stiff, normal, and compliant sclera. First principal strains in the ONH are lowest with a stiff sclera (Eilaghi et al. 2010).

1.3 Collagen Crosslinking

A large body of research exists on various collagen crosslinking agents for a myriad of applications, e.g. increasing the rigidity of tissue grafts to recipient heart valves (Sung et al. 2000; Yoo et al. 2011), stem cell scaffolds (Rowland et al. 2013), acellular plug treatment for osteochondral defects (Hrabchak et al. 2010), and hydrogels used for drug delivery (Hennink and van Nostrum 2002). In many of these applications, collagen crosslinking agents are applied *ex vivo* before being used *in vivo*, because one of the major drawbacks of using collagen crosslinking agents is the high level of toxicity. For instance, one of the most commonly used collagen crosslinkers, glutaraldehyde, is highly toxic and thus unacceptable for *in vivo* use (Coudrillier, Campbell, et al. 2016; Gough, Scotchford, and Downes 2002). For applications in which collagen crosslinking agents are applied *in vivo*, more research needs to be performed on other less-toxic, natural, collagen crosslinking agents.

1.3.1 *Ocular Use of Collagen Crosslinking Agents*

Ocular collagen crosslinking has been proposed as a potential therapeutic treatment for not only glaucoma, but also for keratoconus and myopia. Keratoconus is a disease in which the cornea becomes thinner, weaker, and misshapen, thus distorting vision (Chunyu et al. 2014). Collagen crosslinking with riboflavin, photoactivated by Ultraviolet-A light, was proposed as a therapy for keratoconus (Spoerl, Huhle, and Seiler 1998; Wollensak, Spoerl, and Seiler 2003). This treatment, which increases corneal stiffness, has been recently clinically approved and is currently used worldwide (Hersh et al. 2017; Chunyu et al. 2014). In myopia, or nearsightedness, scleral remodeling leads to axial ocular elongation which contributes to increased refractive error (Harper and Summers 2015; Rada, Shelton, and Norton 2006). Collagen crosslinking of the sclera has been hypothesized as a treatment to slow or reverse scleral remodeling that leads to increased axial length and thus refractive error in myopia (Levy, Fazio, and Grytz 2018; Liu and Wang 2017). Unfortunately, the riboflavin + Ultraviolet-A collagen crosslinking method used to treat keratoconus is toxic to the retina, and cannot be used for scleral crosslinking (Glickman 2011; Wollensak et al. 2005). For this reason, development of alternative collagen crosslinking approaches is necessary to safely stiffen the posterior sclera for potential treatment of myopia and glaucoma.

1.3.1.1 Biocompatible Collagen Crosslinking Agents

Through an extensive literature search evaluating potential biocompatible, non-photoactivated, collagen crosslinking agents, genipin has emerged as a viable option for scleral crosslinking (Avila and Navia 2010; Hrabchak et al. 2010; Hwang et al. 2011; Liu,

Luo, et al. 2014; Liu and Wang 2013; Wang and Corpuz 2015; Wong et al. 2012; Xu, Chow, and Zhang 2011). As such, the vast majority of scleral crosslinking research has been focused on genipin crosslinking (Avila and Navia 2010; Hwang et al. 2011; Liu, Luo, et al. 2014; Liu and Wang 2013; Wang and Corpuz 2015; Wong et al. 2012; Xu, Chow, and Zhang 2011; Levy, Fazio, and Grytz 2018; Dias et al. 2015; Liu and Wang 2017). Genipin has been shown to have anti-inflammatory and anti-angiogenic properties (Koo et al. 2004), can induce stable crosslinks in biological tissue (Sung et al. 2001), and is significantly less cytotoxic than glutaraldehyde (Sung et al. 1999; Chang et al. 2002) and riboflavin (Song et al. 2017; Avila, Gerena, and Navia 2012).

Of several studies that have evaluated genipin-induced scleral crosslinking, only two have evaluated both the efficacy and safety of genipin-induced scleral crosslinking *in vivo* (Liu and Wang 2017; Wang and Corpuz 2015). These studies examined the biomechanical properties of genipin-stiffened scleral strips, gross ocular anatomy via slit-lamp exams after treatment, and histological and immuno-histological sections of ocular tissues in rabbits (Liu and Wang 2017) and guinea pigs (Wang and Corpuz 2015). These studies found that genipin successfully stiffened the sclera and did not cause any gross changes in ocular structures. However, to date no study has evaluated whether genipin-induced scleral collagen crosslinking affects visual and retinal function *in vivo*. Therefore, Chapter 4 and Chapter 5 will thoroughly evaluate the stiffening duration and functional effects of genipin-induced scleral stiffening, respectively. These experiments will lay the groundwork for studying the efficacy of scleral stiffening as a treatment for glaucoma (Chapter 7).

1.3.1.2 Previous Scleral Crosslinking Studies

There are several differences between the previously published collagen crosslinking study by Kimball et al. and our proposed study (Kimball et al. 2014). These include differences in the animal model, injection procedure, volume, agent, and concentration (described in detail in Chapter 7). In addition to these differences, several studies have confirmed the toxicity of glyceraldehyde (Kitahara et al. 2008; Usui et al. 2004; Koriyama et al. 2015). We thus hypothesize that scleral stiffening with a proven nontoxic agent will provide neuroprotection in glaucoma.

1.4 **Rat Model of Glaucoma**

1.4.1 *Similarities Between Human and Rat Pathophysiology*

For our study, we have chosen to use a rat model of glaucoma, one of several available. Rats are a very widely used animal model for glaucoma because of many parallels to glaucoma in humans. Ocular hypertensive rat models of glaucoma involve restricting the outflow of aqueous humor to elevate the animal's IOP. These models have been shown to yield ONH tissue deformations and demonstrate the ONH 'cupping' clinically present in humans (Morrison, Cepurna Ying Guo, and Johnson 2011; Quigley and Green 1979; Johnson et al. 2000). They also present similar features, including: RGC apoptosis (Guo et al. 2005), remodeling of extracellular matrix components in the ONH (Johnson et al. 2000), and the ONH being a main and early site of damage (Morrison, Cepurna Ying Guo, and Johnson 2011). Rat and human optic nerves also possess several anatomical similarities including: unmyelinated axonal fiber bundles within the anterior nerve, astrocytes aligned transversely to these axons, and a similar RGC damage pattern

(Morrison, Cepurna Ying Guo, and Johnson 2011; Johnson et al. 2000). Further, rodents are more cost effective and desirable from an ethical viewpoint when compared to non-human primates. The rat eye is twice the size of the mouse eye, and rats are therefore easier to work with than mice when delivering ocular injections and carrying out mechanical testing (Remtulla and Hallett 1985). IOP measurements in mice are typically performed under anesthesia, which leads to underestimating the IOP (Jia et al. 2000a). The Brown Norway rat that we have chosen is notably more docile than other strains, and therefore we can measure IOP in awake rats. Together, these reasons make the Brown Norway rat a good animal model of glaucoma for our purposes.

1.4.2 *Success of the OHT Model*

There are several rat models currently used in glaucoma research, the majority of which aim to induce OHT. The general methodology behind these models is to increase outflow resistance of aqueous humor, thus leading to an increase in IOP. Although hindering aqueous humor outflow seems simple in theory, in practice there are several complications due to the dynamic flow patterns within the trabecular meshwork, limited access to the outflow pathway, and the small size of the rat eye (Goel et al. 2010; Bouhenni et al. 2012). Once the outflow pathway has been restricted, the resultant IOP is extremely variable, with fluctuations over time within a single animal and within a cohort of animals (Levkovitch-Verbin et al. 2002; Chen and Zhang 2015; Feola et al. 2019; Kwong et al. 2013), which can result in extremely high IOPs, e.g. more than twice the baseline pressure (Foxton et al. 2013; Samsel et al. 2011; Dai et al. 2012; Bunker et al. 2015). This IOP history differs from the clinical presentation and such elevated pressures can even cause ischemic damage to the ONH and other retinal layers (as discussed in 0), adding difficulty

to determining the effect of a treatment (Bunker et al. 2015; Bui et al. 2013). Because of these complexities, there is unfortunately no ideal rat model of OHT. Here, I will briefly describe the currently used rat models of OHT and each of their potential limitations. It should be noted that there are other models of OHT which elevate IOP for acute periods, but these will not be described below (Levkovitch-Verbin et al. 2002; Lani et al. 2019).

1.4.2.1 Classic Models of OHT

1.4.2.1.1 Hypertonic Saline/Morrison Model

An early rat model of OHT is known as the Morrison model (Figure 4A), or hypertonic saline model of OHT (Morrison et al. 1997). In this method, hypertonic saline is injected into the episcleral limbal veins to induce sclerosis in the outflow tract and consequently elevate IOP. The resultant IOP elevation has been shown to last 4 to 8 weeks and RGC axonal damage patterns are similar to the clinical presentation (Morrison et al. 1997; Feola et al. 2019). The Morrison model is a difficult surgical procedure to perform because the episcleral veins are incredibly small, and thus requires extensive training (Morrison et al. 1995). This model of OHT also has a large amount of variability in IOP elevation for individual rats (Jia et al. 2000b) and it is difficult for labs to obtain similar IOP elevations to published results (Levkovitch-Verbin et al. 2002).

1.4.2.1.2 Episcleral Vein Cauterization

At a similar time as the development of the Morrison model, Shareef et al. developed a model of OHT involving cauterization of 2 to 3 episcleral veins (Figure

4B)(Shareef et al. 1995). Application of this method showed sustained IOP elevation for up to 6 months with approximately 40% RGC loss (Sawada and Neufeld 1999). However, an invasive surgery is necessary to access the episcleral veins and there is a risk of burning the sclera which leads to necrosis. Also, the resulting IOP is extremely high, reaching up to 60 mmHg under anesthesia; thus the unanesthetized IOP is even higher, since anesthesia depresses IOP by as much as 50% (Mittag et al. 2000; Jia et al. 2000a; Shareef et al. 1995). More recent research on this model has shown that OHT is induced by restricting blood flow and not aqueous outflow, which leads to a uniform RGC damage pattern instead of an initial superior RGC axon loss seen in other models of OHT (Mittag et al. 2000; Morrison 2005; Morrison, Cepurna Ying Guo, and Johnson 2011).

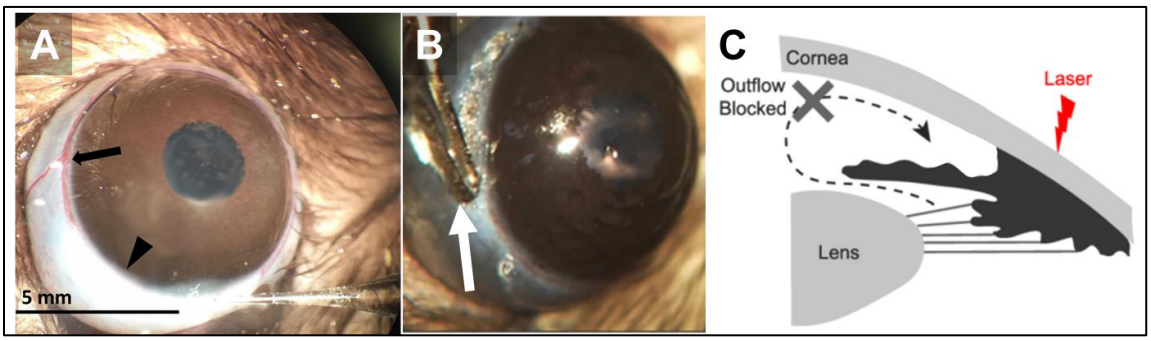

Figure 4: Classic rat models of OHT. A) Morrison Model: Arrowhead shows blanching effect of saline in the episcleral venous plexus and arrow indicates a portion of the episcleral venous plexus that has not yet blanched (Gossman, Linn, and Linn 2016). B) Episcleral Vein Cauterization: Arrow shows tip of the cautery applied on the limbal plexus, where the superior portion has already been cauterized (Lani et al. 2019). C) Laser Photocoagulation: Schematic of anterior chamber which shows laser illumination (Chen et al. 2015).

1.4.2.1.3 Laser Photocoagulation

Other investigators have taken an approach which utilized a laser to burn either the trabecular meshwork, the episcleral veins, or both (Figure 4C) to restrict aqueous humor outflow (Levkovitch-Verbin et al. 2002; Ueda et al. 1998). This method is more attractive

that the Morrison or cauterization methods because it is less surgically invasive, requires only use of a slit lamp, and takes just 3 minutes per rat to perform. Levkovitch-Verbin et al. also used this method after failing to obtain sufficient IOP elevation to produce RGC loss using these two previous methods (Levkovitch-Verbin et al. 2002). Consequently, using laser translimbal photocoagulation showed IOP elevation lasting 6 weeks and resulted in approximately 50-60% RGC axon loss. However, some of the limitations of this method are the need for an expensive diode or continuous wave laser, the fact that IOPs can reach up to 50 mmHg under anesthesia (which introduces the same issues stated in the previous paragraph), and the need for multiple lasering sessions to achieve significant RGC loss (Ueda et al. 1998; Levkovitch-Verbin et al. 2002).

1.4.2.2 Recently Developed Models of OHT

1.4.2.2.1 Microbead Model of OHT

Currently, the most widely used rat model of glaucoma in rodents is the microbead model (Figure 5A) in which microbeads (ranging from 1 to 15μm) are injected into the anterior chamber to increase resistance to aqueous humor outflow (Morgan and Tribble 2015). This method was first developed for non-human primates (Weber and Zelenak 2001) and was first adapted in use in rats by Urcola et al. (Urcola, Hernandez, and Vecino 2006). Variations in microbead sizes, injection volumes, and injection media have been explored by various labs (Dai et al. 2012; Smedowski et al. 2014). One of the main limitations of this method is that microbeads tend to obstruct the visual axis. Samsel et al. improved the method to use magnetic microbeads instead of polystyrene (non-magnetic) beads (Samsel et al. 2011). In this modified method, a handheld magnet is placed around the limbus of the eye so that the magnetic microbeads are pulled tightly into the angle,

thereby preserving clarity of the visual axis. Microbead model studies have reported successful IOP elevation lasting between 2 and 6 weeks (Sappington et al. 2010; Dai et al. 2012; Bunker et al. 2015; Matsumoto et al. 2014; Morgan and Tribble 2015; Samsel et al. 2011; Foxton et al. 2013), and those that have performed multiple injections have reported elevation of up to 27 weeks (Urcola, Hernandez, and Vecino 2006). Limitations of this model include the variations in IOP elevation and duration, anterior chamber inflammation, obstruction of the visual axis, and high IOP spikes which can cause corneal edema or ischemia (Urcola, Hernandez, and Vecino 2006; Morgan and Tribble 2015; Smedowski et al. 2014).

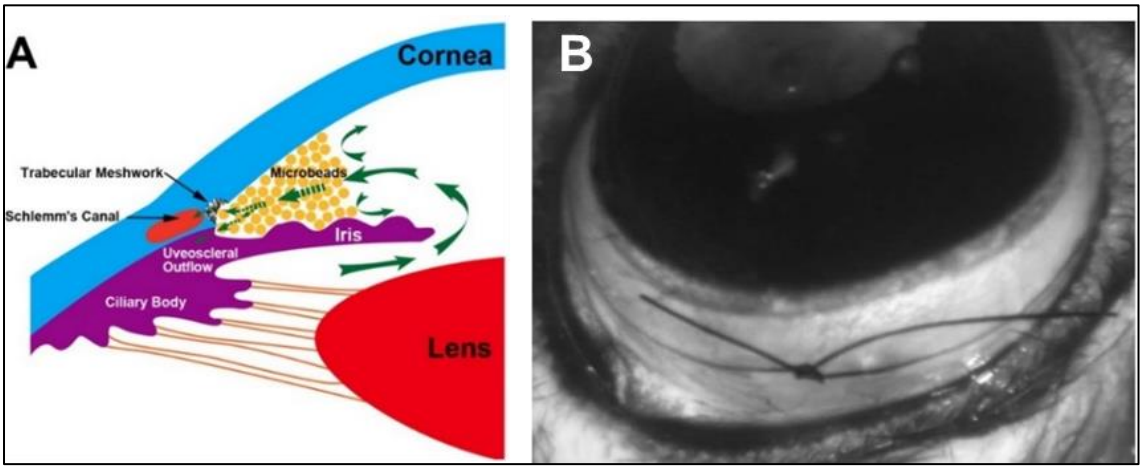

1.4.2.2.2 Circumlimbal Suture Model of OHT

More recently, investigators have developed a circumlimbal suture technique (Figure 5B) in which a suture is applied to the conjunctiva behind the limbus of the eye, which results in OHT for 8-15 weeks (He et al. 2018; Liu et al. 2015). Studies utilizing this

Figure 5: Recently Developed Models of OHT: A) Microbead model, showing a schematic of the anterior chamber with aqueous humor flow path depicted by green arrows with yellow microbeads in the iridocorneal angle (Yang et al. 2012). B) Circumlimbal suture model, showing a suture tied firmly posterior to the limbus of the rat eye (Liu et al. 2015).

method see a mild loss of RGC function after 8 weeks of elevated IOP as well as retinal nerve fiber layer thinning and minor RGC density loss after 15 weeks of elevated IOP (Liu et al. 2015). There are several limitations of using the circumlimbal suture model of hypertension, including: 1) the need for a trained surgeon to properly implement the model, 2) a high IOP spike of up to 81 mmHg immediately after suture application, 3) uncertainty about the exact method of IOP elevation, and, most importantly, 4) only transient RGC functional loss, i.e. RGC function has been shown to recover to baseline levels after removing the circumlimbal suture at 8 weeks after initial application (Liu et al. 2017).

Upon close evaluation of each of these models and evaluation of preliminary data, we have chosen to implement the magnetic microbead model of OHT. We have adapted the procedures used by Foxton et al. and Bunker et al. (Foxton et al. 2013; Bunker et al. 2015).

1.5 Assessing Glaucomatous Damage

Typically, when evaluating a treatment for glaucoma, rodent models rely on molecular assays and RGC quantification instead of evaluating visual or retinal function (Chen et al. 2011; Wareham et al. 2019; Yang et al. 2012; Foxton et al. 2013). These include measurement of anterograde axonal transport (Lambert et al. 2011), immunohistochemical analysis of protein levels (Inman et al. 2013), and/or qualitative fundus and histological examinations (Levkovitch-Verbin et al. 2002). Visual and retinal function are rarely assessed in glaucoma studies (Ishikawa et al. 2015). Here we review several possible outcome measures to assess glaucomatous damage.

1.5.1 *Morphological Outcome Measures*

1.5.1.1 RGC Axon Counts

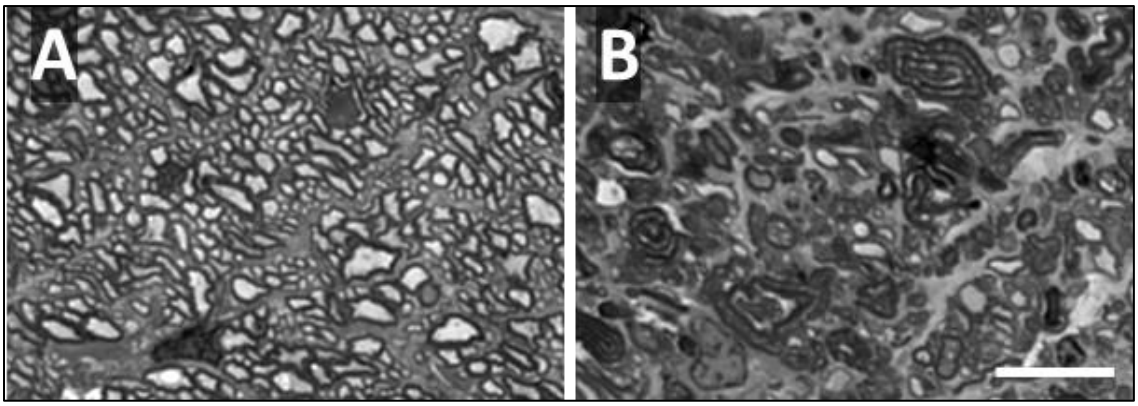

Figure 6: Optic nerve cross sections with healthy (A) and severely damaged (B) RGC axons. Healthy axons have a homogeneous interior surrounded by a uniform myelin sheath. Damaged axons have heterogeneous interiors and are typically hyper-myelinated. Scalebar is 10µm.

Quantification of RGC axons is currently the gold standard for analyzing glaucomatous damage in animal models, since studies suggest that up to 25-35% RGC loss can occur before a significant decrease in visual function outcomes can be detected (Medeiros et al. 2013) using tests such as electroretinography (ERG) and optomotor response (OMR) (see below). Healthy axons present a homogeneous texture and light interior color surrounded by a thin myelin sheath and relatively simple shapes resembling ellipses or circles (Figure 6A). Degenerating axons present darker and irregular interior color and texture and are surrounded by much thicker myelin sheaths and/or show highly irregular shapes (Figure 6B)(Read and Govind 1997).

Currently, manual counting performed by an expert is considered the most reliable method for quantification of optic nerve axons. However, as rat optic nerves contain tens of thousands of axons (Templeton et al. 2014), manual counts are extremely time- and labor-intensive. Indeed, it is possible to count only part of the full nerve cross section, and thus investigators extrapolate such limited counts to estimate the full count. This approach

saves time but suffers from inevitable counting variability within and between experts. Another method, the semi-automated approach, combines human selection of regions of homogeneous damage and computer-assisted counting within those regions (Marina, Bull, and Martin 2010b). Although more desirable than full or partial manual counts, a fully automated technique remains preferable to a semi-automated approach.

Fully automated counting methods attempt to provide counts with higher repeatability in a shorter time than manual or semi-automated counting. Existing automated counting software such as AxonMaster (Reynaud et al. 2012) involve thresholding and edge-finding algorithms targeting myelin sheaths, as they are darker and easily distinguishable from the optic nerve extracellular matrix. AxonMaster has been validated for use in healthy and glaucomatous non-human primate ONs, but not in rodents. Therefore, for this work, we developed a machine learning-based algorithm to automatically count normal RGC axons in rodents and non-human primates (described in Appendix A).

1.5.1.2 Optical Coherence Tomography

Optical Coherence Tomography (OCT) is an interferometric imaging technique used to visualize, among other tissues, the retinal layers and ONH *in vivo* (Szigeti et al. 2014; Schuman, Hee, Arya, et al. 1995). Glaucoma can be clinically diagnosed using OCT imaging to visualize structural changes at the ONH and retinal thinning (Quigley and Sommer 1987; Schuman, Hee, Puliafito, et al. 1995). Although it is difficult to accurately measure rat retinal thickness using OCT, studies have been able to resolve changes in retinal thickness measurements using OCT in glaucomatous rats (Feola et al. 2019; Nagata

et al. 2009). Thickness measurements using OCT also have been correlated to thickness measurements in paraffin-embedded sections (Figure 7), adding to the reliability of this metric (Nagata et al. 2009).

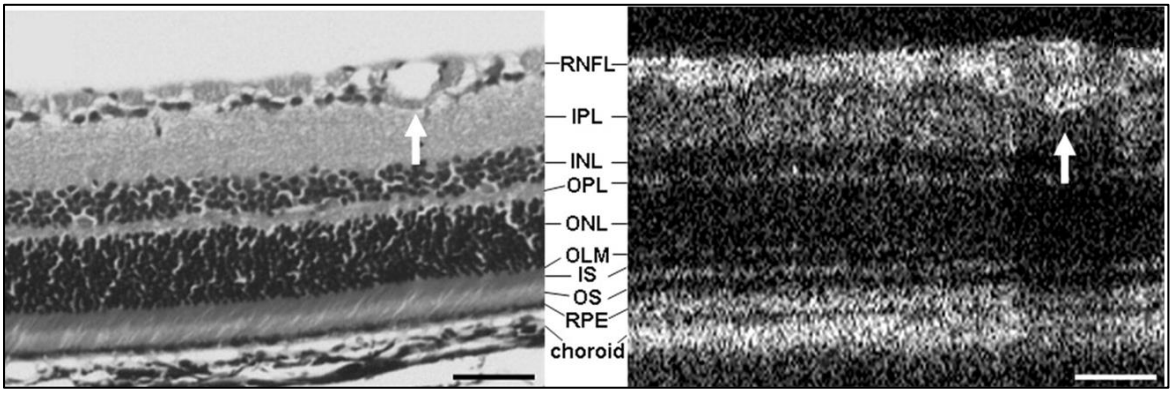

Figure 7: Paraffin-embedded retinal section (left) and corresponding in vivo OCT (right) from rat. Arrows indicate a major blood vessel. Scale bar, 50 μm. Adapted from (Nagata et al. 2009).

1.5.2 *Functional Assessment of Glaucomatous Damage*

Functional assessments are incredibly important when evaluating a potential treatment for glaucoma, since one must ensure that a proposed treatment has in fact preserved some visual function. The optomotor response (Prusky et al. 2004; Douglas et al. 2005) evaluates visual acuity and contrast sensitivity and is important to evaluate retinal toxicity (Redfern et al. 2011). This technique has recently been applied to assess glaucomatous damage in rats (Sapienza et al. 2016; Feola et al. 2019). Sapienza et al. induced OHT using episcleral vein cauterization and found a significant decrease in spatial frequency threshold at 7 days after induction (Sapienza et al. 2016). Feola et al. used the hypertonic saline/Morrison model of glaucoma to induce OHT and obtained significant deficits in both spatial frequency and contrast sensitivity at 4 weeks after induction (Feola et al. 2019).

The electroretinogram (ERG) is a tool to evaluate function of specific retinal neuronal layers using flash stimuli of varying intensities. Extensive research on ERG parameters by Porciatti, Bui, Fortune, et al. have led to several different procedures that can be used to selectively stimulate RGCs. These include analysis of the photopic negative response (PhNR), scotopic threshold (STR), and a variation of the ERG called the pattern ERG (Porciatti et al. 1996; Bui and Fortune 2004). Although the pattern ERG is widely used to assess RGC damage, we did not have access to an in-house validated pattern ERG experimental set-up. Therefore, I will explain the two former assessment techniques which use a full-field ERG.

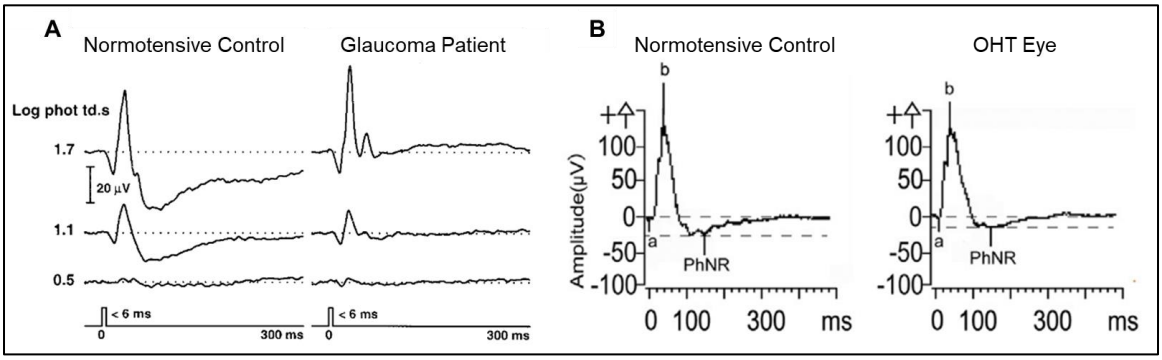

The PhNR is the negative potential that follows the b-wave in light-adapted (photopic) ERGs (Viswanathan et al. 1999). Clinical studies have shown significant reduction in the PhNR amplitude in glaucoma patients (Figure 8A), even when visual sensitivity losses are minimal (Viswanathan et al. 2001). However, is debate about whether the PhNR of rodents is affected after induction of OHT (Bui and Fortune 2004; Porciatti

Figure 8: Representative ERG waveforms from human (Viswanathan et al. 2001) and rat (B) eyes. A) Human ERG intensity series from age-matched normotensive eye and glaucomatous eye. B) Rat ERG from normotensive control and ocular hypertensive eye 7 days after microbead injection (Huang et al. 2018). A, b, and PhNR labels denote the a-wave, b-wave, and photopic negative response (PhNR) of each waveform, respectively. The decline in the PhNR amplitude is qualitatively more apparent in the human case when compared to the rat case.

2015). Huang et al. have evaluated changes in the PhNR after inducing OHT using the microbead model of glaucoma and found a significant decrease (Figure 8B)(Huang et al. 2018). In contrast, Liu et al. did not find any significant changes after using an optic nerve crush model in mice (Liu, McDowell, et al. 2014). We have also measured the PhNR in OHT eyes after using the microbead model of glaucoma. We failed to find any significant differences in PhNR amplitude, even when there was significant loss of visual function measured via OMR (data not shown). Therefore, we hypothesize that changes in a rat's PhNR after OHT may be more difficult to quantify than in humans, as we can qualitatively see in Figure 8.

Another outcome measure used to assess RGC function is the STR (Bui and Fortune 2004). The dark-adapted full-field ERG response at very dim flash intensities, also known as the scotopic threshold, has been shown to be due to RGCs in several different animals, including rats (Bui and Fortune 2004). Within the STR, there exists positive and negative potentials, known as the pSTR and nSTR, respectively. Bui et al. have also shown that the pSTR appears to be more sensitive to OHT damage than the nSTR (Bui and Fortune 2004). In our preliminary studies, we have found similar results, i.e. the pSTR appears to be affected before the nSTR when inducing OHT using the microbead model of glaucoma (data not shown).

From these literature studies, we have identified an ERG protocol to assess RGC function (STR), as well as two OMR outcome measures to assess visual function (spatial frequency and contrast sensitivity). These functional outcome measures, along with morphological outcome measures (RGC axon counts and retinal thickness) will be used to evaluate our proposed scleral stiffening treatment in the rat microbead model of OHT.

Specific Aims

1.6 Aim 1: Evaluate the efficacy of potentially biocompatible non-photoactivated collagen crosslinking agents on posterior rat sclera *ex vivo.*

Various natural collagen crosslinkers have been used to stiffen collagenous ocular tissues *ex vivo*. However, the dose-response relationship for these agents has not been explored nor evaluated for use in rat sclera. **Approach:** Rat eyes will be partially incubated overnight in one of three different crosslinking agents at varying concentrations *ex vivo.* We will use whole globe inflation tests to determine the relative stiffness between treated and untreated regions of the eyes. We will use these data to develop dose-response curves for each agent and select which candidate crosslinking agent provides the most viable and efficacious results for our *in vivo* studies. **Impact:** The mechanical results will: i) demonstrate the first use of collagen crosslinking agents to stiffen the rat sclera *ex vivo,* and ii) provide information on the effective dosage required to stiffen the posterior sclera by a desired amount.

1.7 Aim 2: Optimize the in *vivo* delivery technique of a chosen stiffening agent selected in Aim 1, and characterize the resulting duration of increased scleral stiffness, and potential adverse effects *in vivo.*

Although considered biocompatible, there have been no studies to evaluate the potential toxicity of our candidate crosslinking agents, nor of the longevity of the resultant increased scleral stiffness. **Approach:** After selecting a crosslinking agent based on data from Aim 1, we will determine the injection approach, volume, and concentration that

optimize the effects of the stiffening agent on the posterior globe. Animals will be sacrificed at 1 day and 4 weeks post-injection and we will perform whole globe inflation tests on enucleated eyes to determine stiffening effects in the posterior sclera relative to the contralateral sham-treated control eye. Evaluation of adverse effects will be determined by visual acuity assays including electroretinography (ERG) and optomotor response (OMR) at 0, 1, 2, and 4 weeks post-injection. We will assess damage RGC damage by creating machine-learning based software to automatically count normal RGC axons in optic nerve sections. **Impact:** We will determine an optimal delivery technique, the resulting longevity of scleral stiffening, and any cytotoxic effects due to the stiffening agent. This will inform any future studies utilizing this agent in the eye, as well as Aim 3.

1.8 Aim 3: Determine efficacy of stiffening the posterior sclera as a possible neuroprotective therapy in glaucoma.

In a rat model of glaucoma, we will stiffen the sclera, induce ocular hypertension and evaluate retinal and visual acuity throughout a two-week study, assess retinal ganglion cell morphology, and confirm scleral stiffening. **Approach:** We will inject our chosen stiffening agent using the methodology determined in Aim 2 and then induce ocular hypertension using a rat model of glaucoma. Over the course of the 14 day study, we will measure intraocular pressure regularly, evaluate retinal and visual function using ERG and OMR weekly, and assess retinal morphology through optical coherence tomography (OCT) imaging. After sacrifice, we will conduct RGC axon counts from optic nerve cross sections and perform whole globe inflation testing to verify the success of scleral stiffening. **Impact:** These assays will allow us to determine whether delivery of a stiffening agent to

the posterior sclera provides neuroprotection in glaucomatous eyes; if successful, this work may translate to future clinical trials.

Quantification of Efficacy of collagen cross-linking agents to induce stiffening of rat sclera

1.9 Submission Details

Authors: Ian C. Campbell, **Bailey G. Hannon**, A. Thomas Read, Andrew J. Feola, Joseph M. Sherwood, Stephen A. Schwaner, and C. Ross Ethier

Status: Published in Journal of the Royal Society Interface, **14**(129): 20170014.

Contributions: **Bailey G. Hannon** helped to design and troubleshoot the DIC inflation test, determined efficacious crosslinking agents for use, performed all inflation experiments, and helped write the paper.

Ian C. Campbell was a post-doc in the Ethier lab who played a key role in developing the DIC inflation testing hardware and software, performed the data analysis for this paper, and helped write the paper.

1.10 Abstract

The concept of scleral stiffening therapies has emerged as a novel theoretical approach for treating the ocular disorders glaucoma and myopia. Deformation of specific regions of the posterior eye is innately involved in the pathophysiology of these diseases, and thus targeted scleral stiffening could resist these changes and slow or prevent progression of these diseases. Here, we present the first systematic screen and direct comparison of the stiffening effect of small molecule collagen cross-linking agents in the posterior globe, namely using glyceraldehyde, genipin, and methylglyoxal (also called

pyruvaldehyde). To establish a dose-response relationship, we used inflation testing to simulate the effects of increasing intraocular pressure in freshly harvested rat eyes stiffened with multiple concentrations of each agent. We used digital image correlation to compute the mechanical strain in the tissue as a metric of stiffness, using a novel treatment paradigm for screening relative stiffening by incubating half of each eye in cross-linker and using the opposite half as an internal control. We identified the doses necessary to increase stiffness by approximately 100%, namely 30 mM for glyceraldehyde, 1 mM for genipin, and 7 mM for methylglyoxal, and we also identified the range of stiffening possible to achieve with such agents. Such findings will inform development of *in vivo* studies of scleral stiffening to treat glaucoma and myopia.

1.11 Introduction

Vision loss has been ranked in patient surveys as the worst possible type of health outcome, equivalent to a diagnosis of cancer, HIV/AIDS, and losing a limb (Scott et al. 2016). It is therefore unfortunate that there is no known cure for either glaucoma, the second leading cause of blindness (Tham et al. 2014), or myopia, the most common vision disorder (Foster and Jiang 2014) with incidence rates approaching 90% in some countries (Morgan, Ohno-Matsui, and Saw 2012). Although both diseases can be treated, these treatments are not successful in all patients and are not a true cure. In glaucoma, for example, 25-45% of patients continue to lose vision even with treatment (Anderson et al. 2001; Heijl et al. 2002; Noecker 2006). At present, all therapies for glaucoma are based upon the notion of reducing intraocular pressure (IOP); when these approaches fail, there is no alternative treatment paradigm. Thus, there is significant clinical need for novel treatments for vision loss from glaucoma and myopia.

Some evidence suggests that stiffening the sclera may be a beneficial treatment for these diseases (reviewed extensively in (Campbell, Coudrillier, and Ethier 2014)). In glaucoma, the elastic modulus of the peripapillary sclera (the region immediately surrounding the optic nerve) has been shown in computer models and physical tests to strongly influence deformation of the lamina cribrosa, the region where axonal damage first starts (Campbell, Coudrillier, and Ethier 2014; Sigal, Flanagan, and Ethier 2005; Anderson and Hendrickson 1974; Quigley and Anderson 1976; Coudrillier, Campbell, et al. 2016; Coudrillier, Geraldes, et al. 2016). In myopia, the stiffness of the sclera may play a role as well, although conflicting data exists, warranting further study (Grytz and Siegwart 2015; Phillips and McBrien 2004). Finally, corneal stiffening is currently used as a clinical treatment for keratoconus (Goldich et al. 2012), suggesting that the eye can tolerate local modulation of the stiffness of its collagenous tissues.

Pursuant from this evidence, *in vivo* testing of scleral stiffening therapies for disorders of the posterior eye is indicated. This requires dose-response relationships for suitable such agents to be well understood. Collagen crosslinking agents have been used in the orthopedic and ophthalmic literature to modulate stiffness, and based upon this evidence, three agents have emerged with potential for posterior eye scleral stiffening: glyceraldehyde (Danilov et al. 2008; Hwang et al. 2013; Kimball et al. 2014; Spoerl, Boehm, and Pillunat 2005; Wollensak and Iomdina 2008a, 2008b; Wollensak and Spoerl 2004; Mattson et al. 2010), genipin (Avila and Navia 2010; Hrabchak et al. 2010; Hwang et al. 2011; Liu, Luo, et al. 2014; Liu and Wang 2013; Wang and Corpuz 2015; Wong et al. 2012; Xu, Chow, and Zhang 2011), and methylglyoxal (Spoerl, Boehm, and Pillunat 2005; Stewart et al. 2009; Wong et al. 2012) (also called pyruvaldehyde). Glutaraldehyde

is known to increase scleral stiffness (Coudrillier, Campbell, et al. 2016; Kimball et al. 2014) but is toxic *in vivo* (Ballantyne and Myers 2001), and riboflavin, used in treatment of keratoconus, requires ultraviolet light to induce crosslinking (Goldich et al. 2012), which adds complications for posterior eye delivery in a clinical setting.

Although these agents have been identified and studied in an ocular context, no studies to date have directly compared the dose-stiffening relationship of all these agents for sclera. A few studies have examined multiple agents (Spoerl, Boehm, and Pillunat 2005; Wong et al. 2012) or more than two concentrations of a single agent (Avila and Navia 2010; Liu and Wang 2013; Stewart et al. 2009) side by side, but the paucity of agents interrogated with identical testing methodologies limits the ability to widely compare the dose-stiffening relationship of scleral collagen crosslinking agents. Given the prevalence and acceptance of rodent models in pre-clinical studies of treatments for vision disorders, there is also significant need for a well-characterized dose of scleral stiffening agents to be used in animal trials. Here, we hypothesize that incubation in collagen cross-linking agents will locally reduce the strain in the sclera resulting from elevated IOP in a dose-dependent manner. In this study, our specific objective is to determine the dose-response of each agent's effect on scleral stiffness with a goal of approximately doubling scleral stiffness (roughly the magnitude observed in prior trials (Kimball et al. 2014)) for future use *in vivo*.

1.12 **Methods**

1.12.1 *Animals*

Eyes were freshly harvested from a total of 67 euthanized male, retired breeder (approximately 9–12 months old) Brown Norway rats (Charles River Laboratories, Inc.,

Wilmington, MA) that were otherwise experimentally naïve. All procedures were approved by the Institutional Animal Care and Use Committee at the Georgia Institute of Technology, and all experiments were performed in compliance with the ARVO Statement for the Use of Animals in Ophthalmic and Vision Research. Female retired breeders were not used in this initial study, as estrogen is known to modulate collagen density and turnover with mechanical consequences (Wei et al. 2012), and female rats that have had numerous litters (such as retired breeders) may have atypical estrogen levels. Further work will consider animals of both genders.

Based upon the results of preliminary studies performed during methods development, we used an *a priori* power analysis to estimate that we needed 3 rats/concentration/agent (nested 2-factor ANOVA [agent and concentration]; α=0.05; ratio of treatment effect to error effect size = 1.2; 95% power). To be conservative, we harvested 5 eyes per group and used all that were not excluded due to methodological problems (e.g. puncture while cleaning or air bubble when inflating) except for two groups where we harvested 8 eyes (62.5 mM and 125 mM glyceraldehyde). Eyes were randomized.

1.12.2 *Tissue Preparation*

1.12.2.1 Stiffening Agents

Stiffening agents and administered concentrations were chosen based on published studies (Avila and Navia 2010; Danilov et al. 2008; Hrabchak et al. 2010; Hwang et al. 2013; Hwang et al. 2011; Kimball et al. 2014; Liu, Luo, et al. 2014; Liu and Wang 2013; Mattson et al. 2010; Spoerl, Boehm, and Pillunat 2005; Stewart et al. 2009; Wang and Corpuz 2015; Wollensak and Iomdina 2008a, 2008b; Wollensak and Spoerl 2004; Wong

et al. 2012; Xu, Chow, and Zhang 2011). We used three agents: Genipin (078-03021, Wako Pure Chemical Industries, Ltd., Richmond, VA), Glyceraldehyde (G5001-5G, Sigma-Aldrich Corp., St. Louis, MO), and Methylglyoxal (W296902-100G, Sigma-Aldrich Corp., St. Louis, MO). Several concentrations (Table 1) of each agent were used to establish a dose-response curve of concentration and relative stiffness. All dilutions were made in phosphate-buffered saline (PBS) except for glyceraldehyde, which was made at stock concentration (500 mM) in deionized water to obtain an osmolality similar to extracellular fluid, then diluted further with PBS.

Table 1: Concentrations of all stiffening agents tested.

Stiffening Agent	Concentration (mM)	Concentration (% w/v in PBS)
Genipin	0.25, 0.50, 1.0, 7.5, 15, 30	0.006, 0.011, 0.023, 0.170, 0.339, 0.679
Glyceraldehyde	10.0, 30.0, 62.5, 125	0.090, 0.270, 0.563, 1.126
Methylglyoxal	3.5, 7.0, 14	0.025, 0.050, 0.101

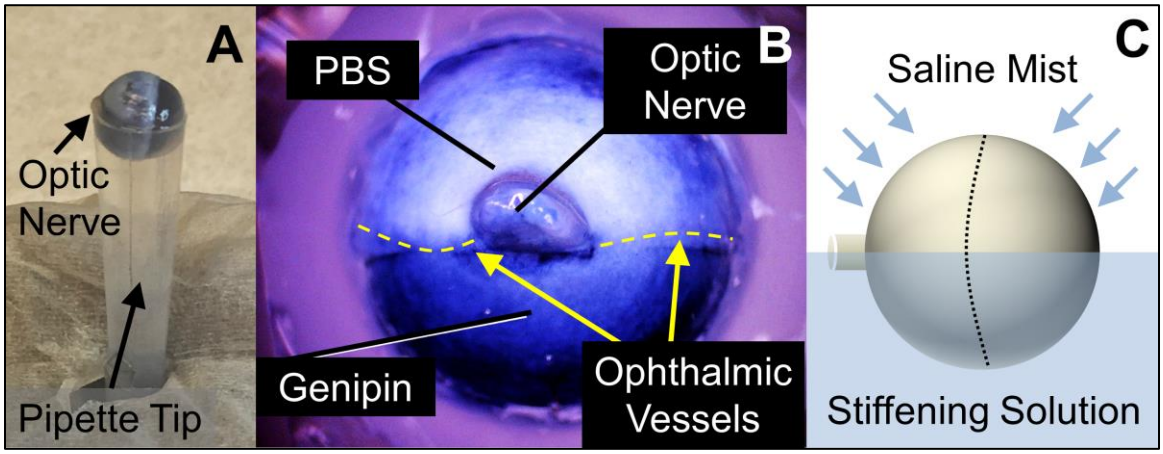

Figure 9: Eyes were partially immersed in cross-linking agents, exposing approximately half the eye to a stiffening agent overnight by mounting it in a trimmed pipette tip (A). Genipin, which is also used as a blue dye, provides a visual indicator of its location (B). This is closely localized to the treated region and demonstrates little evidence of wicking. Regions appearing blueish near the top of panel (B) are actually thin regions of translucent sclera where choroid is visible, not regions exposed to genipin. Eyes were then incubated overnight while misting the tissue-draped control half with PBS to keep it moist (C). Dashed line indicates limbus.

1.12.2.2 Partial Incubation Technique

Intact eyes were incubated in stiffening agents overnight, such that half the sclera was immersed in the stiffening solution (treated) and the other half (control) was moistened by PBS. Freshly harvested rat eyes were cleaned under a dissecting microscope by carefully removing excess fat, connective tissue, and musculature from the posterior sclera. A 3 ml polypropylene transfer pipette (225, Samco Thermo Scientific, Waltham, MA) was then trimmed to yield a cone approximately the diameter of the eye (approximately 6.5 mm). The eye was then gently placed into the cut pipette with the anterior-posterior axis (identified by the position of the optic nerve) parallel to the cut

Figure 9A) with the ophthalmic blood vessels aligned with the cut and serving as natural landmarks to aid in identifying the scleral region exposed to stiffening agent. Two small (approximately 1 mm diameter) droplets of glue (Loctite Super Glue Ultragel Control, Henkel Corporation, Westlake, OH) were applied to the cornea with a toothpick, attaching the cornea to the pipette, and a third droplet was carefully applied to the face of the distal optic nerve so that no glue touched the sclera. Drops of PBS were applied to keep the eye moist during handling. Stiffening agent (Table 1) was injected slowly into the pipette tip with a hypodermic needle until all air was evacuated.

Once the pipette was filled with the agent, a small rectangle (4 x 8 mm) of paraffin film was tightly wrapped around the opening at the bottom of the pipette to prevent any stiffening agent from leaking out. A Kimwipe was cut into a 5 x 5 cm cross shape, wetted with PBS, draped over the top of the eye, and then wetted with PBS to maintain moisture in the region not immersed in stiffening solution. The entire assembly (pipette, eye, and

Kimwipe) was then placed into a PBS-filled 1.5 ml microtube with the dangling strips of the Kimwipe allowing PBS to wick up to keep the control portion of the eye moist. To further maintain physiological conditions overnight, the microtube was placed in a floating rack in a 37°C water bath (Precision Shallow Chamber Water Bath 280, Thermo Scientific, Waltham, MA) and misted from above (Monsoon RS400, EXO TERRA, Mansfield, MA) every 3 minutes with PBS (Figure 9C). Eyes were carefully removed from the tube the next day (approximately 16 hours incubation time) and mounted for inflation testing.

1.12.3 *Inflation Testing*

Stiffening agents were evaluated by comparing mechanical strain measurements (stiffened vs. control regions) during whole globe inflation tests. We modulated the intraocular pressure of each eye while submerged in a PBS bath at physiological temperature. Calibrated stereo cameras (including compensation for refraction through PBS) imaged a speckle pattern on the surface of the eye throughout the inflation test, and 3D digital image correlation (DIC) was used to quantify surface strain (Q-400 DIC, Dantec Dynamics, Holtsville, NY).

1.12.3.1 Testing Chamber Construction

The eye was submerged in a temperature controlled, PBS-filled plastic chamber (Kritter Keeper, Lee's Aquarium & Pets, San Marcos, CA) during experimentation. To model physiological conditions *ex vivo*, the temperature of the PBS in the chamber was maintained at 37°C ± 2°C throughout the experiment by pumping saline through a thermoelectric heater assembly (LA-045-24-02-00-00, Laird Technologies, London, UK; temperature controller TC-XX-PR-59; measured by thermistor TC-NTC-1 immersed next

to the eye) using a peristaltic pump (BT300L, Golander LLC, Duluth, GA; pump head DT15-44; tubing #25 [ID 4.8 mm, OD 8 mm]) at 60 ml/min. This low flow rate was selected so as not to produce any turbulence and resultant optical distortion in the PBS around the eye.

To avoid evaporation of PBS during experimentation, a 1/8" thick borosilicate glass sheet was placed over the chamber and warmed to 70°C to prevent condensation (3682K25, McMaster Carr, Douglasville, GA; PID controller 36815K71). The mounted eye was then illuminated from above with dual gooseneck lighting (Mi-LED-US-DG, Dolan-Jenner Industries, Boxborough, MA).

An adjustable-height pressure reservoir (Sherwood et al. 2016) was connected to the base of the chamber through silicone tubing connected to a bulkhead fitting. This presented a female luer connection on the inside surface of the chamber where we could attach mounted eyes and modulate their IOP using hydrostatic pressure.

1.12.3.2 Mounting Procedure

Prior to experimentation, custom-made mounting blocks (Figure 10) were manufactured from acrylic sheets (8560K369, McMaster Carr, Douglasville, GA). A 1/4" diameter ball end mill created a hemispherical cradle for rat eyes, and a thin channel was drilled through the block with a 1/16" drill bit. This hole was widened opposite the indentation for the eye using a 3/16" drill bit that could accept a luer fitting adaptor

Following overnight (16 hours) incubation, the orientation of the eye relative to the solution was recorded. The cornea was blotted dry with a Kimwipe, and a small, continuous

bead of gel superglue was applied along the inner rim of the mounting block hemisphere. The eye was then placed onto the hemisphere, cornea-side down, with the optic nerve centered upwards, and excess glue was scraped away. The mounting block was marked with a waterproof marker to record the region of the eye that was incubated in stiffening solution.

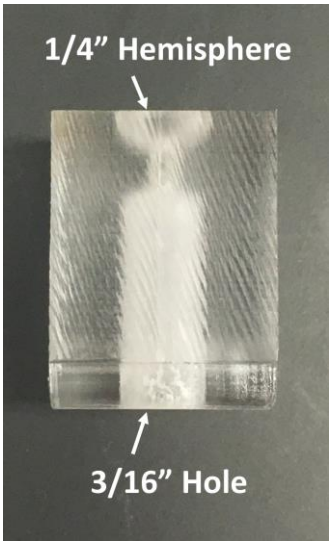

Figure 10: Side view of acrylic mounting block. Eyes are placed in the hemisphere at top, and a threaded luer fitting mates with the hole in the bottom.

In order for DIC to evaluate displacements, a speckle pattern must be applied to the tissue. For this study, the speckle pattern was applied to the posterior sclera with graphite powder (#970 PG, General Pencil Company, Inc., Redwood City, CA). Graphite was poured onto a fine mesh sieve (Tensile bolting cloth #60, Amazon) and an airbrush was used to blow the powder through the sieve onto the external surface of the eye and allowed to dry briefly. This method was repeated until the graphite powder formed a speckle pattern that did not detach from the surface of the eye when submerged in PBS. Eyes were immersed in ice-cold PBS until testing began.

1.12.3.3 Experimental Procedure

Prior to testing each day, the PBS chamber was filled and heated to temperature, and the intrinsic stereo calibration parameters of the cameras were determined using a standardized checkerboard calibration target. To inflate the eye, the cornea was punctured by inserting a 1 mm biopsy punch through the 3/16" hole in the mounting block and twisting gently until slight collapse of the eye was observed. Care was taken to ensure the eye not detach from the mounting block, nor the biopsy punch deeply penetrate the eye. A threaded male luer fitting (EW-45505-84, Cole-Parmer, Vernon Hills, IL) was then glued into the 3/16" hole.

The pressure reservoir was set to the height corresponding to the baseline IOP of 3 mmHg (approximately the minimum necessary to prevent the eye globe from buckling under its own weight). PBS was injected through polyethylene tubing into the lumen of the mounting block to purge all air bubbles. The eye was then submerged in the PBS chamber 25 mm below the surface, imparting an external pressure of approximately 2 mmHg to the eye, and attached to the luer fitting at the base of the chamber connected to the pressure reservoir. Extrinsic camera calibration parameters were then determined after the eye was mounted to account for refraction through the borosilicate glass sheet and PBS (Kunz and Singh 2008).

Effective IOP was calculated by subtracting the external pressure on the eyes (2 mmHg from the tissue bath) from the internal hydrostatic pressure from the reservoir. Images were captured every 30 seconds at an exposure time of 20 milliseconds for 30 minutes (see DIC system characterization results) at each of 3 pressures: 3

(low/hypotensive IOP), 13 (normal/normotensive IOP), and 28 mmHg (high/hypertensive IOP). The pressure reservoir was raised after each set of 60 images to the next height via stepper motor at a speed of 5 mm/second. Eyes were not preconditioned prior to inflation testing.

1.12.4 *Strain Calculation*

Dantec's Istra 4D software (v4.4.1) was used to compute displacement and resulting principal strains from the image dataset using DIC. Correlation settings were: 99 pixel facets, 45-pixel grid spacing, maximum permissible start points accuracy 0.2 pixels, residuum of 30 gray values, and 3D residuum of 1.1 pixels. All strain calculations were performed from smoothed displacement data using a 2D bicubic spline function to the data set. The grid reduction factor (minimizes the difference between the data point and the spline function) was set to 3 for displacement and 2 for contours, and the smoothness factor (straightens the filtered data) was set to 0 for both items.

Strain was computed relative to the reference state (3 mmHg after 30 minutes). Exported strain data for each image was then segmented (Figure 11) in custom MATLAB software (R2016a, MathWorks, Natick, MA) by manually tracing the experimental and control regions of the posterior sclera (excluding the optic nerve) based upon the markings made on the mounting block prior to testing. Relative stiffness as a percent change between E_{exp} (elastic modulus in the experimental region) and E_{con} (elastic modulus in the control region, see Appendix B for derivation) was defined as:

$$\text{Relative Stiffness} = \frac{E_{exp} - E_{con}}{E_{con}} = \frac{\varepsilon_{con} - \varepsilon_{exp}}{\varepsilon_{exp}} \times 100\% \quad (1)$$

where ε_{con} represents strain in the control region and ε_{exp} represents strain in the stiffened region. The calculation was performed following outlier removal, as described in Data Analysis

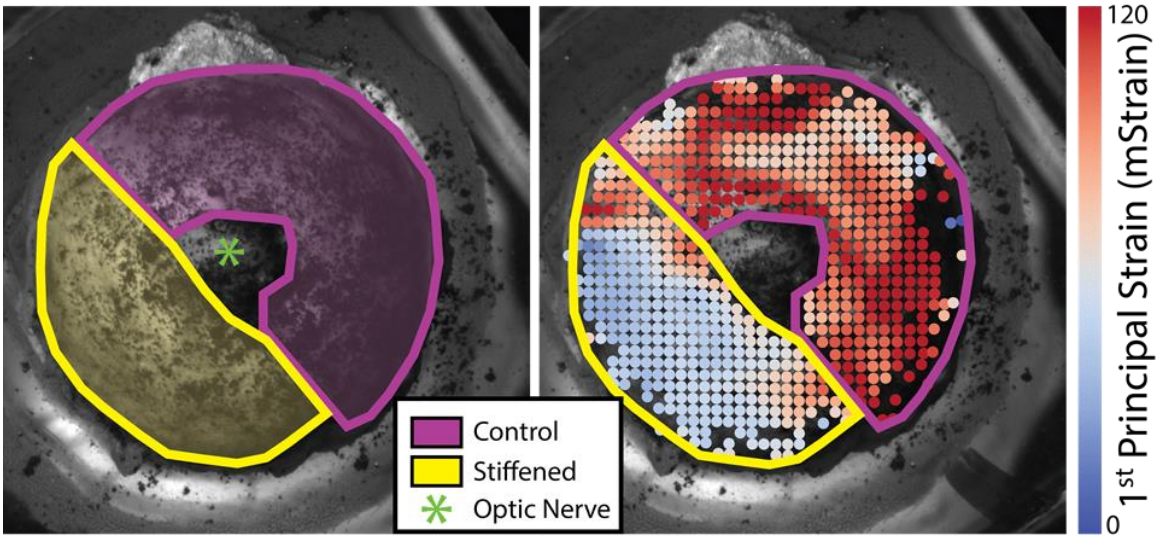

Figure 11: Digital image correlation was used to spatially resolve the surface strains in individual eyes. At left, the speckle pattern on the posterior sclera is overlaid with manually-traced masks (made prior to calculating strain) denoting the locations treated with cross-linking agent or PBS as a control, taking care not to include the optic nerve. At right, we have overlaid these same masks on the computed surface strains at an inflation pressure of 13 mmHg (normotensive). Regions of comparatively low and high strain match closely with the treatment and control zones.

1.12.5 *Data Analysis*

DIC data is noisy, particularly when dealing with small strains, as tiny errors in displacements become amplified in strain computations. Although smoothing displacements helps minimize this type of error, we required outlier detection to remove spurious data points. Having verified that the data was normally distributed within both the experimental and control regions of each eye at each time point (Anderson-Darling

normality test, $p>0.05$), the median absolute deviation (MAD) was calculated according to 1.4826 times the median of the absolute values of the difference between each data point and the median (Leys et al. 2013). Any values that were more than 2 MADs away from the median were considered to be outliers and removed from the data set.

We then computed the mean and standard deviation of the 1st principal Lagrange strain, as this metric is sensitive to deformation in the direction of local stretching were then calculated for a given control or experimental region at each time point. The primary deformation mode of a spherical eye is expected to be a hoop deformation, which would result in in-plane extension of the sclera; thus, the principal Lagrange strains should capture this effect. Following outlier removal, we used a weighted linear fit of this strain metric (weighted by $1/\sigma^2$) using Matlab's `lmfit` function using strains from the final 10 minutes at normotensive and hypertensive IOPs each. If the slope of this fit was above 0.5 millistrain (mStrain) per minute, we assumed the eye was creeping and had not reached its steady state, and thus the eye was discarded from further analysis (2 of 73 total inflation tests were excluded under this criterion). We then recorded the intercept of fits that were not excluded as well as the 95% confidence interval of the intercept of this fit as an indication of the uncertainty of the test.

Finally, we used equation 1 to compute the relative stiffness at normotensive and hypertensive IOPs for both the control and experimental halves of the eye. Using a nested 2-factor ANOVA (relative stiffening as a function of pressure nested within concentration; R 3.3.1), we compared the relative stiffness of each ocular region as a function of treatment and inflation pressure.

1.13 Results

1.13.1 *DIC System Characterization:*

We characterized two aspects of our inflation testing system. First, to estimate the baseline correlation noise of the system, we speckled a glass sphere approximately the same radius as a rat eye (3.25mm radius, 8996K25, McMaster-Carr), immersed it in our PBS bath, and imaged it for 8 hours. Noise was < 2 mStrain, indicating this level as the minimum resolvable strain magnitude.

To study the viscoelastic relaxation of pressurized rat eyes, we also imaged an untreated pair of rat eyes at pressure levels corresponding to baseline/hypotensive, normotensive, and hypertensive IOPs (3, 13, and 28 mmHg) for 2 hours per pressure level. We fit a standard Kelvin-Voigt model of viscoelastic relaxation

$$\epsilon(t) = A\left(1 - e^{-\frac{1}{\tau}t}\right) + C \tag{2}$$

to this strain ε as a function of time t in Matlab with fitting constants A, C, and τ, and we found that the time constant τ was approximately 1 minute. Out of abundance of caution, specifically to avoid confounding our stiffness findings with biomechanical creep of the scleral shell, we thus maintained our treated eyes for 30 minutes at these same three pressure levels and only analyzed data from the final 10 minutes of each pressure step.

1.13.1.1 Partial Immersion of Eyes in Collagen Crosslinking Agents:

Eyes were partially immersed in various stiffening agents overnight such that approximately half the eye was exposed to the collagen cross-linking agent and the other half to PBS as a control. Genipin, which is also used as a blue dye, acted as a visual reporter of its presence, confirming that the agent stayed constrained to the incubation region and did not diffuse or wick into the control region (Figure 9B). We also visually confirmed that agents did not adversely affect the structure of the eye. In preliminary experiments (not shown), we incubated eyes overnight in 500 mM glyceraldehyde, as has been done previously (Kimball et al. 2014; Spoerl, Boehm, and Pillunat 2005; Wollensak and Iomdina 2008a). However, the eyes were visibly dehydrated the following day. We calculated that the osmolarity of 500 mM glyceraldehyde is approximately 800 mOsm, whereas the osmolarity of aqueous humor and PBS is about 300 mOsm (Agarwal, Agarwal, and Apple 2002). Thus, we diluted the glyceraldehyde and only used lower concentrations in these experiments.

1.13.2 *Average Strain Magnitudes:*

In almost all eyes, the mean 1st and 2nd principal strains (representing stretch in the direction of greatest local deformation and the stretch orthogonal to this direction, both tangent to the surface of the eye) in the control half the eye were on the order of 40-150 mStrain at 13 and 28 mmHg, respectively, relative to the reference configuration at 3 mmHg. These strain values are well above the noise floor of our system. In the stiffened half of the eye, strains were lower, generally 10-50 mStrain, again above the noise floor. Strains stabilized within minutes of a change in pressure in all but 2 cases, and the

difference in strain between baseline/hypotensive and normotensive pressures was always considerably larger than between the normotensive and hypertensive pressures (Figure 12). 2nd principal strains in the posterior sclera were approximately half the magnitude of 1st principal strains, consistent with current understanding that there is a direction of preferential collagen fiber alignment but that the posterior sclera is quasi-transversely isotropic tangent to the scleral surface (Baumann et al. 2014). The distribution of strains within each region at any given timepoint followed a normal distribution (Anderson-Darling test; $p>0.05$).

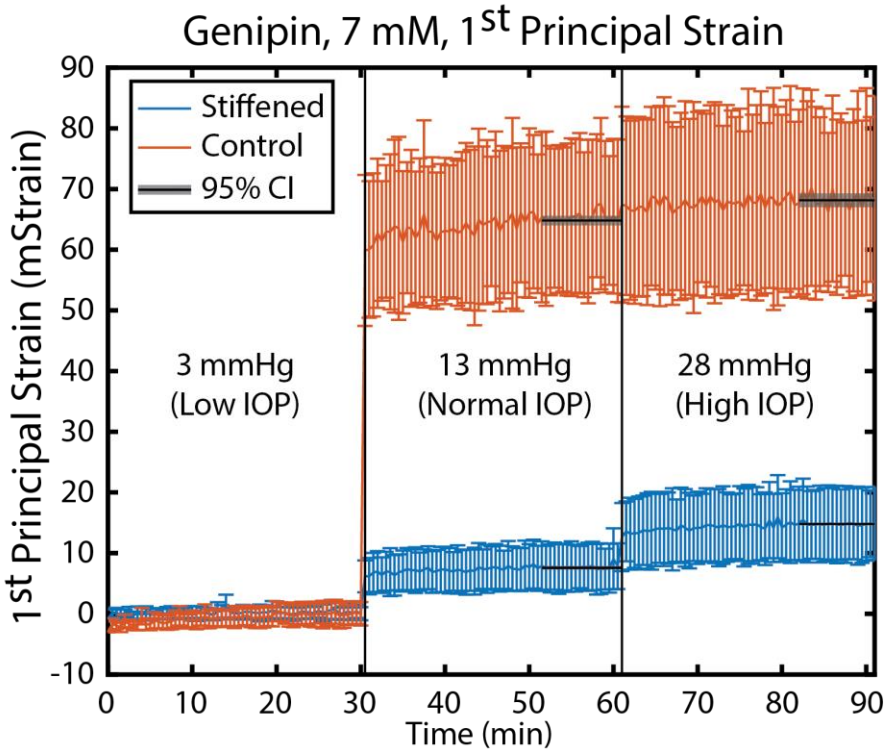

Figure 12: Representative plot of average 1st principal strain as a function of time from a single eye during our inflation experiment. Eyes were maintained for 30 minutes at each of 3 pressures representing different ranges of IOP. Strains were considerably higher in the control region of eye than in the treated region, indicating that the treated region is stiffer. Black overlays represent the 95% confidence interval about the mean during the final 10 minutes of each pressure step, when the eye reached steady state. Error bars: standard deviation over the interrogated region.

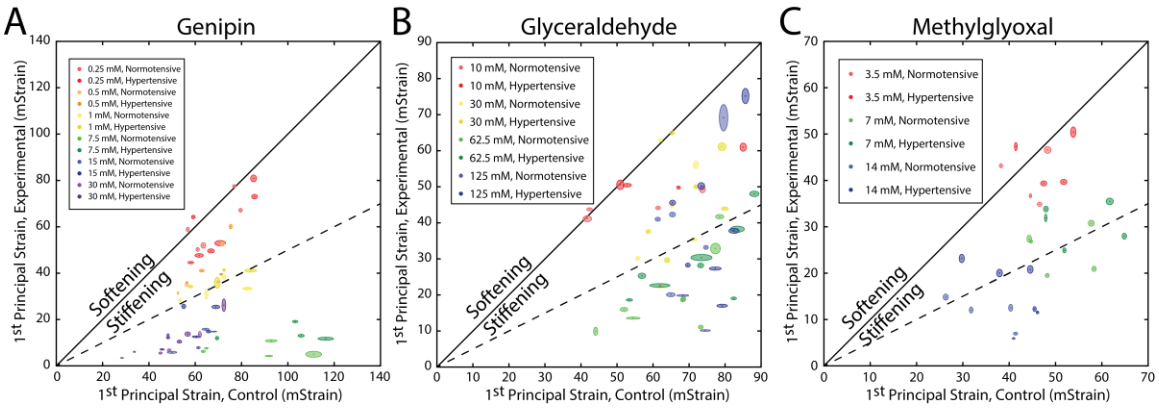

Figure 13: Average 1st principal strains for control (horizontal axis) and stiffened (vertical axis) regions of eyes treated with (A) genipin, (B) glyceraldehyde, or (C) methylglyoxal. Each dot represents the mean steady-state strain for one eye, and the surrounding oval represents the 95% confidence interval of that point from linear fitting. Points falling below the unity line (black line) indicate that the treated eye has been stiffened relative to the control, and mutatis mutandis. The dotted line represents 100% stiffening. Eyes in red lie very close to the unity line, suggesting that this low dose has minimal stiffening effect. Higher concentrations lie farther from the unity line until reaching a maximum effective dose around 7 mM for genipin, 62.5 mM for glyceraldehyde, and 14 mM for methylglyoxal. Higher concentrations do not further stiffen the experimental half the eye but do reduce strain in the control portion of the eye, possibly as result of diffusion into the internal tissues of the eye and crosslinking them.

1.13.3 *Relative Stiffening:*

We observed a significant ($p = 1.03\times10^{-9}$) stiffening effect (relative stiffening as a function of pressure nested within concentration; Table 2) pooled over all agents. All three agents demonstrated a dose-dependent stiffening effect where increasing the concentration of the solution increased the relative stiffness of the treated region. However, at very high concentrations (for genipin, above 7.5 mM; for glyceraldehyde, above 62.5 mM), increasing concentration did not increase stiffness. For genipin (Figure 13A), we observed stiffness increases between 14.7% and 1320%. For glyceraldehyde (Figure 13B), stiffness increased between 21.8% and 273%, and for methylglyoxal (Figure 13C), stiffness increased between 11.9% and 310% at the concentrations included in these studies. In order to achieve a target increase in stiffness of approximately 100% (Coudrillier, Geraldes, et

al. 2016), the appropriate dose for a rat eye overnight is therefore approximately 1 mM for genipin, 30 mM for glyceraldehyde, and 7 mM for methylglyoxal.

Table 2 Relative stiffening expressed as a percentage. Values are mean ± standard deviation.

Agent	Concentration (mM)	Relative Stiffening (%) at 13 mmHg	Relative Stiffening (%) at 28 mmHg	Number of Eyes (n)
Genipin	0.25	15 ± 14	19 ± 17	6
	0.5	64 ± 23	54 ± 23	4
	1	108 ± 28	86 ± 16	4
	7.5	1,321 ± 703	577 ± 220	5
	15	503 ± 252	253 ± 130	4
	30	576 ± 164	348 ± 137	5
Glyceraldehyde	10	22 ± 26	20 ± 20	4
	30	73 ± 64	55 ± 40	6
	62.5	273 ± 143	165 ± 75	8
	125	192 ± 214	131 ± 120	7
Methylglyoxal	3.5	12 ± 20	11 ± 19	4
	7	108 ± 52	81 ± 38	5
	14	310 ± 222	160 ± 119	5

1.14 Discussion

This study offers the first quantification of the efficacy of scleral stiffening agents in the rat eye, a common and important animal model of experimental glaucoma. It also offers the first demonstration of the efficacy of genipin and methylglyoxal in the rodent eye, an important milestone for use in mice, whose eyes have similar collagen composition to rats and are widely used in glaucoma and myopia research. We found that each agent is capable of stiffening the sclera by several hundred percent but that there exists an upper bound to this stiffening effect. This quantification sets a range on the magnitude one might be able to achieve using collagen crosslinking approaches to scleral stiffening. Researchers investigating the physiological consequences of scleral stiffening using these agents should not expect to increase stiffness by more than several hundred percent.

While we cannot determine the mechanism causing genipin to achieve its highest stiffness around 7 mM and glyceraldehyde around 30 mM from the data at hand, we hypothesize that the collagen crosslinking sites have become fully saturated at these higher concentrations. Thus, the presence of additional crosslinker may have no further effect. Although we did observe a drop in relative stiffness at the highest concentrations of genipin and glyceraldehyde in this study, this resulted from a decrease in strain in the control portion of the eye without change in the treated portion. Thus, this phenomenon should not be interpreted as a drop in efficacy at the highest concentrations. Instead, it is likely that the agents at these very high concentrations diffused through the eye into the internal tissues or even into the control portions, potentially crosslinking them and reducing strain, thereby decreasing the relative stiffness of the eye.

Our novel approach to treating approximately half an eye with stiffening agent overnight while using the other half as a control provides a powerful tool for studying the efficacy of small molecule collagen crosslinking agents. Although these agents may diffuse outside the desired region of the eye at very high concentrations, we do not believe this is a problem at the more moderate concentrations examined in this study. Genipin yields a visible blue dye at sites where it is present (Figure 9B), and this color change has previously been shown to correlate with scleral stiffness (Liu, Luo, et al. 2014), suggesting its relevance as a visual reporter of cross-linking. Glyceraldehyde and methylglyoxal have approximately half the molecular weight of genipin, and thus they may diffuse slightly faster but are not expected to considerably enter the control half of the eye. Strain maps for these eyes similar to Figure 11 show a relatively sharp line of demarcation between the two halves. To avoid confounding our analysis with any diffusion effects, however minor, we

also avoided including regions closest to the line of demarcation when computing average strain. As seen in Figure 11, the perimeters of the regions of interest do not overlap perfectly where they come closest to intersecting (there are no points included that are underneath the visible perimeters) in order to exclude strain measurements in the transition zone. Additionally, it is important to remember that the relatively higher strains in the stiffened region close to its boundary with the control region result from cross-linker not fully diffusing into this region, so we err on the side of under-diffusion, not cross-linker bleed-over. We also used outlier removal to eliminate any data points that deviated considerably from the median, such as those resulting from edge effects, and by computing the mean relative stiffness from several hundred data points per region after outlier removal, the effect of any small bleed-over should be small.

Our method of using half of each eye as experimental and control groups to compute relative stiffening is especially powerful when we consider the inter-eye variability in strains in naïve regions of eyes (and confirmed in fully untreated eyes, data not shown). Even in two eyes from a single rat, strains in PBS-treated regions can vary by a factor of approximately three (see dispersion of data points along X-axis in Figure 11). Thus, by using the two halves of each eye as an internal comparison, we can minimize the effects of inter-eye variability. While it is certainly true that strains are somewhat heterogeneous even within regions of a single eye (as in Figure 11) our technique for computing relative strain allows us to only introduce intra-eye variability without adding the effect of inter-eye variability to each relative strain calculation.

An additional benefit of using half the eye as an internal control and making a relative comparison is that the need for preconditioning is greatly reduced. Prior work such

as that of Wong et al. (Wong et al. 2012) used up to 10 cycles of preconditioning before the eye converged to a stable relation between inflation and strain. With our testing methodology, we are comparing the relative stiffness of two halves of a single eye such that preconditioning effects, or lack thereof, should be approximately uniform between the two halves. Thus, the strain magnitudes quantified in this study may not exactly equal ocular strains in the rat eye at various magnitudes of IOP, but the relative stiffening effect should still be relevant to future *in vivo* studies in the rat.

This study focused exclusively on eyes *ex vivo*, although we took care to freshly harvest eyes and maintain them at physiological temperatures during testing. We treated eyes overnight in order to simulate the stiffening effect that might result if such agents were delivered to the posterior eye within the Tenon's capsule. However, because this is a relatively un-explored frontier of ophthalmology, it is unclear what the body's clearance of such agents would be *in vivo*. Recently, Kimball et al. investigated the efficacy of glyceraldehyde scleral stiffening *in vivo* in a mouse model of glaucoma and found that its use was detrimental to visual function (Kimball et al. 2014). In an attempt to recreate the conditions of their study, we first attempted to study eyes incubated in 500 mM glyceraldehyde, identical to the Kimball et al. paper. However, eyes became significantly dehydrated and collapsed with this treatment, presumably from a significant osmolarity mismatch. Such an effect would clearly be problematic *in vivo* and could explain the negative findings of the Kimball study, but active transport of fluids in a living mouse also might be able to compensate for any osmolar mismatch. Further investigation is certainly warranted.

Eyes were freshly harvested from rats daily and randomized to a treatment agent and concentration. However, in an effort to ensure that our stiffening solutions were freshly-mixed from a stock solution, all eyes studied in a single day (usually 2-3 pairs) were incubated in a single agent, although often at different concentrations of that agent. Thus, one limitation of the present work is that some treatments were from both eyes of a single rat. Although Brown Norway rats are an inbred strain and thus should have low genetic variability, as previously mentioned, in initial testing prior to this study using naïve eyes (not shown), variability in average strain between two eyes from a single rat were high enough that, for this study, we assumed that each eye was an independent sample regardless of which rat it came from.

Although the eyes in this study were all studied within 24 hours of harvest, another unknown factor for scleral stiffening therapies is the temporal efficacy of such agents. Previously, Wollensak et al. showed that glyceraldehyde increases scleral stiffness for at least 8 months in rabbits (Wollensak and Iomdina 2008b), a promising finding. However, further work is necessary to characterize the temporal profile of the stiffening agents in this study, both in terms of how long the eye must be incubated in order to derive a stiffening effect as well as in terms of how long the eye maintains its increased stiffness before collagen turnover and remodeling negates the effects of treatment.

Eyes were incubated in agents for approximately 16 hours each, with an unavoidable variability of several hours as result of practical aspects of the eye mounting procedure, tissue cleaning, etc. Per Fick's law, the rate of diffusion into the tissue should drop as the concentration of cross-linker equalizes between the solution and the tissue. Additionally, we can approximately estimate an upper bound on the effects of different

incubation times using the fact that the diffusion distance is proportional to the square root of elapsed time, so a deviation of two hours less than our approximated 16 hours would lead to a variation in the extent of cross-linking of roughly 8-9% ($\sqrt{14/16}$), considerably smaller than the stiffening effects of 100% or more observed in this study. Further study is certainly warranted to better characterize the dynamics of cross-linking treatments to ocular tissues, but in the present study, we attempted to characterize the role of collagen cross-linking at various starting concentrations with the understood limitation that some modest variability in stiffening may result from variations in tissue preparation.

Having characterized these three collagen crosslinking agents *ex vivo*, our next step will be to deliver them to rats *in vivo* to answer the questions raised by this and other studies. Future work will need to characterize how well-tolerated these agents are by delicate neural tissues of the retina and optic nerve head, as well as by the scleral fibroblasts providing collagen turnover in the eye. If the stiffening agents have any sort of toxic effect to these components of the eye, it may be necessary to take care to use highly targeted delivery of such agents using novel drug delivery techniques. Such approaches might involve delivering agents with an activatable reservoir of cross-linker or by flushing away agents from undesired locations, but such techniques will need to be evaluated after determining whether scleral stiffening offers any benefit for glaucoma or myopia as well as which agents are the safest for *in vivo* use. It will also be important to quantify whether the same magnitude of relative stiffening for the concentrations of the agents measured here exists *in vivo* and how long the stiffening is maintained. Most importantly, future studies should build upon this foundation in order to evaluate the efficacy of various scleral

stiffening approaches for ocular diseases such as glaucoma and myopia in order to improve our clinical ability to preserve vision.

1.15 Conclusion

Here, we have reported the first direct comparison of the dose-response relationship of three stiffening agents in sclera. All three collagen cross-linking agents examined in this study, genipin, glyceraldehyde, and methylglyoxal, exhibited dose-dependent stiffening behavior, with maximum relative stiffening of several hundred percent at higher concentrations. Thus, all 3 agents can be titered to achieve a desired magnitude of stiffening. Future studies will examine the efficacy of these agents *in vivo* to ensure the stiffening effect is maintained in longitudinal studies and, more importantly, to assess whether scleral stiffening agents protect against vision loss in diseases like glaucoma and myopia.

Sustained scleral stiffening in rats after a single genipin treatment

1.16 Submission Details

Authors: **Bailey G. Hannon***, Stephen A. Schwaner*, Elizabeth M. Boazak, Brandon G. Gerberich, Erin J. Winger, Mark R. Prausnitz, C. Ross Ethier

Status: Published in Journal of the Royal Society Interface, 2019. **16**(159): 20190427.

Contribution: ***Bailey G. Hannon** co-authored this manuscript and contributed to the development of the inflation testing hardware improvements, performed all experiments, and wrote this paper.

*Stephen A. Schwaner co-authored this manuscript and contributed to the development of the inflation testing hardware improvements and created the MATLAB data analysis code.

1.17 Abstract

Scleral stiffening has been proposed as a therapy for glaucoma and myopia. Previous *in vivo* studies have evaluated the efficacy of scleral stiffening after multiple treatments with a natural collagen crosslinker, genipin. However, multiple injections limit clinical translatability. Here, we examined whether scleral stiffening was maintained after four weeks following a single genipin treatment. Eyes from Brown Norway rats were treated *in vivo* with a single 15 mM genipin retrobulbar injection, sham retrobulbar injection, or were left naïve. Eyes were enucleated either one day or four weeks post-injection and underwent whole globe inflation testing. We assessed first principal Lagrange

strain of the posterior sclera using digital image correlation as a proxy for scleral stiffness. Four weeks post-injection, genipin treatment resulted in a 58% reduction in scleral strain as compared to controls ($p = 0.005$). We conclude that a single *in vivo* injection of genipin effectively stiffened rat sclera for at least four weeks which motivates further functional studies and possible clinical translation of genipin-induced scleral stiffening.

1.18 Introduction

Scleral biomechanical properties are thought to play a role in two major ocular pathologies: glaucoma and myopia (Levy, Fazio, and Grytz 2018; Campbell, Coudrillier, and Ross Ethier 2014). Glaucoma, the leading cause of irreversible blindness worldwide (Cook and Foster 2012), is characterized by the loss of retinal ganglion cells (RGCs) at the optic nerve head (ONH). Although the exact etiology remains unknown, a major risk factor for glaucoma is elevated intraocular pressure (IOP) (Bengtsson and Heijl 2005). Elevated IOP leads to deformation of the ONH, which may negatively affect RGCs via several mechanisms, including changes in blood flow and chronic cellular mechanostimulation (Burgoyne 2011; Hernandez 2000). Previous work has shown that chemical crosslinking of the peripapillary sclera decreased IOP-induced ONH deformation (Coudrillier, Campbell, et al. 2016), making scleral crosslinking a potential therapeutic strategy for glaucoma patients.

Scleral crosslinking has also been proposed as a treatment for patients suffering from myopia (nearsightedness). Myopia is the most common refractive error and is expected to affect nearly half of the world's population by the year 2050 (Holden et al. 2016). In myopia, the eye elongates and the sclera becomes weaker and thinner due to

active remodeling of collagen (Rada, Shelton, and Norton 2006). Therefore, it is hypothesized that scleral crosslinking could slow or reverse the effects of the scleral remodeling to prevent late stage complications, more common in cases of high myopia (Saw et al. 2005).

Chemical crosslinking has been widely used to stiffen hydrogels and biological tissues (Sung et al. 2000; Yoo et al. 2011; Rowland et al. 2013). Recently, photochemical crosslinking of corneal collagen has been approved as an effective clinical treatment for keratoconus, in which the cornea becomes weaker and misshapen, resulting in impaired visual acuity (Hersh et al. 2017). This treatment uses Ultraviolet-A (UVA) irradiated riboflavin to induce crosslinking; however, this method has been shown to be cytotoxic to the retina when applied to stiffen the sclera (Glickman 2011; Wollensak et al. 2005). Therefore, alternative biocompatible treatments that avoid retinal UVA exposure are better suited for scleral stiffening (Backhouse and Gentle 2018).

Previous research in our lab has investigated the efficacy of three crosslinkers (methylglyoxal, glyceraldehyde, and genipin) to stiffen the rat sclera ex vivo (Campbell et al. 2017). Of these agents, genipin demonstrated effective stiffening at low concentrations and has been reported to be a biocompatible collagen crosslinker (Song et al. 2017; Sung et al. 2001). Further, Avila et. al (Avila, Gerena, and Navia 2012) evaluated genipin and riboflavin/UVA crosslinking in porcine corneas and found that both treatments yielded similar amounts of stiffening and minimal toxicity. Genipin has also been used to effectively stiffen tree shrew (Levy, Fazio, and Grytz 2018) and porcine (Wong et al. 2012; Liu, Luo, et al. 2014) sclera ex vivo, as well as rabbit (Liu and Wang 2017) and guinea pig (Wang and Corpuz 2015) sclera *in vivo*. A widely demonstrated scleral stiffening effect

and high biocompatibility of make genipin an excellent candidate for eventual clinical translation.

The current study presents new support for the use of genipin as a scleral crosslinker by demonstrating the ability of a *single in vivo* genipin injection to produce sustained stiffening in the rat (a useful model of ocular disease), with improved mechanical testing methods. All previously published *in vivo* studies have implemented multiple injections of genipin over time to stiffen the sclera (Liu and Wang 2017; Wang and Corpuz 2015). To assess translational potential, we tested whether scleral stiffness modifications were sustained for four weeks after a single injection of genipin. Additionally, these previous tests of *in vivo* genipin treatment have been evaluated by uniaxial strip testing. While these biomechanical tests measure intrinsic scleral stiffness, they are known to have significant limitations (Lari et al. 2012), including the inability to test the sclera under physiological modes of deformation. Thus, we utilized whole globe inflation testing, which more closely mimics *in vivo* scleral loading conditions (Campbell et al. 2017). Since glaucoma is a disease that progresses over decades, we were primarily interested in assessing the effects of our crosslinking treatment on the mechanical stiffness of the sclera at steady state than on assessing scleral viscoelastic properties, although the viscoelastic properties of the sclera may also be important in glaucoma due to fluctuations in IOP (Coleman and Trokel 1969).To focus on steady state properties, we chose a creep test rather than a ramp-hold test to assess the effects of our treatment on the sclera. Further, there were technical advantages to using a creep test (see Discussion). Finally, no previously published *in vivo* scleral stiffening studies have been conducted using rat eyes. The rat is a widely used model for vision research, and has several advantages for use as a glaucoma therapy test bed

(Morrison, Cepurna Ying Guo, and Johnson 2011), including the fact that there are established methods for inducing rat ocular hypertension that result in glaucomatous damage (Bunker et al. 2015; Bouhenni et al. 2012). Furthermore, evidence indicates that the rat sclera is structurally similar to that of the human, being composed mainly of collagen fibers (Cone-Kimball et al. 2013; Coudrillier et al. 2015) that are organized in a circumferential pattern near the optic nerve head and are less organized further from optic nerve head (Girard et al. 2011). In addition, the rat affords advantages over other glaucoma models. Namely, rat eyes are larger and much easier to test biomechanically than mouse eyes, and rats are more amenable for high subject studies compared to monkeys, due to their low cost, ease of animal husbandry, and low genetic variability between individuals. Rat models of myopia have also been reported (Shinohara et al. 2018; Zhang et al. 2013). Therefore, this study represents the successful development of methods to investigate genipin-induced scleral stiffening as a therapy for common ocular pathologies in an affordable animal model.

1.19 **Methods**

1.19.1 *Overview of Experimental Design*

In brief, rat eyes were treated *in vivo* with either a genipin or sham retrobulbar injection or were left naïve (Figure 14). Eyes were enucleated one day or four weeks post-injection and prepared for whole globe inflation testing to determine scleral stiffness. Whole globes were attached cornea-side down to a mounting block and IOP was controlled by raising and lowering a hydrostatic pressure reservoir in fluidic connection with the eye. Images were taken of the posterior sclera throughout the inflation test and analyzed by

digital image correlation (DIC) software to compute scleral surface displacement and strains. Pressure-strain data were fit with a constitutive equation that was then used to quantify scleral stiffening.

1.19.2 *Animals*

This study used twenty-eight retired breeder (male, 6–13 months old) Brown Norway rats (Charles River Laboratories, Inc., Wilmington, MA). All procedures were approved by the Institutional Animal Care and Use Committee at the Georgia Institute of Technology. Some rats from the starting cohort were removed from this study according to exclusion criteria, as described below.

1.19.3 *Scleral Stiffening Procedure*

Rats were anesthetized systemically with ketamine (60 mg/kg) and xylazine (7.5 mg/kg), and a drop of topical tetracaine (1%) was applied to the eye. Rats were randomly assigned to one of two groups for stiffening treatment (Figure 14). The first group (HBSS/Naïve) received a single (unilateral) retrobulbar injection of Hank's Balanced Salt Solution (HBSS; 150 µl), while the contralateral eye was left as a naïve control. The second group (Genipin/HBSS) received a single retrobulbar injection of genipin (Wako Pure Chemical Industries, Ltd., Richmond, VA) mixed in HBSS (15 mM, 150 µl), while the contralateral eye received a single retrobulbar injection of HBSS (150 µl). This genipin concentration was motivated by our previous ex vivo study (Campbell et al. 2017) and recent *in vivo* work (Table 3) (Liu and Wang 2017; Wang and Corpuz 2015). Eyes were randomized to each treatment. After injections, rats were given topical antibiotic (Certi-sporyn, Kansas City, MO) to prevent infection and antisedan (1 mg/kg) to reverse

anesthesia (Turner and Albassam 2005). Genipin/HBSS rats were divided into two subgroups and euthanized (via CO_2 overdose) either one day or four weeks post-injection. enucleated and refrigerated until testing, which always occurred within 6 hours of euthanasia. All Naïve/HBSS rats were euthanized one day post-injection. Eyes were immediately after euthanasia.

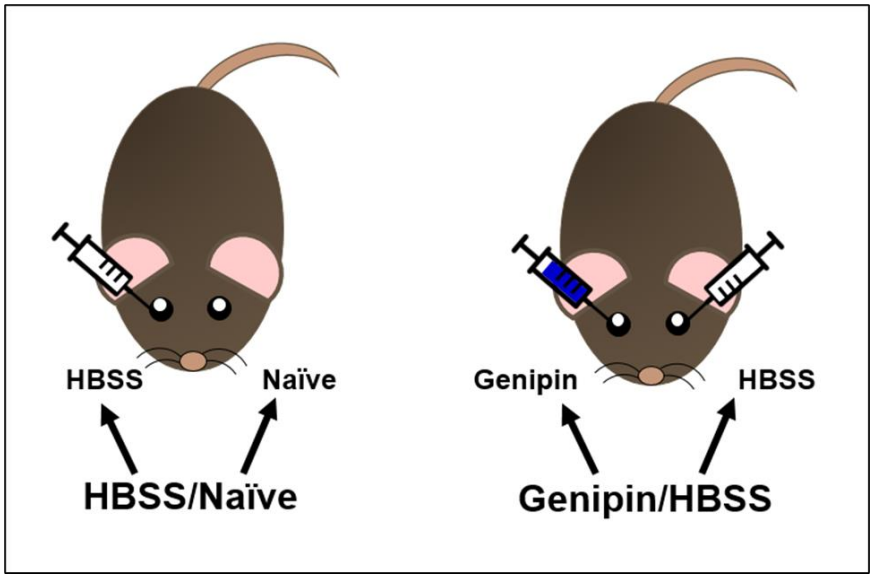

Figure 14: Experimental groups: HBSS/Naïve rats received a single (unilateral) retrobulbar injection of HBSS, while Genipin/HBSS rats received a unilateral retrobulbar injection of genipin and a unilateral retrobulbar injection of HBSS contralaterally.

Table 3: Comparison of in vivo genipin studies.

Study	Animal	Genipin Concentration	Injection Type	Volume Injected	Number of Injections	Time Between Injections	Minimum Duration of Stiffening	Mechanical Testing Method
Liu et al. 2017	Rabbit	0.5 mM	Sub-Tenon	500 µL	Four	2-3 days	Two Weeks	Uniaxial Strip
Wang et al. 2015	Guinea Pig	22 mM	Sub-Tenon	100 µL	Three	7 days	Three Weeks	Uniaxial Strip
Current Study	Rat	15 mM	Retrobulbar	150 µL	One	N/A	Four Weeks	Whole Globe Inflation

1.19.4 *Whole Globe Inflation Testing*

1.19.4.1 Eye Mounting Procedure

Eyes were carefully cleaned under a dissecting microscope with micro-scissors to remove all fat, episclera, and extraocular muscles from the sclera. Since genipin-induced collagen crosslinks are known to autofluoresce (Hwang et al. 2011), we then imaged whole globes using an epifluorescent scope (Leica DM6 B, Leica Microsystems, Wetzlar, Germany) to confirm posterior scleral coverage of genipin crosslinks (Figure 15).

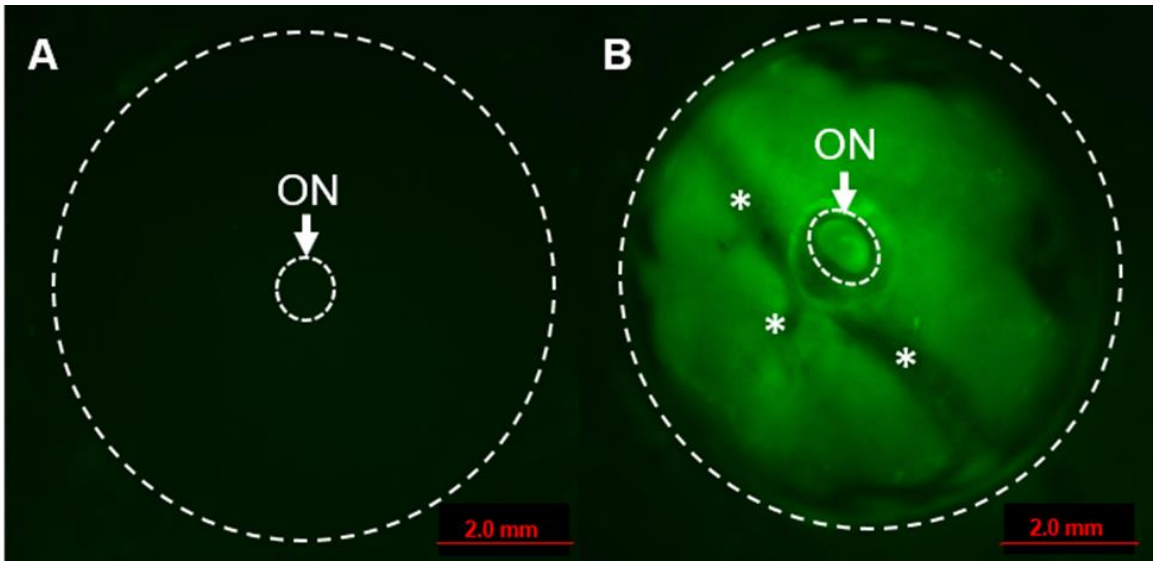

Figure 15: Whole globe autofluorescence of HBSS (A) and genipin (B) injected paired eyes from Genipin/HBSS rat at four weeks post-injection. The arrow and corresponding outline indicate the approximate optic nerve (ON) location on each eye, while the outer dashed outline indicates the approximate size of the eye. Asterisks: vessel locations on posterior sclera. Photos taken using Y5 filter cube ((590-650 nm)/(660-740 nm)) excitation/emission). The fluorescence induced by genipin-induced crosslinks was evident and suggested a relatively even distribution of genipin over much of the posterior sclera. Exposure level and gain settings were identical in both images.

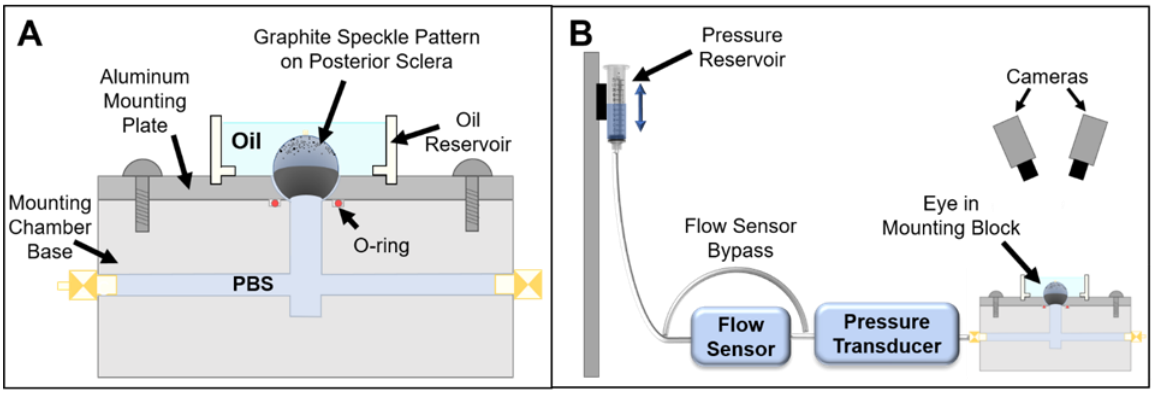

Figure 16: Inflation testing schematic. A) Mounting chamber, including rat eye mounted cornea-side down. B) Testing apparatus with hydrostatic pressure reservoir, flow sensor, pressure transducer, mounting block, and DIC cameras. The flow sensor bypass was used to eliminate the lag in pressure experienced by the eye (e.g. during preconditioning cycles), as described more fully in the text.

After imaging, a hole, approximately 4 mm in diameter, was cut in the cornea using micro-scissors. A thin ring of ethyl 2-cyanoacrylate adhesive (CAS#7085-85-0, Henkel, Rocky Hill, CT) was applied around the interior edge of a hemispherical well on an aluminum mounting plate (Figure 16A) and the eye was glued cornea-side down into the well. Care was taken to ensure that the limbus of the eye was in full contact with the glue and the ONH was centered upwards. The glue was cured with phosphate-buffered saline (PBS) to create a seal between the plate and limbus. After the eye was securely attached, the lens and vitreous humor were removed through the 4 mm hole in the cornea by gently pressing on the posterior sclera, as previously described (Bianco 2018). The mounting plate was then attached with screws to the base of the empty mounting chamber (Figure 16A) and securely fastened to create a watertight seal. The sealed chamber was flooded with PBS and purged of air bubbles using two ports on opposite sides of the chamber which were re-sealed once all air bubbles had been cleared. Throughout the cleaning and mounting process, the eye was kept hydrated by frequent applications of PBS.

To provide a high-contrast pattern for DIC analysis, a uniform speckle pattern was applied to the posterior scleral surface using graphite powder (#970 PG, General Pencil Company, Inc., Redwood City, CA). Finally, a 3D printed oil reservoir (Figure 16A) was attached to the top of the mounting block and filled with mineral oil (CAS# 8042-47-5, McMaster-Carr, Douglasville, GA) to prevent the eye from dehydrating during testing while allowing camera visibility to the posterior sclera.

1.19.4.2 Inflation Testing Experimental Hardware:

The experimental setup used for inflation testing is shown in Figure 16B. IOP was elevated by increasing the height of a hydrostatic pressure reservoir attached to a stepper motor. Flow rates into the eye were measured with an in-line flow sensor (SLG64-0075; Sensiron, Stafa, Switzerland), and IOP was measured downstream of the flow sensor with a gage pressure transducer (142PC01G; Honeywell, Charlotte, NC). The flow sensor, pressure transducer, and eye mounting block were connected to a fluid manifold to enable modifications to the flow path as needed during calibration and inflation testing. While flow measurements were useful (e.g., to facilitate leak detection), the inclusion of a flow sensor in the system also introduced a high fluidic resistance between the pressure reservoir and eye. This resistance to flow, together with the compliance of the eye, led to a delay during pressurization/filling of the eye, as well as the ocular pressure being less than the reservoir pressure. Thus, we included tubing to bypass the flow sensor when rapid pressurization of the eye was desired (Figure 16B). iPerfusion software was used to record pressure and flow data, and to initiate pressure stepping protocols (Sherwood et al. 2016). Throughout inflation tests, scleral deformation was recorded with two stereo cameras (Dantec Dynamics, Holtsville, NY).

The measurement hardware was calibrated regularly before testing. The pressure transducer was zeroed to atmospheric pressure at the free surface of the mineral oil by using a custom-built chamber filled with PBS to simulate the hydrostatic pressure of mineral oil on the eye, which accounted for the difference in specific gravity between PBS and mineral oil. The pressure transducer was calibrated by setting the reservoir to a series of pressure (height) steps to correlate sensor voltage with known pressure steps. Weekly intrinsic and daily extrinsic calibrations of the stereo cameras were performed with a calibration target according to manufacturer protocols. For extrinsic calibrations, the calibration target was submerged in mineral oil in the custom calibration chamber to ensure compensation for the refractive index of mineral oil. The surface of the eye was imaged throughout the inflation test with a 100 ms exposure time.

1.19.4.3 Preconditioning and Creep Procedure:

After attaching the mounting chamber to the system hardware, the flow sensor was bypassed, and the pressure was set to 2 mmHg. With the flow sensor in-line, image recording was initiated (1 image per minute), and the pressure reservoir was set to 15 mmHg to check for leaks. Based on preliminary testing, an eye was considered leak-free if the flow rate dropped below 600 nl/min and the eye pressure reached 11 mmHg in less than 20 minutes. If a leak was present at this step, the eye (and fellow contralateral eye) was excluded from the study. The non-zero steady state flow rate was likely due to several possible outflow passages from the eye, including remnants of the trabecular meshwork in the anterior eye, vortex veins exposed by removal of the vitreous, and micro-leaks in the glue. In certain instances, outflow from the vortex veins created a fluid bubble in the oil that distorted the cameras' view of the speckle pattern, resulting in a large fraction of the

scleral surface that could not be tracked by the DIC algorithm. Eyes (and fellow contralateral eyes) affected by either exclusion criteria: 1) a leak in the eye, or 2) a fluid bubble impeding sufficient DIC analysis, were excluded from the study (13 of 28 rats).

The flow sensor bypass was then opened, causing the pressure to immediately increase from the approximately 11 mmHg reached during the leak check to the 15 mmHg set pressure. The eye was then held at 15 mmHg for 5 minutes as an acclimatization step. The eye was subsequently subjected to 10 load-unload cycles from 3 to 15 mmHg at a rate of 0.5 mmHg/second and images were taken every 4 seconds (Figure 17). We determined empirically that 10 cycles were sufficient to ensure that variation in the mean peak scleral strain was no greater than 2% between cycles (Figure 18). In preliminary testing, we found that the acclimatization step was very important to reach a preconditioned state within the 10 cycles. When the eye was subjected to load-unload cycles only, the number of cycles required was variable. After preconditioning, eye pressure was lowered to 3 mmHg, and the flow sensor bypass was closed, which added the flow sensor back into the flow path.

The eye was then subjected to a creep testing protocol comprising three pressure steps of 10, 20, and 30 mmHg (Figure 17). Pressure steps were initiated only after the flow reading reached a designated stability criterion based on measured flow rate of ± 2 nl/min/s of variation over a 10-minute window. This flow stability criterion ensured that posterior ocular tissues had sufficient time to creep under the applied pressure, resulting in stabilized strain readings for each pressure step (Figure 19). Note that since the flow sensor had a high fluid resistance, there was a small pressure drop, usually 0.5 to 2 mmHg, between the

pressure applied to the system and IOP. Throughout the creep testing, images were captured every 30 seconds.

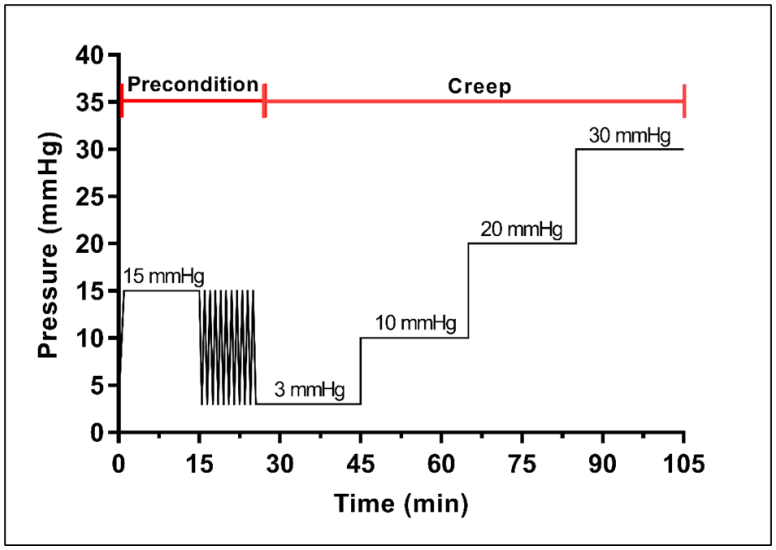

Figure 17: Overview of the reservoir pressure during inflation testing protocol. The preconditioning protocol consisted of an acclimatization step where the pressure reservoir was set to 15 mmHg, followed by 10 preconditioning cycles from 3 to 15 mmHg. The creep testing protocol included three pressure steps: 3 to 10 mmHg, 10 to 20 mmHg, and 20 to 30 mmHg. The timing of pressure steps varied, with typical step timing shown here. Note that this figure represents the set reservoir pressure and not the eye pressure as measured by the pressure transducer. It is important to note that the actual measured eye pressure was used in data fitting.

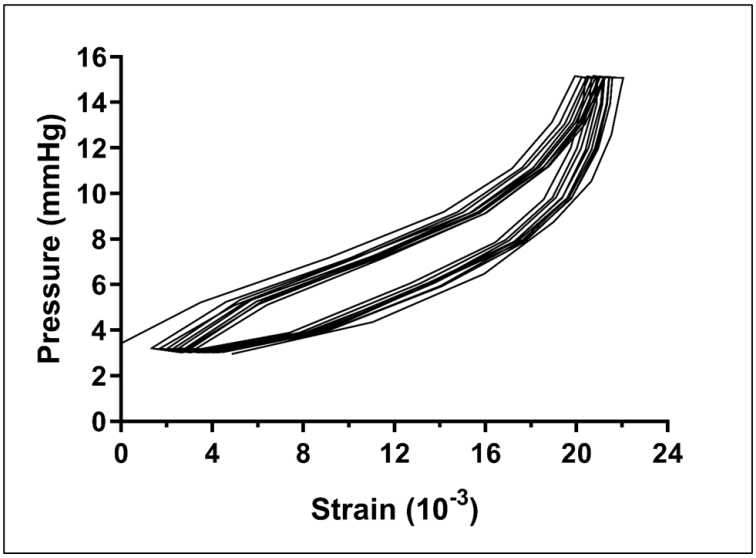

Figure 18: Representative pressure-strain plot for cyclic loading from 3 to 15 mmHg during preconditioning. The difference in maximum first principal Lagrange strain value between two consecutive cycles reached an equilibrium (< 2% change) by 10 cycles.

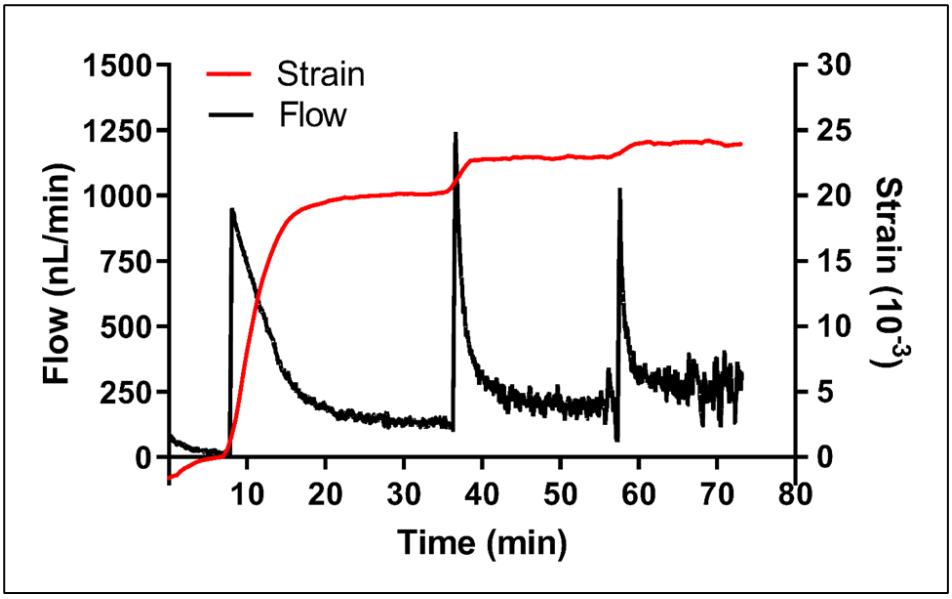

Figure 19: Representative flow sensor and strain measurements during a creep test. Flow sensor output is shown by the black line (left y-axis), where peaks correspond to pressure steps. Mean first principal strain averaged over the posterior sclera is shown by the red line (right y-axis). Strain values are referenced to the end of the first pressure step of 3 mmHg. Time shown is relative to the start of the creep test.

1.19.5 *Data Analysis*

Dantec's Istra 4D software (v4.4.1, Dantec Dynamics, Holtsville, NY) was used for image analyses. The reference configuration for local surface strain calculations was chosen as the frame one minute before the first pressure step, at which point the eye was exposed to a pressure of approximately 3 mmHg. The following correlation settings were used: facet size of 45 pixels, grid spacing of 28 pixels, maximum permissible start point accuracy of 0.2 pixels, residuum of 30 grey values, and 3D residuum of 1.1 pixels. In 3D space, the resulting grid spacing between facets was approximately 150 µm. Displacement data was smoothed prior to strain calculations using parameters recommended by Dantec Dynamics: a grid reduction factor (minimizing the difference between the data point and the spline function) of 2 for displacement and contours, and a smoothness factor (straightens filtered data) of -0.5 for displacement and 0 for contours.

A custom Matlab code (2018b; MathWorks, Natick, MA) was used for further analysis. First, facets that were correlated in fewer than 75% of the images were removed. Further, facets from each image whose first principal strain values were in the top and bottom 5th percentile ranges were excluded from that image as outliers. The mean first principal strain averaged over the entire posterior sclera, excluding the ONH region and the excluded facets, was then calculated in each frame by averaging the x, y, and xy components of Lagrange strain from all facets, populating a 2x2 matrix with these averages, and calculating the two eigenvalues. The more positive eigenvalue was taken as the average first principal strain magnitude. The mean strain for each pressure step was computed by averaging the first principal strain over the five frames prior to the increase in pressure. The mean pressure for each step was computed by averaging the recorded pressure values for the last 5 minutes of the step. Pressure-strain data from each eye was fit to an isotropic Fung-type model, similar to the approaches used in (Wong et al. 2012) and (Schultz et al. 2008):

$$Applied\ Pressure = \frac{A}{B}(e^{B\varepsilon} - 1) + C \tag{3}$$

where ε represents the first principal Lagrange strain, C represents the intraocular pressure reached at the reference pressure step (reservoir pressure of 3 mmHg), and A and B are fitting coefficients. An R-squared value was computed for the Fung model fit to the experimental data, and if either R-squared value for a pair of eyes was lower than 0.9, that pair was excluded from the study according to this exclusion criteria (2 of 28 rats). This fit was then used to compute the strain at 22 mmHg, which is the physiological IOP of awake

normotensive Brown Norway rats recorded in our lab, which is similar to that reported in other labs (Jia et al. 2000b). This procedure allowed us to compare scleral deformations in all eyes at an equal IOP.

We computed the difference in strain at 22 mmHg by subtracting control strain from experimental strain. In the genipin/HBSS group, the experimental eye was the genipin-treated eye, and in the HBSS/naïve group, the HBSS eye was the experimental eye. Negative values indicated that the experimental eye was stiffer. Relative difference in strain for each rat was computed using the equation:

$$Relative\ difference\ in\ strain = \frac{\varepsilon_{experimental} - \varepsilon_{control}}{\varepsilon_{control}} \cdot 100 \qquad (4)$$

where $\varepsilon_{experimental}$ and $\varepsilon_{control}$ are the strains at 22 mmHg in the experimental eye and control eye, respectively.

1.19.5.1 Statistical Analysis

Fifteen rats were removed from the study due to the exclusion criteria described above. Thus, thirteen rats were used for statistical analysis, broken down as follows: Naïve/HBSS rats one day post-injection (n = 4), Genipin/HBSS rats one day post-injection (n = 4), and Genipin/HBSS rats four weeks post-injection (n = 5).

Difference in strain for each group was compared using one-way ANOVA with a Holm-Sidak post-hoc test, and percent strain reduction for each group was compared using Kruskal-Wallis with a Dunn's post-hoc test (GraphPad Software v8, San Diego, CA). Results are presented as mean ± standard deviation, unless otherwise noted.

1.20 Results

The Fung model provided an excellent fit to each set of pressure vs. strain data, with an average R-squared value of 0.99 ± 0.015 as seen in Figure 20. All curves for genipin-treated eyes were clustered towards the left side of the graph, indicating a stiffer sclera in these eyes. In contrast, the curves for all HBSS and naïve eyes were dispersed throughout the middle and right portions of the graph, indicating a softer sclera and higher variability in these eyes.

As expected, the mean difference in strain in the HBSS/Naïve rats was approximately zero (0.0002 ± 0.00022 strain), indicating that HBSS (sham) injection did not affect scleral stiffness one day post-injection. Genipin/HBSS rats showed a reduction in strain at both one day (-0.0098 ± 0.0052 strain) and four weeks (-0.0154 ± 0.006strain) post-injection (Figure 21), i.e. there was less scleral strain in the genipin-treated eyes. There was a significant scleral stiffening effect due to genipin treatment [one way ANOVA: $F(2, 10) = 11.25$, $p = 0.0028$] as evidenced by the greater difference in strain in the Genipin/HBSS groups compared with the HBSS/Naïve group (Holm-Sidak post-hoc: one day, $p = 0.016$; four weeks, $p = 0.002$). Relative difference in strain (Figure 22) in Genipin/HBSS rats one day (-41.2 ± 14.1%) and four weeks (-58.3 ± 15.6%) post-injection were greater in magnitude than Naïve/HBSS rats (1.6 ± 6.5%); however, this result was only significant at four weeks post-injection (Kruskal-Wallis, $p < 0.001$; Dunn's post-hoc, HBSS/Naïve vs Genipin/HBSS at one day: $p = 0.170$ and HBSS/Naïve vs Genipin/HBSS at four weeks: $p = 0.005$).

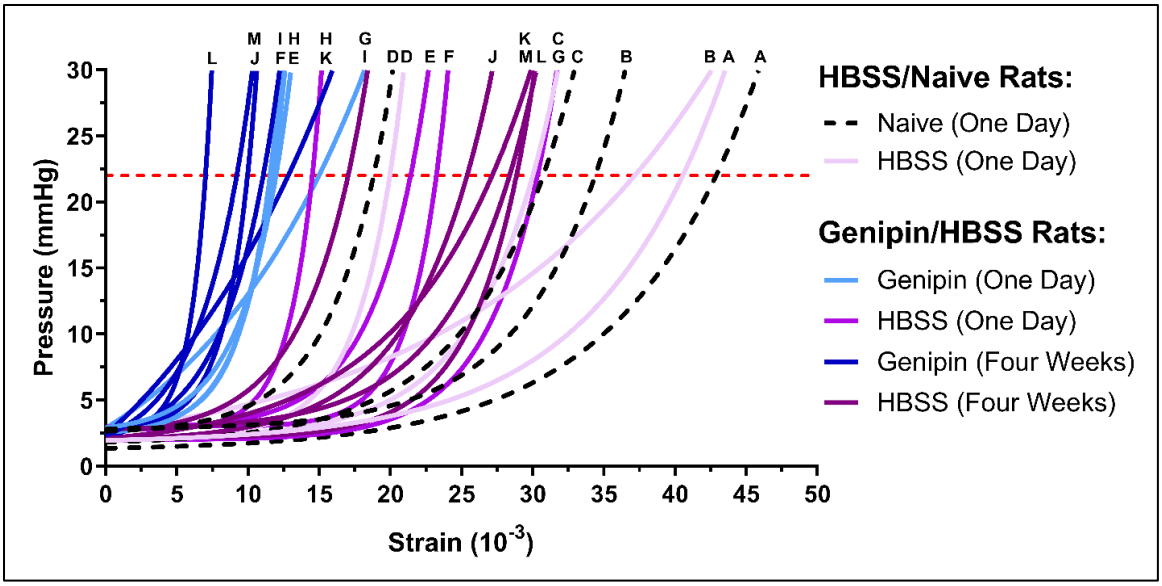

Figure 20: Genipin treated eyes yielded visibly stiffer pressure-strain curves. Fit of isotropic Fung-type constitutive model to pressure-strain data from each eye (all R2 > 0.93). Naïve eyes are shown in dashed black lines, HBSS eyes are shown in various shades of purple, and genipin eyes are shown in various shades of blue. Dotted red line denotes 22 mmHg, at which the difference in strain and percent strain reduction were computed. Letters above curves indicate paired eyes from each rat (A-M). For overlapping curves, the letter corresponding to the leftmost curve is on top.

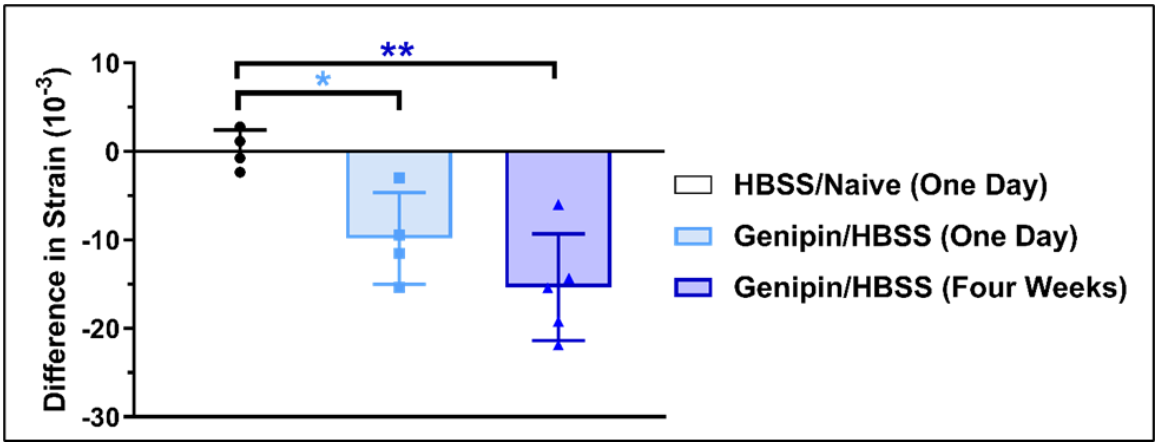

*Figure 21: Genipin treatment resulted in greater relative difference in strain. Relative difference in strain at 22 mmHg for HBSS/Naïve rats (n = 4) one day post-injection and for Genipin/HBSS rats one day (n = 4) and four weeks (n = 5) post-injection. The plotted quantity is the difference in average first principal scleral strain relative to the contralateral control eye for each rat, all evaluated at 22 mmHg, and provides an alternative way of presenting the data shown in Figure 8. Relative difference in strain was significantly greater at four weeks after injection. Bars show mean ± SD. (** indicates $p \leq 0.01$ by Kruskal-Wallis test, Dunn's post-hoc).*

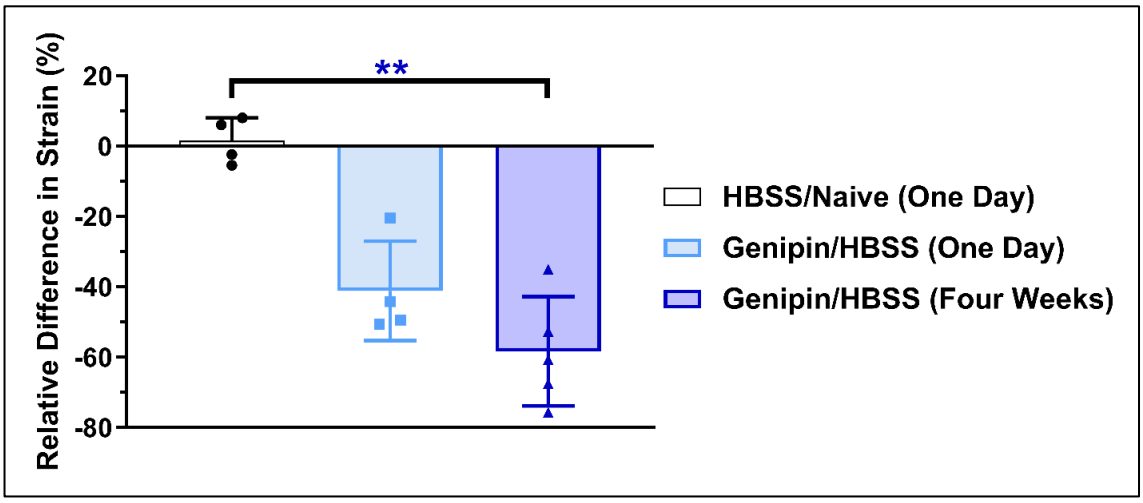

Figure 22: Genipin treatment resulted in reduced scleral strain. Difference in strain at an IOP of 22 mmHg for HBSS/Naïve rats (n = 4) one day post-injection and for Genipin/HBSS rats one day (n = 4) and four weeks (n = 5) post-injection. The plotted quantity is the average first principal scleral strain in the contralateral control eye minus the strain in the experimental eye for each rat, all evaluated at 22 mmHg. There was a greater difference in strain in Genipin/HBSS rats compared to HBSS/Naïve rats at one day and four weeks. Bars show mean ± SD (indicates $p \leq 0.05$, ** indicates $p \leq 0.01$, both by one-way ANOVA, Holm-Sidak post-hoc).*

1.21 Discussion

In this study, we show that a single retrobulbar *in vivo* injection of 15 mM genipin can effectively stiffen rat sclera and that the effect is sustained for at least four weeks post injection. This finding is significant because it justifies the use of a single injection in future studies evaluating the effects of scleral stiffness, whereas previous protocols utilized multiple injections (Table 3). We expect that this improvement will greatly simplify future studies, since each injection introduces risk and variability, and may eventually increase the potential for translation of genipin stiffening treatments in the eye.

The degree of scleral stiffening that is required to provide an effective treatment for glaucoma is not known. However, we can predict minimum efficacious stiffening levels based on the stiffening magnitude needed to significantly reduce strains in the ONH. Coudrillier et al. evaluated the effects of posterior scleral stiffening via glutaraldehyde on

ONH strain in ex vivo porcine eyes (Coudrillier, Campbell, et al. 2016). Specifically, a -40% relative difference in scleral strain (at an IOP of 22 mmHg) led to a relative difference in ONH strain of -47% and -39% at 15 mmHg and 30 mmHg, respectively. In this study, we reduced scleral strain at 22 mmHg by a similar amount at one day (-41.2%) and four weeks (-58.3%) post-injection, suggesting that our genipin treatment is likely to markedly reduce ONH strains in the rat eye. In the context of myopia, Wang et al. demonstrated a significant decrease in refractive error after genipin treatment (Wang and Corpuz 2015). However, it is challenging to directly compare our stiffening results due to differences in uniaxial loading regime (Wang and Corpuz 2015).

More broadly, we note that the ultimate clinical benefits of scleral stiffening in glaucoma remain to be determined. A preliminary study suggested that increasing scleral stiffness provides neuroprotection in glaucoma (Ethier 2015), yet a larger study by Kimball et al. (Kimball et al. 2014) reported that stiffening the posterior mouse scleral increased (rather than decreased, as hypothesized in this study) glaucomatous damage. While these results are important, the stiffening technique described in this study has significant differences compared to Kimball et al.'s study, including: animal type, number of injections, type of injection, volume of crosslinker, concentration of crosslinker, and type of crosslinker. There are also the observations that the sclera becomes stiffer in glaucoma, and that African descent is associated with a higher peripapillary scleral stiffness and a higher incidence of glaucoma. These data could suggest that a stiffer sclera increases glaucoma risk, or alternatively they could mean that scleral stiffening is a beneficial adaptive response to mitigate glaucomatous damage/risk. Considering all of the above, the reality is that we do not know whether scleral stiffening will provide neuroprotection in

glaucoma, and we expect that research such as described in this work will help to answer this fundamental question. We have confirmed a successful genipin retrobulbar injection by visualizing autofluorescent genipin-induced collagen crosslinks (Figure 15), observing a relatively uniform autofluorescence distribution posteriorly, with reduced autofluorescence as the limbus was approached. This reduced cross-linking in the more anterior portions of the sclera was expected, since the conjunctiva acts as an anatomical barrier for fluid transport from the retrobulbar space. Importantly, when considering the posterior sclera, there was no obvious correlation between the local variations in autofluorescence and local variations in strains as measured by DIC (data not shown). This is likely because the stiffness and thickness of the sclera naturally vary by location even before genipin treatment. Therefore, regional differences in strain magnitude as shown by DIC could be due to natural variations in structural stiffness that existed before genipin injection, to a localized effect of the stiffening agent, or both.

This study introduces several methodological improvements as compared to our previously published inflation testing procedure (Campbell et al. 2017). First, we included a preconditioning protocol to reduce variability between samples. Preconditioning was not required in our previous study because we utilized a partial incubation protocol that allowed us to determine a treatment effect using only a single eye. Since the present study compared strains between treated and contralateral eyes, reducing the testing variability increased the power of the study. Second, we incorporated a flow sensor into the testing setup to determine when the eye reached equilibrium at each pressure step. The time to reach equilibrium is expected to vary with viscoelastic properties and outflow rates, both of which are variable in normal populations and may be altered with genipin treatment. Yet

without a flow sensor, pressure steps could only be initiated at fixed time intervals, since the DIC software was unable to provide information about sample deformation while a test was in progress. The flow sensor also enabled accurate identification and exclusion of eyes with unstable leaking or creeping phenomena that would have biased the results. Finally, we developed an improved mounting procedure similar to that described by Bianco et al. (Bianco 2018). Specifically, we removed the lens from each eye to prevent it from occluding the flow of PBS into the eye. We also used an eye bath of mineral oil rather than PBS to prevent evaporation of fluid during the test while maintaining tissue hydration.

These changes have also introduced some minor but notable limitations, were outweighed by their benefits, as follows. First, the addition of a flow sensor (with its inherent flow resistance) makes it difficult to precisely set the pressure in the eye. Since the flow rate entering each eye can differ, an eye-specific pressure drop occurs across the flow sensor and this difference becomes more significant as the IOP changes. However, eye pressure throughout the duration of the test is directly measured in the described set up. This allows for all test data to be referenced to a common IOP through use of a Fung-type constitutive model which permits comparisons across eyes with different starting pressures. Also, by specifying a creep test rather than a ramp-hold test, we were able to minimize the potential importance of this effect. Second, since the eye was pressurized with PBS but was tested in a bath of mineral oil, leaking PBS from the eye, even at very low flow rates, occasionally resulted in a bubble of PBS that distorted the image of the underlying speckle pattern seen by the cameras. Finally, we chose to implement a preconditioning procedure which used cyclic loads between 3 and 15 mmHg, whereas our creep pressure steps were higher than this range (20 mmHg and 30 mmHg). Because of

this, our results could potentially be affected by the Mullins effect, in which a material's softening effect is dependent on the maximum load the tissue is subjected to during its preconditioning loading history. We chose our preconditioning pressures to minimize leakage from eyes, which occurred more often when eyes were dynamically loaded to higher pressures during preconditioning. Additionally, while preconditioning is extremely important in uniaxial and biaxial strip testing, it has been shown that the sclera exhibits only modest preconditioning effects during inflation tests in other species (Tonge et al. 2013; Coudrillier et al. 2012; Myers et al. 2010). These results are encouraging and motivate further testing with genipin.

Although this study did not explicitly evaluate any potential toxicity of genipin, animals were monitored after retrobulbar injections with either genipin or HBSS. In all rats, there was a small bleb of fluid visible in the inferior and nasal regions of the conjunctiva which resolved within one to five days post-injection. Adverse effects from the retrobulbar injections included a few eyes in which there was a small amount of bleeding from the periocular space immediately following the injection, presumably due to a blood vessel being accidentally damaged during the injection. Further, we do not expect genipin treatments to be cytotoxic, since Liu et al. demonstrated no cytotoxicity due to genipin treatment in rabbits (Liu and Wang 2017). However, Liu et al. used a lower concentration than that used in the present study (Table 3), and future work must assess potential genipin-induced cytotoxicity. We are currently evaluating the safety of genipin injections and plan to describe this in a separate publication in due course. Future work should also determine the maximum duration of this stiffening effect.

1.22 Conclusion

We have demonstrated stiffening of rat sclerae after a single *in vivo* injection of genipin in rats. The stiffening effect was sustained for at least four weeks, longer than previously demonstrated. This is important for simplifying research studies and facilitating possible future clinical translation, where frequent injections are undesirable. These findings were enabled by development of an improved inflation testing protocol for measuring strain in genipin-treated eyes. Altogether, these results will be used to guide future *in vivo* studies aimed at evaluating the efficacy of scleral stiffening via genipin injection as a treatment for glaucoma, myopia or other applications.

Assessment of visual and retinal function following *in vivo* genipin-induced scleral crosslinking

1.23 Submission Details:

Authors: **Bailey G. Hannon**, Coralia Luna, Andrew J. Feola, Matthew D. Ritch, A. Thomas Read, Sandra S. Stinnett, Harrison Vo, Machelle T. Pardue, Pedro Gonzalez, C. Ross Ethier

Status: Submitted to Translational Vision Science & Technology, March 14, 2020

1.24 Abstract

Purpose: Genipin has been proposed as a possible neuroprotective therapy in myopia and glaucoma. Here, we aim to determine the effects of prolonged genipin-induced scleral stiffening on visual function.

Methods: Eyes from Brown Norway rats were treated *in vivo* with either a single 15 mM genipin retrobulbar injection or sham retrobulbar injection and were compared to naïve eyes. Intraocular pressure, optomotor response, and electroretinograms were repeatedly measured over four weeks following retrobulbar injections to determine visual and retinal function. At four weeks we quantified retinal ganglion cell axon counts. Finally, molecular changes in gene and protein expression were analyzed via RT-PCR and proteomics.

Results: Retrobulbar injection of genipin did not affect IOP or retinal function, not did it have a sustained impact on visual function. While genipin-treated eyes had a small decrease in retinal ganglion cell axon counts compared to sham-treated eyes (-8,800 ± 20,698, mean

± SD), this decrease was not statistically significant ($p = 0.238$, $n = 9$). Lastly, we did not observe any changes in gene or protein expression due to genipin treatment.

Conclusions: Posterior scleral stiffening with a single retrobulbar injection of 15 mM genipin causes no sustained deficits in visual or retinal function or at the molecular level in the retina and sclera. Retinal ganglion cell axon morphology appeared normal.

Translational significance: These results support future *in vivo* studies to determine the efficacy of genipin-induced posterior scleral stiffening to help treat ocular diseases like myopia and glaucoma.

1.25 Introduction

Scleral collagen crosslinking has been proposed as a therapeutic treatment for myopia and glaucoma. In myopia, refractive error is largely caused by scleral remodeling which leads to axial elongation (Harper and Summers 2015; Rada, Shelton, and Norton 2006), and crosslinking the posterior sclera has been hypothesized as a treatment to slow or reverse this process (Levy, Fazio, and Grytz 2018; Liu and Wang 2017). In glaucoma, intraocular pressure (IOP) causes excessive biomechanical strains on the optic nerve head, which is the main and early site of retinal ganglion cell (RGC) damage. It is hypothesized that reducing such excessive strains by crosslinking the posterior sclera surrounding the optic nerve may protect against RGC loss in glaucoma (Sigal, Flanagan, and Ethier 2005; Campbell, Coudrillier, and Ross Ethier 2014).

Ocular collagen crosslinking has recently been clinically approved for the treatment of keratoconus, where the cornea becomes weak and misshapen (Hersh et al. 2017). This

treatment uses a collagen crosslinker, riboflavin, that is photoactivated by Ultraviolet-A (UVA) light to strengthen the cornea. Unfortunately, scleral crosslinking using riboflavin and UVA light is known to be toxic to the retina (Glickman 2011; Wollensak et al. 2005). Thus, alternative collagen crosslinking approaches have been evaluated to stiffen the posterior sclera for myopia and glaucoma treatment.

Genipin, a naturally occurring, non-photoactivated, collagen crosslinking agent extracted from the *Gardenia* fruit, has been previously investigated as a collagen crosslinker for ocular use (Avila and Navia 2010; Liu, Luo, et al. 2014; Wang and Corpuz 2015; Levy, Fazio, and Grytz 2018; Dias et al. 2015; Liu and Wang 2017). Genipin acts as an anti-inflammatory and anti-angiogenic agent (Koo et al. 2004) and can induce stable crosslinks in biological tissue (Sung et al. 2001). Genipin-induced crosslinking increases tissue stiffness by similar magnitudes as do glutaraldehyde (Huang et al. 1998) and riboflavin (Song et al. 2017; Avila, Gerena, and Navia 2012), yet is significantly less cytotoxic than are glutaraldehyde (Sung et al. 1999; Chang et al. 2002) and riboflavin (Song et al. 2017; Avila, Gerena, and Navia 2012).

Of several studies that have evaluated genipin-induced scleral crosslinking, only two have evaluated both the efficacy and safety of genipin-induced scleral crosslinking *in vivo* (Liu and Wang 2017; Wang and Corpuz 2015). These studies examined the biomechanical properties of genipin-stiffened scleral strips, gross ocular anatomy via slit-lamp exams after treatment, and histological and immuno-histological sections of ocular tissues in rabbits (Liu and Wang 2017) and guinea pigs (Wang and Corpuz 2015). These studies found that genipin successfully stiffened the sclera and did not cause any gross

changes in ocular structures. However, to date no study has evaluated whether genipin-induced scleral collagen crosslinking affects visual and retinal function *in vivo*.

We have previously shown the efficacy of genipin (15 mM) to induce sustained scleral stiffening for up to four weeks after retrobulbar injection in Brown Norway rat eyes (Hannon et al. 2019). However, it is important to ensure that long-term scleral stiffening is safe and has negligible adverse effects on visual function. Here, we aim to evaluate the potential use of genipin-induced collagen crosslinking in the sclera on visual and retinal function over four weeks.

1.26 Methods

1.26.1 *Animals*

This study used 37 retired breeder (7-13 months old) Brown Norway rats (Charles River Laboratories, Inc., Wilmington, MA). Most rats used in this study (n = 34 rats) were male, while a small group of female rats (n = 3) were used in a preliminary proteomics study. All rats were housed on a 12-hour light (fluorescent 25-200 lux)/12-hour dark cycle and were provided with food and water ad libitum. All procedures were approved by the Institutional Animal Care and Use Committee at the Georgia Institute of Technology, Duke University, and the Atlanta VA Healthcare System. All procedures adhered to the ARVO Statement for the Use of Animals in Ophthalmic and Vision Research. The numbers of rats used for each outcome parameter are listed in Table 4.

1.26.2 *Experimental Groups and Crosslinking Procedure*

Rats were randomly assigned to one of three groups for this study, as displayed in Figure 14. The first group of rats (Naïve/Naïve, n = 7 animals) were from a previous study in our lab in which both eyes were left completely naïve. Optic nerves were removed from these eyes and used for RGC axon count comparisons (Schwaner et al. 2020). Rats in the second group (HBSS/Naïve, n = 10) received a single (unilateral) retrobulbar injection of Hank's Balanced Salt Solution (HBSS; 150 µl) unilaterally, while the contralateral eye was left as a Naïve control. Rats in the third group (Genipin/HBSS, n = 20) received a single retrobulbar injection of genipin (Wako Pure Chemical Industries, Ltd., Richmond, VA) mixed in HBSS (15 mM, 150 µl) unilaterally, while the contralateral eye received a single retrobulbar injection of HBSS (150 µl). For all retrobulbar injections, rats in the remaining two groups were anesthetized with a cocktail of ketamine (60 mg/kg) and xylazine (7.5 mg/kg) and a drop of topical tetracaine (0.5%, Alcon, Geneva, Switzerland) was applied as a local anesthetic to both eyes. All retrobulbar injections were performed using a sterile 31G insulin syringe needle (BD 300 µl Insulin Syringe Ultra-Fine™ needle, Becton, Dickinson and Company, Franklin Lakes, New Jersey) inserted into the inferior quadrant. A genipin concentration of 15mM was previously used in our *in vivo* stiffening study (Hannon et al. 2019), and successfully stiffened the posterior rat sclera for four weeks. Rats received a topical antibiotic (Certi-sporyn, Kansas City, MO) to avoid infection and antisedan (1 mg/kg) to reverse anesthesia (Turner and Albassam 2005). All rats were euthanized (via CO_2 overdose) either one day, one week, or four weeks post-injection, depending on the experiment.

Table 4: Number of rats in each group for each outcome measure. Columns indicate cohorts of rats within each group. Asterisks indicate rats that were used in multiple outcome measures.

Outcome Measure	Timepoints Measured	Naïve/Naïve (n = 7)	HBSS/Naïve (n = 10)			Genipin/HBSS (n = 20)				
IOP (Tonometry)	Day 1, 3, 7, 10, 14, 21, and 28		5*			6*				
Visual Function (OMR - Spatial Frequency)	Day 0, 1, 7, 14, 21, and 28		5*			6*				
Visual Function (OMR - Contrast Sensitivity)	Day 0, 14, and 28		5*			6*				
Retinal Function (ERG)	Day 0, 7, 14, and 28		5*			6*				
RGC Axon Morphology (Axon Counts)	Day 28	7				4*	5			
Scleral and Retinal mRNA Expression (RT-PCR)	Day 7			2				3		
	Day 28				3				3	
Scleral Expression of ECM Proteins (Proteomics)	Day 28									3
Total Rats in Cohort		**7**	**5***	**2**	**3**	**6***	**5**	**3**	**3**	**3**

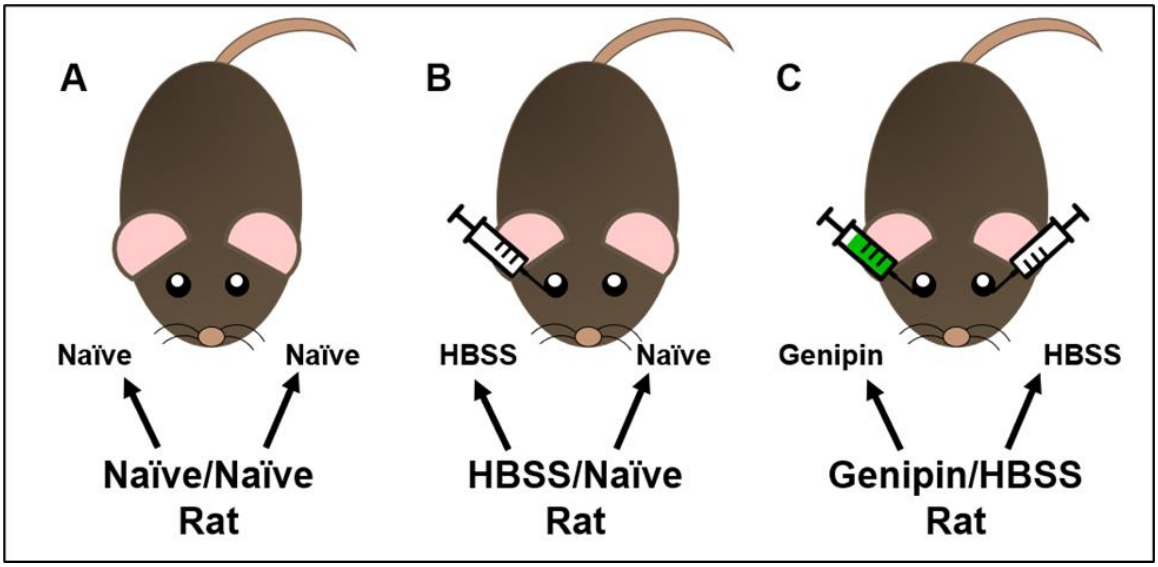

Figure 23: Schematic of three groups of rats used in this study: Naïve/Naïve rats (A) were completely naïve control rats. HBSS/Naïve rats (B) received a single (unilateral) retrobulbar injection of HBSS, and Genipin/HBSS rats (C) received a unilateral retrobulbar injection of genipin and a contralateral retrobulbar injection of HBSS.

1.26.3 *Tonometry and Eye Exams*

IOP measurements were taken between 9:00am and 11:00am using a Tonolab rebound tonometer (Icare Finland Oy, Vantaa, Finland) in HBSS/Naïve (n = 5) and Genipin/HBSS (n = 6) rats. The tonometer was previously calibrated on a cannulated eye, in which we externally set IOP ranging from 5 to 50 mmHg using an external reservoir (data not shown). Awake rats were gently restrained by hand while eight tonometer readings were recorded on each eye. We removed the lowest and highest IOP values and averaged the remaining six measurements to represent IOP from that eye. IOP measurements were recorded at 0 (baseline, just before injection), 3, 7, 10, 14, 21, and 28 days relative to the time of retrobulbar injection. At each of these timepoints, rat eyes were also grossly observed for any abnormalities arising from the retrobular injections.

1.26.4 *Optomotor Response*

The optomotor response (OMR) was used to assess visual function (OptoMotry®; Cerebral-Mechanics, Lethbridge, AB, Canada (Douglas et al. 2005)) at 0 (baseline), 1, 7, 14, and 28 days after retrobulbar injection. We evaluated the OMR in HBSS/Naïve (n = 5) and Genipin/HBSS (n = 6) rats. In brief, awake rats were placed on a platform in the center of a chamber consisting of four flat screen computer monitors. Each monitor displayed vertical black and white gratings which produced a virtual drum rotating at a speed of 12 degrees/second (deg/s). A video camera above the platform was used by a trained observer to visualize the rat's reflexive head movements during the experiment. Gratings rotated in a clockwise or counter clockwise direction to separately stimulate the responses of the left and right eyes, respectively (Douglas et al. 2005). To determine a rat's spatial frequency

threshold, the vertical bands were displayed at 100% contrast starting at 0.042 cycles/degree and the spatial frequency of the bands was adjusted until the rat no longer demonstrated an OMR, as determined by a lack of reflexive head movement. Contrast sensitivity was measured at baseline, week two, and week four. To determine contrast sensitivity, spatial frequency was set to 0.064 cycles/degree, while the contrast was adjusted from 100% following a staircase paradigm until the animal no longer displayed a reflexive response. Contrast sensitivity is reported as the reciprocal of the Michelson contrast from the screen's luminance, as previously described (Prusky et al. 2004).

1.26.5 *Electroretinogram*

To assess inner and outer retinal function we performed electroretinograms (ERGs). ERG measurements on HBSS/Naïve (n = 5) and Genipin/HBSS (n = 6) rats were taken at baseline, 1, 2, and 4 weeks post-injection. For each timepoint, rats were dark-adapted for 30 minutes and anesthetized using a cocktail of ketamine (60 mg/kg) and xylazine (7.5 mg/kg), after which drops of tetracaine (0.5%) and tropicamide (1%) were applied topically to anesthetize corneas and dilate pupils, respectively. Reference needle electrodes were carefully inserted subcutaneously in each cheek and a ground electrode was placed in the tail. Custom gold-loop corneal electrodes were placed on the cornea of each eye under a layer of carboxymethylcellulose (Celluvisc, Allergan, Dublin, Ireland) to ensure electrical conductivity and prevent the eye from drying. Electrical responses to various full-field flash stimuli in a Ganzfield dome were recorded and differentially amplified (1-1500 Hz) using a signal-averaging ERG system (UTAS BigShot; LKC Technologies, Gaithersburg, MD) that was calibrated according to manufacturer's specifications. Under dark-adapted conditions, a five-step series of increasing flash

intensities (-3.0 to 2.1 log cd s/m^2) was used to selectively isolate rod and mixed rod/cone dominated photoreceptor responses. Interstimulus intervals increased from 2 to 70 seconds at each stimulus level to provide full recovery of the retina before the next flash. 3 to 10 flashes were averaged to generate a waveform for each scotopic flash. Rats were then light-adapted for 10 minutes (30 cd/m^2) before being presented with a three-step series of increasing light stimuli (0.4 to 1.4 log cd s/m^2) followed by a flickering light stimulus (1.9 log cd s/m^2 at 6 Hz) to isolate cone photoreceptor responses. Each photopic waveform was averaged from 25 flashes. Oscillatory potentials (OPs) were filtered with a 65-275 Hz bandpass fifth order Butterworth filter and then measured on the leading edge of the b-wave starting with the first trough. Amplitudes and implicit times were measured as follows: baseline to trough (a-waves and photopic negative responses (PhNR)) and trough to peak (OPs, b-waves, and flicker response).

1.26.6 *RGC Axon Counting*

RGC axon numbers were quantified in Genipin/HBSS (n = 9) and Naïve/Naïve (n = 7) rats at four weeks post-injection. Immediately after euthanasia, optic nerves were dissected from the enucleated eye and fixed in isotonic PBS (Sorensen's buffer) containing 2.5% glutaraldehyde and 2% paraformaldehyde (PFA, EMS, Hatfield, PA). The tissue was then post-fixed in 1% osmium tetroxide, dehydrated through an ethanol series, embedded in Araldite 502/Embed 812 resin (EMS, Hatfield, PA) and cured in a 60 °C oven for 24 h. Semi-thin cross sections (0.5 µm thick) were then cut approximately 1.0 mm posterior to the sclera, using a Leica EM UC7 ultramicrotome (Leica Microsystems, Buffalo Grove, IL) with a diamond or glass knife. Cross-sections were then dried and stained with 1% toluidine blue on a 70 °C hotplate for 15 seconds and imaged with a Leica DM6 microscope

(Leica Microsystems) at an objective power of X100. Tiled images were collected and merged together to produce a montage of the entire optic nerve cross-section. From this image, normal-appearing axons were then automatically counted using the AxoNet fully convolutional neural-network software, as described previously (Ritch et al. 2019) as well as in APPENDIX A.

1.26.7 *RT-PCR*

A preliminary study was performed to assess genipin treatment's effect on abundance of extracellular matrix (ECM) proteases in the sclera and inflammatory markers in the retina. RT-PCR was performed on HBSS/Naïve (n = 6) and Genipin/HBSS (n = 6) rats at one week and four weeks (n = 3/group) post injection. Whole globes were enucleated immediately after euthanasia and stored in RNA later (ThermoFisher Scientific, Waltham, MA) until processing. Sclerae were cleaned of fat, tissue, and muscle, cut along the limbus, and opened to create four quadrants. Retinas were separated and put in a biomasher tube (Kimble, Tokyo, Japan) with trizol (Thermo Fisher Scientific). RPE was gently peeled and then scraped off from the sclera with a blade and the sclera was washed in PBS, cut into small pieces and then put into a biomasher tube with trizol. Retina and sclera tissues were then homogenized, mixed with chloroform (200 µl per ml of trizol) and centrifuged at 4^{o}C for 15 minutes at 12,000g. The upper phase containing RNA was collected, cleaned, and concentrated using RNeasy MiniElute Cleanup Kit (Qiagen, Germantown, MD) according to the manufacturer's instructions.

Once RNA was acquired, strand cDNA was synthesized from total RNA (700 ng) by reverse transcription using oligodT and Superscript III reverse transcriptase (Thermo

Fisher Scientific, Waltham, MA) according to manufacturer's instructions. Q-PCR reactions were performed in 20µl mixture containing 1µl of the cDNA preparation, 1X iQ SYBR Green Supermix (Biorad, Hercules, CA) and 10µM primers, using the following PCR parameters: 95^{o}C for 5 minutes followed by 40 cycles of 95^{o}C for 15 seconds, 55^{o}C for 15 seconds and 72^{o}C for 15 seconds. β-Actin and GADPH were used as internal standards of mRNA expression. The absence of nonspecific products was confirmed by the analysis of the melt curves. The primers used for Q-PCR amplification are shown in table S1. During this processing, one globe from a four week HBSS/Naïve rat was damaged and could not be used for further analysis.

1.26.8 *Proteomics*

1.26.8.1 Sample Preparation

Proteomics analysis was performed on sclerae from Genipin/HBSS (n = 3) rats at four weeks post injection to determine the effect of genipin treatment on the abundance of various proteins involved in various functions, including protein binding, cell motility, and ECM structural support. Eyes were enucleated immediately after euthanasia and kept in cold PBS until processing. The sclera was first cleaned of conjunctiva, retina, muscle, and fat, and the RPE was gently peeled and scraped off from the sclera with a blade. The sclera was then washed in PBS, cut into smaller pieces, transferred to an Eppendorf tube, and frozen in liquid nitrogen. Frozen scleral pieces were ground using a CryoGrinder kit (OPS Diagnostics, Lebanon, NJ) and then suspended in 300µl of lysis buffer (10 mM HEPES, 42 mM KCl, 0.1 mM EDTA, 0.1 mM EGTA, 1 mM DTT (all from Sigma-Aldrich, St. Louis, MO), 1× protease inhibitor (Thermo-Fisher Scientific)) and homogenized in a biomasher tube. Samples were sonicated on ice three times for 10 seconds and SDS was added for a final concentration of 2% (w/v). Samples were incubated at room temperature for 10 minutes to lyse the cells and extract the proteins, then spun for 45 minutes at 14 000 × g, at room temperature. SDS-soluble proteins were kept on ice, while SDS-insoluble proteins were processed further by adding 10 volumes of urea buffer (8M urea; 4% SDS, 60 mM Tris-HCl, (Sigma-Aldrich) 12.5 EDTA in deionized water) to samples, incubating 30 minutes at room temperature, and then centrifuging at 16,000g for 5 minutes. Supernatant was precipitated using methanol/chloroform, resuspended on 2% SDS, and

combined with SDS-soluble protein. Samples were reduced with DTT (10mM) at 60 °C for 20 minutes, alkylated with iodoacetamide (IAA, 25mM, Sigma-Aldrich) for 30 minutes at room temperature in the dark. The IAA was then quenched with DTT. Samples were precipitated using methanol/chloroform, and resuspended in digestion buffer (8M urea, 0.1M Tris pH 8.0) containing trypsin-Lys-C mix (Promega) and incubated overnight at 37 °C. The following morning, 50mM ammonium bicarbonate (Sigma-Aldrich) was added containing 1:40 trypsin/Lys-C and samples were incubated for 3 more hours with 10% trifluoroacetic acid (Sigma-Aldrich). Peptides were cleaned up using C18 tips (Nest Group, Southborough, MA), following manufacturer's instructions and dried by Speed Vac.

1.26.8.2 Mass Spectrometry Analysis and Protein Quantification

Tryptic peptides eluted from the beads were dried under vacuum and dissolved in 2% acetonitrile and 0.25% formic acid. Peptides (typically 0.5-1µg) were analyzed using a NanoAcquity UPLC system coupled to a Synapt G2 HDMS mass spectrometer (Waters Inc., Milford, MA) employing a LC-MS/MS experiment in a data-independent acquisition mode complemented with ion mobility separation (HDMSE). Samples were analyzed in duplicate on a 1.7 mm 75 mm x 150 mm C18 130 A BEH column (Waters Inc.) using a 90 minute, 5% to 30% gradient of acetonitrile in 0.1% formic acid at a flow rate of 0.3 ml/min at 35^{o}C. Eluting peptides were sprayed into the ion source of the Synapt G2 using the 10 µm PicoTip emitter (Waters Inc.) at a voltage of 2.5 kV.

Duplicate data-independent analyses (HDMSE) for each sample were conducted with similar LC settings for simultaneous peptide identification and quantification. For robust peak detection and alignment of individual peptides across all HDMSE runs, we

performed automatic alignment of ion chromatography peaks representing the same mass/retention time features using Progenesis QI software. To perform peptide assignment to the features, PLGS 2.5.1 (Waters Inc.) was used to generate searchable files that were submitted to the IdentityE search engine incorporated into Progenesis QI for Proteomics. For peptide identification, we searched against the UniProt rat protein database (July 2016 release) using Cys carbamidomethyl as constant modification and Met oxidation as variable modification. Protein abundances in control and treated samples were calculated from the sum of all unique peptide ion intensities for each protein normalized to the same total ion current intensity of all peptides in all experimental samples. Conflicting peptides for different proteins and their isoforms were excluded from the calculations. All identified proteins were ranked based on their abundance ratios between control (HBSS) and treated (Genipin) samples.

1.26.9 *Statistical Analysis*

All data were analyzed using one of the following approaches, depending on the number of groups and independent variables: two-way repeated measures (RM) ANOVA with Tukey post-hoc, two-way ANOVA with Sidak post-hoc, one-way ANOVA with Tukey post hoc, multiple t-tests with Holm-Sidak correction, or one sample t-test (GraphPad Software v8, San Diego, CA). For two-way RM ANOVA, the reported F statistic is the interaction effect unless otherwise stated. All statistical tests used for each assay are reported in figure legends and results.

For RT-PCR results, fold change was computed as the increase in expression of the experimental eye normalized to the control eye. In HBSS/Naïve rats, the experimental eye

was the HBSS eye and for Genipin/HBSS rats the experimental eye was the genipin-treated eye. Outliers were detected and removed based on Graphpad's ROUT method with a threshold of 0.1% to remove definitive outliers (Motulsky and Brown 2006). Proteomic results were analyzed using Progenesis QI for Proteomics software (Waters Inc., Durham, NC) which was used to compute q- and p-values for each protein. Significant changes in protein expression were defined as any $q < 0.05$ (Liu et al. 2019). All results are presented as mean ± SD.

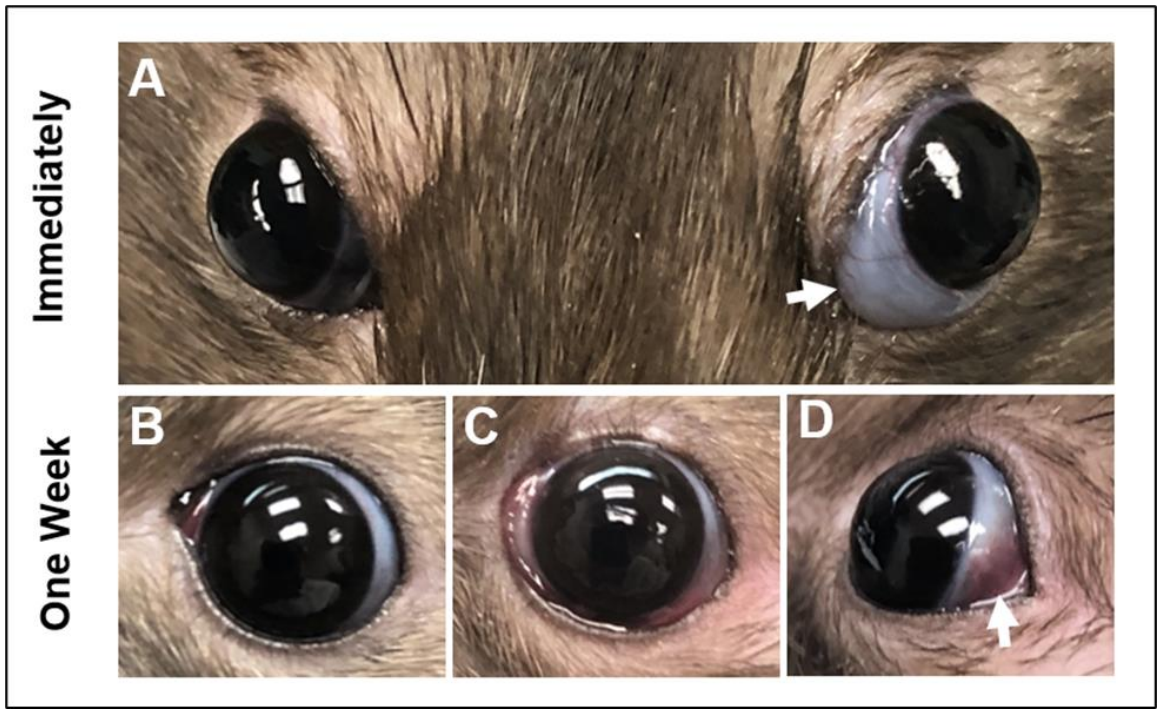

Figure 24: Ocular examination of eyes immediately and one week after retrobulbar injections show mild transient complications. In all eyes receiving a retrobulbar injection (HBSS or genipin), a bleb (A) appeared in the nasal quadrant immediately after injection. One such bleb is indicated by an arrow (OS) and can be compared to the Naïve OD eye (prior to retrobulbar injection). Typically, the bleb would resolve one week after injection (B). In a few cases, eyes had mild conjunctival chemosis (C) or subconjunctival hemorrhage (D, arrow). All images taken one week after injection are oriented such that the nasal portion of the eye is on the left.

1.27 Results

Throughout the experiments, animals were carefully observed to determine whether complications occurred from the retrobulbar injection itself (HBSS eyes) or from genipin

retrobulbar injections (Genipin eyes). A bleb was visible in the nasal/inferior region of the conjunctiva immediately after retrobulbar injection in all eyes, regardless of injection fluid (Figure 24A). All blebs resolved within one to three days post-injection. In approximately 5% of genipin-treated eyes, we saw chemosis which lasted approximately one week after injection (Figure 24C); compared to a normal-appearing genipin-treated eye one week after injection, (Figure 24B). Additionally, we observed a small amount of conjunctival bleeding upon removal of the needle after the a retrobulbar injection, likely due to damaging small conjunctival blood vessels when inserting the needle. After blotting with gauze, bleeding quickly subsided and, in a few cases, caused a subconjunctival hemorrhage that was visible one week post-injection (Figure 24D).

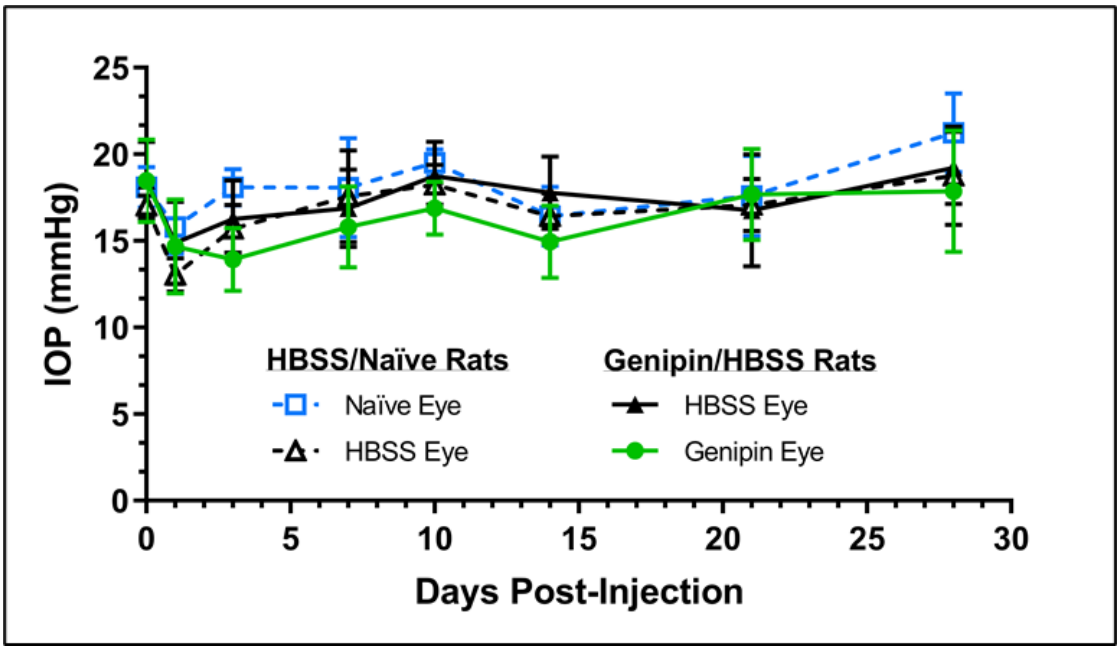

Figure 25: Genipin-induced scleral stiffening did not affect IOP. No significant differences in IOP were found in any group at any timepoint up to four weeks post-injection. RM ANOVA, $F(21,133) = 0.976$; $p = 0.497$. All data shown as mean ± SD, all $n \geq 5$

Genipin treatment of the posterior sclera did not affect IOP for up to four weeks following injection (Figure 25; RM ANOVA, interaction of time and treatment: $F(21,133) = 0.976$; $p = 0.497$), although there was a mild transient decrease in IOP in all injected

eyes. OMR assessment of visual function did not reveal any changes in spatial frequency (Figure 26A; RM ANOVA, interaction of time and treatment: $F(15, 95) = 1.33$; $p = 0.201$), but did show mild transient changes in contrast sensitivity (Figure 26B, RM ANOVA, $F(3, 38) = 3.099$; $p = 0.014$). Specifically, at two weeks post injection, the contrast sensitivity of genipin treated eyes was lower than in Naïve eyes (Tukey post-hoc, $p = 0.002$) and in HBSS eyes from Genipin/HBSS rats (Tukey post-hoc, $p = 0.043$). This deficit recovered by four weeks post injection (all $p > 0.05$).

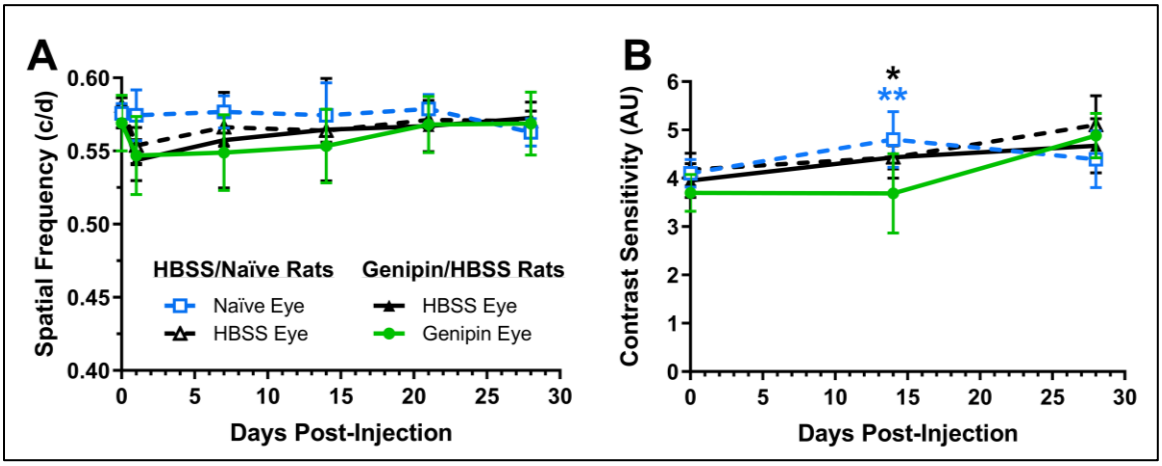

*Figure 26: Genipin treatment did not have a sustained effect on spatial frequency or contrast sensitivity. Spatial frequency (A) and contrast sensitivity (B) for HBSS/Naïve and Genipin/HBSS rats. Spatial frequency was not significantly decreased in any of the groups over the course of the experiment (RM ANOVA, $F(15, 95) = 1.33$; $p = 0.201$). Contrast sensitivity was transiently decreased at day 14 in genipin eyes compared to Naïve eyes ($p = 0.002$, denoted by **) and in HBSS eyes (of Genipin/HBSS rats) vs. genipin eyes ($p = 0.043$, denoted by *). All data shown as mean ± SD and analyzed by RM ANOVA, Tukey post-hoc used when appropriate; all $n \geq 5$.*

Retinal function assessment via full-field ERGs showed no differences between treatment groups in implicit time or amplitude over time at any flash intensity for both dark adapted and light adapted ERGs (Figure 27; RM ANOVA, all $p > 0.05$). Representative waveforms from genipin and Naïve eyes at one- and four-weeks post-injection from the brightest flash in dark adapted (2.1 log cd s/m^2, Figure 27A and B) and light adapted (1.4 log cd s/m^2, Figure 27E and F) protocols are plotted for qualitative analysis.

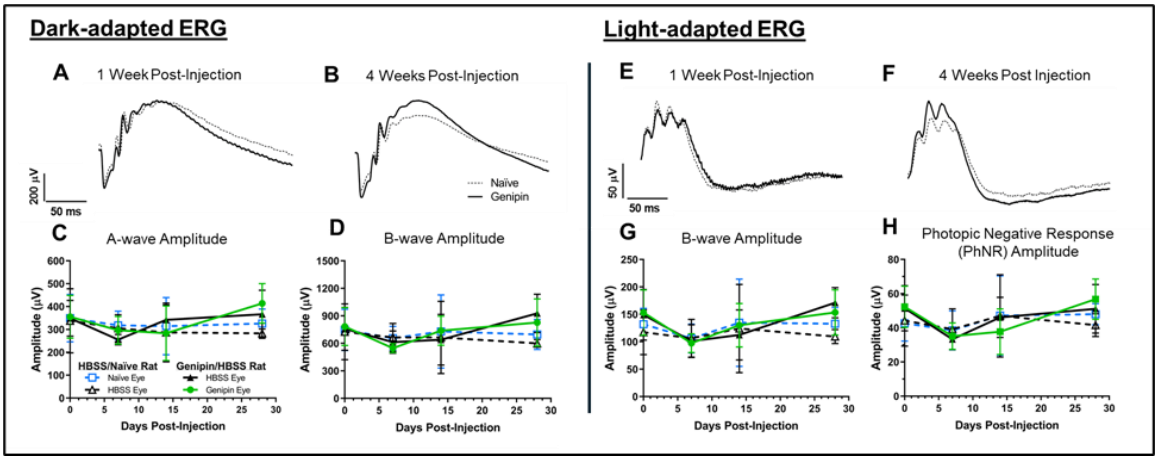

Figure 27: Retinal function was not altered by HBSS or genipin injections up to four weeks post-injection. Electroretinogram Naïve responses for dark-adapted (A-D) and light-adapted (E-H) testing conditions. Plotted are representative waveforms at 1-week (A and E) and 4 weeks (B and F) post-injection for Naïve (black dotted) and genipin (black solid) eyes. Mean amplitude and implicit time of all genipin (or Naïve) eyes were computed at each timepoint and flash intensity to select waveforms that most closely matched the means to ensure proper representative waveforms. A-wave and B-wave amplitudes from the brightest dark-adapted flash (2.1 log cd s/m2) are plotted vs. time in (C) and (D) respectively. Additionally, B-wave and PhNR amplitudes from the brightest single photopic flash (1.4 log cd s/m2) are plotted vs. time in (G) and (H). All ERG data was analyzed with a two-way RM ANOVA. No significant interactions of time and treatment were found for any flash intensity (all $p > 0.05$). All data shown as mean ± SD, all $n \geq 5$.

RGC axon counts from Naïve, HBSS, and genipin eyes were not significantly different from one another (Figure 28A; One-way ANOVA, $F(2, 22) = 0.733$, $p = 0.492$). However, the mean axon counts of genipin treated eyes (70,523 ± 19,668, mean ± SD) showed a trend towards being lower than that of HBSS (79,323 ± 18,215) and Naïve (79,328 ± 12,581) eyes. We further analyzed the axon counts in a paired manner by computing the difference in axon count between genipin and HBSS eyes (Figure 28B), with a negative value indicating the genipin-treated eye had fewer axons than the contralateral HBSS injected eye. The difference in axon count was not significantly different than zero (one sample t-test, $t = 1.276$, $df = 8$, $p = 0.238$), although the mean value was negative (-8,800 ± 20,698 axons). These differences translate to an 8.1% ± 29.8%

axonal loss in genipin-injected eyes compared to fellow HBSS-injected eyes and were also not statistically significant (one sample t-test, t = 0.82, df = 8, p = 0.4366, data not shown). Qualitative evaluation of a genipin/HBSS rat shows healthy axon morphology with uniform myelin sheath surrounding homogenous axonal interior in both HBSS (Figure 28C) and genipin (Figure 28D) eyes.

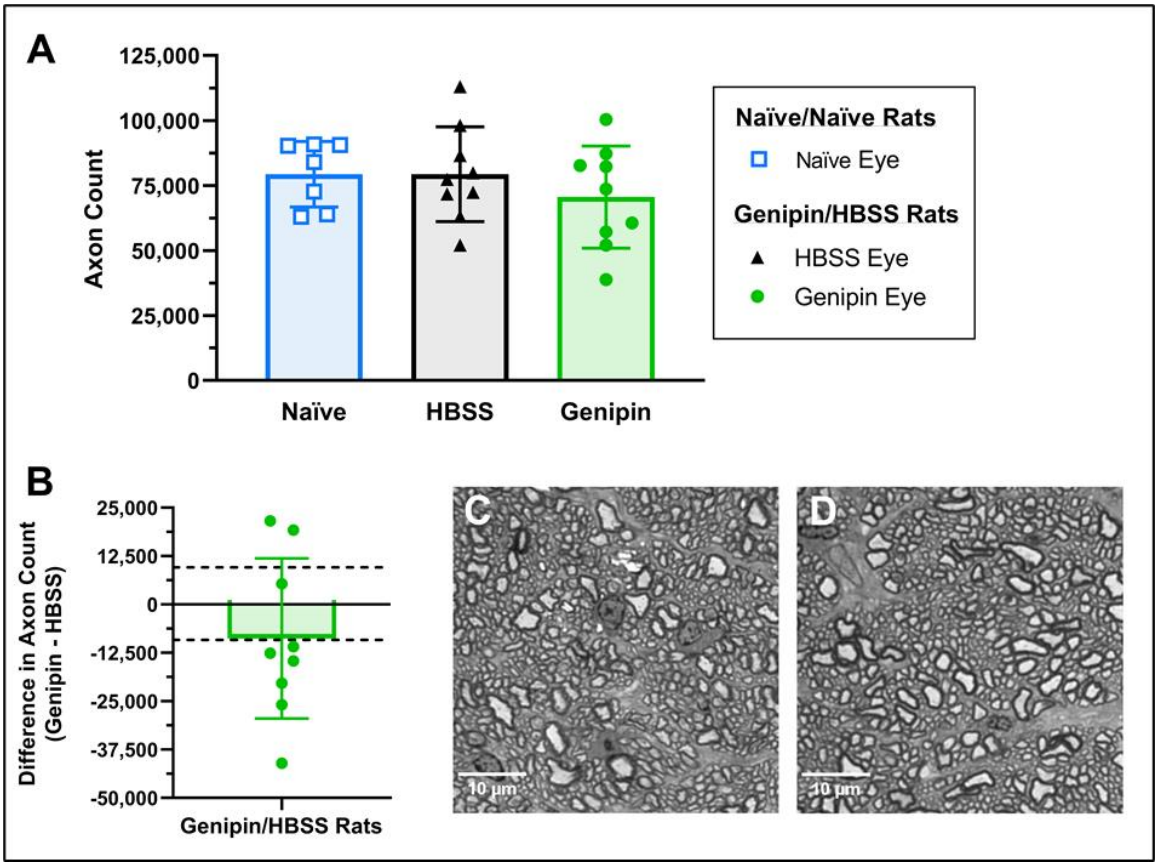

Figure 28: Genipin treatment results in a minor, non-statistically significant, loss of RGC axons: (A) Whole nerve counts from Naïve (n = 7, randomly selected as OD or OS eye), HBSS (n = 9), and genipin (n = 9) eyes. Nerve counts were not different in any cohort (One-way ANOVA, F(2, 22) = 0.733, p = 0.492). (B) Contralateral optic nerve axon count differences for Genipin/HBSS rats at four weeks post-injection. Differences are computed as whole nerve axon count in genipin eye minus whole nerve axon count in contralateral HBSS eye. (One sample t-test, t = 1.276, df = 8, p = 0.238, black dashed lines represent SD of axon count differences from 5 Naïve rats). Data shown as mean ± SD. (C) and (D) show representative subregions from the central region of optic nerves from a Genipin/HBSS rat, with (C) being the HBSS eye and (D) being the genipin eye. Axons appear to be normal with homogenous interiors surrounded by uniform myelin sheaths.

RT-PCR was used to evaluate message abundance for ECM proteases in the sclera and inflammatory markers in the retina (Appendix C: Table 7) at one and four weeks after injection. No significant changes in message for ECM proteases in the sclera or pro-inflammatory cytokines in the retina were found at one week or four weeks after injection (Appendix C: Figure 50, multiple t-test, all $p > 0.05$). We also used proteomic analysis to determine the amount of various scleral proteins involved in protein binding, cell motility, and ECM structural support at four weeks post-injection (Appendix C: Table 8). Protein levels were not significantly different in genipin-injected eyes compared to their contralateral HBSS-injected eyes (all $q > 0.05$).

1.28 Discussion

Previous work from our lab demonstrated successful stiffening of the posterior rat sclera for four weeks after a single retrobulbar injection of genipin (Hannon et al. 2019) as a possible therapy to mitigate axial elongation in myopia or optic neuropathy in glaucoma. In the present study, we have used the same genipin injection procedure to evaluate potential adverse effects of genipin-induced scleral crosslinking at the molecular and functional levels in the eye. We conclude that genipin-induced scleral crosslinking had no sustained effect on visual and retinal function over a 4 week period, although there was a trend towards a slight (non-statistically significant) loss of retinal ganglion cell axons. These results are the first to assess functional outcomes of genipin stiffening, required for eventual clinical translation of a potential therapy for myopia or glaucoma.

Although no change in steady-state IOP was found in this study, it is important to note that fluctuations in IOP are a risk factor for glaucomatous damage (Asrani et al. 2000).

Clayson et al. (2017) found that scleral stiffening with glutaraldehyde increased the magnitude of IOP spikes in ex vivo porcine eyes, although to a much lesser extent than corneal crosslinking (Clayson et al. 2017). Future research with genipin-induced scleral crosslinking should evaluate the potential effects on the magnitude of IOP fluctuations.

A slight decrease in visual acuity (spatial frequency) was measured at one day post injection in all eyes receiving a retrobulbar injection with any fluid (HBSS or genipin). This initial deficit was most likely due to the retrobulbar injection itself, which seemed to cause a nonsignificant, recoverable, deficit. Also, at two weeks post injection, genipin-treated eyes had significantly lower contrast sensitivity compared to Naïve and HBSS (of Genipin/HBSS rats) eyes; however, this deficit recovered by week four. Because contrast sensitivity was only evaluated at baseline, week two, and week four, no conclusions can be made about whether genipin affected contrast sensitivity within the first two weeks after injection. However, there appears to be no sustained deficit in spatial frequency or contrast sensitivity due to a single retrobulbar injection of genipin.

A robust ERG protocol was implemented in this study to selectively stimulate retinal layers and cell types. Amplitude and implicit time of each wave were analyzed to evaluate retinal function and kinetics. In all parameters evaluated, no significant effects of treatment over time were found. Therefore, genipin-induced scleral stiffening does not appear to affect retinal function in any retinal layer as detectable by ERGs.

Even though no sustained visual or retinal functional deficits were found, it was important to assess RGC axon counts at four weeks after injection. Genipin/HBSS rats did not have a statistically significant loss in RGC axons in the genipin-treated eye, but these

eyes showed on average a loss of approximately 8,800 axons, or 8.1% of total axons (using paired analysis). The mean difference between axon counts in genipin and contralateral HBSS eyes was within one standard deviation of axon count differences from contralateral eyes of naïve rats. This amount of axonal loss appears not to have been functionally significant, but is nonetheless a potential concern. Clinical studies have estimated that patients with glaucoma with the earliest detectable vision loss may already have on average around 30% RGC loss (Medeiros et al. 2013; Kerrigan-Baumrind et al. 2000). If one extrapolates from human clinical data to the rat, one could state that the amount of RGC axon loss that we observed is roughly three times smaller than the threshold for visual deficits; however, any RGC axonal loss is worrisome, especially if genipin is to be considered as a treatment for glaucomatous optic neuropathy. Therefore, if genipin treatment is used to treat glaucoma or myopia in the future, RGC axonal loss due to minor genipin toxicity should be carefully evaluated. Additionally, a lower dose of genipin (volume or concentration or combination of the two) could be considered to potentially mitigate the slight loss of RGC axons that we observed, although we note that the dose and concentration that we used was selected since it was the lowest dose that achieved a desired level of scleral stiffening (Hannon et al. 2019).

Several studies have found that genipin is cytotoxic at low concentrations (0.02 – 0.50 mM) when cultured with various cell types (Kim et al. 2005; Kreiter et al. 2019; Kim et al. 2014; Wang et al. 2011). These concentrations of genipin are much lower than the 15 mM concentration used in this study. It is important to note that 15 mM was the concentration that was injected into the periocular space, and therefore the exact concentration of genipin that scleral fibroblasts or retinal cells were exposed to is unknown.

In our pilot study evaluating molecular changes in gene expression and protein levels, we also did not find any significant changes in scleral gene expression related to ECM turnover, or in retinal gene expression for inflammatory cytokines. Since these molecular analyses were based upon a small number of animals, this data should be considered as a pilot study to identify large effects of genipin treatment on transcript and protein levels. We did not identify any such effects, but further studies are warranted.

Retrobulbar injections are used clinically to anesthetize the globe and extraocular muscles for cataract and retinal surgery (Alhassan, Kyari, and Ejere 2015). Some of the major complications of retrobulbar injections include: inadvertent globe perforation, retrobulbar hemorrhage, central retinal artery occlusion, and even death (Patel et al. 1996; Vasavada, Baskaran, and Ramakrishnan 2017). None of these serious complications occurred in any of the injected rats in this study. Other minor complications of retrobulbar injections include chemosis and subconjunctival hemorrhage (Jacobi, Dietlein, and Jacobi 2000; Patel et al. 1996). Here, we did observe a few eyes with chemosis that persisted for approximately one week after injection, but which spontaneously resolved by two weeks after injection. Since no signs of chemosis were seen in HBSS injections, we infer that the genipin treatment itself could have caused minor transient conjunctival inflammation. On the other hand, subconjunctival hemorrhage was seen in both HBSS- and genipin-injected eyes, and thus we conclude that subconjunctival hemorrhage was a complication from the injection rather than from the genipin per se.

1.29 Conclusion

Previous research has shown that retrobulbar injection of 15 mM genipin produces sustained posterior scleral stiffening. Here, we find that the same injection protocol does not cause prolonged decrease in visual or retinal function. However, we did observe some possible signs of toxicity when evaluating RGC axons and gross anatomy of eyes after injection. This work lays the groundwork for future *in vivo* studies to evaluate genipin-induced scleral crosslinking for treatment of myopia and glaucoma.

Using retinal function to define ischemic exclusion criteria for animal models of glaucoma

1.30 Targeted Submission Details:

Authors: **Bailey G. Hannon**, Andrew J. Feola, Brandon G. Gerberich, A. Thomas Read, Mark R. Prausnitz, C Ross Ethier, Machelle T. Pardue

Target Journal: Experimental Eye Research

1.31 Introduction

Glaucoma is the most common cause of irreversible blindness worldwide (Quigley and Broman 2006). While glaucoma can occur at any level of intraocular pressure (IOP), elevated IOP remains a major causal risk factor for developing glaucoma. Ocular hypertension (OHT) is commonly used in animal models to study the mechanisms, progression, and potential treatments for glaucomatous optic neuropathy (Bouhenni et al. 2012). A variety of techniques are used to induce OHT, including: impeding the aqueous humor from the eye by limbal injection of hypertonic saline, episcleral vein cauterization, microbead occlusion, or laser trabeculoplasty; altering trabecular meshwork biology; or delivering steroids to the eye (Morrison, Cepurna Ying Guo, and Johnson 2011; Urcola, Hernandez, and Vecino 2006; Morrison, Johnson, and Cepurna 2008). However, a difficulty with many of these inducible models is that the resulting IOPs can become very high (Morrison et al. 1997; Morgan and Tribble 2015; Shareef et al. 1995; Foxton et al. 2013). For example, in awake Brown Norway rats Foxton et al. reported a mean peak IOP of 55.2 mmHg after microbead occlusion (Foxton et al. 2013) and Morrison et al. estimated

a mean IOP of up to 60 mmHg after injection of hypertonic saline (Morrison et al. 1997). In anesthetized rats, studies have reported IOPs up to 60 mmHg after episcleral vein cauterization (Shareef et al. 1995) and translimbal laser photocoagulation (Levkovitch-Verbin et al. 2002). Moreover, the unanesthetized (true) IOP is likely much higher, since anesthesia can underestimate IOP by almost 50% in ocular hypertensive eyes (Jia et al. 2000a). Such IOPs are higher than those typically seen clinically in open-angle glaucoma patients (32 ± 11 mmHg, mean ± SD)(Mafwiri et al. 2005).

Severely elevated IOPs raise concerns of retinal ischemia, which is an undesirable confounding factor in experimental studies of glaucomatous optic neuropathy, inasmuch as ischemia can affect retinal function independent of retinal ganglion cell pathology. Zhi et al. examined the impact of IOP "spikes" on retinal ischemia, as assessed by retinal vascular occlusion, using optical coherence tomography/optical microangiography (OCT/OMAG) to image Brown Norway rat eyes at IOPs ranging from 10-100mmHg (Bui et al. 2013; Zhi et al. 2012). Blood flow in retinal vessels was affected by IOPs above 30 mmHg and choroidal filling was affected at IOPs above 60 mmHg. Further analysis by Bui et al. utilized electroretinography (ERG) and found that retinal function was adversely affected at IOPs above 50 mmHg (Bui et al. 2005). These IOP spikes affected not only the retinal ganglion cell layer, but also caused functional changes in photoreceptors (as assessed by the ERG a-wave) and bipolar cells (b-wave). Although these functional changes recovered after IOP was returned to baseline levels (He, Bui, and Vingrys 2006), prolonged ischemic IOPs are known to permanently damage non-RGC cell types, especially the bipolar cells in the inner retina (Zhao et al. 2013; Schmid et al. 2014).

In an attempt to create models of OHT in which damage is isolated to RGCs alone, i.e. avoiding pan-retinal ischemia, several studies have defined IOP "thresholds" and excluded animals whose IOP exceeded this threshold value (Bunker et al. 2015; Struebing et al. 2018; Smedowski et al. 2014). However, for practical reasons, most studies conduct IOP measurements at most two or three times per week (Matsumoto et al. 2014; Dai et al. 2012; Bunker et al. 2015; Foxton et al. 2013), which is insufficient to reliably detect IOP spikes throughout a study. Further, rodents show diurnal fluctuation in IOP; specifically, the IOP in normotensive rats can increase by approximately 10 mmHg at night (Jia et al. 2000b), and OHT rats have a much more variable diurnal IOP response (Jia et al. 2000b; Kwong et al. 2013). These facts together suggest that ischemic levels of IOP can be frequently missed in OHT studies, especially with daytime IOP measurements, so that animals with ischemic damage can be inappropriately included in studies of the role of OHT in glaucomatous optic neuropathy. Thus, our goal was to develop an alternative technique to evaluate ischemia, based on analysis of the scotopic b-wave in ERGs previously used in the study of central retinal artery occlusion (Hayreh 2004; Hayreh, Kolder, and Weingeist 1980). We specifically compared two ischemic exclusion criteria based on: (1) an IOP threshold and (2) a threshold based on scotopic b-wave ERG amplitude. We hypothesize that an ERG-based exclusion criterion to identify eyes experiencing ischemia is superior to typically used, infrequent IOP measurements.

1.32 Methods

1.32.1 *Animals*

This study used 74 retired breeder (male, 8 - 10 months old) Brown Norway rats (Charles River Laboratories, Inc., Wilmington, MA). All procedures were approved by the Institutional Animal Care and Use Committee at the Georgia Institute of Technology and adhered to the Association for Research in Vision and Ophthalmology (ARVO) Statement for the Use of Animals in Ophthalmic and Vision Research.

1.32.2 *Microbead Injection Preparation and Procedure*

The magnetic microbead model of glaucoma was used to induce unilateral ocular hypertension, using 2 µm and 6 µm diameter PEGylated magnetic microbeads (micromer®-M, Micromod, Rostock, Germany) mixed in a 1:1 ratio. Microbeads were autoclaved (manufacturer's specifications: 3500 mbar pressure for 20 minutes at 121 °C) and then thoroughly cleaned by washing five times with sterile Hank's balanced salt solution (HBSS; H8264, Sigma-Aldrich, St. Louis, MO). Microbeads were suspended in HBSS at a concentration of 2.25×10^6 to 4.5×10^6 beads total per 25 µl injection.

Rats were anesthetized with ketamine (60mg/kg) mixed with xylazine (7.5 mg/kg) and a drop of tetracaine (0.5%) was applied to the eye as a local anesthetic. A 25µl microbead suspension was vortexed to mix the suspension, pipetted onto a piece of parafilm, and drawn into sterile, disposable syringes with 31 G needles (BD 300 µl Insulin Syringe Ultra-Fine™ needle, Becton, Dickinson and Company, Franklin Lakes, New Jersey). A neodymium, grade N40, nickel-plated annular magnet (H125D, Amazing

Magnets, Anaheim, CA) was placed around the limbus of the eye and the magnetic microbead suspension was injected into the anterior chamber. To minimize fluid reflux, the needle was held in the anterior chamber for a minute after injection and then slowly removed. The magnet was then held on the eye for 10 minutes to ensure that beads had settled into the iridocorneal angle. Both eyes (hypertensive and uninjected contralateral normotensive control) received topical antibiotic (Vetropolycin, Dechra Pharmaceuticals, Northwich, United Kingdom) to prevent infection. Saline eye drops were then placed on each eye to maintain hydration. Rats were placed on heating pads until ambulatory. If the experimental (injected) eye did not demonstrate at least one day of OHT, defined as an IOP elevation of > 5 mmHg compared to the contralateral control eye within 7 days of injection, the eye was considered to be a non-responder and was then reinjected with 15 µl of microbead solution on Day 7 (n = 12 of 74 total rats).

1.32.3 *Tonometry*

IOP measurements were taken between 7:00am and 10:00am using a Tonolab rebound tonometer (Icare Finland Oy, Vantaa, Finland). The rebound tonometer was previously calibrated on an intact post-mortem rat eye, by setting IOP from 5 to 50 mmHg in nine 5 mmHg steps using an external reservoir attached to a needle cannulating the eye and making Tonolab IOP measurements at each set IOP level (data not shown). Calibration results showed good agreement between set IOP values and measured IOP values, and thus no IOP correction was necessary.

During each measurement session, eight tonometer measurements were taken from each eye of awake rats. The highest and lowest IOP measurements were discarded and the

remaining six values were averaged to obtain an IOP measurement for that eye. IOP measurements were recorded at day 0 (baseline), 1, 3, 5, 7, 10, and 14 days post-injection. We then calculated the IOP burden, also referred to as cumulative IOP difference (Frankfort et al. 2013), IOP exposure (Sappington et al. 2010), or positive integral IOP (Mabuchi et al. 2003), which provides an estimate of the total IOP "insult" to the hypertensive eye. We defined IOP burden as the area between the OHT and normotensive eyes on the IOP versus time plot. If the measured IOP in the OHT eye was transiently lower than IOP in the contralateral (normotensive) eye, the IOP difference was set to zero at that time point, i.e. we did not allow negative contributions to the IOP burden.

1.32.4 *Electroretinogram*

Retinal function was evaluated using dark-adapted bright flash ERG at baseline, 7, and 14 days after microbead injection. At each timepoint, rats were dark-adapted for 30 minutes and anesthetized using ketamine (60 mg/kg) and xylazine (7.5 mg/kg). After induction of anesthesia, both eyes received a drop of tetracaine (0.5%) and tropicamide (1%) to locally anesthetize and dilate pupils, respectively. A ground electrode was inserted into the tail and reference electrodes were inserted subcutaneously into each cheek. Custom gold-loop electrodes were placed on the cornea of each eye and a layer of carboxymethylcellulose (Celluvisc, Allergan, Dublin, Ireland) was placed onto the corneal electrode to ensure electrical conductivity and prevent drying. Under dark-adapted scotopic conditions, a 6-step series of increasing flash intensities (-6.0 to 2.1 log cd s/m^2) was used. Electrical responses to various full-field flash stimuli in a Ganzfield dome were recorded using a signal-averaging ERG system (UTAS BigShot; LKC Technologies, Gaithersburg, MD). Here, we only report data from the brightest flash (2.1 log cd s/m^2) 14 days after

microbead injection, since bright scotopic flashes more reliably detect bipolar cell disfunction under ischemic conditions (Matsumoto, Shinoda, and Nakatsuka 2011). This flash intensity stimulates components from both the inner and outer retina, and the a-wave amplitude thus represents the combined response of the rod/cone photoreceptors. The a-wave amplitude and corresponding implicit time were measured from baseline to the peak negative (trough) response after the flash stimulus (Aung et al. 2013)(Figure 29A). We also measured the b-wave amplitude and implicit time, which represent the function of the bipolar cells (Khan et al. 2015). The b-wave amplitude was measured from the trough (a-wave) to the positive peak of the rising curve (Figure 29A).

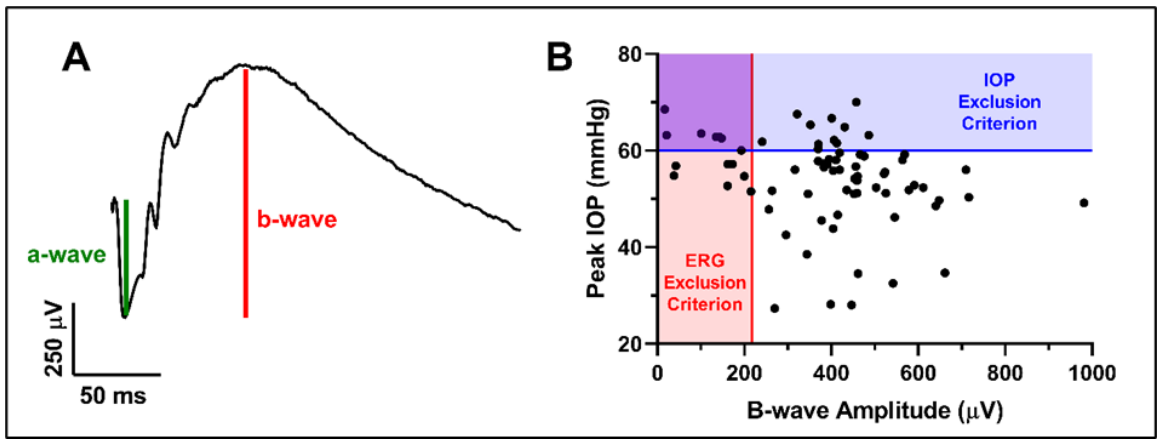

Figure 29: (A) Representative ERG waveform from a normotensive control eye. Green and red lines depict how a-wave and b-wave amplitudes were defined, respectively. (B) Peak measured IOP is plotted vs b-wave amplitude at day 14 in hypertensive eyes (n = 74 eyes). Blue line denotes peak IOP of 60 mmHg, above which rats were excluded based on the IOP Exclusion Criterion. Red line denotes the lower 99.5% confidence interval of b-wave amplitude at day 14 from contralateral normotensive control eyes, below which rats were excluded based on the ERG Exclusion Criterion.

1.32.5 *RGC Axon Counting*

Rats were euthanized (via CO_2 overdose) 14 days after microbead injection and optic nerves were dissected from whole globes to count retinal ganglion cell axons from cross sections using AxoNet, a fully convolutional neural-network program previously

developed in our lab (Ritch et al. 2019) and Appendix A. Optic nerves were fixed with isotonic Sorensen's buffer containing 2.5% glutaraldehyde and 2% paraformaldehyde (EMS, Hatfield, PA), post-fixed in osmium tetroxide, dehydrated through an ethanol series and embedded in Araldite 502/Embed 812 resin (EMS, Hatfield, PA). Semithin sections (0.5 µm thick) were cut on a Leica UC7 Ultramicrotome (Leica Microsystems, Buffalo Grove, IL) and stained with toluidine blue (1%). Sections were imaged using a Leica DM6 B microscope (Leica Microsystems, Buffalo Grove, IL) with a 63x lens and 1.6x multiplier for a total magnification of 100x. Z-stack tile scans of the entire optic nerve were imaged and the optimally focused image within each z-stack tile was chosen using the "find best focus" feature in the LAS-X software (Leica Microsystems, Buffalo Grove, IL). Contrast was then adjusted for each tile by maximizing grey-value variance and AxoNet was used to count normal axons in the entire optic nerve section as described in (Ritch et al. 2019) and Appendix A. We also sectioned and counted a representative subset of normotensive contralateral control eyes to provide a database of axon counts in normotensive eyes, finding axon counts of 80,546 ± 10,096 axons (mean ± SD, n = 53) which is similar to previous studies (Morrison 2005; Marina, Bull, and Martin 2010a).

1.32.6 *IOP- and ERG-Based Exclusion Criteria*

Here, we explore two exclusion criteria for rats with OHT. The first is termed the "IOP Criterion", and was adopted from Bunker et al. (Bunker et al. 2015). Specifically, we excluded rats if any IOP measurement exceeded a threshold of 60 mmHg (Figure 29B). This threshold value was based on previous research reporting decreased choroidal perfusion (Zhi et al. 2012) and significant reduction in ERG amplitude (Bui et al. 2013) in rats when IOP exceeded 60 mmHg. The second exclusion criteria is termed the "ERG

Criterion", and was based on the expectation that rats experiencing damaging levels of IOP would have functional losses in bipolar cells and photoreceptors (Bui et al. 2005; Block and Schwarz 1998). We specifically focused on the b-wave amplitude at the conclusion of the study (day 14), since bipolar cell function (related to b-wave amplitude) is known to be sensitive to ischemic damage (Zhao et al. 2013; Block and Schwarz 1998; Hayreh, Kolder, and Weingeist 1980; Lima et al. 2010). We calculated the 99.5% confidence interval of the b-wave amplitude for all normotensive control eyes (n = 74) using the mean, standard deviation, and corresponding z-score (2.807). We then excluded both eyes of a rat if the measured b-wave amplitude in the OHT eye fell below this confidence interval (Figure 29B).

1.32.7 *Statistical Analysis*

IOP vs. time data were analyzed using a two-way repeated measures (RM) ANOVA with a Sidak post-hoc test. IOP burden and axon count data were analyzed using a one-way ANOVA with Sidak post-hoc test (GraphPad Software v8, San Diego, CA). Linear regressions were analyzed based on the null hypothesis that the slope significantly differed from a hypothetical value of 0. All comparisons were considered significant if $p \leq 0.05$.

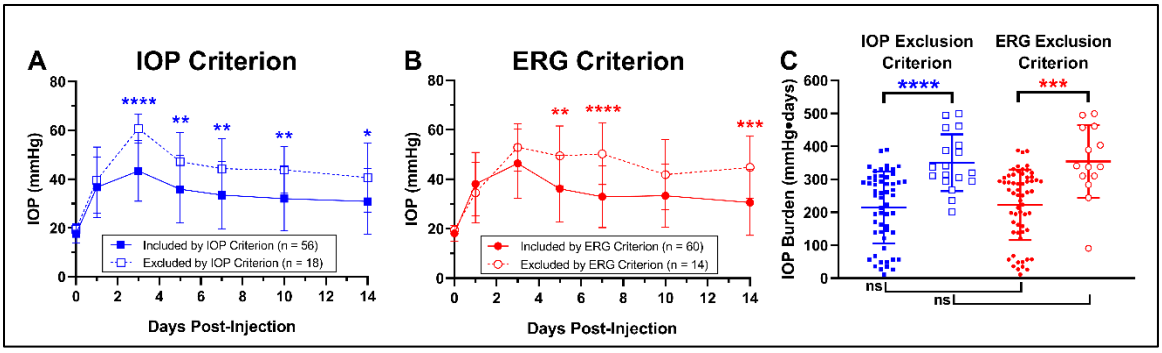

*Figure 30: IOP measurements from OHT eyes, showing rats that were included (solid) and excluded (hollow symbols) based on the IOP Criterion (A) or on the ERG Criterion (B). Excluded eyes had higher IOP values at 3, 5, 7, 10, and 14 days and 5, 7, and 14 days after microbead injection using the IOP Criterion or ERG Criterion, respectively (RM ANOVA, Effect of IOP Criterion: $F(1, 72) = 23.74$, $p < 0.0001$; Effect of ERG Criterion: $F(1, 72) = 13.59$, $p = 0.0004$; Sidak post-hoc). IOP burden (C) was larger for excluded rats than for included rats for either exclusion criteria (One-way ANOVA, $F(3, 144) = 13.33$, $p < 0.0001$; Sidak post-hoc: IOP Criterion $p < 0.0001$, ERG Criterion $p = 0.0002$). Data shown as mean ± SD ("ns" indicates not significant, * indicates $p \leq 0.05$, ** indicates $p < 0.01$, *** indicates $p < 0.001$, **** indicates $p < 0.0001$).*

1.33 Results

Of the 74 hypertensive eyes included in this study, 18 had peak IOP measurements exceeding 60 mmHg and were therefore excluded based on the IOP Criterion (Figure 29B). The 99.5% confidence interval for the b-wave amplitude (2.1 log cd s/m^2) measured in normotensive contralateral control eyes was 217.47 – 754.84 µV. In the same cohort of 74 hypertensive eye, 14 rats had a b-wave amplitude that fell below the lower bound of this confidence interval and were therefore excluded based on the ERG Criterion (Figure 29B). Of the 74 rats, 7 were excluded by both criteria, while 49 were included by both criteria. 7 rats were included based on the IOP Criterion only and 11 rats were included based on the ERG Criterion only.

IOP values in hypertensive eyes were lower in included rats vs. excluded animals, based on either the IOP Criterion or the ERG Criterion (Figure 30A and B; RM ANOVA, effect of IOP Criterion: $F(1, 72) = 23.74$, $p < 0.0001$; effect of ERG Criterion: $F(1, 72) =$

13.59, p = 0.0004; Sidak post-hoc). Considering the IOP Criterion, excluded hypertensive eyes had higher IOP values at days 3, 5, 7, 10, and 14 (p< 0.002, p = 0.0035, p =0.0065, p = 0.0021, and p = 0.0194, respectively; Figure 30A), while hypertensive eyes excluded based on the ERG Criterion had higher IOP values at 5 (p = 0.0016), 7 (p < 0.0001), and 14 (p = 0.0006) days after microbead injection (Figure 30B). Further, the IOP burden for excluded rats was significantly higher vs. that of the included rats using either exclusion criterion (Figure 30C; One-way ANOVA, F (3, 144) = 13.33, p < 0.0001; Sidak post-hoc: IOP Criterion p < 0.0001, ERG Criterion p = 0.0002).

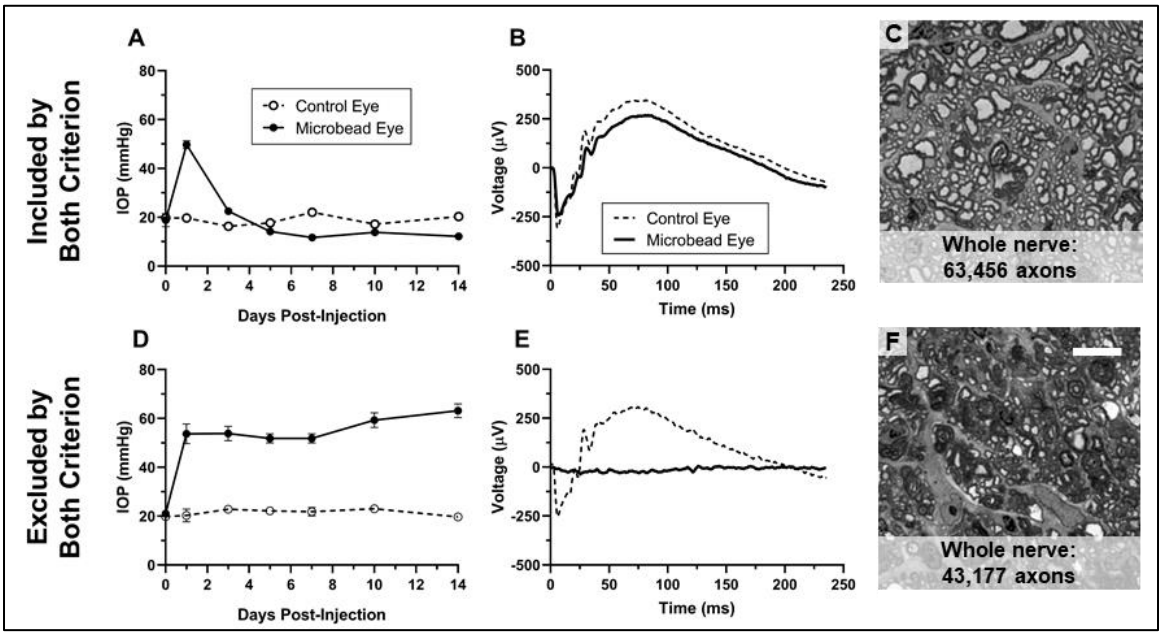

Figure 31: Examples of data from rats included (A, B, and C) or excluded (D, E, F) by both IOP and ERG exclusion criteria. Plotted are IOP traces vs. time (A and D), ERG waveforms (B and E), and central region of optic nerve cross sections with the total axon count from the whole optic nerve superimposed (C and F). Data shown as mean ± SD, scalebar for optic nerve images is 10 µm.

It is useful to consider several "case studies" of animals that were included and/or excluded by various criteria. First, we consider a representative rat that was included by both IOP and ERG criteria. The IOP trace and ERG waveform look normal/healthy (Figure 31A and B), and the optic nerve demonstrates mostly healthy-looking axons (Figure 31C,

axon count = 63,456, or 78.8% of the mean value for normotensive control eyes). Next, we consider a rat that was excluded by both the IOP and ERG criteria (Figure 31D-F). The IOP reached a value slightly above 60 mmHg (Figure 31D), while the ERG waveform was completely flat (Figure 31E) and significant axon damage was evident in optic nerve cross-section (Figure 31F, axon count = 43,177, or 53.6% of the mean value for normotensive control eyes).

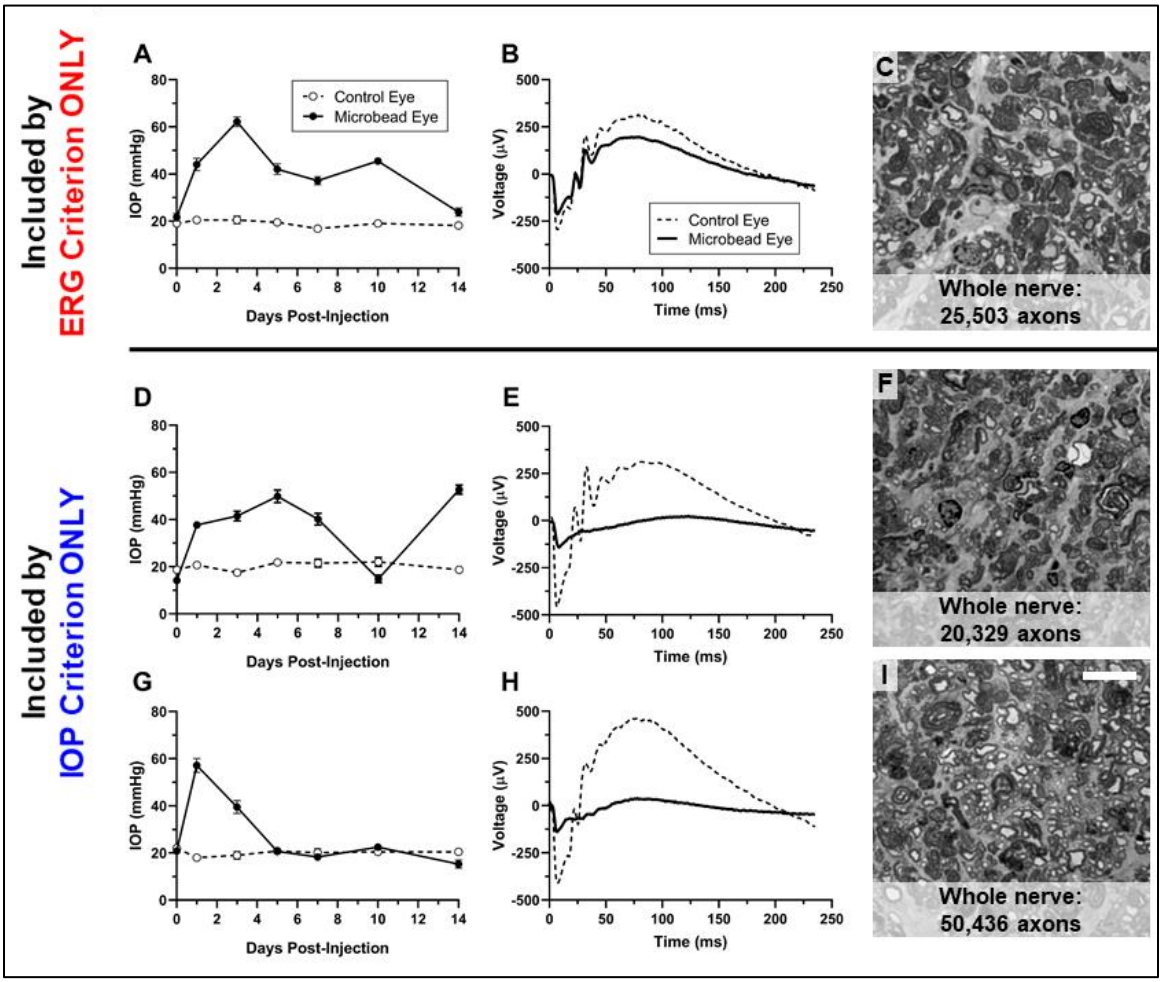

Figure 32: Data from a rat that was included by ERG Criterion only, (A-C) and from two rats that were included by IOP Criterion only (D-I). Shown are IOP traces over time (A, D and G), ERG waveforms (B, E, and H), and central regions of optic nerve cross sections with the total axon count from the whole optic nerve superimposed (C, F, and I). Data shown as mean ± SD, scalebar for optic nerve images is 10 µm.

We next consider cases where the exclusion criteria did not agree (Figure 32). For example, some animals were included by ERG Criterion, but experienced a spike in IOP and thus were excluded by IOP Criterion (Figure 32A). In one such case, there was no significant decrease in b-wave amplitude (Figure 32B), yet a large loss of RGC axons was seen (Figure 32C, axon count = 25,503, or 31.7% of the mean value for normotensive control eyes). On the other hand, some rats were included by the IOP Criterion (only mild elevations in IOP), yet were excluded by the ERG Criterion, with extremely low b-wave amplitudes (Figure 32D – I). Even within this cohort, there were very dissimilar amounts of axon damage (axon count = 20,329, or 25.2% of normotensive control eyes [Figure 32F] vs. 50,436, or 62.6% of normotensive control eyes [Figure 32I]).

1.34 Discussion

We here consider the vexing problem of how best to identify ischemic damage due to IOP "spikes" in rodent studies investigating the role of OHT in glaucomatous optic neuropathy, and propose a new method to exclude such ischemic animals. Currently, researchers identify potentially ischemic animals by defining IOP "thresholds" and excluding animals whose IOP exceeds this threshold (Bunker et al. 2015; Struebing et al. 2018; Smedowski et al. 2014). However, measuring IOP at discrete time points provides a limited picture of the IOP history and thus little insight into the overall function of the retina. Our proposed ERG Criterion provides an alternative method to identify animals that have suffered ischemic retinal damage, known to lead to a loss of bipolar cell function as detected by abnormal ERG b-wave amplitudes. At the same time, this criterion allows for inclusion of rats who experience transient IOP spikes that are too short to induce permanent

ischemic damage (Bui et al. 2005; Bui et al. 2013; He, Bui, and Vingrys 2006) without the need to continuously monitor IOP.

Our ERG Criterion was based only on b-wave amplitude and did not explicitly consider IOP. However, there was a large overlap between the excluded ERG and IOP Criterion groups; specifically, the ERG Criterion removed 66.2% of the same animals as the IOP Criterion. This is consistent with the idea that high IOP induces ischemic damage, as previously shown (Bui et al. 2005; He, Bui, and Vingrys 2006). Further, rats excluded by the ERG Criterion had higher IOPs and IOP burdens than those included based on the ERG Criterion (Figure 30), which indicates that assessing ERG function at the end of the study can identify a majority of rats that had very high IOPs.

In the case study examples presented in Figure 31, the IOP traces and corresponding ERG waveforms showed the expected findings, i.e. rats with lower IOP measurements had better bipolar cell and photoreceptor function (Figure 31A-C), while those with higher IOP measurements had abnormal bipolar and photoreceptor function (Figure 31D-F). The more surprising finding was situations where there were conflicts between the two criteria (Figure 32). We suggest that such disagreement is due to the lack of continuous IOP monitoring. More specifically, in cases included by IOP Criterion only (Figure 32A-C), the observed IOP spike may have been of very short duration, thus allowing the bipolar and photoreceptor neurons to recover (Bui et al. 2013). On the other hand, in cases excluded by ERG Criterion only (Figure 32D-I), it is likely that these rats experienced an undetected significant interval of elevated IOP, i.e. between scheduled IOP measurement times, that induced permanent ischemic damage. For these reasons, it is important to evaluate the b-

wave amplitude at the end of the study in order to obtain an accurate estimate of rats who may have acute (Figure 32A-C) vs. long-term (Figure 32D-I) retinal functional deficits.

In our dataset, eye axon counts in hypertensive eyes did not differ between cohorts included by either IOP or ERG criterion (Supplemental: Figure 51; axon counts in eyes included by IOP Criterion = 44,458 ± 21,075; axon counts in eyes included by ERG Criterion = 42,869 ± 21,231; axon counts in entire cohort = 40,657 ± 20,541; mean ± SD). However, it is important to note that ischemia causes damage to *all* retinal neurons, including RGCs (Adachi et al. 1996) and thus we expect to observe a decrease in RGC axon counts in both glaucoma *and* ischemia. Thus, inability to suitably exclude animals with ischemic damage can lead to misleading conclusions. For example, if a treatment designed to preserve vision is tested in an OHT model and provides preservation of RGC axons, an investigator might conclude that this treatment was efficacious. However, without suitably excluding animals with ischemic damage, the observed protection against axon loss could in fact mean that the treatment protected against axon loss due to ischemia, rather than IOP-associated glaucomatous damage. Our ERG Criterion provides a way to exclude animals with permanent loss of bipolar cell function, focusing on animals with RGC-specific damage.

In future, it would be useful to continuously monitor IOP to determine the duration and magnitude of elevated IOP that leads to ischemic damage as measured by ERG. Although continuous IOP monitoring in rodents is rarely performed, the exact IOP history is also available in the acute CEI model (Morrison et al. 2016). Further, Bello et al. recently developed a “smart pump” to continuously monitor a rat’s IOP (Bello, Malavade, and Passaglia 2017b), i.e. allowing determination of the exact IOP history of an eye.

Continuous IOP monitoring could also be used to obtain a more exact IOP burden measurement, which would lead to more accurate results in analyses which use IOP burden as a covariate (Huang et al. 2018; Frankfort et al. 2013; Mabuchi et al. 2003). However, even with continuous IOP monitoring, an ERG Criterion should still be considered because the exact level and duration of IOP elevation that result in ischemic damage is variable between animals (Bui et al. 2013).

1.35 Conclusion

We suggest that an exclusion criterion based on the ERG may detect unwelcome, undetected IOP-induced ischemic damage in animal models of OHT. Since brief IOP spikes do not necessarily lead to permanent retinal damage, and because extended periods of elevated IOP may be missed, an ERG-based exclusion criterion may prove useful in future animal studies of OHT and glaucomatous optic neuropathy.

Genipin-induced scleral stiffening in a rat model of glaucoma

Authors: **Bailey G. Hannon***, Brandon G. Gerberich*, A. Thomas Read, Matthew D. Ritch, Elisa Schrader, Lauren Nichols, Cahil Pontis, Shreesh Sridhar, Stephen A Schwaner, Maya G. Toothman, Hannah Huang, Gabby S. Gershon, Andrew J. Feola, Machelle T. Pardue, Mark R. Prausnitz, C. Ross Ethier

Target Journal: Proceedings of the National Academy of Sciences (will be reformatted to fit the specifications of this journal).

Contribution: **Bailey G. Hannon** co-authored this chapter and performed IOP, OMR, ERG, and OCT experiments, determined proper timepoints and protocols for each outcome parameter tested, implemented and further developed the microbead model of OHT, performed data analysis, and helped to write this chapter.

Brandon G. Gerberich co-authored this chapter and executed DIC inflation tests, aided with induction of microbead model of glaucoma, organized data from outcome parameters, researched and implemented the complex statistical analysis, and helped to write this chapter.

1.1 Introduction

Glaucoma is the leading cause of irreversible blindness and affects an estimated 80 million people worldwide (Quigley and Broman 2006). This optic neuropathy is characterized by the loss of retinal ganglion cell axons in the optic nerve head, which is the main and early site of damage in the disease (Quigley et al. 1981). Since a major risk factor

for glaucoma is elevated intraocular pressure (IOP), current treatments aim to lower IOP by increasing aqueous outflow or by decreasing aqueous humor production (Weinreb and Khaw 2004; Klein et al. 1992). Although these treatments can be successful in slowing or preventing progression of glaucomatous damage, they are not always effective; further, medication-based treatments have poor patient compliance (Heijl et al. 2002; Gurwitz et al. 1998). Therefore, treatments that overcome the limitations of current therapies are desirable.

It is known that elevated IOP leads to increased biomechanical strain in the ONH tissues which is thought to promote RGC loss in glaucoma, and thus a promising alternative treatment approach for glaucomatous optic neuropathy is to protect against mechanical insult at the ONH due to ocular hypertension. Finite element modelling studies have analyzed the main factors that influence ONH mechanical insult, finding that scleral stiffness is the main such factor (Sigal, Flanagan, and Ethier 2005; Sigal et al. 2004). Experimentally, Coudrillier et al. found that localized stiffening of the peripapillary sclera reduced strain in the lamina cribrosa in *ex vivo* porcine eyes (Coudrillier, Campbell, et al. 2016). Therefore, it is hypothesized that scleral stiffening may confer protection against IOP-induced glaucomatous damage (Campbell, Coudrillier, and Ethier 2014).

A previous study (Kimball et al. 2014) assessed the effects of scleral stiffening on glaucomatous damage in mice. Specifically, Kimball et al. induced scleral stiffening in ocular hypertensive mice using the collagen crosslinking agent glyceraldehyde. Contrary to the expected outcome, they found that scleral stiffening *increased* rather than decreased glaucomatous damage. There are several possible explanations for this observed outcome. For example, whole globe scleral stiffening is known to increase the magnitude of IOP

fluctuations (Clayson et al. 2017), which may in turn damage RGC axons (Asrani et al. 2000). Alternatively, glyceraldehyde toxicity may have outweighed the neuroprotection due to scleral stiffening.

To further investigate the neuroprotective potential of scleral stiffening, we considered two different stiffening approaches (Table 10). In the first, we specifically stiffened only the peripapillary sclera, hypothesizing that such a localized stiffening would prevent glaucomatous damage by reducing ONH strain while maintaining the native compliance of the globe and thus minimizing IOP fluctuations. Our second approach was to stiffen the entire posterior sclera using a well-tolerated collagen crosslinking agent. For this purpose we used genipin, which has recently been shown to provide prolonged scleral stiffening at a much lower concentration than glyceraldehyde (Campbell et al. 2017; Hannon et al. 2019) and which has a promising safety profile (Huang et al. 1998; Avila and Navia 2010; Liu and Wang 2017; Song et al. 2017). We here assess the protective effects of these two stiffening paradigms in a rodent model of ocular hypertension.

1.2 Methods

1.2.1 *Rationale for Using the Rat Model of Glaucoma*

We chose to use the widely-used rat model of glaucoma because of its many parallels to glaucoma in humans. Specifically, rat models of OHT demonstrate several of the clinical hallmarks of glaucoma, including: the ONH being a main and early site of damage, RGC apoptosis, remodeling of extracellular matrix components in the ONH, and ONH ‘cupping’ (Johnson et al. 2000; Guo et al. 2005; Morrison, Cepurna Ying Guo, and Johnson 2011). Rodents are also more cost-effective and ethically defensible than non-

human primates. Considering only rodents, rat eyes are twice the size of mouse eyes and are therefore easier to work with than mice, e.g. for surgical techniques related to our targeted crosslinking procedure and for mechanical testing (Remtulla and Hallett 1985). Additionally, IOP measurements in mice are typically performed under anesthesia, which has been shown to underestimate the IOP by as much as 50% in OHT mice (Jia et al. 2000a). Our chosen strain of rat, the Brown Norway rat, is notably more docile than other strains and therefore IOP can be measured without anesthesia. Further, we can confidently assess visual function in Brown Norway rats because they are a pigmented strain, and thus have a strong optomotor response (OMR), whereas albino rodents have little to no OMR (Douglas et al. 2005). Together, these reasons make the Brown Norway rat model of glaucoma suitable for evaluating our two stiffening paradigms.

1.2.2 *Decision to Implement an Unpaired Treatment Paradigm*

Our study design (Figure 33) was guided by the desire to prioritize statistical power for comparing axon counts between crosslinking treatment groups in microbead-treated eyes. In other words, we wished to minimize variance for axon counts in crosslinked microbead-treated eyes. Thus, an unpaired experimental design ("Design A") was used in this study in which, for each rat, one eye was received both a scleral stiffening treatment and microbeads to induce OHT (hypertensive experimental), while the contralateral eye was untreated (naïve normotensive control). Three alternative study designs were considered involving the hypertensive experimental eye treatment above but with different normotensive control eye treatments, including: (1) a paired design in which the control eye received a crosslinking treatment only ("Design B"), (2) a paired design in which the control eye received an HBSS (vehicle) injection only ("Design C"), and (3) a paired design

in which the contralateral eye received a microbead injection only ("Design D"). Design C was eliminated because preliminary data suggested that HBSS injections do not cause significant axon loss and would only risk adding potential damage due to bilaterial injection . Design D was eliminated due to ethical concerns for animal wellbeing.

Table 5: Relative variance and strengths/weaknesses of various treatment designs and statistical comparisons considered for our scleral stiffening study design.

Design	**Axon Comparison**	**Variance**	**Strengths/Weaknesses**
A (Unpaired)	I (Unpaired)	Lowest variance	Does not account for parity between eyes or for treatment toxicity in individual rats
A (Unpaired)	II (Paired)	Moderate variance due to computed difference	Accounts for parity between eyes of individual rats
B (Paired)	I (Unpaired)	Moderate variance due to injection variability	Accounts for treatment toxicity in individual rats
B (Paired)	II (Paired)	High variance due to both computed difference and injection variability	Accounts for both parity between eyes and for treatment toxicity in individual rats

In addition to the two remaining options (Designs A and B) for control eye conditions discussed above, we considered two ways to assess RGC axon count differences between crosslinking treatment groups, including: (1) using raw values of axon counts in crosslinked hypertensive eyes ("Comparison I"), or (2) computing the difference in axon counts between the crosslinked hypertensive eye and control eye for each rat ("Comparison II"). The four possible combinations of two study designs and two comparisons are listed in Table 5 with our assessment of advantages and disadvantages of each.

The key advantage of a paired design is the ability to account for (or explain) animal-specific variance in axon count comparisons between crosslinking groups. However, a paired design only increases statistical power if the required control eye treatment does not introduce greater variability. Therefore, merits of various design and comparison combinations rely on (1) the expected degree of parity between eyes of the

same rat and the expected variance between rats, and (2) the expected variance in axon counts attributed to the control eye treatments. While axon count parity between eyes of healthy rats has been demonstrated previously (Morrison et al. 2005), we believe that injection variability and measurement variability offset the potential statistical advantage gained by using a paired design. Additionally, we did not observe significant contralateral parity in outcomes from baseline electroretinography (ERG), OMR, or optical coherence tomography (OCT) measurements (Appendix E: Figure 53).

In further support of an unpaired design, we have previously observed that crosslinking treatments increase variance in axon counts. Additionally, preliminary data in our lab suggested that bilateral crosslinking treatment leads to greater axon loss than a unilateral treatment, possibly due to increased systemic inflammation from two injections instead of one. In conclusion, we considered consequences of control eye injections and statistical comparisons involving parity between eyes. We concluded an unpaired design would maximize statistical power while sacrificing the ability to account for within-rat toxicity effects of each treatment.

1.2.3 *Animals and Study Design*

86 male, retired breeder Brown Norway rats (8 - 10 months old) were purchased from Charles River Laboratories (Wilmington, MA). All procedures involving animals were approved by the Georgia Institute of Technology Institutional Animal Care and Use Committee and the Atlanta VA Medical Center Institutional Animal Care and Use Committee (IACUC). All procedures complied with the ARVO statement for the Use of Animals in Ophthalmic and Vision Research.

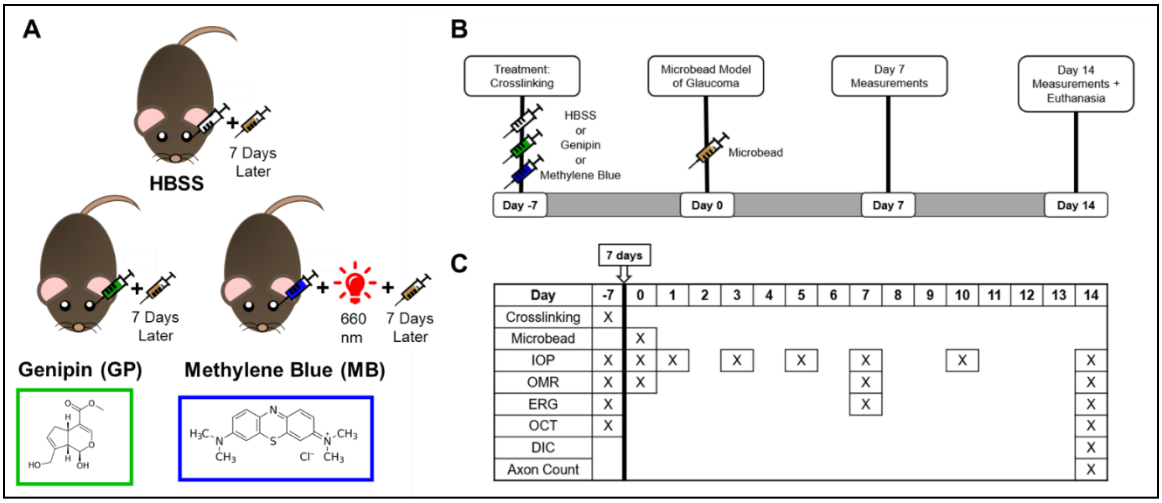

Figure 33: A) Scleral crosslinked eyes received one of three treatments by retrobulbar injection: HBSS (vehicle), Genipin (GP), or Methylene blue (MB). Those in the MB group also received 30 minutes of localized red light (660nm) to selectively stiffen the peripapillary (but not peripheral) sclera. B) Timeline of experiments. Seven days after scleral stiffening treatment. the treated ("experimental") eye received a microbead injection to induce ocular hypertension. Ocular hypertension was induced at Day 0. Rats were sacrificed at Day 14. C) Timing of experiments. IOP measurements were taken at Days -7, 0, 1, 3, 4, 7, 10 , and 14. OMR measurements were taken at Days 0, 7, and 14. ERG measurements were taken at Days -7, 7, and 14, and OCT measurements were taken at Days -7 and 14. DIC and axon count measurements were necessarily taken post mortem after collecting the sclerae and optic nerves on Day 14 immediately after euthanasia.

Our study design followed a "crosslink then OHT" approach. In other words, animals received a scleral stiffening treatment (or sham) unilaterally, were allowed to recover for one week, and then received a treatment to induce ocular hypertension in the same crosslinked eye. We chose to stiffen the sclera *prior* to inducing OHT to facilitate comparison of our results with those of Kimball et al. (Appendix E: Table 10) (Kimball et al. 2014). We used the well-established magnetic microbead model to induce OHT, which was applied to all eyes that received scleral crosslinking treatment (or sham). As noted above, all contralateral eyes were naïve, i.e. received no scleral crosslinking treatments (or sham) and no microbead injections. Animals were followed for 2 weeks after induction of OHT and then sacrificed.

In more detail, rats were randomly divided into three “treatment groups” (Figure 33A and Figure 52). Hanks balanced salt solution (HBSS) was used as the vehicle for treatments and as the sham injectate. One group (HBSS rats, n = 32) received this sham injection. The second group (GP Rats, n = 27) received genipin chemical crosslinking. The third group (MB Rats, n = 27) received methylene blue photocrosslinking. Treatments were applied unilaterally seven days prior to microbead injections using retrobulbar injections for the HBSS Rats (“HBSS hypertensive experimental” eyes), GP Rats (“GP hypertensive experimental” eyes), and MB Rats (“MB hypertensive experimental” eyes). Contralateral eyes received no injections and therefore served as normotensive controls for each animal (“HBSS normotensive control” eyes, “GP normotensive control” eyes, and “MB normotensive control” eyes). Within each animal, the eye (left (OS) or right (OD)) receiving treatment was randomly assigned.

1.2.4 *Intraocular Pressure Measurements*

IOP measurements for each rat were taken between 7:00am and 10:00am using a Tonolab rebound tonometer (Icare Finland Oy, Vantaa, Finland) at baseline and at Day 0, 1, 3, 5, 7, 10, and 14 after microbead injection. Awake rats were gently restrained by hand while eight tonometer readings were acquired from each eye. The lowest and highest IOP values were excluded from each set of daily measurements and the remaining six IOP values were averaged to obtain a representative IOP measurement. Prior to this study, the rebound tonometer was calibrated using a cannulated intact rat eye in which IOP was externally imposed using a hydrostatic pressure reservoir set to heights ranging from 5 to 50 mmHg (data not shown). Calibration results showed good agreement between set IOP values and measured IOP values, and thus no IOP correction was necessary. We then

calculated the IOP burden, also referred to as cumulative IOP difference (Frankfort et al. 2013), IOP exposure (Sappington et al. 2010), or positive integral IOP (Mabuchi et al. 2003), which provides an estimate of the total IOP "insult" to the hypertensive eye. We defined IOP burden as the area between the OHT and normotensive eyes on the IOP versus time plot. If the measured IOP in the OHT eye was transiently lower than IOP in the contralateral (normotensive) eye, the IOP difference was set to zero at that time point, i.e. we did not allow negative contributions to the IOP burden.

1.2.5 *Crosslinking Injection Preparation*

Genipin and methylene blue solutions were both freshly prepared the morning of the retrobulbar injection. Genipin (Wako Pure Chemical Industries, Ltd., Richmond, VA) and methylene blue of USP grade (Apollo Scientific, Stockport, UK) were obtained in powder form and dissolved in Hank's balanced salt solution (HBSS). Genipin was solubilized at a concentration of 15 mM by vortexing the solution for 15 minutes. Methylene blue was solubilized at a concentration of 3 mM by vortexing the solution in a microcentrifuge tube and heating to a temperature not greater than 100 degrees Celsius for 5 minutes. Care was taken to minimize light exposure of the methylene blue solution to prevent possible photodegradation.

1.2.6 *HBSS and Genipin Crosslinking Injection Procedures*

For HBSS and genipin retrobulbar injections, rats were anesthetized with a ketamine (60 mg/kg) and xylazine (7.5 mg/kg) cocktail. Once anesthetized, rats were placed on a heating pad and received a drop of topical tetracaine (0.5 %, Tetracaine Steri-Units, Alcon, Geneva, Switzerland) as a local anesthetic. Retrobulbar injections were

performed on the eye designated as hypertensive experimental by gently proptosing the eye with curved forceps and inserting a disposable insulin syringe with a 31 G needle (BD 300 µl Insulin Syringe Ultra-Fine™ needle, Becton, Dickinson and Company, Franklin Lakes, New Jersey) into the muscle cone through the inferior quadrant of the conjunctiva. 150µl of either HBSS or genipin (15 mM) was then injected into the muscle cone. After injections, rats were given topical antibiotic (Vetropolycin, Dechra Pharmaceuticals, Northwich, United Kingdom) to prevent infection and antisedan (1 mg/kg) to reverse anesthesia (Turner, 2005).

1.2.7 *Methylene Blue Photocrosslinking Procedure*

Rats were anesthetized with isoflurane/oxygen (5%/700 mL/min) and placed in a stereotaxic head mount (Kopf Instruments, Tujunga, CA) equipped with tooth bar over a heating pad, allowing facile manipulation of head position. 0.5% tetracaine (Tetracaine Hydrochloride Ophthalmic Solution, Amici Pharmaceuticals, Melville, New York) was applied topically as a local anesthetic to the eye designated as MB hypertensive experimental, followed by topical application of a 1% tropicamide eye drop (Tropicamide Ophthalmic Solution, Henry Schein, Melville, New York). An additional eye drop of 1% tropicamide was applied after 5 minutes and allowed to take effect for another 10 minutes to ensure maximal dilation of the iris. A hydrating eye lubricant (Puralube Vet Ointment, Dechra Pharmaceuticals, Northwich, United Kingdom) was applied to the contralateral eye designated as normotensive control, to prevent dehydration during the procedure. After dilation of the eye designated as MB hypertensive experimental, a 100 µL retrobulbar injection of 3 mM methylene blue was administered using a sterile 31 G insulin needle and syringe.

Immediately after injection, a contact lens was placed on the corneal surface to eliminate refraction from the cornea/lens, allowing for visualization of the fundus (Appendix E: Figure 54). The rat's head was positioned with the eye designated as hypertensive experimental aligned on the optical axis of a custom-designed microscope capable of simultaneously imaging the fundus and projecting an annular beam of light tuned to excite methylene blue at 660 nm wavelength. Upon alignment of a low intensity guide beam (<0.1 mW) with the optic nerve, the light intensity was increased to a dose of 10mW for 30 minutes to facilitate scleral crosslinking. During this time, beam position relative to the optic nerve head was monitored with the microscope and adjusted if necessary, using micropositioners to move the microscope position relative to the eye. At the conclusion of the 30-minute illumination period, the light source was turned off, the contact lens was removed, and once ambulatory on the heating pad, the rat was returned to its cage.

1.2.8 *Microbead Injection Preparation and Procedure*

The magnetic microbead model of glaucoma was used to induce unilateral ocular hypertension in the eyes designated as hypertensive experimental. All microbead injections occurred at Day 0, which was seven days after crosslinking procedures. A mixture (1:1) of 2 µm and 6 µm magnetic polystyrene microbeads (micromer®-M, Micromod, Rostock, Germany) with PEG-COOH surface chemistry (to promote biocompatibility) was used for microbead injections. Beads were autoclaved according to manufacturer's specifications (20 minutes at 121 °C and 3500 mbar pressure) and then rinsed five times with sterile HBSS using cell culture sterility practices. Rats were anesthetized with a single dose of ketamine (60mg/kg) mixed with xylazine (7.5 mg/kg) and placed on a heating pad.

Tetracaine (0.5%, Tetracaine Steri-Units, Alcon, Geneva, Switzerland) was then applied to the eye. The bead suspension was vortexed for 15 seconds to suspend the beads, and a volume of 25µl was pipetted onto a sheet of wax parafilm. Deposited solutions were then drawn into sterile, disposable syringes with 31 G needles.

The eye designated as hypertensive experimental was proptosed with a small section of a latex glove so that an annular magnet could be placed within the same plane as the iridocorneal angle. A neodymium, grade N40, nickel plated annular magnet (H125D, Amazing Magnets, Anaheim, CA) with dimensions of 7.14 mm inner dimeter, 12.70 mm outer diameter, and thickness of 3.18 mm was placed around the limbus after proptosing, and the eye received a intracameral injection of magnetic microbeads (2.25×10^6 to 4.5×10^6 beads total per 25 µl injection) into the anterior chamber. The needle was held in the anterior chamber for 60 seconds following injection and then slowly removed to minimize fluid reflux. After injection, the section of latex glove was removed, and the magnet was placed back on the eye for 10 minutes to ensure that beads had settled into the iridocorneal angle. Both eyes (hypertensive experimental and normotensive control) of each rat received topical antibiotic (Vetropolycin, Dechra Pharmaceuticals, Northwich, United Kingdom) to prevent infection and hydrate the eye. Rats were placed on heating pads until ambulatory.

IOP was measured 1, 3, 5, and 7 days following induction of ocular hypertension via microbead injection. If the experimental (injected) eye did not demonstrate at least one day of OHT, defined as an IOP elevation of >5 mmHg compared to contralateral control eye within 7 days of injection, the eye was considered to be a non-responder and was then reinjected with 15 µl of microbead solution on Day 7 (n = 12 of 74 total rats). Rats for

which IOP elevation failed 7 days after reinjection were removed from the study (n = 3) and therefore no rat was reinjected with microbeads more than once. Additionally, 7 rats were removed from the study upon reaching IACUC endpoint criteria for health/safety and 2 rats died during anesthesia recovery, leaving a total of 74 rats analyzed in the study.

1.2.9 *Assessment of Retinal Function: Electroretinography*

Dark-adapted ERGs were used to assess inner and outer retinal neuronal function. ERG measurements were taken at baseline, before both the crosslinking procedure and microbead injection, and at 7 and 14 days after microbead injection. At each timepoint, rats were dark-adapted for 30 minutes under dim red light and anesthetized using a cocktail of ketamine (60 mg/kg) and xylazine (7.5 mg/kg). Once asleep, both eyes received drops of tetracaine (0.5%) and tropicamide (1%) topically to anesthetize corneas and dilate pupils, respectively. A ground electrode was inserted into the tail of the rat and reference needle electrodes were inserted subcutaneously into the cheek by each eye. Custom gold-loop electrodes were placed on the cornea of each eye and a layer of carboxymethylcellulose (Celluvisc, Allergan, Dublin, Ireland) was applied over the corneal electrode to ensure electrical conductivity and prevent drying. Under dark-adapted conditions, a 6-step series of increasing flash intensities (-6.0 to 2.1 log cd s/m^2) was used. Electrical responses to various full-field flash stimuli in a Ganzfield dome were recorded using a signal-averaging ERG system (UTAS BigShot; LKC Technologies, Gaithersburg, MD). Oscillatory potentials (OPs) were filtered with a 65-275 Hz bandpass fifth order Butterworth filter. Amplitudes and implicit times were measured in the following way: baseline to peak (positive scotopic threshold (pSTR)), baseline to trough (negative scotopic threshold (nSTR) and a-wave), trough to peak (b-waves and OPs). We elected to analyze ERG

amplitudes of the positive scotopic threshold (pSTR) and negative scotopic threshold (nSTR) at -6.0 log cd s/m^2, the b-wave at -3.0 log cd s/m^2 (b-wave), and the third OP (OP3) at 2.1 log cd s/m^2 because these amplitudes have been shown to be associated with retinal ganglion cell damage in rodent models of glaucoma (Chen et al. 2015; Bui et al. 2005; Bui and Fortune 2004; Bui et al. 2013).

1.2.10 *Ischemic Damage Exclusion Criteria*

Rats with likely ischemic damage to the retina were excluded from analysis. As described in detail in Chapter 6, exclusion was based on the b-wave amplitude from the brightest flash (2.1 log cd s/m^2) at Day 14, since bipolar cell function (which drives b-wave amplitude) is known to be sensitive to ischemic damage at bright scotopic flashes (Matsumoto, Shinoda, and Nakatsuka 2011; Zhao et al. 2013). The 99.5% confidence interval of the b-wave amplitude was computed for all normotensive control eyes (n = 74). If the b-wave amplitude of the hypertensive experimental eye lay below this 99.5% confidence interval, that rat was excluded from analysis. Of the 74 rats analyzed, 14 rats were excluded by this criterion. The final total number of animals was thus 60, divided into HBSS rats (n = 21), GP rats (n = 20), and MB rats (n = 19).

1.2.11 *Assessment of Visual Function: Optomotor Response*

Visual function was assessed via quantitative analysis of OMR thresholds of spatial frequency and contrast sensitivity (OptoMotry®; Cerebral-Mechanics, Lethbridge, AB, Canada). OMR was measured at baseline (prior to crosslinking treatment), Day 0 (7 days after crosslinking procedure, but prior to microbead injection that day), Day 7, and Day 14, following a protocol similar to that of Prusky and Douglas (Douglas et al. 2005; Prusky et

al. 2004). In brief, rats were placed on a raised platform in the middle of a box consisting of four flat screen monitors which displayed black and white vertical gratings that rotated at a speed of 12 degrees/second (d/s) to create a virtual drum. A trained observer then monitored the rat for a positive or negative reflexive head movement in response to the rotating gratings moving in a clockwise or counterclockwise direction, assessing the responses of the OS and OD eyes, respectively (Douglas et al. 2005). To determine an animal's spatial frequency threshold, the vertical bands were held at 100% contrast and spatial frequency was adjusted in a staircase paradigm starting at 0.042 cycles/degree (c/d) until the threshold where the rat could no longer see the gratings was established. Contrast sensitivity threshold was determined using a similar staircase paradigm, but the spatial frequency was held at 0.064 (c/d) while the contrast was decreased from 100% until the threshold was determined. Contrast sensitivity is reported as the reciprocal of the Michelson contrast from the screen's luminance, as previously described (Prusky et al. 2004). Prior to OMR measurements, each rat eye was carefully inspected for any opacity or speckling of microbeads in the anterior chamber that might occlude the rat's visual axis. If this was the case, that eye's OMR was not recorded, making the final number of data used in OMR analysis 48, with 16 rats in each treatment group.

1.2.12 *Assessment of Retinal Morphology: Optical Coherence Tomography*

A spectral-domain OCT system (Bioptigen 4300, Leica Microsystems, Buffalo Grove, IL) was used to measure total retinal thickness and qualitative retinal morphology in the posterior eye at baseline and Day 14. Total retinal thickness was measured at locations 0.5 mm and 1.2 mm from the center of the ONH. Rats were anesthetized using ketamine/xylazine, and eyes received drops of tetracaine and tropicamide as described

above. A 3-mm radial scan (1,000 A-scans per B-scan) centered at the optic nerve head was acquired in both normotensive control and hypertensive experimental eyes. B-scans from the superior-inferior and nasal-temporal axes of all eyes were assessed manually by a trained technician blinded to treatment group using a customized MATLAB program (MATLAB R2019a, Mathworks, Natick, MA). If fewer than two scans were of sufficient quality to measure retinal thickness accurately, the rat was eliminated from the OCT retinal thickness dataset. Measurements were taken at locations avoiding local vasculature, and these individual values from each quadrant were averaged together.

1.2.13 *Optic Nerve Sectioning and Axon Counting*

Immediately after euthanasia via CO_2 overdose, rat optic nerves were dissected from enucleated eyes and fixed in isotonic Sorensen's buffer containing glutaraldehyde (2.5%) and PFA (2%, EMS, Hatfield, PA). Tissue was post-fixed in osmium tetroxide, dehydrated in an ethanol series, infiltrated and embedded in araldite-epon plastic (Araldite 502/Embed 812, EMS, Hatfield, PA). Semi-thin sections of (0.5 µm thick) were cut on a Leica UC7 Ultramicrotome (Leica Microsystems, Buffalo Grove, IL) approximately 1.5mm posterior to the sclera. Sections were stained with 1% toluidine blue and imaged with a Leica DM6 B microscope (Leica Microsystems, Buffalo Grove, IL) using a 63x lens and 1.6x multiplier for a total magnification of 100x. The entire nerve was imaged with a series of z-stack tile scans from which, the optimally focused image within each z-stack tile was selected using the "find best focus" feature in the LAS-X software (Leica Microsystems, Buffalo Grove, IL). Contrast was then adjusted for each tile by maximizing grey-value variance. Finally, normal axons were automatically counted using AxoNet, a

fully convolutional neural-network previously developed in our lab (Ritch et al. 2019) and Appendix A.

1.2.14 *Whole Globe Inflation Testing*

After euthanasia, eyes underwent inflation testing as previously described (Hannon et al. 2019). A few modifications to the previously published method were made to adapt to the altered mechanical properties of microbead-injected eyes. In brief, when eyes were pressurized during whole globe inflation testing, we observed leakage of phosphate buffered saline (PBS) through the scleral shell via vasculature and the scleral canal. Such leakage was not previously observed in untreated eyes. Therefore, to reduce leaking, we substituted previously used PBS or mineral oil with a more viscous silicone oil as the pressurization medium.

After enucleation, eyes were refrigerated on ice in PBS until preparation for inflation testing. Orbital muscle, fat, and connective tissues were removed to expose the posterior sclera. Eyes were blotted dry and adhered to a custom-designed thin aluminum plate incorporating a machined cup in the surface perforated with a hole, as follows. The cornea was positioned in this cup so the posterior sclera faced upward (away from the plate), and cyanoacrylate-based adhesive was cured with PBS to adhere the eye to the plate, taking care to remove any air bubbles that might have been trapped in the adhesive with the tip of a 30-gauge needle. The cornea was then carefully excised through the hole in the bottom side of the mounting plate, allowing for removal of the aqueous humor, lens, and vitreous humor. Silicone oil was used to replace the contents of the eye to reduce leakage of fluid through the sclera upon pressurization as noted above. The eye and aluminum plate

were then mounted onto a threaded acrylic base with screws such that the interior of the eye was in fluidic communication with channels in the acrylic plate. PBS was perfused through tubing connecting an adjustable pressure reservoir to the acrylic base. The eye was then pressurized to maintain its natural shape and blotted dry atop the aluminum plate. Black graphite powder (#970 PG, General Pencil Company, Inc., Redwood City, CA) was applied to the scleral surface with a cotton Q-tip to form a speckled pattern on the surface. Residual powder was flushed away with water and the eye was covered with PBS solution facilitated by placement of a removable reservoir atop the aluminum plate. Silicone oil was added to cover the surface of PBS in the reservoir, thus reducing loss of water through evaporation during testing as visualized in (Hannon et al. 2019) and Figure 16.

Mounted scleral shells were subsequently prepared for inflation testing. Sensors were used to monitor pressure (142PC01G; Honeywell, Charlotte, NC) and flow rate (SLG64-0075; Sensirion, Stafa, Switzerland) of PBS into the eye. After confirming absence of major leaks at 15 mmHg, pressure was maintained at 15 mmHg for 5 minutes. Shells were then preconditioned for 10 cycles at a rate of 1 cycle per minute with pressure linearly varied from 3 mmHg to 15 mmHg and back to 3 mmHg as previously described (Hannon et al. 2019). At the conclusion of preconditioning, pressure was set to 1 mmHg and allowed to stabilize for 10 seconds. Pressure was then increased sequentially to 3, 10, 20, and 30 mmHg at time intervals dictated by a flow rate stabilization criterion. Specifically, we required the magnitude of the measured rate of change in flow rate to be less 2 (nl/min)/s over a 10 minute window, thus allowing the shells to reach steady state at each pressure level. During inflation, images of the scleral surface were captured using a digital image correlation system (Dantec Dynamics, Skovlunde, Denmark).

At the conclusion of testing, Lagrange first principal strain over the scleral shell was computed from images using Dantec's Istra 4D software (v4.4.1, Dantec Dynamics, Holtsville, NY). Data were exported to MATLAB for analysis with a customized script which identified/removed outliers as previously specified (Hannon et al. 2019). Steady state strain values at each pressure step were averaged over the peripapillary and over the non-peripapillary regions, and a Fung model was fit to the data. For each region an average strain value at 22 mmHg (physiological condition) was calculated and reported.

1.2.15 *Data Analysis*

Data were analyzed using SPSS (IBM Corp. IBM SPSS Statistics for Windows, Version 25.0. Armonk, NY: IBM Corp) and GraphPad software (GraphPad Software, San Diego, California) and graphed using GraphPad. For each outcome measure, a linear regression was calculated for each treatment group, and outliers were removed by controlling the false discovery rate at 1% in GraphPad. Subsequently, the remaining data were analyzed using a two-way ANCOVA in SPSS with cumulative IOP burden at Day 14 as the covariate. IOP burden was chosen as the covariate since it is a measurable indicator of the degree of biomechanical insult. All data are reported as mean ± standard deviation, unless otherwise stated.

A two-way ANCOVA was used to analyze mean differences for each measured experimental parameter. Simple comparisons were made between hypertensive and normotensive eyes in each of the three crosslinking treatment groups (3 comparisons). Additionally, simple comparisons were made between mean values of the hypertensive eyes of each crosslinking group (3 comparisons). Bonferroni correction was applied for

each parameter analyzed. For DIC strain analysis, a two-way ANCOVA was used with factors of: (1) “Region” having levels of (a) peripapillary sclera and (b) peripheral sclera; and (2) “Crosslinking Treatment” with levels of (a) HBSS, (b) GP, and (c) MB. Unless otherwise specified, all other outcome measures were analyzed with two-way ANCOVAs having two factors defined as: (1) “Microbead Treatment” having levels of (a) normotensive and (b) hypertensive; and (2) “Crosslinking Treatment” with levels of (a) HBSS, (b) GP, and (c) MB. Levene’s test was used to assess inequality of variance. Homogeneity of regression slopes was assessed using interaction terms of the factors and IOP burden covariate. In cases where statistically significant interactions existed for either factor and the IOP burden covariate, significance was interpreted only at the mean value of IOP burden for comparisons involving that factor. Number of animals in each outcome parameter are in Appendix E: Table 9.

We created correlation matrices for ease of visualizing all outcome parameters at once. Parameters were grouped into the categories of “biomechanical”, “morphological”, or “functional”. Specifically, biomechanical parameters were those related to elevated IOP insult, including IOP burden, peripapillary scleral strain, peripheral scleral strain, equatorial diameter, axial length, and anterior chamber depth. Morphological parameters were those related to ON and retinal structure, including ON cross-sectional area, ON axon count, ON axon density, and retinal thicknesses 0.5 mm and 1.2 mm from the ON. Functional parameters were those related to visual acuity and retinal function, including contrast sensitivity, spatial frequency, pSTR amplitude, nSTR amplitude, b-wave amplitude, and oscillatory potential 3 amplitude.

1.3 Results

1.3.1 *Microbead Injection Successfully Increased IOP*

Induction of ocular hypertension after microbead treatment at Day 0 produced an IOP elevation with an initial rapid rise peaking at Day 3, followed by a gradual decrease until Day 14 (Figure 34D). Though not statistically significant, we observed that HBSS-treated eyes tended to have higher mean IOP burden compared to both GP- and MB-treated eyes. We accounted for any possible differences in IOP burden between individual rats or groups of rats by incorporating IOP burden as a covariate in our statistical analyses. Furthermore, to eliminate those rats which may have experienced IOP levels corresponding to ischemic damage, we introduced an ERG-based exclusion criterion. This functional ERG criterion eliminated rats with non-glaucomatous retinal damage.

At all time points after microbead injection, mean IOP in microbead eyes was significantly elevated compared to normotensive controls (two-way RM ANOVA, time x treatment: $F(30, 684) = 8.716$, $p < 0.0001$, Tukey post-hoc) except for the GP cohort at Day 14. No significant differences in IOP were found between experimental treatment groups at any time point. Mean IOP burden values did not differ statistically significantly between treatment groups (Figure 34C one-way ANOVA, $F(2, 57) = 1.629$, $p = 0.21$).

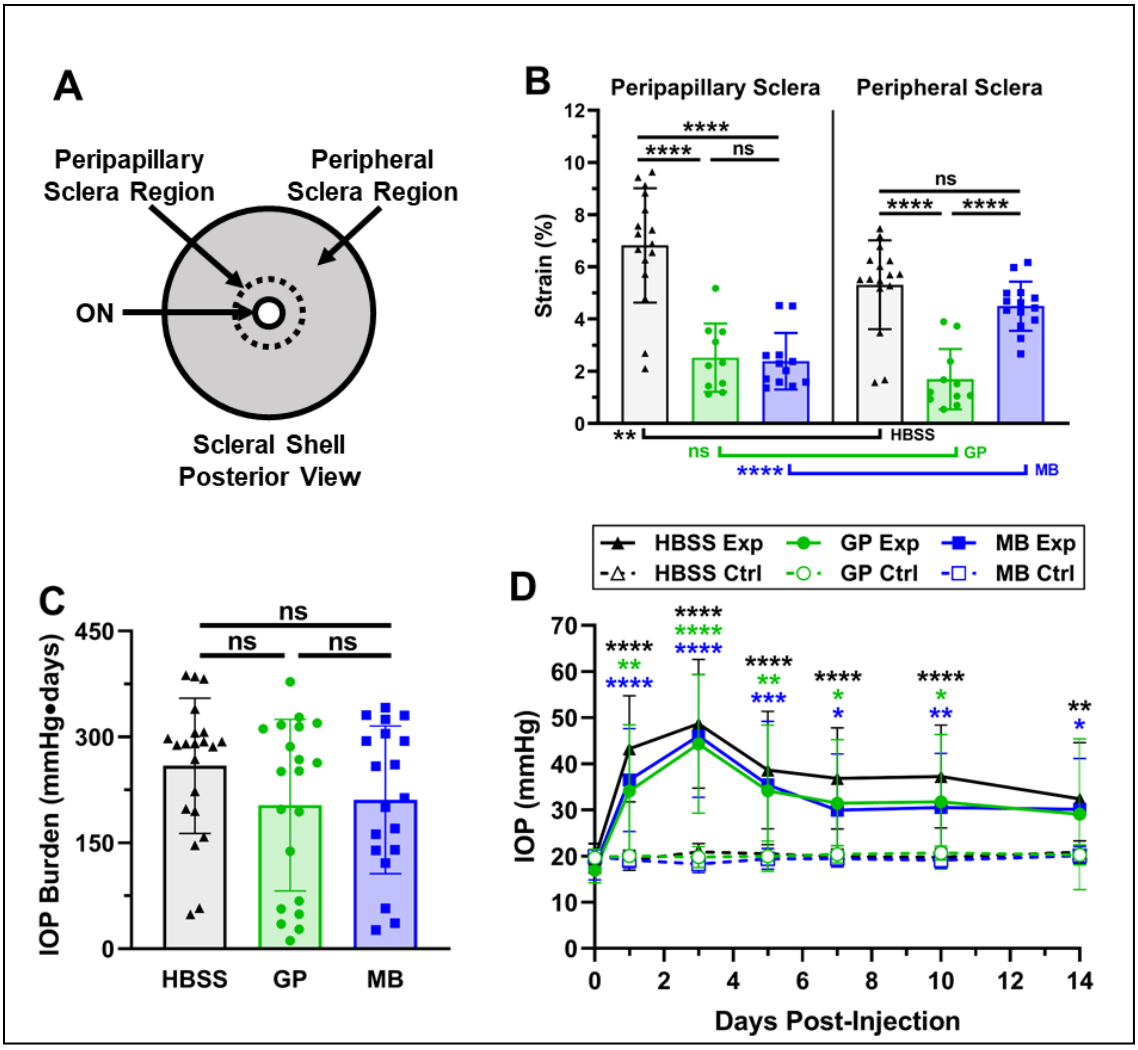

Figure 34: A) Representation of the posterior eye showing the peripapillary sclera, here defined as the region enclosed by a 2 mm diameter circle centered at the ON. The peripheral sclera was defined as the sclera outside this region. B) Whole globe inflation tests indicated whole sclera stiffening with GP and targeted peripapillary sclera stiffening with MB. Mean values are plotted. Statistical comparisons were performed using an ANCOVA and therefore are comparisons of adjusted means. C) Mean IOP burden (pressure x time) did not differ significantly between crosslinking treatment groups. D) IOP levels increased after induction of ocular hypertension at Day 0 in microbead-injected eyes compared to normotensive control eyes. Statistical significance is indicated using the following convention: "" for p < 0.05, "**" for p <0.01, "***" for p < 0.001, and "****" for p < 0.0001.*

1.3.2 *Mechanical Testing Confirmed That Crosslinking Effectively Increased Scleral Stiffness*

It was important to verify that Genipin and MB stiffened the sclera in treated eyes. For this purpose, we conducted inflation testing of post-mortem eyes and quantified their deformation using DIC analysis. We report adjusted mean strains from the ANCOVA analysis over the peripapillary and peripheral scleral regions (Figure 34A), a quantity that is inversely proportional to scleral stiffness. Peripapillary strain was greater than peripheral strain ($p < 0.01$, Figure 34B) in HBSS-injected (control) eyes, likely due to presence of the scleral canal in the peripapillary region. We found that mean scleral strain was 2- to 3-fold lower in both scleral regions in GP eyes compared to the corresponding regions in HBSS eyes ($p < 0.0001$, Table 6), indicating successful whole-scleral crosslinking by GP. There was no significant difference in scleral strains between regions within GP eyes. In MB eyes, peripapillary scleral strain was approximately 3-fold lower than in HBSS-treated eyes ($p < 0.001$, Table 6), but strains in the peripheral sclera did not differ significantly between HBSS and MB eyes, indicating that targeted peripapillary MB stiffening was successful. MB eyes had significantly reduced strain in the peripapillary region compared to the peripheral region within the same MB eye ($p < 0.0001$). Mean scleral strain values in hypertensive experimental eyes were analyzed using a two-way ANCOVA with IOP burden as the covariate (Figure 55; see Methods: Data Analysis). Strains were significantly correlated with IOP burden ($p < 0.01$, Appendix E: Figure 55).

1.3.3 *Retinal Thickness Measurements Suggested Protective Effects of Scleral Stiffening*

We used OCT imaging to measure total retinal thickness, expected to be decreased in eyes experiencing RGC axonal loss. Total retinal thickness at 0.5 mm from the ONH was not significantly different between hypertensive GP and HBSS eyes (Figure 35A, Table 2), and was less in hypertensive MB eyes compared to HBSS eyes ($p < 0.05$, Table 6) and GP eyes ($p < 0.0001$, Table 6). Total retinal thickness at 0.5 mm from the ONH was significantly decreased in hypertensive experimental eyes for both HBSS and MB cohorts compared to respective normotensive controls ($p < 0.0001$, Figure 35A) but not for GP eyes. Total retinal thickness at 0.5 mm from the ONH significantly correlated with IOP burden ($p < 0.05$, Appendix E: Figure 56). Thus, there was a trend (not reaching statistical significance) suggesting that scleral stiffening using GP (but not MB) preserved retinal thickness at 0.5 mm from the ONH in hypertensive eyes.

In contrast to the situation at 0.5 mm from the ONH, hypertensive GP eyes showed significantly larger mean total retinal thickness at 1.2 mm from the ONH compared to HBSS eyes ($p < 0.0001$, Table 6), potentially indicating a protective effect of GP against retinal changes (Figure 35B). No significant differences were observed in this measure of retinal thickness between hypertensive GP eyes and MB eyes, or between MB eyes and HBSS eyes. Total retinal thickness was significantly less in hypertensive experimental eyes compared to normotensive control eyes for HBSS eyes ($p < 0.0001$, Table 6) but not for GP or MB eyes. Representative OCT images shown in Appendix E: Figure 57 reveal minor qualitative differences as well as indications of ‘cupping’ at higher IOP burdens. We

conclude that GP, but not MB, treatment offers some protection against retinal thinning induced by OHT but that this thinning is spatially heterogeneous.

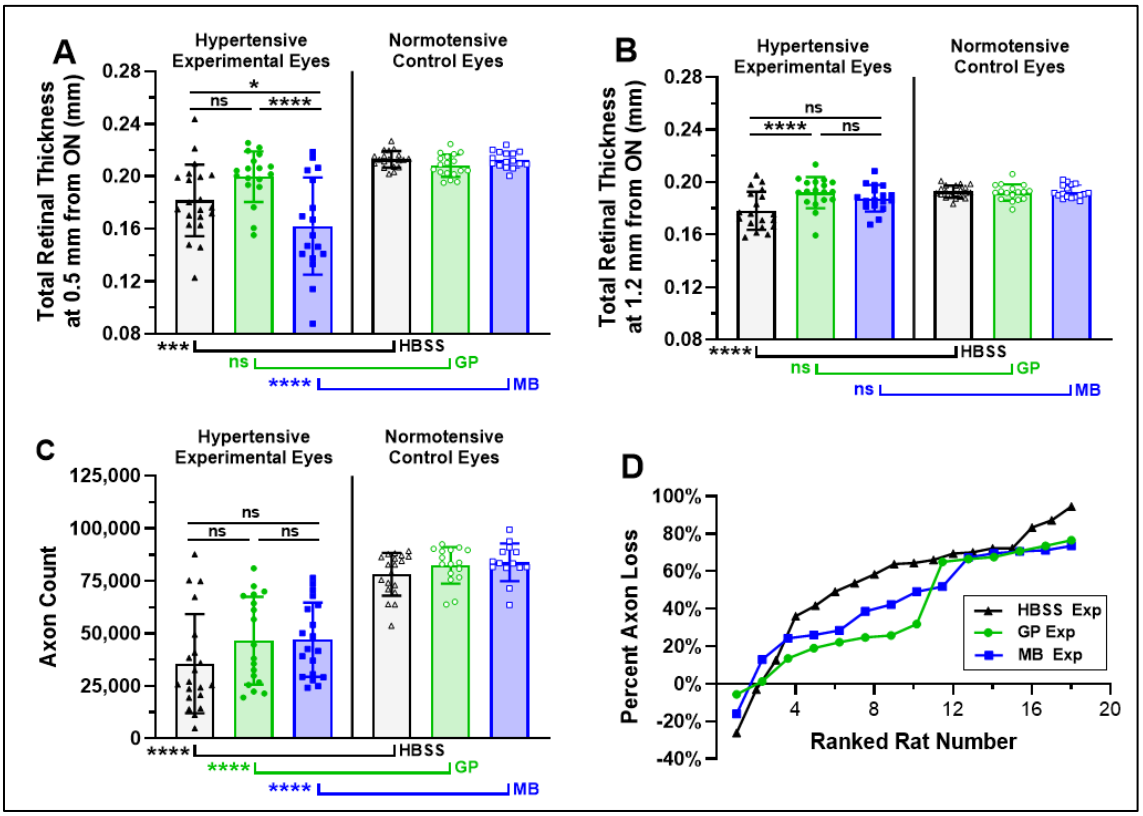

Figure 35: A) Total retinal thickness measured 0.5 mm from the ONH. Retinal thickness in hypertensive GP eyes was not different than in GP normotensive controls, while thickness in hypertensive HBSS eyes was significantly less than in HBSS normotensive controls. Thickness in hypertensive MB eyes was less than in hypertensive GP and HBSS eyes. B) Total retinal thickness measured 1.2 mm from the ONH. Thicknesses in both GP- and MB-treated hypertensive eyes were not significantly different from their respective contralateral eye (normotensive) thicknesses, while thickness in hypertensive HBSS-treated eyes was significantly less than in HBSS normotensive control eyes. Thickness in hypertensive GP eyes was significantly greater than in hypertensive HBSS-treated eyes, suggesting a protective effect of GP against retinal thinning. C) Axon counts derived from ON cross-sections showed no significant protective effects of crosslinking. D) Percent axon loss in hypertensive experimental eyes (compared to normotensive control) ranked by rat number from least to greatest axon loss suggests that axon loss is decreased in GP and MB treated eyes.

Table 6: Adjusted means and simple comparisons for each parameter measured from rat microbead study. Two-way ANCOVAs were used to analyze each parameter with IOP burden as the covariate. Highly significant ($p < 0.0001$) p-values are bolded.

Outcome Parameter	Normotensive Eye Adjusted Means			Hypertensive Eye Adjusted Means			Hypertensive Eye Comparisons			Normotensive-Hypertensive Comparisons		
	HBSS	GP	MB	HBSS	GP	MB	HBSS-GP	HBSS-MB	GP-MB	HBSS	GP	MB
Peripapillary Strain (%)	3.43	2.68	3.04	6.24	2.77	2.68	**<0.0001**	**<0.0001**	n.s.	**<0.0001**	n.s.	n.s.
Peripheral Strain (%)	2.41	1.92	2.20	4.86	1.92	4.58	**<0.0001**	n.s.	**<0.0001**	**<0.0001**	n.s.	**<0.0001**
Equatorial Diameter (mm)	7.29	7.31	7.24	8.01	7.81	8.04	n.s.	n.s.	n.s.	**<0.0001**	**<0.0001**	**<0.0001**
Axial Length (mm)	7.18	7.17	7.08	8.20	8.03	8.10	n.s.	n.s.	n.s.	**<0.0001**	**<0.0001**	**<0.0001**
Anterior Chamber Depth (mm)	2.34	2.31	2.13	2.77	2.74	2.63	n.s.	n.s.	n.s.	<0.001	<0.01	**<0.0001**
Nerve Cross-sectional Area (mm^2)	0.259	0.267	0.277	0.247	0.276	0.275	n.s.	n.s.	n.s.	n.s.	n.s.	n.s.
Axon Count (Axons)	78,900	82,400	83,700	39,400	46200	45500	n.s.	n.s.	n.s.	**<0.0001**	**<0.0001**	**<0.0001**
Axon Density (Axons/mm^2)	306,000	317,000	300,000	152,000	163,000	165,000	n.s.	n.s.	n.s.	**<0.0001**	**<0.0001**	**<0.0001**
Retinal Thickness at 0.5 mm (mm)	0.214	0.209	0.213	0.185	0.198	0.163	n.s.	<0.05	**<0.0001**	<0.001	n.s.	**<0.0001**
Retinal Thickness at 1.2 mm (mm)	0.194	0.193	0.193	0.18	0.194	0.187	**<0.0001**	n.s.	n.s.	**<0.0001**	n.s.	n.s.
Contrast Sensitivity (AU)	5.356	5.574	5.586	2.132	1.774	2.107	n.s.	n.s.	n.s.	**<0.0001**	**<0.0001**	**<0.0001**
Spatial Frequency (c/d)	0.573	0.568	0.579	0.329	0.293	0.302	n.s.	n.s.	n.s.	**<0.0001**	**<0.0001**	**<0.0001**
pSTR Amplitude (μV)	6.77	7.28	8.91	2.27	1.96	1.56	n.s.	n.s.	n.s.	**<0.0001**	**<0.0001**	**<0.0001**
nSTR Amplitude (μV)	6.75	7.84	8.07	4.43	3.75	4.01	n.s.	n.s.	n.s.	<0.05	**<0.0001**	**<0.0001**
B-wave Amplitude (μV)	219.99	242.69	268.20	82.37	100.12	83.68	n.s.	n.s.	n.s.	**<0.0001**	**<0.0001**	**<0.0001**
OP3 Amplitude (μV)	80.86	81.33	91.10	44.64	42.83	45.71	n.s.	n.s.	n.s.	**<0.0001**	**<0.0001**	**<0.0001**

1.3.4 *Axon Counts are Not Preserved by Scleral Stiffening*

We quantified optic nerve axons using a machine learning-based software package (Ritch et al. 2019) in Appendix A. No significant differences were found between any hypertensive eye treatment groups (Figure 35C and Table 6), with adjusted mean axon counts of 78,900 and 39,400 axons in HBSS normotensive and hypertensive eyes, respectively; 82,400 and 46,200 axons in GP normotensive and hypertensive eyes, respectively; and 83,700 and 45,500 axons in MB normotensive and hypertensive eyes, respectively. Axon count and axon density were both lower in hypertensive experimental eyes compared to their respective normotensive controls (all $p < 0.0001$, Table 6). Axon counts and axon density were also significantly correlated with IOP burden ($p < 0.001$, Appendix E: Table 11 and Figure 58). Representative optic nerve images in Appendix E: Figure 59 qualitatively show a increase in axonal damage with increased IOP burden. As alternative measures of RGC axon count, we calculated axon density (axon count divided by ON cross-sectional area). We observed no significant differences between any hypertensive eye treatment groups (Table 6) when considering axon density and ON cross-sectional area, nor a significant correlation with IOP burden (Appendix E: Table 11).

1.3.5 *Eye Size Increased with IOP Burden*

Eye size was measured to understand possible sources of glaucomatous damage and physiological differences compared to clinical glaucoma. Hypertensive experimental eyes were significantly larger than normotensive control eyes for all three crosslinking treatment groups, as measured by axial length, equatorial width, and anterior chamber depth (all $p < 0.05$, Table 6). Further, all eye size measurements were correlated with IOP

burden ($p < 0.0001$, Appendix E: Table 9 and Figure 60). No significant differences in any eye size measurements were found between any hypertensive eye treatment groups. This increase in eye size differs from the situation in human adult glaucoma, where elevated IOP is not known to lead to ocular enlargement. However, other rodent models of OHT have observed similar findings of OHT-induced globe enlargement (Frankfort et al. 2013; Kimball et al. 2014).

1.3.6 *Visual Function is Not Preserved by Scleral Stiffening*

Spatial frequency and contrast sensitivity thresholds were measured to assess possible preservation of visual function due to crosslinking treatment. No significant differences were found between mean resolved spatial frequencies of any hypertensive eye treatment groups. Spatial frequency and contrast sensitivity thresholds were significantly decreased in hypertensive experimental eyes compared to normotensive control eyes for all three crosslinking treatment groups ($p < 0.0001$, Table 6). Both spatial frequency and contrast sensitivity were significantly correlated with IOP burden ($p < 0.0001$, Appendix E: Table 11). Hypertensive eye spatial frequency and contrast sensitivity were not significantly different for comparisons between crosslinking treatment groups.

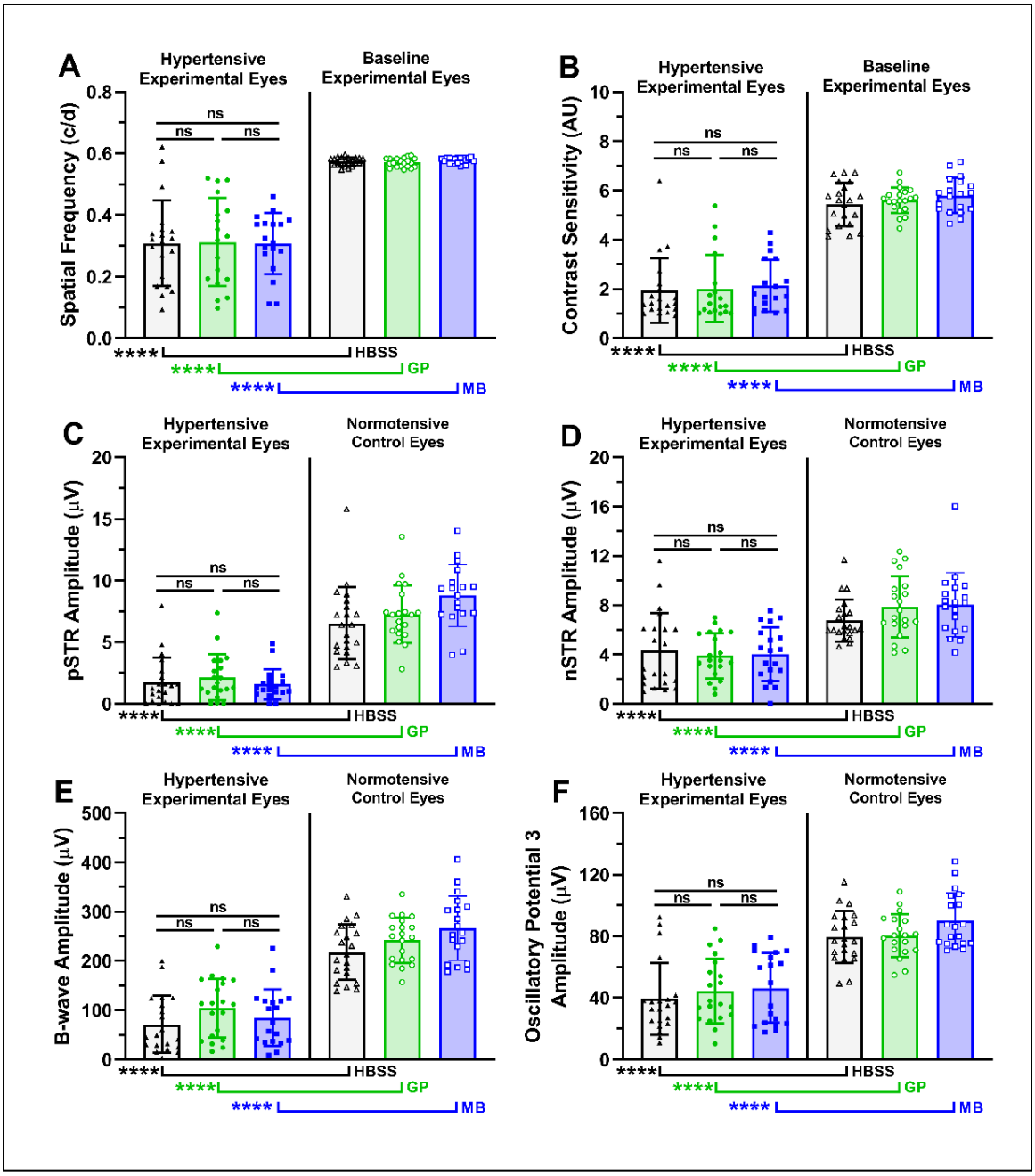

Figure 36: Functional outcome measurements across crosslinking treatment groups. We show OMR measurement outcomes, namely A) spatial frequency and B) contrast sensitivity; and ERG outcomes, namely C) pSTR amplitude, D) nSTR amplitude, E) b-wave amplitude, and F) oscillatory potential 3 amplitude. In all cases, a significant deficit was observed for hypertensive experimental eyes compared to normotensive control eyes. No significant differences were found between hypertensive eye treatment groups. These data indicate crosslinking did not preserve visual acuity or retinal function as measured by OMR and ERG.

1.3.7 *RGC Function is Not Preserved by Scleral Stiffening*

No significant differences in mean pSTR, nSTR, b-wave, nor oscillatory potential 3 (Figure 36C-F) amplitudes were found between any hypertensive eye treatment groups (Table 6). Significant decreases in mean pSTR, nSTR, b-wave, and oscillatory potential 3 amplitudes were observed in hypertensive experimental eyes compared to normotensive control eyes for all three crosslinking treatment groups (all $p < 0.05$, Table 6). pSTR and Oscillatory potential 3 amplitudes were significantly correlated with IOP burden ($p < 0.05$, Appendix E: Table 11 and Figure 61). Hypertensive eye ERG outcomes were not significantly different for comparisons between crosslinking treatment groups, indicating that our treatments did not protect against RGC functional loss.

1.3.8 *Outcome Parameter Correlation Trends Differ by Treatment*

Parameters measured in the study were cross correlated to detect associations between biomechanical, morphological, and functional outcomes within treatment groups, and differences in these associations across treatment groups (Figure 37). We found that the strength of associations (either positive or negative) were different between groups, with ranking HBSS > GP > MB (ranked stronger to weaker). This was particularly evident for the comparison of morphological and functional outcomes with biomechanical insult. We believe this indicates that either: (1) MB treatment generally reduced the impact of biomechanical insult on morphological and functional outcomes, or (2) that MB-treated eyes experienced greater variability in the relationship between functional/morphological outcomes and mechanical insult, leading to the observed weaker correlation.

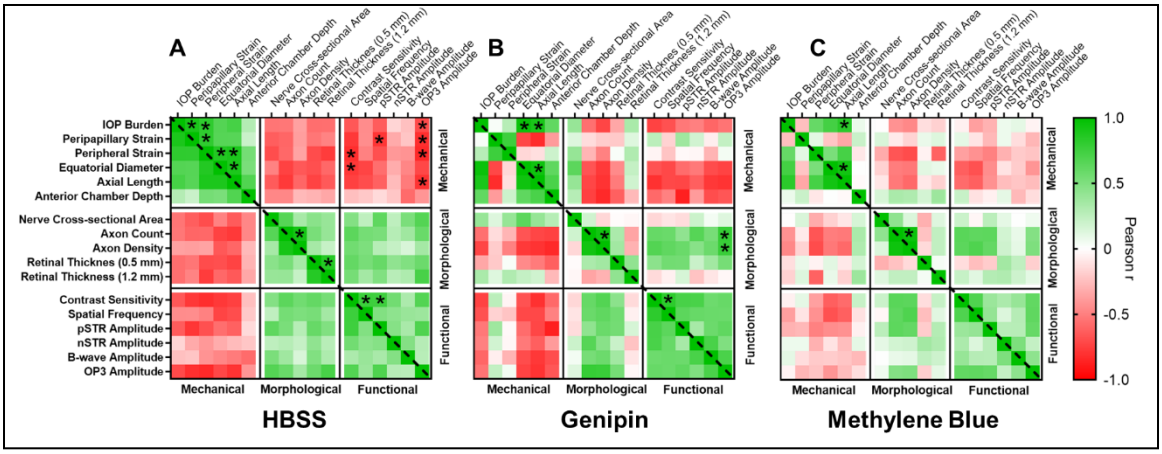

Figure 37: Parameters measured in hypertensive rat eyes were cross correlated and organized by mechanical, morphological, and functional categories for each crosslinking treatment. Stronger correlations were found for HBSS than for GP-treated rats, and for GP-treated rats compared to MB-treated rats, particularly in the relationship between morphological/functional with biomechanical parameters. Mechanical parameters included IOP burden, scleral strain, and eye dimensions. Morphological parameters include optic nerve size, axon count/density, and retinal thickness. Functional parameters include OMR and ERG data. A) HBSS hypertensive experimental eye matrix. B) GP hypertensive experimental eye matrix. C) MB hypertensive experimental eye matrix. Statistical significance was calculated for null hypothesis of zero correlation (significance indicated with "" for the Bonferroni-corrected $p<0.05$ level).*

1.4 Discussion

We assessed the effects of peripapillary (targeted) scleral stiffening and whole-globe scleral stiffening on glaucomatous outcomes in a microbead model of ocular hypertension in rats. We successfully stiffened the sclera, as confirmed by inflation testing of whole globes, and, as expected, we observed significant changes in morphological and functional outcomes in hypertensive eyes compared to normotensive eyes.

In general, we did not observe significant protective effects of scleral stiffening on retinal ganglion cell function as measured by ERG, nor on visual function as measured by spatial frequency or contrast sensitivity. Further, we did not observe a significant preservation of retinal ganglion cell axons by scleral stiffening. However, we did observe preservation of retinal thickness at 1.2 mm from the ONH in GP-treated eyes compared to HBSS treated eyes (although not in MB-treated eyes), suggesting that stiffening may confer

some protective effects against hypertension-induced morphological changes in the retina. We conclude that scleral crosslinking did not preserve retinal or visual function but might slow the progression of morphological glaucomatous damage. Importantly, we saw no evidence to conclude that scleral stiffening worsens glaucomatous damage, in contrast to a previous report (Kimball et al. 2014).

1.4.1 *Toxicity of Crosslinking Treatments May Have Contributed to RGC Loss*

We have previously evaluated the toxicity of HBSS, GP, and MB treatments in healthy rats at 4 weeks, 4 weeks, and 6 weeks (respectively) following injections. The average axon losses in these cohorts, compared to untreated controls, were 0%, 8%, and 24% for HBSS, GP, and MB respectively. Additionally, deficits in retinal function as measured by ERG were observed in MB-treated rats. In the current study, we observed deficits in visual function measured by OMR seven days following crosslinking treatments, but prior to microbead injections (Figure 62). Thus, it is clear that GP and MB-treatments have inherent toxicity in the absence of ocular hypertension, which likely accounts for some of the damage observed in this study. With this understanding, one could interpret a finding of no difference in axon counts between stiffened eyes and sham-treated eyes as indicating protection by scleral stiffening against IOP-induced axon loss, which was offset by inherent toxicity of the stiffening agent. Indeed, there was a trend (that did not reach statistical significance) of axon preservation in GP- and MB-treated eyes, suggesting some inherent benefit of stiffening due to IOP-induced axon loss. Unfortunately, it is difficult to statistically separate the contributions of treatment toxicity and hypertension-induced damage, and thus we cannot make definitive conclusions in this regard.

1.4.2 *Limitations of the Microbead Model Complicate Interpretation of Results*

Intracameral delivery of microbeads may be associated with some inflammation which could lead to retinal/RGC axon injury. It was thus of interest to estimate microbead procedure "toxicity", which we did by extrapolating axon counts in low-IOP burden rats. More specifically, the y-intercept of the linear axon loss regression versus IOP burden can be considered to yield an estimated value of axon loss due to the microbead procedure alone without IOP elevation. These y-intercepts for the hypertensive HBSS, GP, and MB groups were 69,400 ± 14,000, 68,000 ± 9,000, and 62,300 ± 9,100 axons, respectively, which can be compared to average axon count values for normotensive controls in our study of 78,100 ± 7,200, 82,400 ± 4,700, and 83,800 ± 7,400 axons, respectively. Comparing the axon counts in low IOP burden rats to those of the normotensive controls, we estimate axon losses of 11% for HBSS, 17% for GP, and 26% for MB rats due to the crosslinking and microbead injections alone. These values are higher than the losses due to crosslinking treatment alone which were 0%, 8%, and 24% for HBSS, GP, and MB, respectively. Subtracting axon losses due to crosslinking toxicity alone from axon losses calculated in this study at low IOP burden, we find losses due to microbead treatment to be 11%, 9%, and 2% for HBSS, GP, and MB treatments. These data support the hypothesis that the microbead procedure itself in Brown Norway rats leads to some axon loss, in an IOP-independent manner.

In interpreting our results, it is important to recall that the model of ocular hypertension that we used caused rapid and large pressure elevations after microbead delivery, representing a severe challenge compared to a typical IOP history seen in open-angle glaucoma. In other words, the biomechanical insult seen in our study was perhaps

more severe than would be observed clinically. Furthermore, our 14-day study duration was far shorter than time scales in open-angle glaucoma with OHT, so that adaptive responses such as collagen remodeling in the sclera would have had less chance to take effect in our study. Therefore, we interpret the results of our study to conservatively support the conclusion that scleral stiffening does not worsen glaucomatous damage and may confer some protection against aggressive mechanical insult.

1.4.3 *Scleral Stiffening May Protect Against Morphological, but Not Functional RGC Damage*

Interestingly, we did not observe functional protection due to crosslinking, yet did observe some evidence of structural protection (retinal thickness preservation, a trend towards RGC axon preservation). Previously it has been shown that axon loss precedes retinal thinning, which may explain the relatively large deficit in axon count observed compared to the more minor retinal thinning in our study (Calkins 2012). We attribute the loss of retinal thickness in MB eyes at 0.5 mm distance from the ONH to localized toxicity of the photocrosslinking procedure. Recall that the region 0.5 – 1.0 mm from the ONH was selectively targeted for treatment in these eyes, likely inducing more damage at 0.5 mm than at 1.2mm. Another interpretation of this result is the potential of retinal edema which would balance out the loss of RGCs. However, histological analysis of the retina after GP and MB treatment alone did not show any signs of retinal edema (data not shown).

It should be noted that our OCT measurements are of total retinal thickness because we could not confidently resolve the retinal nerve fiber layer in our imaging. However, we suspect our measurement of total retinal thinning at both locations (0.5 mm and 1.2 mm

from the ONH) was caused in part by retinal nerve fiber layer thinning since we also observed significant loss of RGC axons (Figure 35C) and RGC function (Figure 36C-F) in HBSS hypertensive experimental eyes compared to normotensive controls.

Although we did not observe any significant differences in RGC axon counts among hypertensive experimental eyes treated with GP or MB compared to HBSS eyes, we did see a trend towards preservation of axons with both treatments (Figure 35C). We hypothesize that over the short timescale of our experiment (14 days) RGC bodies were still present in the retina despite RGC axonal death, which explains why we saw preservation of the retinal thickness, but not RGC axon counts.

Although our ERG results suggest a loss of RGC function across all treatment groups, differences were not seen between HBSS and GP or MB groups, suggesting that variability in the ERG and OMR data was large compared to effect size, thus yielding statistically insignificant differences. Functional outcomes are perhaps most relevant to clinical translation irrespective of morphological changes. Although we observed some protection against retinal thinning, we hypothesize that remaining RGCs had impaired function which may indicate scleral stiffening has the ability to slow the progression of glaucomatous damage.

1.4.4 *We Were Able to Successfully Stiffen the Posterior Sclera with Both Targeted and Non-Targeted Treatments*

Scleral strain measured post mortem by whole globe inflation testing confirmed successful targeted peripapillary stiffening with MB and whole sclera stiffening with GP. We observed increasing strain values (decreased stiffness) with increasing IOP burden in

HBSS eyes, indicating weakening of the sclera under hypertensive conditions in this study. These effects have been observed on short time scales previously (Fazio et al. 2019).

An unexpected observation in this study was the apparent similarity in measured strain values of HBSS eyes with those of GP and MB treated eyes at low IOP burdens. We have previously shown that MB and GP treatments reduce scleral strain significantly compared to HBSS in healthy rats. Since microbead-treated rats experiencing low IOP burdens should have scleral mechanical properties comparable to those of healthy rats, the observed similarity is difficult to explain. This observed effect could be an artifact of low sample (n = 2) size when only considering low IOP burden values, or due to inflammatory processes associated with the microbead model as discussed above.

1.4.5 *Key Differences Exist Between This Study and a Similar Previous Study*

It is of interest to compare our results with those of the related study of Kimball et al. To stiffen the sclera, Kimball et al. used glyceraldehyde in 100 mM sodium phosphate (Na_3PO_4), the latter having an osmolarity of 400 mOsm (Kimball et al. 2014). After addition of 500 mM glyceraldehyde, the solution's final osmolarity would have been 900 mOsm, well in excess of the physiological osmolarity of 285-295 mOsm (Fox 2011). Therefore, some of the axon loss observed may be attributed to hyperosmolarity of the injection solution.

Additionally, Kimball et. al did not assess any functional or morphological outcomes in glaucomatous eyes. We have expanded upon this previous research by including assessments of visual function (OMR), retinal function (ERG), and retinal

thickness (OCT), helping to paint a more complete picture of the effects of scleral stiffening on clinically relevant outcomes.

1.5 Conclusion

Neither targeted peripapillary nor non-targeted posterior scleral stiffening worsened morphological and functional outcomes in a glaucomatous rat model. We found a modest potential preservation of total retinal thickness by genipin-induced scleral stiffening. Interpretation of these results is hindered by drawbacks of the microbead model of ocular hypertension (high variability, some inherent retinal toxicity). Further research is needed to investigate the impact of scleral stiffening on glaucomatous damage.

Conclusions and Future Directions

There is a need to develop glaucoma treatments which go beyond simply lowering IOP and instead provide neuroprotection. One possible route towards this goal is to decrease the damage due to IOP-induced strains in the ONH. Previous biomechanics research suggests that stiffening the posterior sclera can reduce ONH strains, and thus could potentially preserve RGC function in glaucoma. The purpose of this dissertation was to develop and evaluate a scleral stiffening treatment meant to decrease ONH strain and thereby mitigate glaucomatous damage, as laid out in three specific aims. Below, I summarize the conclusions, limitations, and future directions for each aim.

1.6 **Specific Aim 1: Evaluate the efficacy of potentially biocompatible non-photoactivated collagen crosslinking agents on posterior rat sclera *ex vivo*.**

1.6.1 *Conclusions*

In Chapter 3 of this dissertation we showed that we can successfully stiffen the posterior rat sclera *ex vivo* using three non-photoactivated collagen crosslinking agents: glyceraldehyde, genipin, and methylglyoxal. These results demonstrated the efficacy of using DIC whole globe inflation tests to discern changes in scleral mechanical properties. From these data, we selected genipin for future *in vivo* use in Aims 2 and 3, because genipin yielded the highest stiffening to concentration ratio with a promising toxicity profile (Liu and Wang 2017).

1.6.2 *Limitations*

Although our partial incubation technique minimized the effects of inter-eye variability, it allowed potential diffusion of crosslinking agents from the incubated (experimental) region to the control region of the eye. This likely explains why we observed slightly lower strains in the control regions at higher concentrations of glyceraldehyde and genipin, i.e. control regions in these eyes may have been stiffened, causing an artificially lower magnitude of relative stiffening at higher concentrations of genipin and glyceraldehyde. Further, strains in the experimental portions of glyceraldehyde- and genipin-treated eyes only decreased as concentrations increased up to a point, indicating a possible upper limit to stiffening.

There were also several limitations with the inflation testing set-up which introduced error and caused us to exclude several eyes from analysis. These included: 1) optical issues from glare or poor speckling coverage, 2) undesired movement of speckles due to flow from the peristaltic pump, 3) decreased IOP from undetected leaks in the eye, and 4) eyes not reaching an equilibrium within the set pressure step time. We acknowledged these limitations and made subsequent significant improvements to the DIC inflation testing set-up as described in Chapter 4. These modifications included the addition of a preconditioning procedure to reduce testing variability and a flow sensor to better determine when and if an eye had reached equilibrium.

1.6.3 *Future Work*

Each of the small molecule crosslinking agents were able to stiffen the posterior rat sclera by several hundred percent, which can inform future studies investigating effective

dosages for stiffening the posterior rat sclera. Additionally, these results provide evidence of an apparent saturation of stiffening, as seen in our genipin and glyceraldehyde results and consistent with other studies (Mi et al. 2001; Bi et al. 2011). Since crosslinking agents are potentially toxic, *in vivo* concentrations should be chosen as to not exceed this "point of diminishing returns", where increasing an agent's concentration no longer results in an increase in the tissue's stiffness. This saturation point has been evaluated using a ninhydrin assay, in which crosslinking extent is determined by quantifying the amount of free crosslinking sites (Bi et al. 2011; Sung et al. 2001). Results from this assay could be used to determine the magnitude of crosslinking necessary to obtain significant changes in material stiffness. Future work could also observe the duration of genipin crosslinking *in vivo* by assessing the percentage of crosslinking at various timepoints after injection.

In this current study, we assessed the efficacy of natural, non-enzymatic collagen crosslinking agents. Enzymatic collagen crosslinkers such as lysyl oxidase act as catalysts for collagen crosslinking reactions *in vivo* and are more biocompatible than non-native crosslinking agents (Gacheru et al. 1990). Further, exogenous lysyl oxidase has been used to stiffen cartilage (Hadidi et al. 2017) and thus may be an attractive method of scleral stiffening in the future. However, lysyl oxidase is much larger (~32,000 Daltons) than the small molecules used in this study (72 to 226 Daltons), reducing lysyl oxidase's ability to penetrate the entire scleral thickness (Ambati et al. 2000). If scleral penetration is a significant problem, genetic modification to upregulate scleral production of lysyl oxidase could be an alternate approach. Future work should consider using enzymatic crosslinking if small molecule crosslinking methods fail to produce safe and efficacious results.

1.7 **Specific Aim 2: Optimize the in *vivo* delivery technique of a chosen stiffening agent selected in Aim 1, and characterize the resulting duration of increased scleral stiffness, and potential adverse effects *in vivo.***

1.7.1 *Conclusions*

After selecting genipin as our crosslinking agent in Aim 1, we conducted *in vivo* assessment of genipin-induced scleral stiffening. In Chapter 4, we successfully stiffened the posterior rat sclera both at one day and four weeks after a single genipin treatment and confirmed the presence of autofluorescent genipin crosslinks. In Chapter 5, we assessed the toxicity of genipin-induced scleral crosslinking. These results show that genipin treatment did not cause sustained deficits in retinal or visual function over four weeks, but did induce a slight, nonsignificant loss of RGC axons (approximately 8%) and minor ocular inflammation.

1.7.2 *Limitations*

One obvious limitation is that whole globe inflation testing is a post-mortem mechanical analysis and therefore cannot be used for longitudinal analysis of genipin-induced scleral stiffening *in vivo*, which would be ideal. Further, although we made several improvements to the DIC inflation testing system for this aim, there remained limitations (detailed in Chapter 4) which led to the exclusion of approximately half of the eyes tested.

The ERG protocol used in Chapter 5 was extremely robust because it selectively stimulated each layer of retinal neurons for a complete assessment of retinal toxicity. At

the time of these experiments, we chose to evaluate RGC function using the photopic negative response (PhNR) which has been shown to decline in glaucoma patients (Viswanathan et al. 2001) and ocular hypertensive rats (Huang et al. 2018). In hindsight, the PhNR recordings may not have thoroughly assessed rat RGC function, as we failed to observe significant decreases in the PhNR of OHT eyes, even with confirmed loss of visual function and RGC axons. Instead, using the STR (as was done in Chapter 7) would have improved our evaluation of RGC function.

Our chosen retrobulbar injection technique for genipin delivery to the posterior eye likely caused collagen crosslinking of the extraocular muscles. This is a serious limitation of our injection technique because stiffening the extraocular muscles could restrict eye movements, which are essential to prevent image blur and preserve image resolution (Land 2019). We attempted to target genipin more closely to the sclera by using a sub-Tenon's injection, but we had difficulties implementing this technique in the rat eye because of its small size and thus, proceeded to use retrobulbar injections with this limitation in mind.

Although our observed RGC axon loss was relatively low, there was a large amount of variability within these measurements. This variability could be attributed to a limitation of our retrobulbar injection technique. Specifically, since the retrobulbar injection is a "blind" injection, we hypothesize that genipin could have been injected at a location closer to the optic nerve in some instances, and not in others, which could explain some or all of this variation.

1.7.3 *Future Work*

The results from Chapter 4's inflation experiments show promise of extended duration genipin-induced scleral stiffening. Future work should assess potential use of *in vivo* methods to longitudinally assess scleral stiffness. One promising new method for future implement is optical coherence elastography, in which OCT imaging is used to perform elastography (Larin and Sampson 2017). This method has been applied *ex vivo* to evaluate corneal properties (Ford et al. 2011), *in vivo* to measure retinal properties using acoustic radiation force (Qu et al. 2018), and *in situ* to measure scleral properties (Singh et al. 2017). This method could be applied in vivo by altering the IOP via cannulation of the anterior chamber and measuring the scleral displacements using OCT. Currently, it is very difficult to image the posterior scleral thickness accurately with OCT in rats, but with more advancements in OCT this could be possible in the future.

Although the work described in Chapters 4 and 5 show the feasibility of genipin-induced scleral crosslinking *in vivo*, we are still concerned about the minor, nonsignificant loss in RGC axons. Future work should determine if a lower concentration or volume of genipin is able to reduce this minor toxicity, while stiffening the posterior sclera to a similar extent as reported in Chapter 4.

If genipin-induced scleral stiffening is applied clinically in the future to treat glaucoma (or myopia), several caveats must be addressed since there are differences between rat and human eyes. For one, the rat has an estimated eye diameter of 6.5 mm and scleral thickness of 0.1 mm (Pazos et al. 2016), while the human has an estimated eye diameter of 24 mm and scleral thickness of almost 1.0 mm near the optic nerve (Olsen et

al. 1998; Silver and Geyer 2000). Because of these eye size differences, we would need to modify the volume and concentration of genipin for crosslinking of the human sclera. We can estimate based on the volume of rat and human eyes that the 150 µl injection volume used in this thesis would be approximately equivalent to a 6.5 ml injection volume in a human, although this is likely an overestimate since the desired injected volume may scale with eye surface area rather than volume. Nonetheless, we do not know the exact volume or concentration necessary for *in vivo* stiffening in humans, because of the complex kinetics of genipin diffusion in the sclera.

With diffusion in mind, some studies have assessed the depth of genipin-induced crosslinking, observing more crosslinking towards the outer layers and less towards the inner layers (Mi et al. 2001). In our study, we were able to confirm full scleral penetration of genipin using cryosections that showed autofluorescent crosslinks throughout the entire scleral thickness. In the thicker human sclera, a higher concentration and/or volume will likely be necessary to achieve uniform genipin crosslinking throughout the sclera. Further, scleral penetration should be confirmed in human eyes, possibly by imaging the autofluorescent genipin crosslinks in scleral cross-sections as we have done.

Future work should evaluate other genipin delivery techniques, such as using a sub-Tenon's injection instead of a retrobulbar injection. A sub-Tenon's injection may be advantageous because Tenon's capsule immediately surrounds the sclera, which would create a more targeted delivery of genipin to the sclera while possibly limiting the stiffening of the extraocular muscles. However, in other studies that have used a sub-Tenon's injection instead of a retrobulbar injection to deliver genipin to the posterior sclera *in vivo,* multiple injections of genipin were needed to obtain the desired stiffening effect (Liu and

Wang 2017; Wang and Corpuz 2015). Since ocular injections are known to have serious complications (Patel et al. 1996; Vasavada, Baskaran, and Ramakrishnan 2017; Wessels and Bowers 1998), keeping the number of injections to a minimum is extremely important when developing a new treatment. With regards to our study in Chapter 4, future work should assess the maximum duration of our genipin-induced stiffening effect to determine when (or if) multiple treatments are needed.

1.8 **Specific Aim 3: Determine efficacy of stiffening the posterior sclera as a possible neuroprotective therapy in glaucoma.**

1.8.1 *Conclusions*

Finally, with our safe, efficacious, stiffening treatment developed in Aims 1 and 2, we aimed to evaluate our treatment's ability to mitigate glaucomatous damage. We induced OHT using the magnetic microbead model, assessed retinal and visual function, evaluated RGC morphology, and confirmed scleral stiffening. In Chapter 6, we detail our ERG exclusion criterion capable of removing animals from the study that likely had permanent ischemic damage. The results from our glaucoma model study (Chapter 7) revealed that genipin-induced scleral stiffening potentially prevented OHT-induced retinal thinning, but failed to provide protection against OHT-induced loss of RGC axons and their function.

It is of interest that our results differed from the findings reported by Kimball et al., who reported that scleral stiffening *increased* glaucomatous damage in OHT mice (Kimball et al. 2014). Our results indicate scleral stiffening minimally reduces or does not change glaucomatous damage in OHT rats. We here propose several explanations for the discrepancy:

1) *Glyceraldehyde-induced scleral stiffening is toxic, and thus was the cause of the observed increase in glaucomatous damage.*

We have reason to believe that the glyceraldehyde treatment may have been toxic, and thus the treatment alone caused the observed increase in damage. The treatment paradigm used by Kimball et al. included three 400µl injections of a hyperosmolar concentration of glyceraldehyde within seven days. The number of injections, volume, and hyperosmolarity are all a concern and it is surprising that the study showed no loss of RGC axons from the treatment alone. Additionally, the ERG analysis of toxicity did not include an evaluation of RGC-specific function, and overall visual function using OMR was not evaluated. All in all, we feel that a more thorough assessment of glyceraldehyde might be necessary to confirm that the glyceraldehyde stiffening treatment was not toxic.

2) *Both studies had disproportionate IOP burdens in treatment groups which led to the contrast in findings.*

Although Kimball et al. did account for IOP burden using a regression analysis as we did in our study, it is important to point out that in both studies, treatment groups did not have the same distribution of IOP burdens. In the Kimball et al. study, eyes treated with glyceraldehyde had significantly higher IOP burdens than untreated eyes which could contribute to the increase in damage. In our study, HBSS treated eyes had a trend towards a higher overall IOP burden compared to our genipin eyes, which could contribute to our results showing little to no changes in damage. These differences in IOP burdens could be the main component affecting both study's conclusions. Further,

the IOP burdens used in these analyses were likely not accurate as stated previously in this section, and thus need to be assessed with caution.

3) *Axonal damage differences observed in Kimball et al.'s study was due to ischemia.*

Kimball et al. used five IOP measurements over the six-week period: 1, 4, 7, 14, and 42 days after the microbead injection and did not apply any exclusion criterion to account for ischemic damage. Further, the measured IOP elevation was 20 mmHg one day after microbead injection in anesthetized mice. As stated previously in this thesis, anaesthesia has been shown to underestimate the IOP by 50%, thus suggesting the possibility that mice had permanent ischemic damage. Therefore, the findings from this study could in fact show that glyceraldehyde-induced scleral stiffening increased ischemic, rather than glaucomatous, damage to RGCs.

4) Scleral stiffening does increase glaucomatous damage as seen in Kimball et al., but our acute model of glaucoma prevented us from observing similar results.

Both studies used the microbead model of OHT, but our study was shorter (2-week duration) than the Kimball et al. study (6-week duration), even though the duration of IOP elevation was approximately two weeks in both studies. Due to the aggressive nature of our microbead model of OHT, we felt that extending the study duration would have led to massive axon loss, making the discovery a potential treatment effect extremely difficult. Even with our shorter 2 week duration, it is possible that scleral stiffening did cause some axonal loss, but because our acute model of OHT was so aggressive, any modest damage induced by scleral stiffening alone was overwhelmed

by the damage from OHT. Further research would be required to evaluate this hypothesis.

5) *Rats and mice are different animals and thus respond differently to scleral stiffening.*

Although rats and mice are both rodents, these animals do have differences, and thus respond differently to treatments affect glaucoma pathophysiology. Using just the simple size comparison from these two studies, scleral stiffening is potentially more efficacious in larger animals, although we only have two data points here to suggest this hypothesis.

1.8.2 *Limitations*

The major limitation of this aim lies with the chosen model of OHT. Even after four years of fine-tuning our microbead model procedure, we still struggled to induce a mild IOP elevation of OHT in a repeatable manner that did not cause ischemic-level IOPs. The ERG Criterion described in Chapter 6 attempted to account for this by excluding animals with severe, non-glaucomatous retinal damage. However, this criterion still allowed animals with mild functional deficits in non-RGC layers to be included in analysis. Although other studies have also reported slight deficits in a- or b-wave amplitudes, these deficits seem to closely correlate with a high IOP burden (Chen et al. 2015; Fortune et al. 2004). This is incredibly concerning for the glaucoma community since ERG measurements are not typically made, leading to the potential inclusion of animals with non-RGC specific damage in experimental studies. Further, even if a study suitably excludes animals with obvious ischemic damage, most models of OHT may only be

modelling an advanced form of glaucoma, in which retinal function in other layers is impaired (Fazio et al. 1986).

Our complex statistical analysis incorporated IOP burden as a covariate to account for the variable degree of IOP insult each animal experienced. This introduces a limitation of this study because our IOP burden is an 'estimated' IOP burden, due to the discrete IOP measurements taken throughout the study. These IOP measurements did not include the daily IOP fluctuations which are known to be variable, especially in OHT eyes (Jia et al. 2000b; Kwong et al. 2013; Agnifili et al. 2015). The analysis might have led to different conclusions if we were able to continuously monitor the IOP to obtain the 'true' IOP burden for each animal.

Finally, we observe that even if the findings from Kimball et al. and our current study agreed, there would still be limitations regarding the chosen rodent model of glaucoma. In contrast to primates, rodents do *not* have a collagenous lamina cribrosa. This is an important anatomical difference, since the lamina cribrosa is known to be the main structural component in the ONH which resists IOP-induced strain. Therefore, future studies should evaluate how scleral stiffening affects RGC damage when there is more structural support in the ONH from the lamina cribrosa.

1.8.3 *Future Directions*

Although our study provided promising results indicating a potential preservation of the retinal thickness from genipin treatment, there could be other factors which led to a lack of retinal thinning observed. For one, we did not analyze retinal health by using retinal histology. Further histological evaluation of the retina would allow us to better understand

whether genipin-treated eyes had signs of retinal edema or scarring, which would tend to increase retinal thickness.

Further, we cannot conclude definitively that scleral stiffening is not efficacious due to experimental limitations described above. To more thoroughly assess the hypothesis of this thesis, an improved rat model of glaucoma is necessary. Future studies should use a model of OHT which induces a more moderate IOP elevation that more closely resembles the clinical presentation of the disease. Ideally, this model would continuously monitor IOP and induce a similar level of IOP burden to each animal.

Bello et al. recently developed a "smart pump" to continuously monitor and adjust a rat's IOP (Bello, Malavade, and Passaglia 2017b, 2017a). This method involves an extremely difficult and long surgery to install the pump "outlet" in the eye and thus requires a trained surgeon to implement. Additionally, the surgery can only be performed on a maximum of two rats per day. Although these limitations seem difficult to overcome, limitations with other models of OHT are also severe, and sometimes impossible to overcome. There are also several advantages of the Bello et al. model. Since IOP exposure would be similar across all animals tested, we expect the outcome parameters to have less variability which would decrease the number of animals necessary to reach significance. Continuous IOP monitoring would also allow for a more exact IOP burden measurement, which would lead to more accurate results in analyses which use IOP burden as a covariate (Huang et al. 2018; Frankfort et al. 2013; Mabuchi et al. 2003). Implementation of an OHT model resembling Bello et al. would be more efficacious for further studies evaluating scleral stiffness along with other treatments. Other models of OHT involving genetic modifications of the Brown Norway rat may also be of interest once they are developed.

Morrison et al. recently developed an acute model of OHT which uses a controlled elevation (CEI) of IOP at 60 mmHg (Morrison et al. 2016). The advantages of this technique are that the exact IOP history is known and that it presents a similar damage pattern to that seen in glaucoma. While these facts are attractive, there are also concerns, specifically that the model appears to have aspects of acute ischemic damage. For example, ERG measurements two days after CEI revealed functional deficits in all retinal layers including photoreceptors (a-wave amplitude), bipolar cells (b-wave amplitude), and RGCs (pSTR). Function in the photoreceptors and bipolar cells recovered to control levels at 14 days after CEI, but there was a sustained deficit in RGC function. One might conclude that this is indicative of early glaucomatous damage. However, another conclusion is that RGCs are simply more prone to develop permanent damage after ischemia. Since there is a known preferential loss for inner retinal neurons compared to outer retinal neurons in ischemic conditions, this conclusion makes sense (Schmid et al. 2014). For these reasons, I believe that the CEI model is not the best option for future studies aiming to evaluate potential clinical treatments for RGC-specific, non-ischemic damage.

1.9 Final Thoughts

This dissertation developed a safe and efficacious genipin-induced scleral stiffening treatment through ex vivo and in vivo experiments in healthy rat eyes. These findings support the clinical translatability of genipin-induced scleral stiffening treatments. When applied in a rat model of glaucoma, there is an absence of a strong protective effect of genipin-induced scleral stiffening on RGC function and structure, which may be due to significant limitations in our rat model of OHT. These findings caution researchers to

thoroughly assess their models of OHT to ensure they are modelling RGC-specific glaucomatous damage.

Publications and Conference Presentations Arising from the PhD:

Refereed Journal Publications Related to Thesis Work:

Aim 1

1. IC Campbell, **BG Hannon**, AT Read, JM Sherwood, SA Schwaner, and CR Ethier, "Quantification of the efficacy of collagen cross-linking agents to induce stiffening of rat sclera", *Journal of The Royal Society Interface,* 14:20170014. (2017). doi: 10.1098/rsif.2017.0014.
2. IC Campbell, J Sherwood, DR Overby, **BG Hannon**, AT Read, J Raykin and C.R. Ethier, "Quantification of Scleral Biomechanics and Collagen Fiber Alignment", *Methods in Glaucoma Research*, 1695:135-159. (2018). doi: 10.1007/978-1-4939-7407-8_13.

Aim 2

3. **BG Hannon***, SA Schwaner*, EM Boazak, BG Gerberich, EJ Winger, MR Prausnitz, and CR Ethier, "Sustained scleral stiffening in rats after a single genipin treatment", *Journal of The Royal Society Interface,* 16:20190427. (2019). doi: 10.1098/rsif.2019.0427.
4. **BG Hannon**, C Luna, AJ Feola, AT Read, MD Ritch, MT Pardue, P Gonzalez, and CR Ethier, "Assessment of visual and retinal function following *in vivo* genipin-induced scleral crosslinking", In Revision June 2020 to *Translational Vision Science and Technology*.
5. MT Ritch, **BG Hannon**, AT Read, AJ Feola, GF Cull, J Reynaud, J Morrison, C Burgoyne, MT Pardue, CR Ethier, "AxoNet: A tool to quantify retinal ganglion cell axons in various species", *Scientific Reports,* 10:8034. (2020). doi: 10.1038/s41598-020-64898-1.

Aim 3

6. **BG Hannon***, BG Gerberich*, AT Read, MD Ritch, E Schrader, L Nichols, C Pontis, S Sridhar, SA Schwaner, MG Toothman, H Huang, GS Gershon, AJ Feola, MT Pardue, MR Prausnitz, CR Ethier, "Peripapillary and Whole-sclera Stiffening in Glaucomatous Rats". In Preparation.
7. **BG Hannon**, AJ Feola, BG Gerberich, AT Read, MR Prausnitz, CR Ethier, and MT Pardue, "Using retinal function to define ischemic exclusion criteria for animal models of glaucoma". In Preparation.

** Denotes co-first author*

Refereed Journal Publications Not Directly Related to Thesis Work:

1. BG Gerberich, **BG Hannon**, A Hejri, EJ Winger, E Schrader, L Nichols, H Gersch, N. MacLeod, AT Read, MD Ritch, MG Toothman, GS Gershon, H Grossniklaus, MT Pardue, CR Ethier, MR Prausnitz, "Spatially targeted scleral photocrosslinking with methylene blue". In Preparation.
2. SA Schwaner, **BG Hannon**, AJ Feola, CR Ethier, "Biomechanical properties of the rat sclera obtained with inverse finite element modeling", In Revision August 2019 at *Biomechanics and Modeling in Mechanobiology*, (2020). doi: 10.1007/s10237-020-01333-4.

Conference Presentations

Podium Presentations

1. **B.G. Hannon**, M.D. Ritch, C. Ford, A.T. Read, A.J. Feola, K. Gao, E. Dyer, J. Reynaud, G. Cull, C. Burgoyne, M.T. Pardue, C.R. Ethier, "Machine Learning-Based Quantification of Axonal Damage in Glaucomatous Rat Optic Nerves ", Podium presentation and abstract presented May 2019 at the Association for Research in Vision and Ophthalmology (ARVO) Annual Meeting in Vancouver, BC.

2. **B.G. Hannon**, I.C. Campbell, A.T. Read, and C.R. Ethier, "Evaluating the efficacy of crosslinking the posterior rat sclera." Podium presentation and abstract presented June 2017 at the Summer Biomechanics, Bioengineering and Biotransport Conference (SB3C) in Tucson, AZ

Poster Presentations

1. **B.G. Hannon**, A.J. Feola, B.G. Gerberich, A.T. Read, M.R. Prausnitz, C.R. Ethier, and M.T. Pardue, 'Using retinal function to define ischemic exclusion criteria for animal models of glaucoma' Abstract accepted for ARVO 2020 in Baltimore, MD. Not presented due to COVID-19 pandemic.

2. **B.G. Hannon**, S.A. Schwaner, A.J. Feola, M.D. Ritch, A.T. Read, M.T. Pardue, C.R. Ethier, "Assessment of visual function and scleral stiffening following a single periocular genipin injection", Poster and abstract presented October 2019 at International Society for Eye Research (ISER)/BrightFocus Glaucoma Symposium in Atlanta, GA.

3. **B.G. Hannon**, J. Fu, R. K. Kim, A.J. Feola, A.T. Read, C.R. Ethier, M.T. Pardue, "Early Deficits in Visual and Retinal Function in the Rat Microbead Model of Glaucoma", Poster and abstract presented September 2018 at ISER in Belfast, UK

4. **B.G. Hannon**, J. Fu, R.K. Kim, A.T. Read, M.T. Pardue, C.R. Ethier, "In vivo assessment of visual acuity following genipin-induced scleral crosslinking", Poster and abstract presented May 2018 at the Association for Research in Vision and Ophthalmology (ARVO) Annual Meeting in Honolulu, HI

5. **B.G. Hannon**, A.T. Read, B.G. Gerberich, J. Raykin, E.J.Winger, C.R. Ethier, "In Vivo Assessment of Genipin-induced Scleral Stiffening in the Rat Sclera", Poster and abstract presented October 2017 at the ISER Glaucoma Symposium in Atlanta, GA

6. **B.G. Hannon**, I.C. Campbell, A.T. Read, M.T. Pardue, and C.R. Ethier, “Determining the efficacy of biocompatible stiffening agents in rat sclera.” Poster presentation and abstract to be presented May 2017 at ARVO Annual Meeting in Baltimore, MD

APPENDIX A. **AxoNet: A deep learning-based tool to count retinal ganglion cell axons**

Submission Details

Authors: Matthew D. Ritch, **Bailey G. Hannon**, A. Thomas Read, Andrew J. Feola, Grant A. Cull, Juan Reynaud, John C. Morrison, Claude F. Burgoyne, Machelle T. Pardue, C. Ross Ethier

Status: In revision for Nature: Scientific Reports.

Contributions: **Bailey G. Hannon** provided optic nerves with varying levels of damage using the microbead model of OHT, performed manual axon counts on the rat dataset, helped to determine which of our proposed automated methods had the most potential, and aided in the manuscript by creating figures and writing.

Matthew D. Ritch is an undergraduate who worked with Bailey Hannon and developed the AxoNet deep learning-based tool. He created a free Image-J plug-in for the software, fine-tuned the axon imaging technique and exporting process, performed complex data analysis of the results, and wrote the majority of this manuscript. This axon counting software was utilized in Chapters 5-7 of this thesis.

Abstract

In this work, we develop a robust, extensible tool to automatically and accurately count retinal ganglion cell axons in optic nerve (ON) tissue images from various animal models of glaucoma. We adapted deep learning to regress pixelwise axon count density

estimates, which were then integrated over the image area to determine axon counts. The tool, termed AxoNet, was trained and evaluated using a dataset containing images of ON regions randomly selected from whole cross sections of both control and damaged rat ONs and manually annotated for axon count and location. This rat-trained network was then applied to a separate dataset of non-human primate (NHP) ON images. AxoNet was compared to two existing automated axon counting tools, AxonMaster and AxonJ, using both datasets. AxoNet outperformed the existing tools on both the rat and NHP ON datasets *as* judged by mean absolute error, R^2 values when regressing automated vs. manual counts, and Bland-Altman analysis. AxoNet does not rely on hand-crafted image features for axon recognition and is robust to variations in the extent of ON tissue damage, image quality, and species of mammal. Therefore, AxoNet is not species-specific and can be extended to quantify additional ON characteristics in glaucoma and potentially other neurodegenerative diseases.

Introduction

Glaucoma is the leading cause of irreversible blindness worldwide (Greco et al. 2016; Kwon et al. 2009), and thus is a significant research focus. This optic neuropathy is characterized by degeneration and loss of retinal ganglion cells (RGCs), which carry visual signals from the retina to the brain. Therefore, an important outcome measure in studying glaucomatous optic neuropathy, particularly in animal models of the disease, is the number and appearance of RGC axons comprising the optic nerve (Mikelberg et al. 1989; Morrison et al. 1998), usually evaluated from images of optic nerve cross sections. Using images obtained by light microscopy is known to result in an axon count underestimation of around 30% relative to counts from images obtained by transmission electron microscopy (Marina,

Bull, and Martin 2010a; Cepurna et al. 2005). However, light microscopy is widely used to count optic nerve axons because of its lower cost and favorable time requirements for tissue preparation. Therefore, in this work we focus on axon counting in optic nerve images generated by light microscopy.

Manual counting is the gold standard approach to quantify RGC axons, but it is extremely labor-intensive, since RGC axon numbers in healthy nerves range from the tens of thousands in mice to more than a million in humans (Sanchez, Dunkelberger, and Quigley 1986). Further complicating axon quantification is the fact that axon appearance can be highly variable. For example, in the healthy nerve, most axons are characterized by a clear central axoplasmic core and a darker myelin sheath; following previous work (Chauhan et al. 2006; Marina, Bull, and Martin 2010a), we will refer to such an appearance as "normal". However, in damaged nerves (and even occasionally in ostensibly heathy nerves), other axon appearances occur, such as an incomplete myelin sheath and/or a darker axoplasmic region. Such variability further increases the time needed for axon counting, since the person doing the counting often needs to decide whether a given feature is (or is not) an axon. Here and throughout we place the term "normal" in quotes. An "abnormal" axon appearance does not necessarily imply non-functionality, and it is important to keep this distinction in mind.

To reduce the time-intensive counting process, various techniques have been developed for assessing axon counts and/or optic nerve damage, including: semi-quantitative, sub-sampling, semi-automated counting, and automated counting. In the semi-quantitative approach, scores based on a damage grading scale are assigned to optic nerves by different trained observers, and then averaged (Chauhan et al. 2006; Jia et al.

2000b). While this method is capable of quickly capturing whole-nerve changes, and can identify subtle changes that may not be detectable by axon counting, it is subjective and requires scorers who have significant experience and training. Sub-sampling is the process of estimating axon loss by manually counting smaller regions of the nerve using either targeted or random sampling and then extrapolating to the whole nerve or providing an RGC axon count per area measurement (Marina, Bull, and Martin 2010a). Sub-sampling is faster than full manual counting, but it is still labor-intensive and can be poorly suited to analyzing nerves with regional patterns of axonal loss (Jia et al. 2000b). Koschade et al. have recently presented an elegant stereological sub-sampling method that eliminates the bias that can occur in sub-sampling, but still requires manual axon counting in 5-10% of the full nerve area (Koschade et al. 2019). While this is feasible in animals with fewer axons per optic nerve like the mouse, counting this proportion may be prohibitive for animals with more axons per optic nerve, as in primates. Semi-automated axon counting methods use algorithmic axon segmentation techniques involving hyperparameters, such as intensity thresholds which are manually tuned for individual sub-images (Cull et al. 2003). These methods are faster than manual counting and more thorough than qualitative or sub-sampling methods, but still require extensive human direction and time. Because of these limitations, there has been a push to develop fully automated counting tools.

Two of the most used automated counting tools are AxonMaster (Reynaud et al. 2012) and AxonJ (Zarei et al. 2016). Both tools are designed to count “normal”-appearing axons, i.e. axons with a clear cytoplasmic core and a dark myelin sheath (Chauhan et al. 2006; Marina, Bull, and Martin 2010a). They use dynamic thresholding techniques to segment axonal interiors from myelin and other optic nerve features. While these tools are

faster and provide more detail than sub-sampling methods, they also suffer limitations. For example, they are not easily extensible to counting features other than "normal"-appearing axons. Further, the two automated counting packages that currently exist were each developed for a specific animal species, and due to inter-species differences, it is not clear how accurate these approaches are for other species. Specifically, AxonMaster (Reynaud et al. 2012) and AxonJ (Zarei et al. 2016) were calibrated and validated for use in non-human primate (NHP) and mouse models of glaucoma, respectively. Recently, AxonMaster has been applied to count RGCs in healthy and damaged tree shrew optic nerves (Samuels et al. 2018), but it has yet to be validated in this animal model. Our preliminary testing using these packages suggested that they are also sensitive to image quality, tissue staining intensity, and nerve damage extent in images of rat optic nerves (see Results).

Our goal was thus to create axon-counting software to overcome the above limitations, i.e. software which was robust to image quality and staining intensity, which could be used in multiple animal models of glaucoma, and which was extensible to quantification of features other than "normal"-appearing axons. Our approach to building this software, which we refer to as AxoNet, is an adaptation of the U-Net convolutional neural network architecture developed by Ronnenberger et al. (Ronneberger, Fischer, and Brox 2015) applied to the count density learning approach of Lempitsky et al. (Lempitsky and Zisserman 2010).

We used a dataset of manually annotated rat optic nerve images for developing and training AxoNet (detailed in

Annotated Dataset Construction). The rat is a widely used animal model for glaucoma research and elevation of IOP produces retinal structural changes and loss of RGC axons similar to those observed in the human pathology (Johnson and Tomarev 2010). We then applied our software to the dataset of NHP optic nerve images which was used to validate AxonMaster by Reynaud et al. (Reynaud et al. 2012). Below we present the detailed methodology of the dataset and software construction used to develop AxoNet, as well as a comparison of AxoNet's automated counting results to those of AxonMaster and AxonJ. We have packaged AxoNet into a user-friendly open source plugin for the widely-used ImageJ image processing platform (Schneider, Rasband, and Eliceiri 2012), as described in greater detail in the Discussion.

Methods

Rat Optic Nerve Dataset

Animals

This study used twenty-seven optic nerves from fourteen (12 male and 2 female) Brown Norway rats aged 3 to 13 months (Charles River Laboratories, Inc., Wilmington, MA). All procedures were approved by the Institutional Animal Care and Use Committee at the Atlanta Veterans Affairs Medical Center and Georgia Institute of Technology and conformed to the Animal Research: Reporting of In Vivo Experiments (ARRIVE) guidelines. All experiments were performed in accordance with relevant guidelines and regulations. Rats used in this study had various degrees of optic nerve health. Each animal had one eye with experimental glaucoma induced unilaterally by either microbead injection (12 animals) (Samsel et al. 2011; Bunker et al. 2015; Hannon et al. 2018) or hypertonic

saline injection (2 animals) (Feola et al. 2019). Optic nerves in the resulting dataset ranged from ostensibly normal to severely damaged due to ocular hypertension. These 14 rats had been used in other studies and both optic nerves were used from each animal. One optic nerve was excluded from the study because it had suffered extreme damage secondary to abnormally high IOP elevation, which made it unsuitable for use in studying experimental models of chronic glaucoma.

Tissue Processing and Imaging

Animals were euthanized via CO_2 and the eyes were enucleated. The optic nerves were transected with micro scissors close (<1 mm) to the posterior scleral surface. Optic nerves were then placed in Karnovsky's fixative, post-fixed in osmium tetroxide, dehydrated in an ethanol series, infiltrated and embedded in Araldite 502/Embed 812 resin (EMS, Hatfield, PA). Semithin sections of 0.5 µm thickness were cut on a Leica UC7 Ultramicrotome (Leica Microsystems, Buffalo Grove, IL) and stained with 1% toluidine blue (Sigma-Aldrich, St. Louis, MO). They were imaged with a Leica DM6 B microscope (Leica Microsystems, Buffalo Grove, IL) using a 63x lens and 1.6x multiplier for a total magnification of 100x. A z-stack tile scan of the entire nerve was taken and the optimally focused image within each z-stack tile was selected using the "find best focus" feature in the LAS-X software (Leica Microsystems, Buffalo Grove, IL). Contrast was then adjusted for each tile by maximizing grey-value variance.

Annotated Dataset Construction

To train the AxoNet algorithm, it was necessary to create a dataset of rat optic nerve images in which axons had been identified. For this purpose, 12 x 12 µm sub-images were

randomly selected from the full 27 nerves, producing a dataset of 1514 partial optic nerve images, with a minimum of 20 sub-images selected from each nerve, as follows:

- 200 images were taken from each nerve from the two female rats. These images were initially 48 x 48 µm, but were subdivided into 16 images, so that each sub-image matched the 12 x 12 µm standard image size.
- 50 images were taken from each nerve from an early cohort of four microbead model rats. The images from this source were initially 24 x 24 µm, and were similarly subdivided to yield 12 x 12 µm standard sub-images.
- 20 to 50 images, each of which was 12 x 12 µm, were selected from each nerve from a later cohort of eight microbead model rats.

All sub-images were 187 x 187 pixels, i.e. image resolution was 15.7 pixels per µm. However, during training and processing, the U-net architecture's four max pooling layers each reduced the image side lengths by half, so all images used by AxoNet were required to have dimensions evenly divisible by 2^4. To comply with this restriction, we used bilinear pixelwise interpolation to resize all dataset images to 192 x 192 pixels, i.e. to the dimensions closest to the images' original size which were divisible by 16.

Selected sub-images varied in image quality and contrast, and were from optic nerve sections that varied in tissue staining intensity and degree of nerve damage (Figure 38). The images in our dataset can be viewed using the code found at github.com/ethier-lab/AxoNet. Four trained counters manually annotated "normal"-appearing axons in 1184 sub-images, where a "normal" axon was defined as a structure with an intact and continuous myelin sheath, a homogenous light interior, and absence of obvious swelling or

shrinkage (Marina, Bull, and Martin 2010a; Chauhan et al. 2006). Each counter annotated one point per axon at the axon's approximate center. The remaining 290 sub-images were annotated by two counters, who annotated one point per axon at the approximate center by consensus. Axons with abnormal morphology were not annotated. Counters were instructed to count axons which lay fully inside the frame of the image or which intersected either the left or top image border and lay more than halfway within the image borders. Manual annotations were made using Fiji's Cell Counter plugin (Schindelin et al. 2012) which recorded the spatial location of each axon marked within the image. There was good agreement between manual counts for most sub-images (**Error! Reference source not f ound.**).

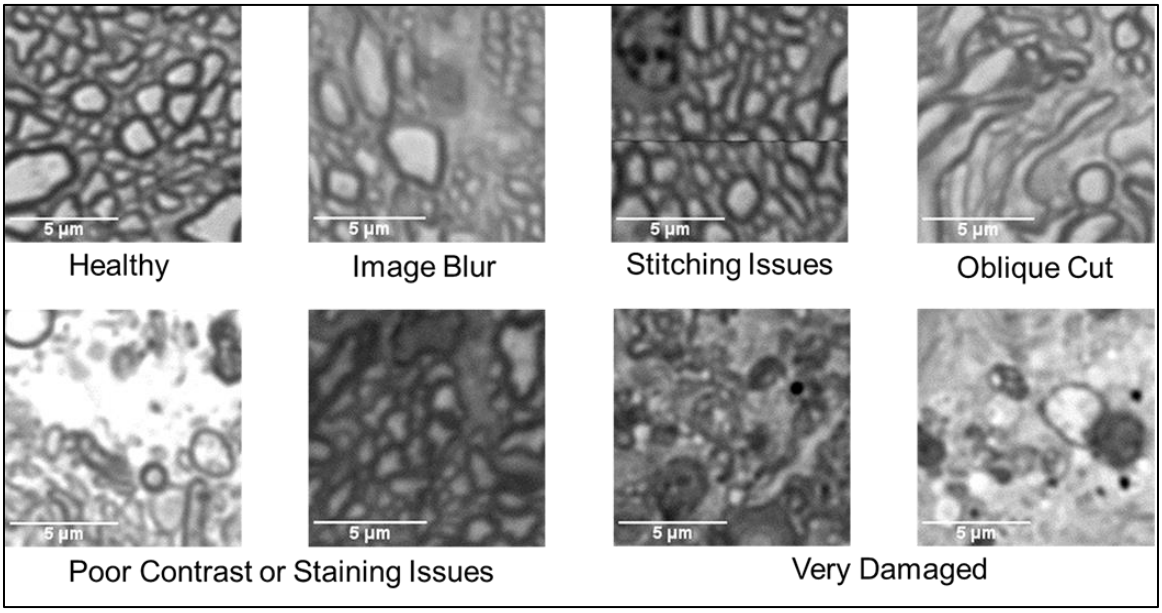

Figure 38: Rat Dataset Image Variety. A representative set of images from the rat optic nerve image dataset is shown. These images include a range of nerve health, variations in sample processing quality, and in image acquisition contrast and quality.

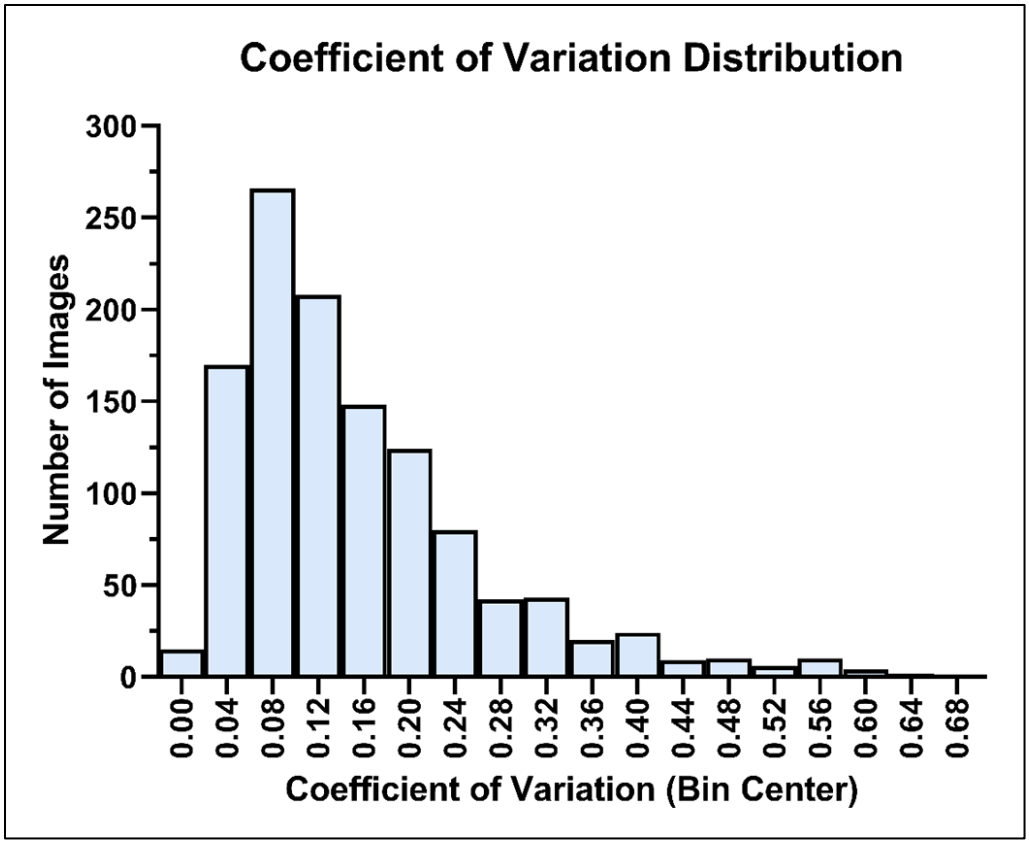

Figure 39: Histogram of Manual Count Variability for Rat Dataset. Variability between counters is expressed as the coefficient of variation (standard deviation of the manual count divided by the mean of the manual count for each image). The median coefficient of variation was 0.12, indicating good general agreement between manual counters.

These manual annotations were then used to create a "ground truth" axon count density matrix for each sub-image, $\boldsymbol{D}$, in which the $(i,j)^{\text{th}}$ entry in the matrix was defined as

$$D(i,j) = \frac{1}{K}\sum_{k=1}^{K} c_k(i,j) \tag{5}$$

where

$$c_k(i,j) = \begin{cases} 1, & \text{if the } (i,j)^{\text{th}} \text{ pixel was annotated by the k}^{\text{th}} \text{ counter} \\ 0, & \text{otherwise} \end{cases}$$

and K was the number of counters for the sub-image in question. Note that the dimensions of $\boldsymbol{D}$ equaled the dimensions (in pixels) of the corresponding sub-image. Entries in $\boldsymbol{D}$ were then distributed ("blurred") according to $\boldsymbol{D_{dist}} = \mathcal{G}(\boldsymbol{D})$, where $\mathcal{G}$ is an isotropic Gaussian blur operator with $\sigma = 8$ and filter size of 33 pixels, chosen empirically to distribute the annotated density values $D(i,j)$ over the full axon. This operation resulted in some of the annotated density values lying outside the edges of the original sub-image. This is a desired effect as an object which lies partially on an image's boundary should not be counted as a full object (Lempitsky and Zisserman 2010). The resulting ground truth matrix $\boldsymbol{D_{dist}}$ provided the spatial distribution of axon count density over the full sub-image, which when summed over all entries, produced the ground truth axon count for the full sub-image or the average count from all experts for that sub-image. All density map values were stored as double-precision floating-point numbers.

Dataset Subdivisions

The dataset was randomly divided into training, validation, and testing image subsets following a 60%-20%-20% split (Ripley 1996). Images selected from each animal's optic nerves were used exclusively for either the training, validation, or testing subsets. AxoNet was trained using the training subset. The validation subset was used to optimize AxoNet's architecture and hyperparameters as well as to construct axon count correction equations, as was done using the calibration set in Reynaud et al. (Reynaud et al. 2012) and as described in the Correction Equations section. Finally, the testing subset was used for final evaluation of tool performance.

NHP Optic Nerve Dataset

We then evaluated the performance of AxoNet on optic nerve sub-images from NHPs with experimental glaucoma. This dataset had been previously annotated using a semi-automated manual method and used to develop one of the existing automated axon counting tools, AxonMaster, as described in Reynaud et al. (Reynaud et al. 2012).

NHP dataset images were randomly divided into validation and testing subsets following a 50%-50% split to match the even proportion of images in the validation and testing subsets of our rat dataset. Each subset contained 247 images. The validation subset was used to construct axon count correction equations, as was done using the calibration set in Reynaud et al. (Reynaud et al. 2012) and as described in the Correction Equations section. The testing subset was used for final evaluation of performance for each tool.

AxoNet Development

Implementation and Network Architecture

We implemented a U-Net based encoder/decoder architecture similar to the original architecture developed by Ronnenberger et al. (Ronneberger, Fischer, and Brox 2015). Specifically, we reduced the number of filters in our convolutional layers by a factor of two, resulting in a feature depth at each layer half of that in the original architecture. This reduction by a factor of two was chosen to reduce the number of parameters in the network, decreasing training time and reducing the danger of overfitting, while retaining the base-two relationship between the feature depths of the encoding and decoding paths of the U-Net. We also tried reducing the feature numbers by a factor of four, but this reduction

decreased network performance. We used a rectified linear unit (ReLU) instead of a sigmoid activation for the final layer, indicated by the red arrow in Figure 40. The change in the final layer allowed us to regress the ground truth pixelwise count density function instead of predicting cell segmentation. A ReLU activation layer is better suited for this task because it produces a linear range of output pixelwise density map values, while a sigmoid activation biases its outputs towards either 0 or 1. We also included padding on all convolutional layers so that feature arrays would not shrink after each convolution. This network was implemented in Python (Version 3.7.3, Python Software Foundation) using Keras (Chollet 2015) and Tensorflow (Ramsundar and Zadeh 2018). The images were normalized by subtracting the mean pixel value for the entire image from the pixelwise values and dividing the resulting pixel values by twice the standard deviation of the image pixel values. This ensured that all pixels with intensities within ±2 standard deviations of the mean fell within the range [-1.0, +1.0]. Finally, outlier pixels were set to either -1.0 or 1.0.

The network was trained for 25 epochs with a batch size of 1 image per step and a learning rate of 10^{-4}. Our modified architecture was developed iteratively by training on the training subset of the rat dataset and evaluating on the validation subset of the rat dataset. Validation performance was used to compare architectures until performance stopped improving.

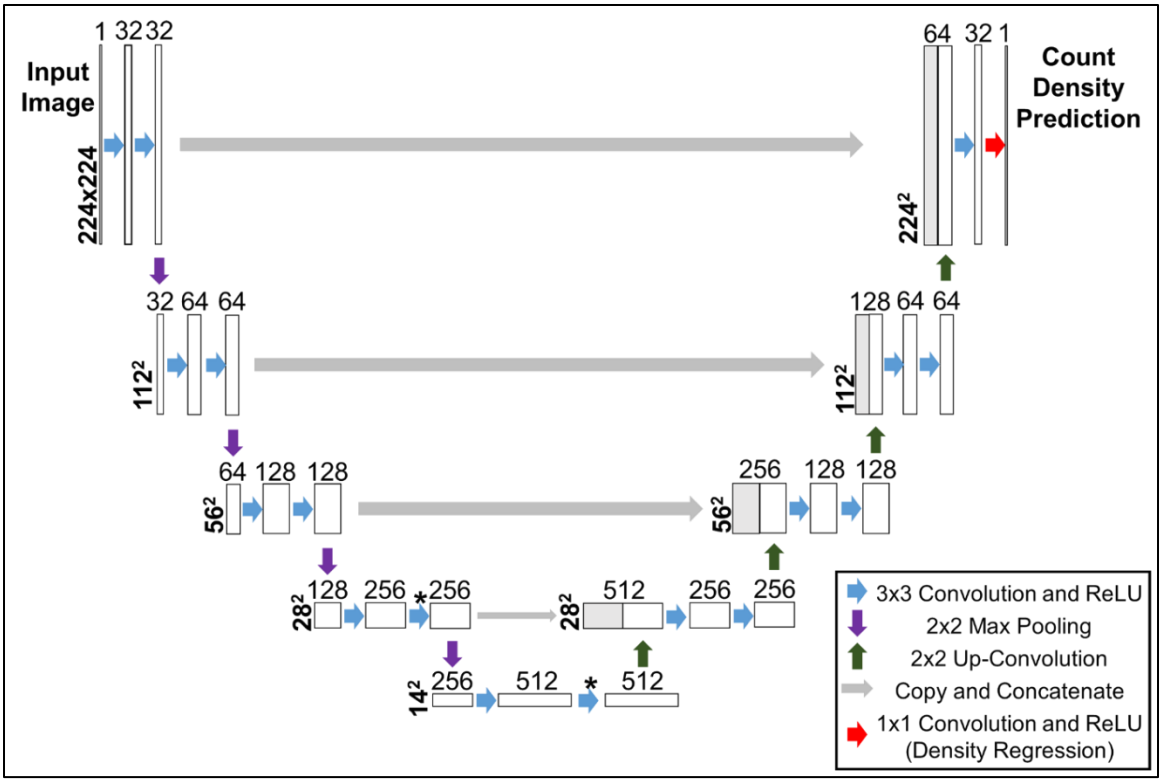

Figure 40: U-Net Architecture. A visual representation of our adapted U-Net convolutional neural network architecture, with the encoding branch on the left and the decoding branch on the right. Each box represents the output array of one of the convolutional network's layer operations, which are represented by colored arrows. The bold numbers to the left of the boxes indicate the row and column sizes of the feature array at those layers. The numbers above the boxes indicate the feature depth of each layer, which is the third dimension of the feature array at that layer. Numbers in the layer operations key indicate the size of that operation's sliding window. Products of feature concatenation are indicated by two boxes sharing a border with the concatenated box in grey. The asterisk indicates dropout with rate = 0.5 applied after convolution. ReLU is an abbreviation for Rectified Linear Unit. Figure adapted from Ronnenberger et al. (Ronneberger, Fischer, and Brox 2015).

Training

We used the Adam optimizer (Kingma and Ba 2014) to minimize a mean squared error loss function evaluated between ground truth and predicted count density function estimates for each image as follows:

$$L(X,\beta) = \frac{1}{N}\sum_{n=1}^{N}\left[\widehat{D}(X_n,\beta\,) - m\,D_{dist}(X_n)\right]^2, \tag{6}$$

where β is the learned network parameter set, N is the number of pixels in the image, $\widehat{D}$ is the predicted pixelwise axon count density function, X_n is the nth pixel in image X, and m is a density scaling factor. The density scaling factor was used to increase the magnitude of the predicted pixelwise density values, allowing better regression convergence. Its value was determined during hyperparameter optimization, resulting in a final value of m = 1000. Since a density scaling factor was used, the trained network overestimated the density predictions by a factor of m. Thus, all density maps predicted during network application were divided by m to accurately reflect ground truth. After density map prediction, we estimated total axon count within an image as follows:

$$Axon\ Count(X,\beta) = \frac{1}{m}\sum_{n=1}^{N}\widehat{D}(X_n,\beta\,). \tag{7}$$

Because dataset sub-images were randomly selected from larger full optic nerve images, their edges could contain cropping artifacts such as axons that intersected the edge. Dataset images and ground truth arrays were thus padded during training and evaluation through

the edge-mirroring process recommended in (Ronneberger, Fischer, and Brox 2015) to prevent the propagation of influence from these edge artifacts and any resulting biases in cell count. When computing the mean squared error loss function (Equation 6), we did not include mirrored pixels. Training images were resized from 187 x 187 pixels to 192 x 192 pixels and extended to 224 x 224 pixels by this edge mirroring, as this size provided the optimum balance between training speed and output accuracy. Extensive data augmentation was used during training. This included image mirroring and rotation at intervals of 90° as well as random multiplicative pixel value scaling. The random multiplicative pixel value scaling was applied by taking the elementwise product of the training image matrix with a matrix of the same shape containing uniformly distributed values between .85 and 1.15.

As expected, our dataset contained only a few images with extreme numbers of axons per image, i.e. very low or very high axon counts. Training with this dataset would therefore lead to higher error in such cases, which we wished to avoid since having few axons per image or many axons per image can be a significant experimental outcome. If we denote the number of manually counted axons per image by manual counts (MC), then we reasoned that we could reduce counting error in extreme cases by creating a data set which had a more uniform distribution of MC over all the images, which we achieved by resampling, as follows. A 10 bin histogram of MC over all images in the training set was created, and we augmented the number of images in any bin that had less than the maximum number of images. This augmentation consisted of replicating all of the images within that bin until the number of images within each bin was approximately the same.

The model did not show signs of overfitting, as shown by the similar loss values for the training and validation set over the course of model training (Figure 41).

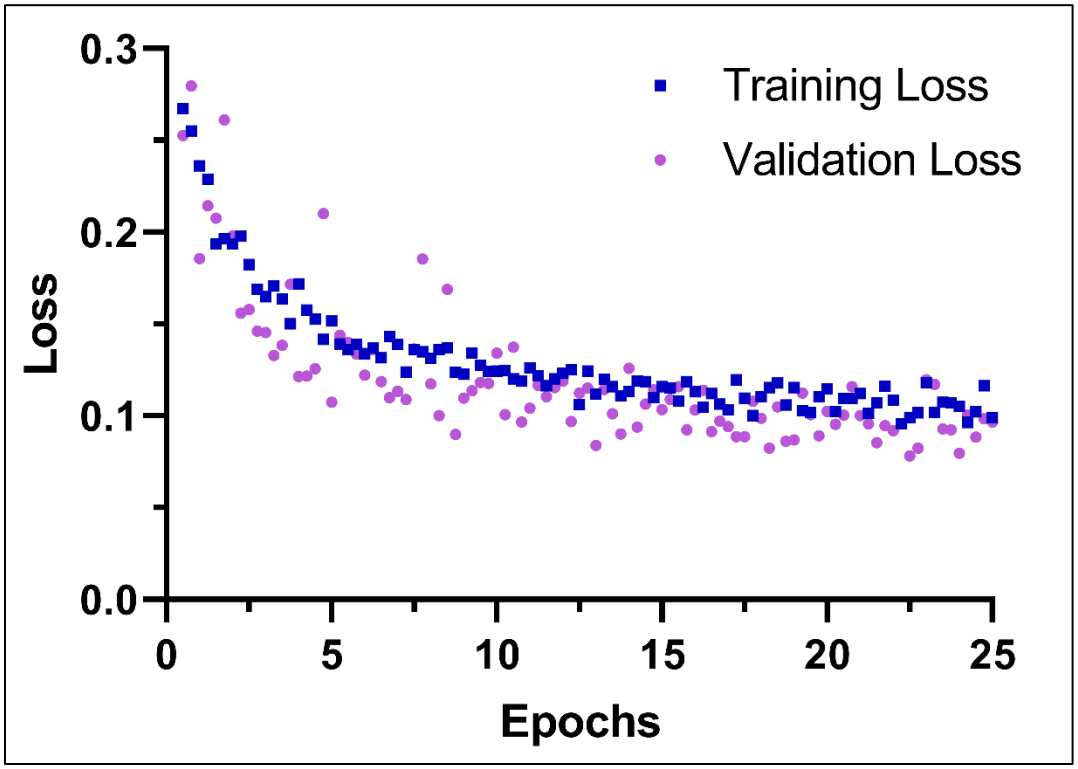

Figure 41: AxoNet Training Loss. Average training and validation set loss for each epoch vs. epoch number. Training and validation set losses do not diverge, indicating that our network did not overfit during training.

Model Evaluation

Correction Equations

The three automated counting tools, AxoNet, AxonMaster, and AxonJ, cannot precisely replicate ground truth. However, empirical observation shows that each tool demonstrated a relatively consistent bias, which could be corrected for. We therefore first used the validation subsets to perform the following linear bias correction, following the method established in Reynaud et al. (Reynaud et al. 2012). In brief, MC and automated

counts (AC) of axons in the validation subset were plotted against one another and fit using a linear least squares regression for each tool,

$$AC = a\,MC + b, \tag{8}$$

where coefficients a and b reflect any systematic linear bias in the estimation of MC by AC for the automated counting tool being considered. We then account for this linear bias by defining a corrected automated count, $AC_{corrected}$, as

$$AC_{corrected} = \frac{AC - b}{a}. \tag{9}$$

Ideally, our automated counting methods would not demonstrate any systematic bias, i.e. our network would learn to correct any such biases during training. However, all automated counting schemes that we are aware of either show some bias, and thus use linear bias correction equations, or do not report results in a manner that allows one to determine whether the scheme shows bias, e.g. by reporting only mean absolute error between ground truth and object counts. We have chosen to use correction equations.

We conducted a series of tests to determine the cause of this systematic linear bias. Specifically, we first intentionally overfit models to determine whether there was a bug in our code causing systematic bias, reasoning that if we could eliminate bias by overfitting, then bias would not be due to a programming error and instead would be related to other factors. We thus trained on downsampled training sets with and without resampling and augmentation and evaluated the bias when the algorithm was applied to the same

downsampled training sets. Second, we tested for underfitting by training our network with randomized initial parameters and for more epochs and comparing the results to our initial results. We also considered differences between the training and testing sets and dataset imbalance as potential sources of bias.

Statistical Analysis of Tool Performance on the Rat Image Dataset

To evaluate the three automated counting tools on the rat image dataset, we applied all three tools to the validation subsets, created correction equations as described above in Equation 9, and applied the relevant correction equation to the automated counting results from the testing subset. Differences in sub-image manual counts and the automated counts produced by each automated axon counting tool were quantified for both datasets through linear regressions, Kruskal-Wallis tests comparing the mean absolute error for each tool, and a comparison of the limits of agreement as defined by the Bland-Altman methodology (Bland and Altman 1999).

In more detail, after linear regression between manual and automated counts, we examined the residual distributions from the regressions, and discovered they were not normally distributed (Shapiro-Wilk test, all $p < 0.05$). However, inspection of the data by histogram and Q-Q plot showed approximate normality with the exception of a small number of outliers and a slight heteroscedasticity for each distribution. In addition, linear regression is known to be robust to such slight deviations from normality, particularly in larger data sets like ours (Williams, Grajales, and Kurkiewicz 2013; Osborne and Waters 2002). We therefore judged these deviations from normality to be minor, and continued to

use simple linear regression to compare model performance, taking a larger R^2 value to indicate a more consistent agreement between manual and automated counts.

We also calculated the mean absolute error between each automated counting tool's axon count and the gold-standard manual axon counts to quantify the accuracy for that tool. None of the mean absolute error distributions for each tool's results were normally distributed (Shapiro-Wilk: all $p < 0.001$), so we compared the tools' mean absolute errors using the Kruskal-Wallis test with Dunn's post hoc test.

Finally, we used Bland-Altman plots (Bland and Altman 1999) to compare the limits of agreement calculated for each method. Ideally, the errors from the automated tools would lie within the range of inter-observer variability. Thus, we aimed for the limits of agreement of these Bland-Altman plots (mean count error ± 1.96•SD of count error) to be within the limits of agreement calculated for individual counters' MC relative to the mean MC. Using this definition, we computed the limits of agreement for our rat dataset as ± 14.3 axons. Additionally, for each image with four manual counters (1184 of 1514 images), corrected ACs were compared to a 95% confidence interval constructed from the four MCs. We defined a success rate as the proportion of images for which the corrected AC fell within this 95% confidence interval. This approach evaluated both automated counting accuracy and precision in the same measurement.

Statistical Analysis of Tool Performance on the NHP Image Dataset

We also evaluated our rat-trained AxoNet algorithm and the two existing axon counting tools on the NHP dataset. To do so, we applied all three tools to the validation subset, created correction equations as stated above, and then applied the correction

equations to the automated counting results from the testing subset. Relationships between semi-automated manual (SAM) and corrected automated counts were assessed in the same manner as they were in the rat image dataset. Since only mean axon counts were available, we were unable to compute the proportion of the automated counts that fell within the 95% confidence interval for the SAM counts or define a desired range for the limits of agreement as we did for the rat optic nerve image dataset. However, we were able to compare the limits of agreement between the corrected ACs and the SAM counts.

Results

Rat Model Dataset Results

We first applied the three automated counting tools to the validation subset of the rat dataset to determine correction equations that accounted for linear bias, as described above (Figure 42). We then applied the automated tools to the testing subset. Before compensating for linear bias using the correction equations, the relationship between AxoNet automated and manual counts (AC and MC) in the testing subset was AC = 0.826*(MC) + 5.36 (R^2 = 0.938), indicating a comparable bias to that seen when our model was applied to the validation subset. For all three automated tools, the corrected linear fit between MC and $AC_{\text{corrected}}$ resulted in regression slopes and intercepts that were mostly significantly different from 1 and 0, respectively (t-test for slope, all p<.05; t-test for intercept, p = 0.0319, p = 0.059, p <.001; all p-values presented in the order: AxoNet, AxonMaster, and AxonJ; Figure 42). These findings indicate that the correction equation method did not fully correct for consistent linear biases, although their effects were reduced.

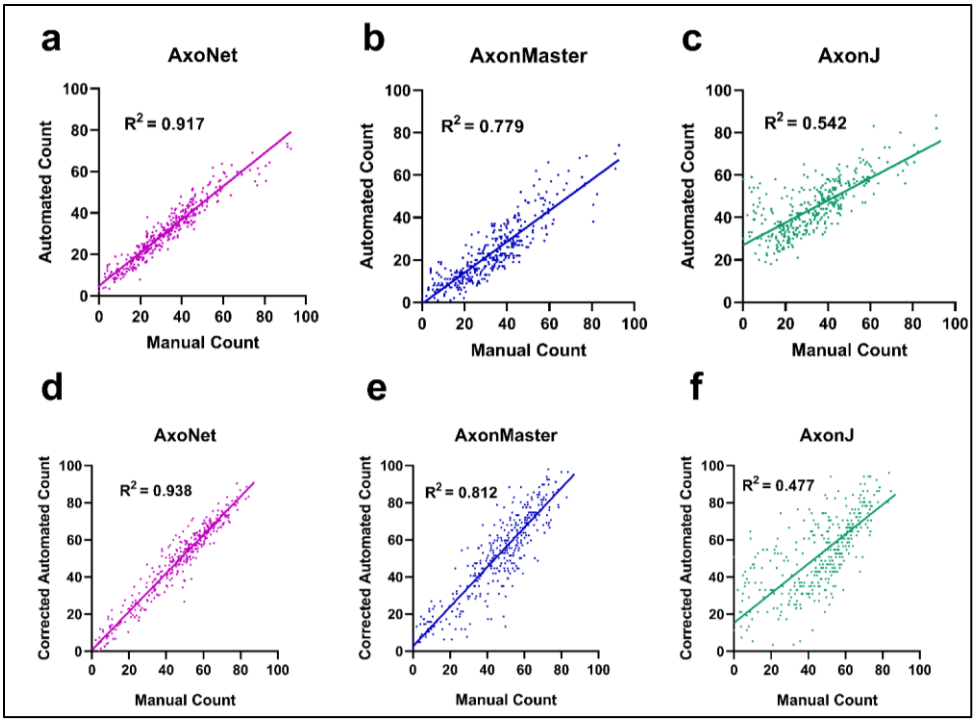

Figure 42: Comparison between automated and manual axon counts for the rat validation and testing subsets. Validation subset results are shown for AxoNet (a), AxonMaster (b) and AxonJ (c). The regression relationships between MC and AC counts were: AxoNet: AC = 0.801(MC) + 4.8; AxonMaster: AC = 0.731*(MC) – 0.633; and AxonJ AC = 0.508*(MC) + 26.2. These relationships were used as correction equations when counting axons in the testing subset. Testing subset results are shown for AxoNet (d), AxonMaster (e) and AxonJ (f). Testing subset mean absolute errors are 4.4, 12.8, and 9.5 axons for AxoNet, AxonMaster, and AxonJ respectively. AC values are shown after applying the correction equations from the validation subset results. Each data point is obtained from a single sub-image from the corresponding subset.*

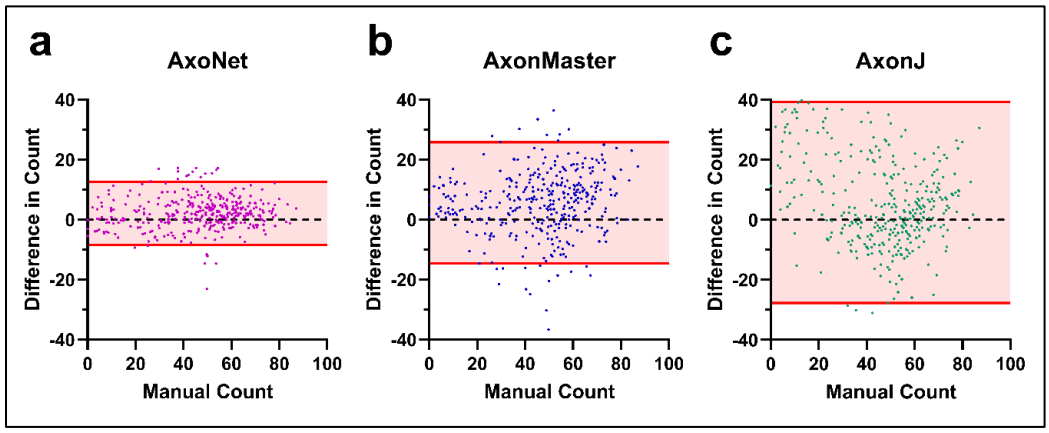

Figure 43: Comparison of error distribution for the rat testing subset. Differences between rat testing subset MC and corrected AC are plotted against manual counts for AxoNet (A), AxonMaster (B) and AxonJ (C) as Bland-Altman plots. Each data point is a single sub-image from the rat testing dataset. Red lines represent the upper and lower bounds for the limits of agreement, calculated as mean error ± 1.96(standard deviation of error). Limits of agreement are [-8.3, 12.6], [-14.59, 25.8], and [-27.7, 39.4] axons for AxoNet, AxonMaster, and AxonJ, respectively.*

Of the three tools, AxoNet achieved the highest correlation between its corrected AC and the MC ($R^2 = 0.938$) as well as the smallest mean absolute error (Kruskal-Wallis: Chi-square = 169.7 and $p < 0.001$; Dunn's post-hoc: all $p < 0.001$, Figure 42). Only AxoNet demonstrated limits of agreement within the threshold determined by the manual count agreement (Figure 43). For the images annotated by four counters, the percentage of corrected ACs that fell within the 95% confidence interval of the manual counts was 83%, 48%, and 58% for AxoNet, AxonMaster, and AxonJ respectively. Taken together, we observe that AxoNet performed the best (i.e. the closest to manual annotations) on the testing subset of the rat dataset.

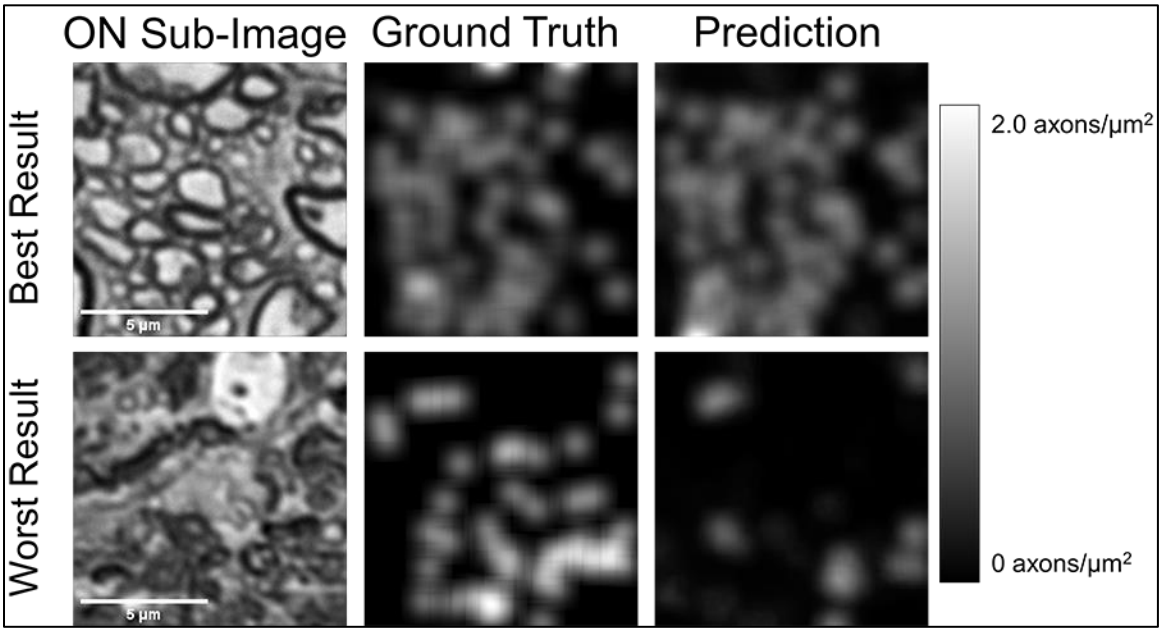

Figure 44: Visualization of AxoNet Performance. The images from the rat testing subset which produced the smallest (top) and greatest (bottom) difference between AxoNet predicted and ground truth manual axon count are shown in the left column. The corresponding manually annotated ground truth axon count density maps are shown in the middle column, and the automatically detected axon count density maps are shown in the right column. The scale bar on the right shows the map used to visualize axon count density as greyscale intensity.

We also visualized the output of AxoNet by determining whether AxoNet was accurately replicating the density maps used during its training by comparing its predicted spatial axon count densities to ground truth (Figure 44). Generally, the density maps produced by AxoNet matched those produced by the manual annotators.

NHP Dataset Results

We then applied these three automated counting tools to the NHP dataset. We first assessed the performance of the three tools using the validation subset of the NHP dataset in order to construct bias correction equations relating each tool's AC to the SAM count. When applied to the validation subset of the NHP dataset, AxoNet achieved a higher correlation between SAM count and AC than the other two tools, although AxonMaster needed less bias correction (Figure 45), likely because it had been optimized for the NHP dataset.

The automated counting methods and their correction equations were then applied to the testing subset of the NHP dataset to directly compare their ability to accurately quantify the number of axons present in each image. For all three automated tools, the corrected linear fit between SAM count and $AC_{\text{corrected}}$ resulted in regression slopes and intercepts that were not significantly different from 1 and 0, respectively (t-test for slope, p = 0.77, p = 0.47, p = 0.81; t-test for intercept, p = 0.77, p = 0.82, p = 0.71; all p-values presented in order: AxoNet, AxonMaster, and AxonJ; Figure 45). Of the three tools, AxoNet achieved the highest correlation between its corrected automated and manual counts (R^2=0.944), with AxonMaster achieving a comparable correlation (R^2=0.938).

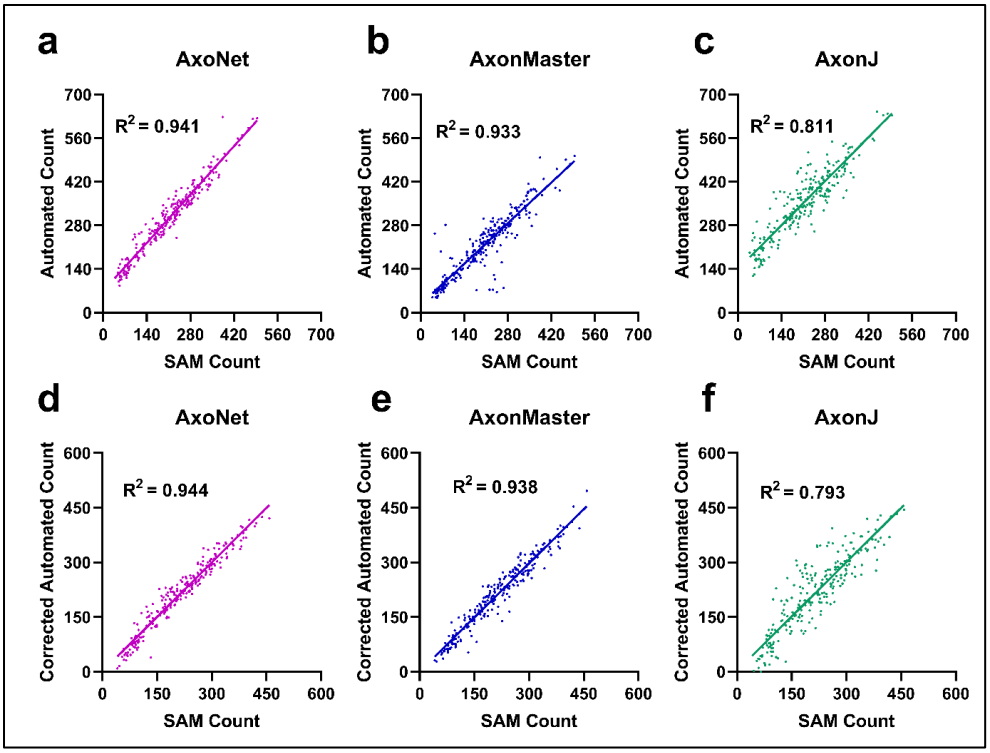

Figure 45: Comparison between automated and manual axon counts for the NHP validation and testing subsets. Validation subset results are shown for AxoNet (a), AxonMaster (b) and AxonJ (c). The regression relationships between SAM and AC counts were: AxoNet: AC = 1.11(SAM) + 69.0; AxonMaster: AC = 0.9849*(SAM) + 17.4; and AxonJ AC = 1.01*(SAM) + 139.2. These relationships were used as correction equations when counting axons in the testing subset. Testing subset results are shown for AxoNet (d), AxonMaster (e) and AxonJ (f). Testing subset mean absolute errors are 17.7, 18.2, and 35.0 axons for AxoNet, AxonMaster, and AxonJ respectively. AC values are shown after applying the correction equations from the validation subset results. Each data point is obtained from a single sub-image from the corresponding subset.*

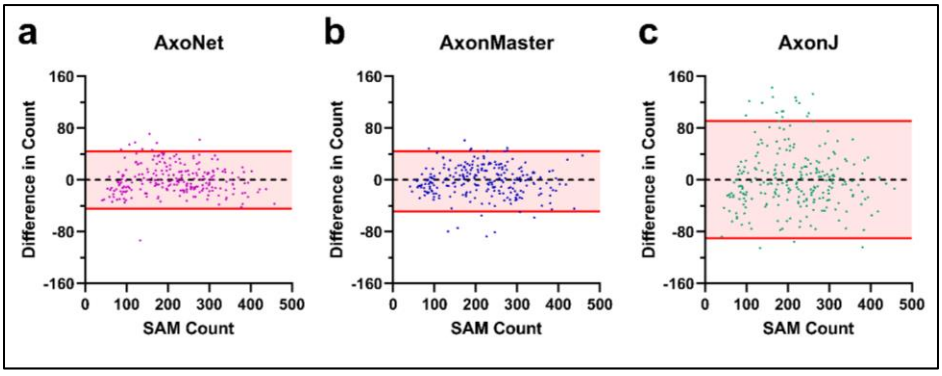

Figure 46: Comparison of error distribution for the NHP testing subset. Differences between NHP testing subset semi-automated manual count and corrected AC are plotted against semi-automated manual count for AxoNet (A), AxonMaster (B) and AxonJ (C) as Bland-Altman plots. Each data point is a single sub-image from the rat testing subset. Red lines represent the upper and lower bounds for the limits of agreement, calculated as mean error ± 1.96(standard deviation of error). Limits of agreement are [-43.9, 42.8], [-48.9, 47.5], and [-91.0, 93.4] axons for AxoNet, AxonMaster, and AxonJ respectively.*

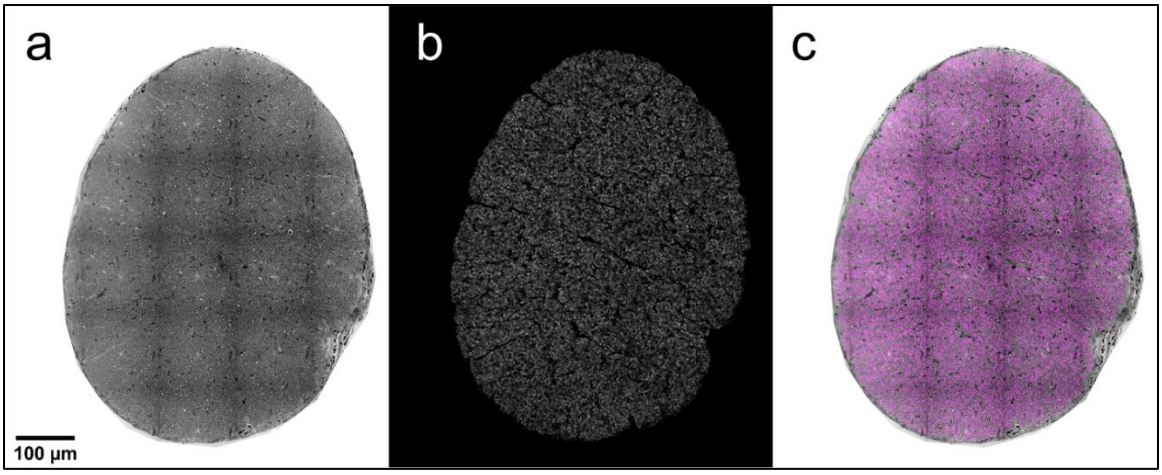

Figure 47: AxoNet Plugin Results. After using the AxoNet plugin for ImageJ and Fiji on an image of a full rat optic nerve (a), the output axon density map (b) and the combination of these two images (c) are displayed. The combination of these two images is shown with the input image (a) in greyscale and the axon density map (b) overlaid in pink. Axon density scale is not provided here because these full images are scaled down significantly for inclusion in the manuscript and color scale is indistinguishable at this resolution. A grid of dark lines is visible in panel a; these lines correspond to tile edges from the microscopy imaging and are an artifact of visualization only since counts are carried out on much smaller portions of the full image.

AxoNet and AxonMaster both had lower mean absolute error when compared to AxonJ (Kruskal-Wallis: Chi-square = 62.57 and $p < 0.001$; Dunn's post-hoc: both $p < 0.001$, Figure 45), while AxoNet and AxonMaster had similar mean absolute error values to one another ($p > 0.9$). AxoNet and AxonMaster produced comparable limits of agreement, whereas AxonJ's limits of agreement were larger (Figure 46).

We packaged AxoNet into a user-friendly plugin for Fiji and ImageJ. This plugin is capable of counting full rat optic nerve images in about 15 minutes (Figure 47). We typically count c. 80,000 "normal"-appearing axons in a healthy nerve, consistent with previous reports (Levkovitch-Verbin et al. 2002; Marina, Bull, and Martin 2010a; Cepurna et al. 2005).

Bias

To investigate the source of the small bias seen in AxoNet, i.e. the fact that there was a difference between the unity line and the best fit regression lines in Figure 42 and Figure 45, we conducted several experiments. In constructing these experiments, we considered the following possible sources of error: (1) a bug in the algorithm; (2) poor convergence of our parameter values during the training phase, i.e. underfitting; (3) inherent differences between the training and testing data sets; and (4) tendency of the algorithm to be biased towards the majority group, which in our case was images with axon counts close to the dataset mean axon count (Johnson and Khoshgoftaar 2019). We consider each of these in turn.

1. *Bug in the algorithm:* We conducted experiments in which we intentionally overfit the network, as follows. We first trained AxoNet on subsets of the full training set of different sizes, and then evaluated the algorithm on those same images. Within this framework, training was conducted using three variations of the training image sets: images that were neither augmented nor resampled, images that were augmented but not resampled, and images that were resampled but not augmented. As data set size decreased, bias decreased; indeed, training on a single repeated image and testing on the same image produced essentially zero error (less than one axon; Figure 48). Because we were able to essentially eliminate bias by overfitting, we concluded that a bug in the code used to train or assess our network was unlikely.
2. *Underfitting*. Our numerical experiments suggested that the parameter optimization process had converged. Specifically, we found that increasing the number of epochs during training did not improve convergence, as measured by the loss function's final

value. Further, using different initial parameter values yielded essentially the same loss function values at the end of training. Thus, we do not believe that bias was due to underfitting.

3. *Inherent differences between data sets:* Error can arise if the training, validation and testing data sets have systematic differences. Such an error source is inherent in supervised machine learning approaches (Neyshabur et al. 2017). In our case, we saw that the bias differed between validation and testing data sets (compare Figure 42 and Figure 45), suggesting subtle systematic differences between image sets. Consistent with this suggestion, the bias was reduced if we trained and tested on the same data set, while image augmentation increased bias if testing was conducted on the training data set (Figure 48; compare red with black symbols). It is interesting to note that training set resampling slightly increased the mean absolute error (compare red with green symbols in Figure 48). We suggest that this occurs because resampling increases the proportion of "hard to count" images, i.e. those with extensive damage or many small axons. However, resampling also reduces error when evaluating different testing and training data sets, and thus is still recommended.
4. *Bias towards the mean:* We note that the algorithm consistently overcounted images with small numbers of axons, and undercounted images with large numbers of axons, suggesting bias towards the mean. Research on evaluating the effects of class imbalances on neural network training for classification and regression shows a similar effect (Johnson and Khoshgoftaar 2019; Krawczyk 2016; Anand et al. 1993) here in our case, images with counts closer to the dataset mean are analogous to the "majority class". To reduce the magnitude of this effect, we resampled our training set images to

produce a uniform distribution of axon counts (see Methods). Even when doing so, a small systematic bias remained, which perhaps reflects a tendency of bias towards the mean even when training occurs on a uniformly sampled image set. Nonetheless, this bias was small and considered acceptable in this application.

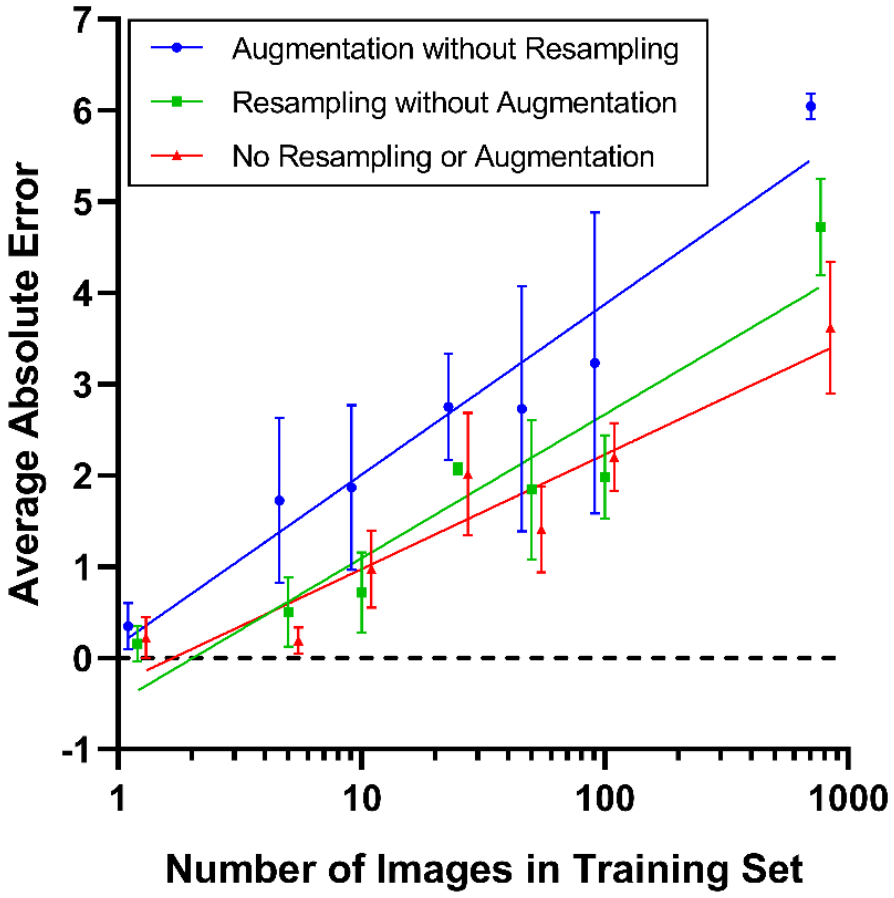

*Figure 48: Training Set Subsampling. The full training data set was sub-sampled to produce training data sets of different sizes (N). AxoNet was then trained with these sub-sampled sets, and subsequently used to count axons in the same data set, i.e. for purposes of generating this figure, the testing and training data set were the same for each realization. We computed a mean absolute error (MAE) over the data set and repeated this process 3 times for each training set size (i.e. 3 replicates) to obtain a mean and standard deviation of the MAE. This full analysis was completed for three training set conditions: training augmentation without resampling (blue symbols), resampling without training augmentation (green symbols), and no training augmentation or resampling (red symbols). The respective fitted relationships for these three conditions were MAE = 0.1 + 1.8*log(N), MAE = -0.4 + 1.5*log(N), and MAE = -0.2 + 1.2*log(N). Note that the horizontal axis is logarithmic and that plotted values at the same training set size are offset slightly in the horizontal direction for visual clarity.*

Discussion

The purpose of this study was to develop and evaluate a new approach to automatically count "normal"-appearing RGC axons in a diverse dataset of healthy and damaged optic nerve cross sections. Such an automated axon counting tool is a useful tool in studying glaucoma and potentially other neurodegenerative disorders. We designed this new approach to work well over a range of image qualities and for multiple mammalian species. AxoNet's predicted axon counts proved to be highly correlated to manual axon counts in both the rat and NHP datasets, indicating that it met our requirements for an automated axon counting tool. As judged by the uniform error over the range of manual axon counts (Figure 43 and Figure 46), AxoNet performed equally well on images of damaged vs. healthy optic nerves. This is significant because axon counting is more difficult in diseased tissue, and suggests promise for the use of AxoNet as a tool for nerve damage analysis in experimental glaucoma.

Prior to building AxoNet, we explored the methodologies previously used to create existing automated axon counting tools. AxonMaster uses a fuzzy c-means classifier as an adaptive thresholding method to segment axon interiors from the darker myelin sheath. These clusters are then filtered by size and circularity before counting axons. AxonJ uses a Hessian operator to identify the darker myelin sheath and then performs similar adaptive thresholding and connected region size filtering region before counting the connected regions as axons. When applied to the rat dataset, these two tools produced adequate segmentation of total axon area in optic nerve images, but often did not produce accurate segmentation of individual axons, leading to inaccurate counts. We also attempted to apply

two other segmentation techniques, ilastik (Sommer et al. 2011) and the basic pixel segmentation U-Net (Ronneberger, Fischer, and Brox 2015). These approaches also resulted in inaccurate counts, especially when applied to damaged tissue; therefore, we adapted an alternate cell counting framework introduced by Lempitsky et al. (Lempitsky and Zisserman 2010). This approach avoids the difficult task of semantic segmentation and instead predicts a pixelwise cell count density estimate. The authors accomplished this through using machine learning with hand-crafted pixelwise features (Lempitsky and Zisserman 2010). More recently, attempts have been made to perform similar count density function estimations using convolutional neural networks (Wang et al. 2018) and adapted U-Net architectures (Valloli and Mehta 2019) for crowd counting, which is a technically similar problem to cell counting. Convolutional neural networks have also been used recently for axon segmentation in scanning and transmission electron microscopy images of mammal and human spinal cord (Zaimi et al. 2018). The tool produced in this work is the result of this synthesis between a convolutional neural network architecture designed for cell segmentation, the U-Net, and a count density prediction strategy. This method avoids the hard problem of axon segmentation in lower-resolution light microscopy, trading the ability to analyze single-axon morphology for the most accurate axon count.

This study was limited by several factors. First, and most important, to date AxoNet has been trained to count only "normal"-appearing axons, similar to existing axon-counting software. The classification of an axon as "abnormal" in appearance does not necessarily imply that the axon is non-functional, and thus our tool may not count axons that are in fact conducting visual information. However, due to AxoNet's generalizability and lack of reliance on hand-crafted features specific to "normal"-appearing axons, it can be extended

to count or even segment other features of both healthy and glaucomatous optic nerves, such as glial processes, nuclei, “abnormal” axons, large vacuoles, and extracellular matrix. We are currently extending AxoNet to quantify these features. Such analysis of features beyond “normal”-appearing axons may provide new insight into the pathophysiological processes of glaucomatous nerve degeneration.

Second, we were unable to fully eliminate systematic biases in the network’s predictions. We investigated the source of this systematic prediction bias and found that it did not originate from errors within the training or prediction code or from underfitting. We posit that some bias may be unavoidable due to subtle differences in the training and testing sets, which can be mitigated by increasing the variability within the training data set. Based on the literature, we also posit that training set imbalance may cause training bias towards common training cases. This source of bias can be mitigated by resampling rarer cases to increase their influence during network training. By doing so, we were able to reduce bias to only a few axons per image. Considering the complexity of our images and the variability from animal to animal in glaucoma models, we judged this level of bias to be acceptable.

Third, the linear bias correction equations determined in this study were suitable for countering systematic bias in our data set, but may not necessarily be accurate for other data sets, since the conditions which create these systematic biases may vary with experimental treatment, imaging protocols, or tissue processing protocols. However, we do not expect such effects to be severe, since we intentionally included these sources of variability within the two image datasets used in this study and AxoNet still performed well. Nonetheless, it would be prudent to calibrate AxoNet for each new application, which

can be done through using correction equations like those created with our validation subsets or network retraining with a new dataset according to the training protocol detailed above.

A fourth limitation is that all manual counts were conducted by members of one lab, and it is possible that manual counts generated in different research groups could be slightly different from ours since manual counting itself is not entirely unambiguous. This uncertainty is inherent in axon quantification and cannot be avoided, although to enhance repeatability we have explicitly described our definition of "normal"-appearing axons and have made the training data publicly available.

Presently, AxoNet regresses a pixelwise count density function which is integrated over the full image to return a count. Fitting the density function is accomplished through the minimization of a mean squared error loss function evaluated at each pixel (Equation 6). This loss function may be overly sensitive to zero-mean noise and other variations in training images. Lempitsky et al. (Lempitsky and Zisserman 2010) originally solved this problem through the Mesa loss function, which used a maximum subarray algorithm to find the image region with the largest difference between automated and manual counts and minimized count error over this region instead of at every pixel. When we attempted to use this loss function during our training, the resulting method was far too computationally expensive and resulted in a prohibitively long training time (on the order of hours per training step). However, developing a new loss function which avoids computing the mean square error at every pixel per iteration but does so without the computational expense may improve AxoNet's performance in terms of accurate axon count insensitive to image noise.

The successful use of the rat-trained AxoNet to count NHP images is indicative of the versatility of our method, even without re-training. However, the network can be easily re-trained on a new counting case if needed. If there is adequate training data in the new set, the deep learning framework can adapt itself to new applications without requiring any changes in handcrafted features. Data augmentations like those described in the methods can be applied to improve network learning from limited datasets, as was done in the first published application of the U-net architecture (Ronneberger, Fischer, and Brox 2015).

We can also use AxoNet to count axons in full rat optic nerve images by subdividing the full image into tiles for individual processing. This tile-based processing was necessary because of the prohibitive computational expense involved in applying the U-net architecture to large images. However, tile-based processing has the potential to create edge artifacts by cutting off portions of cells on the borders of each tile. We correct for this potential error by padding the edges of each processing tile with bordering pixels from adjacent processing tiles. Including this information from bordering tiles meant that the resulting density map prediction was not affected by these potential tile cropping artifacts. Once processed, the resulting density map was cropped back to its original tile size. This padding was not done when it would have required pixels from beyond the image boundaries. These padded tiles were then also mirrored, as described for model training above.

When running on the system used for this study (Windows Desktop, Intel i7-3770 CPU at 3.40 GHz, 16 GB RAM; Dell, Round Rock, TX), AxoNet counts the axons within a full rat optic nerve image in approximately 15 minutes. For comparison, it took AxonJ and AxonMaster approximately 30 minutes and 1 hour, respectively, to count the axons

within a full rat optic nerve image. Therefore, our tool can be applied to analyze full optic nerve images with runtimes comparable to, or better than, those of the existing automated tools.

Conclusion

We have successfully applied a deep learning method to accurately count "normal" axons in both rat and non-human primates, and in both healthy and experimentally glaucomatous optic nerve sections. Additionally, we have compared AxoNet to two previously published automated counting tools and shown that AxoNet performs as well as or better than these two tools in counting healthy axons in these two datasets. Our tool is available online as an ImageJ plugin and can be installed by following the instructions at https://github.com/ethier-lab/AxoNet-fiji. The code and data we used to train the model can be found at https://github.com/ethier-lab/AxoNet.

Data Availability

The rat optic nerve image dataset generated and analyzed during the current study are available in the Github repository, https://github.com/ethier-lab/AxoNet. A spreadsheet containing the count data for each image in both the NHP and rat datasets is available on the same repository. The NHP optic nerve image dataset and AxonMaster software are the property of the Burgoyne Lab, where they are available upon reasonable request.

APPENDIX B. **Supplemental Information for Chapter 3**

Relative Stiffness in Terms of Strain Derivation

The outputs from our DIC inflation tests were strain values on the scleral surface for different IOP levels, as set by a hydrostatic pressure reservoir. Our goal was to use these strain measurements to estimate the stiffness of the experimental region of an eye relative to the control region. Relative stiffness was defined as the stiffness of the experimental material (here sclera) relative to the control material:

$$\text{Relative Stiffness} = \frac{E_{exp} - E_{con}}{E_{con}} \tag{10}$$

where E_{exp} is the effective modulus of the experimental material and E_{con} is the effective modulus of the control material. Since the sclera is not a linearly elastic material and therefore has an elastic modulus that varies as a function of applied stress (or in our case, IOP) we defined the effective modulus as the tangent modulus at a certain point (or IOP) on the stress-strain curve.

By modeling the eye as a thin-walled sphere and assuming a spatially uniform radius and wall thickness, the stress-pressure relationship is given by Laplace's law:

$$\sigma = \frac{PR}{2t} \tag{11}$$

where σ is the hoop stress in the wall of the sphere, P is the internal pressure, R is the radius, and t is the wall thickness of the sphere (see Figure 49).

Since the internal pressure, P, is spatially uniform within the eye, the hoop stresses in the experimental and control regions of the eye, σ_{exp} and σ_{con} , are the same:

$$\sigma = \sigma_{con} = \sigma_{exp} \tag{12}$$

We approximate the tissue behavior as incrementally linear elastic within the loading regime of interest to write:

$$\frac{\sigma_{con}}{\varepsilon_{con}} = E_{con} \, , \frac{\sigma_{exp}}{\varepsilon_{exp}} = E_{exp} \tag{13}$$

where ε_{con} and ε_{exp} are the control and experimental first principal (hoop) strains, respectively.

Using equation (10) we can write:

$$\frac{E_{exp} - E_{con}}{E_{con}} = \frac{\frac{\sigma_{exp}}{\varepsilon_{exp}} - \frac{\sigma_{con}}{\varepsilon_{con}}}{\frac{\sigma_{con}}{\varepsilon_{con}}} = \frac{\sigma\left(\frac{1}{\varepsilon_{exp}} - \frac{1}{\varepsilon_{con}}\right)}{\sigma\left(\frac{1}{\varepsilon_{con}}\right)} \tag{14}$$

Algebraic simplification yields an expression for the relative stiffness in terms of strains at a given pressure step:

$$\text{Relative Stiffness} = \frac{E_{exp} - E_{con}}{E_{con}} = \frac{\varepsilon_{con} - \varepsilon_{exp}}{\varepsilon_{exp}} \tag{15}$$

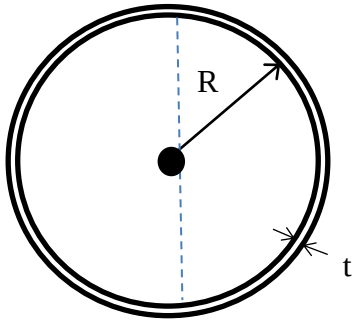

Figure 49: Schematic diagram of quantities used in calculation of relative stiffening

APPENDIX C. **Supplemental Information for Chapter 5**

Table 7: RT-PCR genes analyzed and corresponding primers.

Gene name	Symbol	Gene ID	Forward 5'-3'	Reverse 5'-3'	Length
matrix metallopeptidase 1	Mmp1	ID: 300339	CACTCCCTTGGACTCACTCA	GTTGGCTGGATGGGATTTGG	149 bp
matrix metallopeptidase 2	Mmp2	ID: 81686	ACAGTGGATGATGCCTTTGC	TCCATCTCCATGCTCCCATC	129 bp
matrix metallopeptidase 3	Mmp3	ID: 171045	ACCTATTCCTGGTTGCTGCT	TGGGAGGTCCATAGAGGGAT	168 bp
TIMP metallopeptidase inhibitor 1	Timp1	ID: 116510	GTGCACAGTGTTTCCCTGTT	GGTATTGCCAGGTGCACAAA	158 bp
TIMP metallopeptidase inhibitor 2	Timp2	ID: 29543	ATCCAAGTGGGTTCACGCTA	GCTCTACTCCTGCTGTACCA	172 bp
TIMP metallopeptidase inhibitor 3	Timp3	ID: 25358	CCCTTTGGCACTCTGGTCTA	CAGCCCTGTGTACATCTTGC	186 bp
tumor necrosis factor	Tnf	ID: 24835	GGTCCCAACAAGGAGGAGAA	GCTTGGTGGTTTGCTACGAC	134 bp
interleukin 1 beta	Il1b	ID: 24494	CACTCATTGTGGCTGTGGAG	AGGACGGGCTCTTCTTCAAA	115 bp
Cd68 molecule	Cd68	ID: 287435	ACGGACAGCTTACCTTTGGA	AATGTCCACTGTGCTGCTTG	118 bp
glyceraldehyde-3-phosphate	Gapdh	ID: 24383	AAGATGGTGAAGGTCGGTGT	GCTTCCCATTCTCAGCCTTG	196 bp
actin, beta	Actb	ID: 81822	TCCTCCCTGGAGAAGAGCTA	ACGGATGTCAACGTCACACT	171 bp

Table 8: Proteomic expression levels in the sclera, computed as the fold change of scleral protein amount in genipin-treated eyes compared to contralateral HBSS-treated eyes (n = 3). All q-values > 0.05.

Description: Rattus norvegicus	Molecular Function	Unique peptides	Confidence score	ANOVA (p)	q Value
Myosin_ heavy polypeptide 9_ non-muscle	Actin binding and motor activity	32	283.4	0.248	0.401
RCG55135_ isoform CRA_b	Cell adhesion	24	210.8	0.374	0.454
Complement C3	Immune Response	22	195.6	0.432	0.489
Vimentin	Cytoskeleton structural support	31	335.2	0.331	0.441
Collagen type VI alpha 2 chain	Extracellular matrix structural support	23	236.8	0.189	0.398
Heat shock cognate 71 kDa protein	Protein binding	24	265.0	0.091	0.372
Spectrin alpha chain_ non-erythrocytic 1	Calcium binding	22	148.5	0.199	0.398
Collagen type VI alpha 1 chain	Extracellular matrix structural support	34	361.8	0.299	0.430
Actin_ cytoplasmic 1	Cell adhesion	23	303.0	0.760	0.638
Lamin A_ isoform CRA_b	Cytoskeleton structural support	40	371.7	0.510	0.534
AHNAK 1 (Fragment)	Protein binding	25	195.5	0.094	0.372
Filamin A	Protein binding	37	283.8	0.853	0.677
Collagen type XIV alpha 1 chain	Extracellular matrix structural support	44	401.0	0.030	0.372
Collagen alpha-1(XII) chain	Extracellular matrix structural support	134	1368.9	0.244	0.401
Collagen alpha-2(I) chain	Extracellular matrix structural support	43	370.0	0.413	0.477
Spectrin beta chain	Actin binding and motor activity	29	214.4	0.133	0.372
Myosin heavy chain 1	Actin binding and motor activity	95	1011.0	0.675	0.604

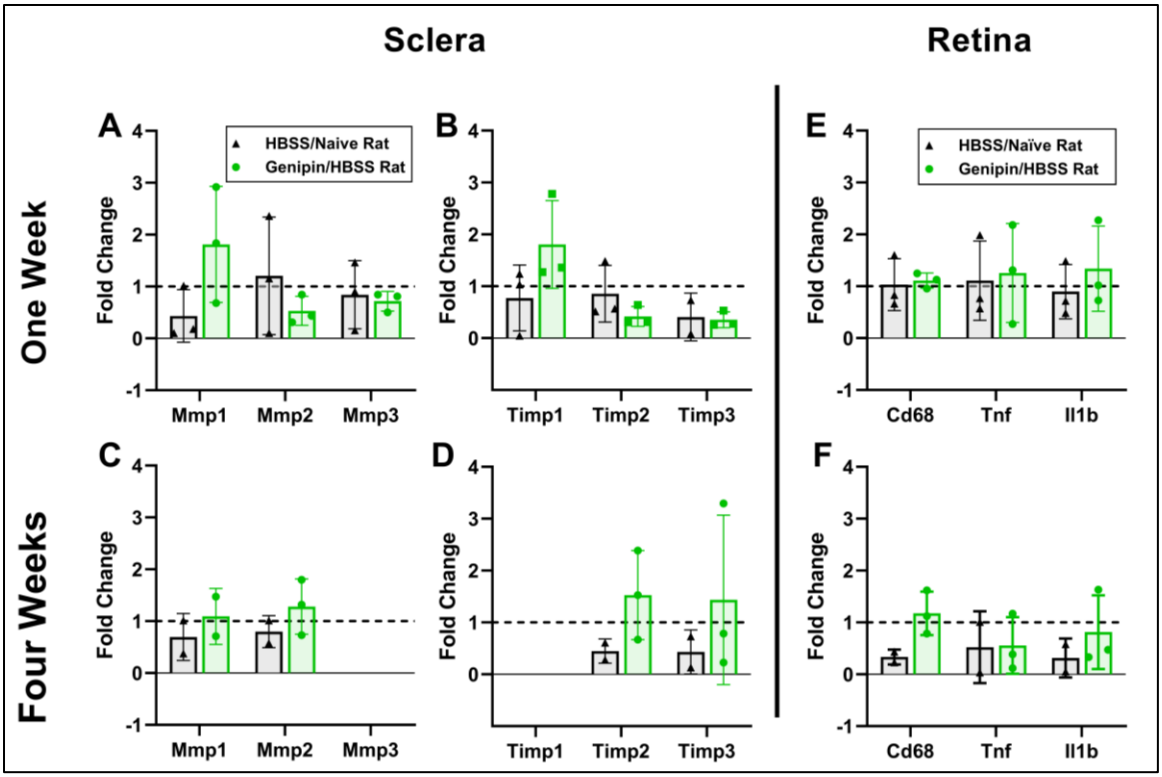

Figure 50: Genipin treatment did not significantly affect message abundance for genes involved in extracellular matrix turnover in the sclera, nor for pro-inflammatory genes in the retina. Plotted is the fold change of message for MMPs (A and C) and TIMPs (B and D) at one week (A and B) and four weeks (C and D) post-injection in the sclera for HBSS/Naïve and Genipin/HBSS rats. In HBSS/Naïve rats, the HBSS-injected eye was normalized to the contralateral Naïve eye, and in Genipin/HBSS rats, the genipin-treated eye was normalized to the contralateral HBSS-injected eye. Values are missing for Mmp3 in (C) and Timp1 in (D) due to lack of data after outlier removal. E and F show fold change of message levels for inflammatory cytokines (Cd68, Tnf, and Il1b) at one week (E) and four weeks (F) post-injection in the retina for HBSS/Naïve and Genipin/HBSS rats. No significant differences were found between contralateral eyes in any tissue at any timepoint. (Multiple t-tests using Holm-Sidak correction, all $p > 0.05$, all data shown as mean ± SD).

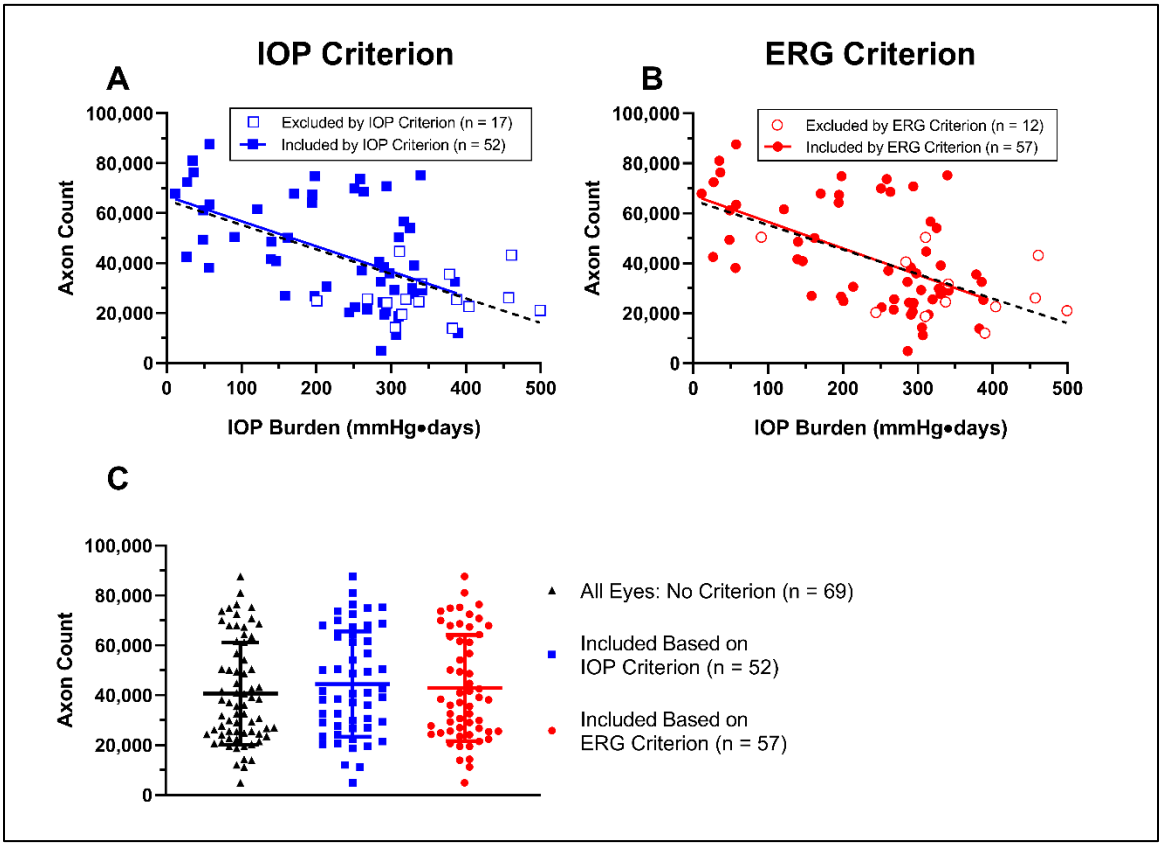

Figure 51: Whole nerve axon counts in hypertensive eyes are plotted vs IOP burden included (solid) and excluded (hollow) based on IOP Criterion (A) and ERG Criterion (B). Axon counts of all hypertensive eyes (black dashed in A and B) and hypertensive eyes included based on both IOP Criterion (A) and ERG Criterion (B) were significantly correlated with IOP burden (all $p < 0.0001$). C) Axon counts of hypertensive eyes from all rats (black), included based on IOP Criterion (blue), and included based on ERG Criterion (red) were not different from one another (One-way ANOVA, $F(2, 175) = 0.5043$, $p = 0.605$). Data shown as mean ± SD.

APPENDIX E. **Supplemental Information for Chapter 7**

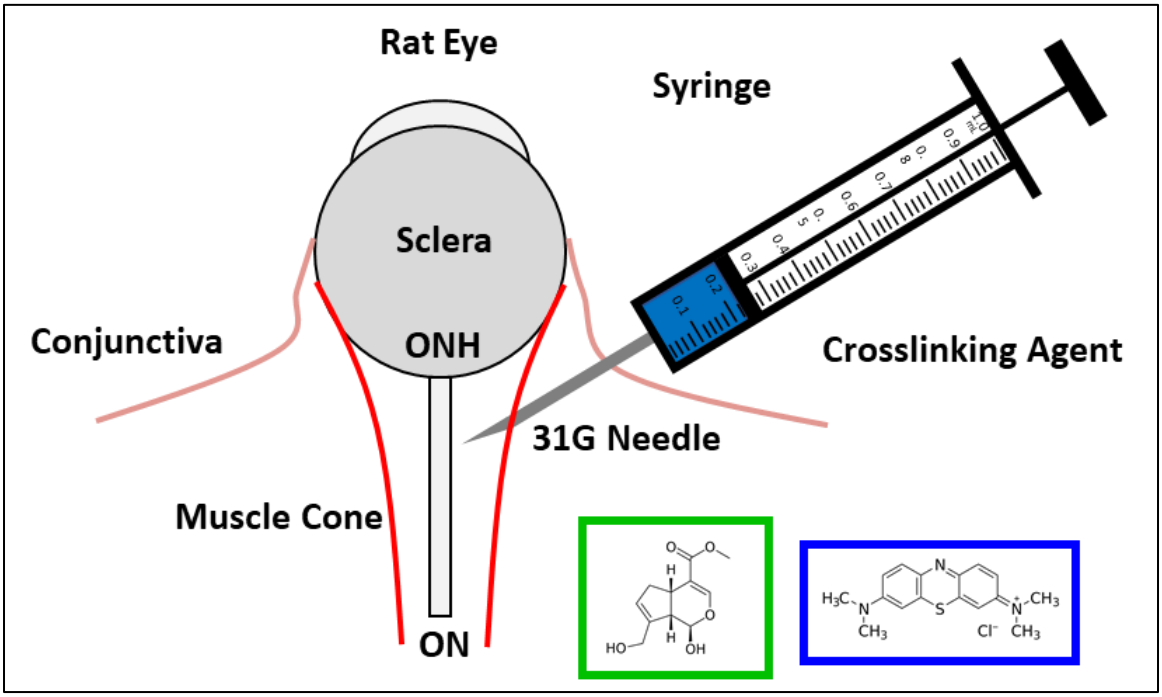

Figure 52: Chemical crosslinker genipin (left inset) or photocrosslinker methylene blue (right inset) were injected by retrobulbar injection to induce scleral crosslinking. Genipin induced non-targeted crosslinking. Methylene blue was activated with a transpupillary light beam to selectively crosslink peripapillary sclera.

Table 9: Tabulated average IOP burden of rats included in each outcome parameter group with number of eyes in each group.

Outcome Parameter	Average IOP Burden (mmHg·days)	Normotensive Eye Sample Size				Hypertensive Eye Sample Size			
		HBSS	GP	MB	**Total**	HBSS	GP	MB	**Total**
Peripapillary Strain	218	15	11	15	41	16	10	13	39
Peripheral Strain	220	15	11	15	41	16	11	14	41
Equatorial Diameter	224	17	12	13	42	17	11	14	42
Axial Length	224	17	12	13	42	17	11	14	42
Anterior Chamber Depth	223	17	12	12	41	17	11	13	41
Nerve Cross-sectional Area	225	19	16	16	51	20	18	19	57
Axon Count	229	19	16	14	49	20	17	19	56
Axon Density	226	18	16	15	49	19	17	19	55
Retinal Thickness at 0.5 mm	222	19	18	16	53	20	18	18	56
Retinal Thickness at 1.2 mm	218	20	18	17	55	19	18	18	55
Contrast Sensitivity	226	21	20	19	60	20	18	18	56
Spatial Frequency	226	21	20	19	60	20	18	18	56
pSTR Amplitude	224	21	20	18	59	21	20	19	60
nSTR Amplitude	225	21	20	19	60	21	20	19	60
b-wave Amplitude	227	21	20	19	60	20	20	19	59
OP3 Amplitude	225	21	19	19	59	21	20	19	60

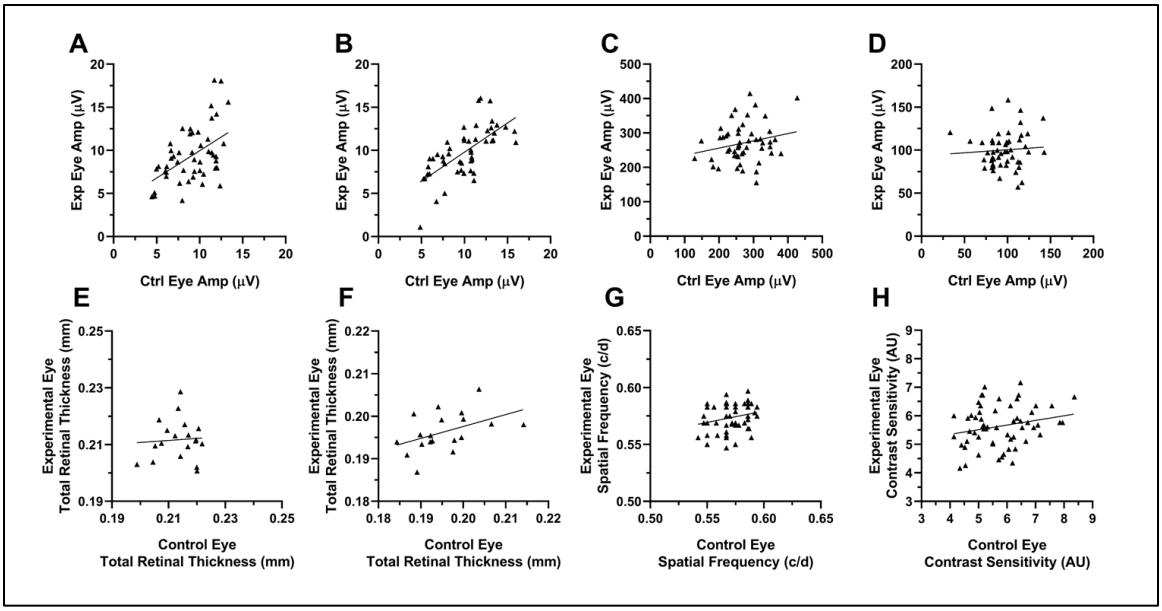

Figure 53: Correlations of baseline control and experimental eye values prior to treatments. "Control" indicates eyes designated to be normotensive. "Experimental" indicates eyes designated to be normotensive (microbead injection). A) pSTR amplitude, B) nSTR amplitude, C) b-wave amplitude, D) oscillatory potential 3 amplitude, E) retinal thickness at 0.5 mm from the ON, F) retinal thickness at 1.2 mm from the ON, G) spatial frequency, and H) contrast sensitivity, showed no significant correlation at baseline between eyes of the same rat.

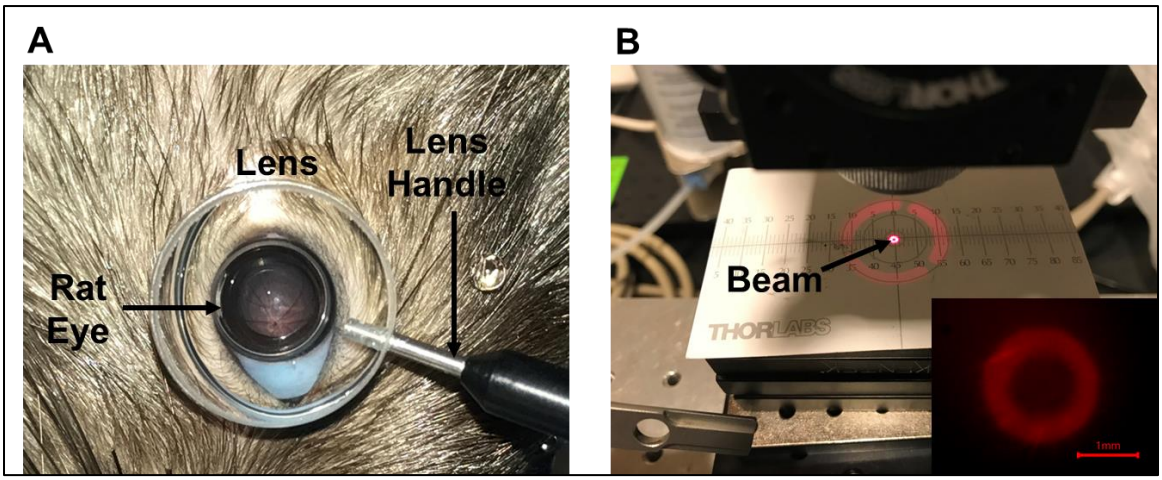

Figure 54: A) Image of BN rat fundus viewed through refraction-negating corneal contact lens showing optic nerve head and retinal vasculature. The lens created a clear optical path facilitating B) projection of an annular beam (measuring 2 mm outer diameter, 1 mm inner diameter) of 660 nm incoherent light from a custom-designed microscope to the peripapillary sclera following retrobulbar injection of MB. The inset shows an image of the beam projected onto a BN rat fundus as viewed using the microscope's camera (inset scale bar = 1 mm).

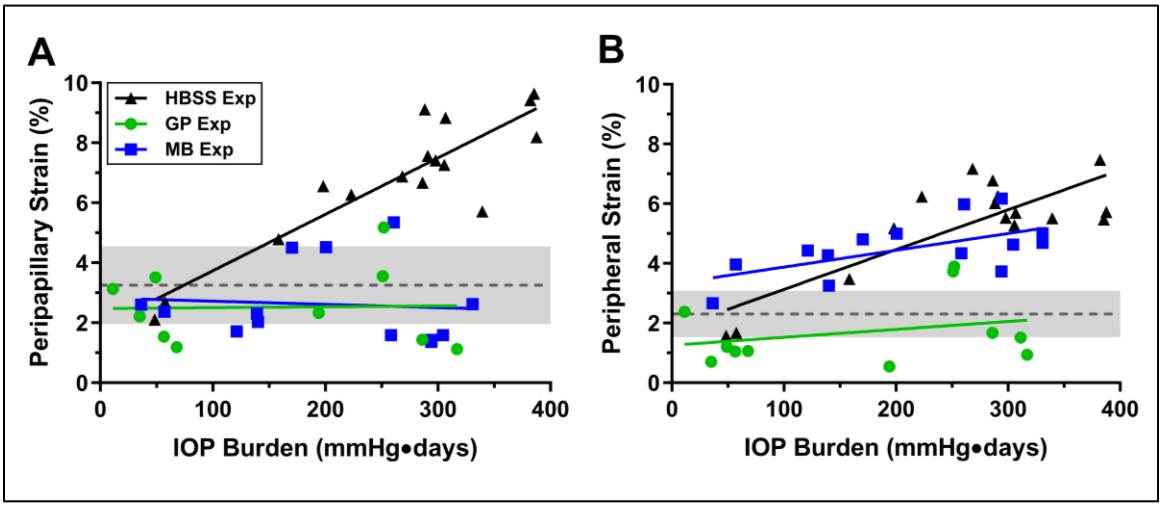

Figure 55: A) Peripapillary and B) peripheral strain as a function of IOP burden. Dashed line represents mean values from normotensive controls and their corresponding standard deviations (grey band).

Table 10: Table of experimental variables investigated in this study compared with those of the Kimball et al. 2014 study which investigated effects of scleral crosslinking on visual/morphological outcomes in glaucomatous mice.

Variable	Kimball et al. (2014)	Genipin Crosslinking	Methylene Blue Crosslinking
Animal	Mouse	Rat	Rat
Model of Glaucoma	Microbead	Microbead	Microbead
Crosslinking Agent	Glyceraldehyde	Genipin	Methylene Blue
Photoactivation	No	No	Yes, 660 nm
Concentration	500 mM	15 mM	3 mM
Targeted scleral region	Sclera	Sclera	Peripapillary Sclera Only
Injection Method	Subconjunctival	Retrobulbar	Retrobulbar
Injection Volume	400 µl	150 µl	100 µl
Number of Injections	Three	One	One

Table 11: Two-way ANCOVA outcomes for measured parameters including main effects of crosslinking treatment (HBSS, GP, MB) and microbead treatment (normotensive, hypertensive) accounting for IOP burden as a covariate. Highly significant ($p < 0.0001$) p-values are bolded.

Outcome Parameter	Main Effects (p-value)			Interaction Terms (p-value)			Homogeneity of Variance (p-value)
	Crosslinking Treatment	Microbead Treatment	IOP Burden	Crosslinking X Microbead	Crosslinking X IOP Burden	Microbead X IOP Burden	Levene's Test
Peripapillary Strain	n.s.	n.s.	<0.01	<0.001	<0.05	n.s.	n.s.
Peripheral Strain	n.s.	n.s.	**<0.0001**	**<0.0001**	<0.05	<0.001	n.s.
Equatorial Diameter	n.s.	n.s.	**<0.0001**	n.s.	n.s.	**<0.0001**	<0.01
Axial Length	n.s.	<0.01	**<0.0001**	n.s.	n.s.	**<0.0001**	n.s.
Anterior Chamber Depth	n.s.	n.s.	n.s.	n.s.	<0.05	<0.05	n.s.
Nerve Cross-sectional Area	n.s.	n.s.	n.s.	n.s.	<0.05	n.s.	n.s.
Axon Count	n.s.	<0.05	<0.001	n.s.	n.s.	<0.01	<0.01
Axon Density	n.s.	<0.05	<0.001	n.s.	n.s.	<0.01	n.s.
Retinal Thickness at 0.5 mm	n.s.	n.s.	<0.05	<0.001	n.s.	<0.05	**<0.0001**
Retinal Thickness at 1.2 mm	n.s.	n.s.	n.s.	<0.01	<0.05	n.s.	<0.001
Contrast Sensitivity	n.s.	**<0.0001**	<0.05	n.s.	<0.05	**<0.0001**	n.s.
Spatial Frequency	n.s.	**<0.0001**	**<0.0001**	n.s.	n.s.	**<0.0001**	<0.01
pSTR Amplitude	n.s.	**<0.0001**	<0.05	<0.05	<0.05	<0.05	<0.05
nSTR Amplitude	n.s.	<0.05	n.s.	n.s.	n.s.	n.s.	<0.05
B-wave Amplitude	n.s.	**<0.0001**	n.s.	n.s.	n.s.	n.s.	n.s.
OP3 Amplitude	n.s.	n.s.	<0.05	n.s.	<0.05	<0.001	<0.05

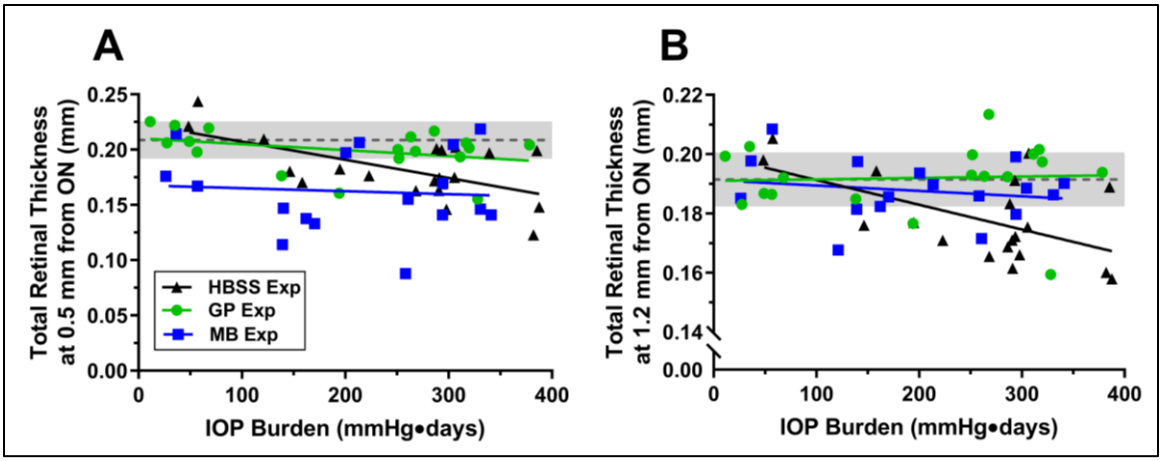

Figure 56: OCT retinal thickness measurements as a function of IOP burden at A) 0.5 mm from the ONH and B) 1.2 mm from the ONH. Dashed line represents mean values from normotensive controls and their corresponding standard deviations (grey band).

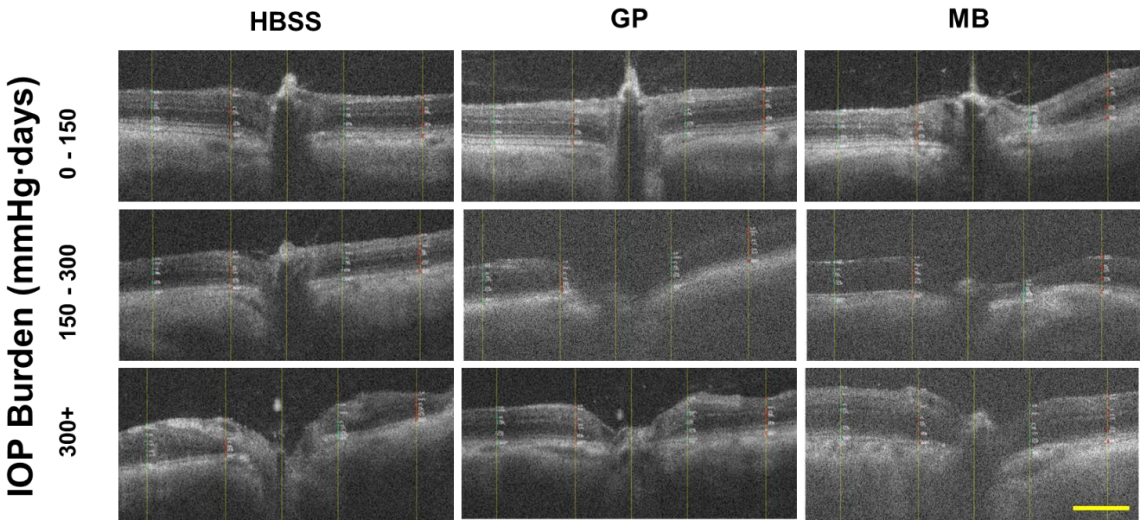

Figure 57: Representative experimental eye optic nerve/retina OCT images from each treatment in specified range of IOP burden. Damage qualitatively increases with increasing IOP burden. "" indicates choroid, "†" indicates optic nerve head. Vertical yellow lines on each image indicate (from left to right), -1.2 mm, -0.5 mm, 0 mm, 0.5 mm, 1.2 mm distances from center of optic nerve head at which retinal thickness measurements were taken. Scale bar = 0.5 mm. Specifically, cupping at the optic nerve head increases in all groups.*

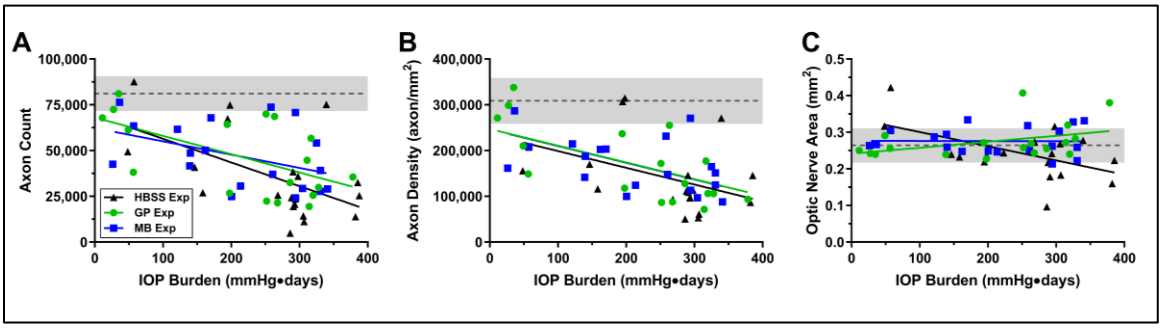

Figure 58: A) Axon count, B) axon density, and C) optic nerve cross-sectional area as functions of IOP burden. Dashed line represents mean values from normotensive controls and their corresponding standard deviations (grey band).

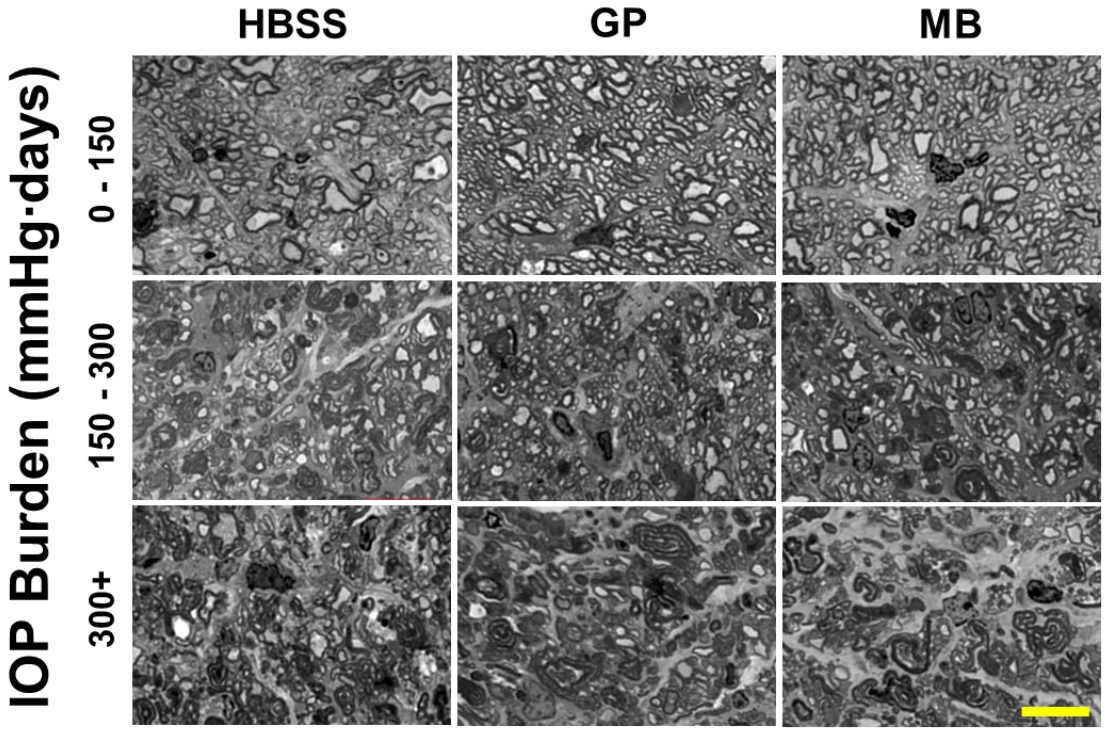

Figure 59: No qualitative differences were found in optic nerve cross-sections of hypertensive eyes between crosslinking treatment groups. Representative images from each treatment in specified range of IOP burden are shown. Images were taken from the central region of each nerve. Scale bar = 10 µm. Damage qualitatively increases with increasing IOP burden.

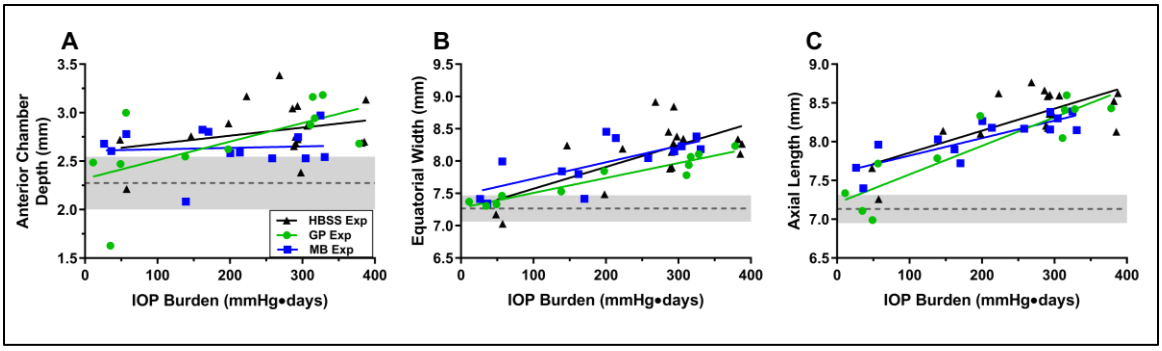

Figure 60: Eye size parameters vs IOP burden including A) anterior chamber depth, B) equatorial width, and C) axial length. Dashed line represents mean values from normotensive controls and their corresponding standard deviations (grey band).

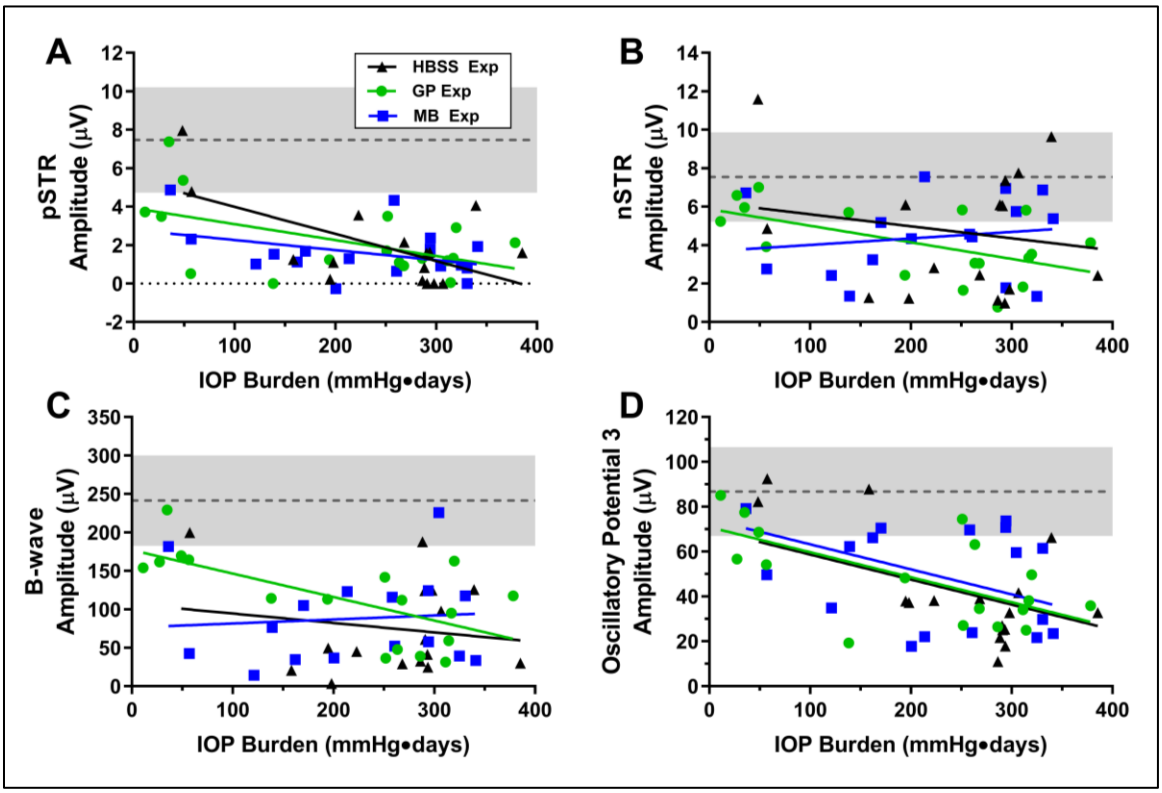

Figure 61: ERG outcomes vs IOP burden for A) pSTR amplitude, B) nSTR amplitude, C) b-wave amplitude, and D) oscillatory potential 3 amplitude. Dashed line represents mean values from normotensive controls and their corresponding standard deviations (grey band).

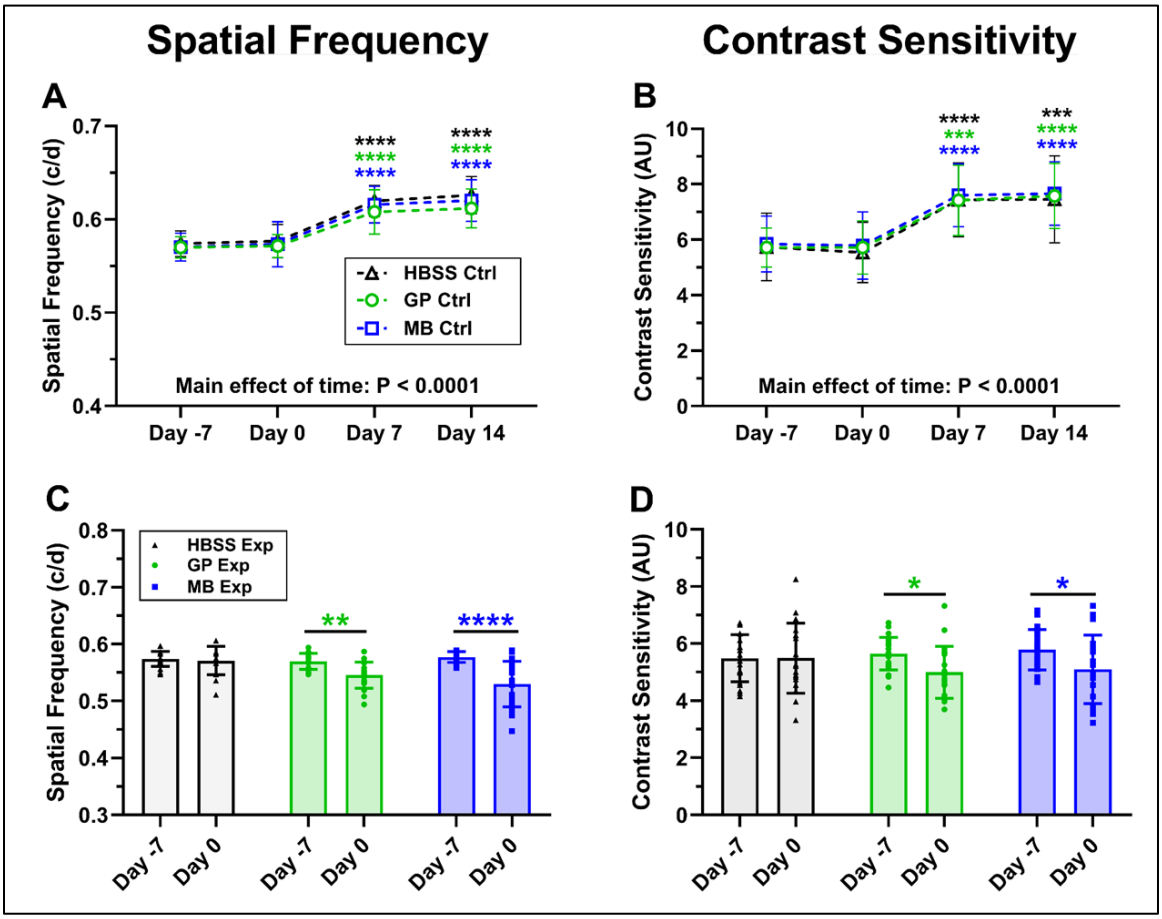

Figure 62: Resolved A) spatial frequency and B) contrast sensitivity of normotensive control eyes at Days -7, 0, 7, and 14 with respect to induction of hypertension at Day 0. Significant differences were found at Day 7 and Day 14 compared to Day -7 (baseline) for spatial frequency and for contrast sensitivity in all crosslinking treatment groups. These findings suggest the presence of a hyperacuity effect in the normotensive eye after induction of hypertension in the contralateral eye C) Spatial frequency differed between Day -7 (baseline) and Day 0 (after stiffening treatment) for GP ($p < 0.01$) and MB ($p < 0.0001$). D) Contrast Sensitivity differed between Day -7 (baseline) and Day 0 (after stiffening treatment) for GP ($p < 0.05$) and MB ($p < 0.05$).

REFERENCES

Adachi, M., K. Takahashi, M. Nishikawa, H. Miki, and M. Uyama. 1996. 'High intraocular pressure-induced ischemia and reperfusion injury in the optic nerve and retina in rats', *Graefes Arch Clin Exp Ophthalmol*, 234: 445-51.

Agarwal, S., A. Agarwal, and D.J. Apple. 2002. *Textbook of Ophthalmology* (Jaypee Brothers).

Agnifili, L., R. Mastropasqua, P. Frezzotti, V. Fasanella, I. Motolese, E. Pedrotti, A. Di Iorio, P. A. Mattei, E. Motolese, and L. Mastropasqua. 2015. 'Circadian intraocular pressure patterns in healthy subjects, primary open angle and normal tension glaucoma patients with a contact lens sensor', *Acta Ophthalmol*, 93: e14-21.

Agoumi, Y., G. P. Sharpe, D. M. Hutchison, M. T. Nicolela, P. H. Artes, and B. C. Chauhan. 2011. 'Laminar and prelaminar tissue displacement during intraocular pressure elevation in glaucoma patients and healthy controls', *Ophthalmology*, 118: 52-9.

Alhassan, M. B., F. Kyari, and H. O. Ejere. 2015. 'Peribulbar versus retrobulbar anaesthesia for cataract surgery', *Cochrane Database Syst Rev*: CD004083.

Alqawlaq, S., J. G. Flanagan, and J. M. Sivak. 2019. 'All roads lead to glaucoma: Induced retinal injury cascades contribute to a common neurodegenerative outcome', *Exp Eye Res*, 183: 88-97.

Ambati, J., C. S. Canakis, J. W. Miller, E. S. Gragoudas, A. Edwards, D. J. Weissgold, I. Kim, F. C. Delori, and A. P. Adamis. 2000. 'Diffusion of high molecular weight compounds through sclera', *Invest Ophthalmol Vis Sci*, 41: 1181-5.

Anand, R., K. G. Mehrotra, C. K. Mohan, and S. Ranka. 1993. 'An Improved Algorithm for Neural-Network Classification of Imbalanced Training Sets', *Ieee Transactions on Neural Networks*, 4: 962-69.

Anderson, D. R., S. M. Drance, M. Schulzer, and Group Collaborative Normal-Tension Glaucoma Study. 2001. 'Natural history of normal-tension glaucoma', *Ophthalmology*, 108: 247-53.

Anderson, D. R., and A. Hendrickson. 1974. 'Effect of intraocular pressure on rapid axoplasmic transport in monkey optic nerve', *Invest Ophthalmol*, 13: 771-83.

Ashton, N. 1952. 'Anatomical study of Schlemm's canal and aqueous veins by means of neoprene casts. II. Aqueous veins', *Br J Ophthalmol*, 36: 265-7; contd.

Asrani, S., R. Zeimer, J. Wilensky, D. Gieser, S. Vitale, and K. Lindenmuth. 2000. 'Large diurnal fluctuations in intraocular pressure are an independent risk factor in patients with glaucoma', *J Glaucoma*, 9: 134-42.

Aung, M. H., M. K. Kim, D. E. Olson, P. M. Thule, and M. T. Pardue. 2013. 'Early visual deficits in streptozotocin-induced diabetic long evans rats', *Invest Ophthalmol Vis Sci*, 54: 1370-7.

Avila, M. Y., V. A. Gerena, and J. L. Navia. 2012. 'Corneal crosslinking with genipin, comparison with UV-riboflavin in ex-vivo model', *Mol Vis*, 18: 1068-73.

Avila, M. Y., and J. L. Navia. 2010. 'Effect of genipin collagen crosslinking on porcine corneas', *J Cataract Refract Surg*, 36: 659-64.

Backhouse, Simon, and Alex Gentle. 2018. 'Scleral remodelling in myopia and its manipulation: a review of recent advances in scleral strengthening and myopia control', *Annals of Eye Science; January 2018*.

Ballantyne, B., and R. C. Myers. 2001. 'The acute toxicity and primary irritancy of glutaraldehyde solutions', *Vet Hum Toxicol*, 43: 193-202.

Baumann, B., S. Rauscher, M. Glosmann, E. Gotzinger, M. Pircher, S. Fialova, M. Groger, and C. K. Hitzenberger. 2014. 'Peripapillary rat sclera investigated in vivo with polarization-sensitive optical coherence tomography', *Invest Ophthalmol Vis Sci*, 55: 7686-96.

Becker, B. 1954. 'Decrease in intraocular pressure in man by a carbonic anhydrase inhibitor, diamox; a preliminary report', *Am J Ophthalmol*, 37: 13-5.

———. 1955. 'The mechanism of the fall in intraocular pressure induced by the carbonic anhydrase inhibitor, diamox', *Am J Ophthalmol*, 39: 177-84.

Bello, S. A., S. Malavade, and C. L. Passaglia. 2017a. 'Development of a Smart Pump for Monitoring and Controlling Intraocular Pressure', *Ann Biomed Eng*, 45: 990-1002.

———. 2017b. 'A Wireless Pressure Sensor for Continuous Monitoring of Intraocular Pressure in Conscious Animals', *Ann Biomed Eng*, 45: 2592-604.

Bengtsson, B., and A. Heijl. 2005. 'A long-term prospective study of risk factors for glaucomatous visual field loss in patients with ocular hypertension', *J Glaucoma*, 14: 135-8.

Bi, L., Z. Cao, Y. Hu, Y. Song, L. Yu, B. Yang, J. Mu, Z. Huang, and Y. Han. 2011. 'Effects of different cross-linking conditions on the properties of genipin-cross-linked chitosan/collagen scaffolds for cartilage tissue engineering', *J Mater Sci Mater Med*, 22: 51-62.

Bianco, Gianfranco; Levy, Alexander Miles; Grytz, Rafael; Fazio, Massimo Antonio. 2018. 'Substantial Preconditioning Effect Observed in the Inflation Tests of Juvenile Tree Shrew Sclera', *investigative ophthalmology & visual science*, 59: 709.

Bland, J. M., and D. G. Altman. 1999. 'Measuring agreement in method comparison studies', *Statistical Methods in Medical Research*, 8: 135-60.

Block, F., and M. Schwarz. 1998. 'The b-wave of the electroretinogram as an index of retinal ischemia', *Gen Pharmacol*, 30: 281-7.

Bouhenni, R. A., J. Dunmire, A. Sewell, and D. P. Edward. 2012. 'Animal models of glaucoma', *J Biomed Biotechnol*, 2012: 692609.

Bovee, C. E., and L. R. Pasquale. 2017. 'Evolving Surgical Interventions in the Treatment of Glaucoma', *Semin Ophthalmol*, 32: 91-95.

Bron, A. 2002. '[Ocular hypertension and glaucoma: the contribution of large studies to daily practice]', *J Fr Ophtalmol*, 25: 641-54.

Bui, B. V., B. Edmunds, G. A. Cioffi, and B. Fortune. 2005. 'The gradient of retinal functional changes during acute intraocular pressure elevation', *Invest Ophthalmol Vis Sci*, 46: 202-13.

Bui, B. V., and B. Fortune. 2004. 'Ganglion cell contributions to the rat full-field electroretinogram', *J Physiol*, 555: 153-73.

Bui, B. V., Z. He, A. J. Vingrys, C. T. Nguyen, V. H. Wong, and B. Fortune. 2013. 'Using the electroretinogram to understand how intraocular pressure elevation affects the rat retina', *J Ophthalmol*, 2013: 262467.

Bunker, S., J. Holeniewska, S. Vijay, A. Dahlmann-Noor, P. Khaw, Y. S. Ng, D. Shima, and R. Foxton. 2015. 'Experimental glaucoma induced by ocular injection of magnetic microspheres', *J Vis Exp*.

Burgoyne, C. F. 2011. 'A biomechanical paradigm for axonal insult within the optic nerve head in aging and glaucoma', *Exp Eye Res*, 93: 120-32.

Burgoyne, C. F., J. C. Downs, A. J. Bellezza, J. K. Suh, and R. T. Hart. 2005. 'The optic nerve head as a biomechanical structure: a new paradigm for understanding the role of IOP-related stress and strain in the pathophysiology of glaucomatous optic nerve head damage', *Prog Retin Eye Res*, 24: 39-73.

Calkins, D. J. 2012. 'Critical pathogenic events underlying progression of neurodegeneration in glaucoma', *Prog Retin Eye Res*, 31: 702-19.

Campbell, I. C., B. Coudrillier, and C. Ross Ethier. 2014. 'Biomechanics of the posterior eye: a critical role in health and disease', *J Biomech Eng*, 136: 021005.

Campbell, I. C., B. Coudrillier, and C. Ross Ethier. 2014. 'Biomechanics of the posterior eye: a critical role in health and disease', *J Biomech Eng*, 136: 021005.

Campbell, I. C., B. G. Hannon, A. T. Read, J. M. Sherwood, S. A. Schwaner, and C. R. Ethier. 2017. 'Quantification of the efficacy of collagen cross-linking agents to induce stiffening of rat sclera', *J R Soc Interface*, 14.

Cepurna, W. O., R. J. Kayton, E. C. Johnson, and J. C. Morrison. 2005. 'Age related optic nerve axonal loss in adult Brown Norway rats', *Exp Eye Res*, 80: 877-84.

Chang, Y., C. C. Tsai, H. C. Liang, and H. W. Sung. 2002. 'In vivo evaluation of cellular and acellular bovine pericardia fixed with a naturally occurring crosslinking agent (genipin)', *Biomaterials*, 23: 2447-57.

Chauhan, B. C., T. L. Levatte, K. L. Garnier, F. Tremblay, I. H. Pang, A. F. Clark, and M. L. Archibald. 2006. 'Semiquantitative optic nerve grading scheme for determining axonal loss in experimental optic neuropathy', *Invest Ophthalmol Vis Sci*, 47: 634-40.

Chen, H., X. Wei, K. S. Cho, G. Chen, R. Sappington, D. J. Calkins, and D. F. Chen. 2011. 'Optic neuropathy due to microbead-induced elevated intraocular pressure in the mouse', *Invest Ophthalmol Vis Sci*, 52: 36-44.

Chen, H., Y. Zhao, M. Liu, L. Feng, Z. Puyang, J. Yi, P. Liang, H. F. Zhang, J. Cang, J. B. Troy, and X. Liu. 2015. 'Progressive degeneration of retinal and superior collicular functions in mice with sustained ocular hypertension', *Invest Ophthalmol Vis Sci*, 56: 1971-84.

Chen, S., and X. Zhang. 2015. 'The Rodent Model of Glaucoma and Its Implications', *Asia Pac J Ophthalmol (Phila)*, 4: 236-41.

Chollet, François. 2015. 'Keras'. https://keras.io.

Chunyu, T., P. Xiujun, F. Zhengjun, Z. Xia, and Z. Feihu. 2014. 'Corneal collagen cross-linking in keratoconus: a systematic review and meta-analysis', *Sci Rep*, 4: 5652.

Clayson, K., X. Pan, E. Pavlatos, R. Short, H. Morris, R. T. Hart, and J. Liu. 2017. 'Corneoscleral stiffening increases IOP spike magnitudes during rapid microvolumetric change in the eye', *Exp Eye Res*, 165: 29-34.

Coleman, D. J., and S. Trokel. 1969. 'Direct-recorded intraocular pressure variations in a human subject', *Arch Ophthalmol*, 82: 637-40.

Cone-Kimball, E., C. Nguyen, E. N. Oglesby, M. E. Pease, M. R. Steinhart, and H. A. Quigley. 2013. 'Scleral structural alterations associated with chronic experimental intraocular pressure elevation in mice', *Mol Vis*, 19: 2023-39.

Cook, C., and P. Foster. 2012. 'Epidemiology of glaucoma: what's new?', *Can J Ophthalmol*, 47: 223-6.

Coudrillier, B., C. Boote, H. A. Quigley, and T. D. Nguyen. 2013. 'Scleral anisotropy and its effects on the mechanical response of the optic nerve head', *Biomech Model Mechanobiol*, 12: 941-63.

Coudrillier, B., D. M. Geraldes, N. T. Vo, R. Atwood, C. Reinhard, I. C. Campbell, Y. Raji, J. Albon, R. L. Abel, and C. R. Ethier. 2016. 'Phase-Contrast Micro-Computed Tomography Measurements of the Intraocular Pressure-Induced Deformation of the Porcine Lamina Cribrosa', *IEEE Trans Med Imaging*, 35: 988-99.

Coudrillier, B., J. Pijanka, J. Jefferys, T. Sorensen, H. A. Quigley, C. Boote, and T. D. Nguyen. 2015. 'Collagen structure and mechanical properties of the human sclera: analysis for the effects of age', *J Biomech Eng*, 137: 041006.

Coudrillier, B., J. Tian, S. Alexander, K. M. Myers, H. A. Quigley, and T. D. Nguyen. 2012. 'Biomechanics of the human posterior sclera: age- and glaucoma-related changes measured using inflation testing', *Invest Ophthalmol Vis Sci*, 53: 1714-28.

Coudrillier, B.;, I. C.; Campbell, A. T. Read, D. M. Geraldes, N. T. Vo, A. Feola, J. Mulvihill, J. Albon, R. L. Abel, and C. R. Ethier. 2016. 'Effects of Peripapillary Scleral Stiffening on the Deformation of the Lamina Cribrosa', *Invest Ophthalmol Vis Sci*, 57: 2666-77.

Cull, G., G. A. Cioffi, J. Dong, L. Homer, and L. Wang. 2003. 'Estimating normal optic nerve axon numbers in non-human primate eyes', *J Glaucoma*, 12: 301-6.

Dai, C., P. T. Khaw, Z. Q. Yin, D. Li, G. Raisman, and Y. Li. 2012. 'Structural basis of glaucoma: the fortified astrocytes of the optic nerve head are the target of raised intraocular pressure', *Glia*, 60: 13-28.

Danilov, N. A., N. Y. Ignatieva, E. N. Iomdina, S. A. Semenova, G. N. Rudenskaya, T. E. Grokhovskaya, and V. V. Lunin. 2008. 'Stabilization of scleral collagen by glycerol aldehyde cross-linking', *Biochim Biophys Acta*, 1780: 764-72.

Dias, J., V. F. Diakonis, M. Lorenzo, F. Gonzalez, K. Porras, S. Douglas, M. Avila, S. H. Yoo, and N. M. Ziebarth. 2015. 'Corneal stromal elasticity and viscoelasticity assessed by atomic force microscopy after different cross linking protocols', *Exp Eye Res*, 138: 1-5.

Douglas, R. M., N. M. Alam, B. D. Silver, T. J. McGill, W. W. Tschetter, and G. T. Prusky. 2005. 'Independent visual threshold measurements in the two eyes of freely moving rats and mice using a virtual-reality optokinetic system', *Vis Neurosci*, 22: 677-84.

Eilaghi, A., J. G. Flanagan, C. A. Simmons, and C. R. Ethier. 2010. 'Effects of scleral stiffness properties on optic nerve head biomechanics', *Ann Biomed Eng*, 38: 1586-92.

Elliot, M. J., P. M. Cullen, and C. I. Phillips. 1975. 'Ocular hypotensive effect of atenolol (Tenormin, I.C.I.). A new beta-adrenergic blocker', *Br J Ophthalmol*, 59: 296-300.

Ethier, Pedro Gonzalez; Coralia Catalina Luna; Ian Campbell; C Ross. 2015. 'Protective Effects of Adenoviral Mediated Subconjunctival Delivery of BMP2 in an Experimental Glaucoma Model', *investigative ophthalmology & visual science*, 56.

Fazio, D. T., J. R. Heckenlively, D. A. Martin, and R. E. Christensen. 1986. 'The electroretinogram in advanced open-angle glaucoma', *Doc Ophthalmol*, 63: 45-54.

Fazio, M. A., M. J. A. Girard, W. Lee, J. S. Morris, C. F. Burgoyne, and J. C. Downs. 2019. 'The Relationship Between Scleral Strain Change and Differential Cumulative Intraocular Pressure Exposure in the Nonhuman Primate Chronic Ocular Hypertension Model', *Invest Ophthalmol Vis Sci*, 60: 4141-50.

Feola, A. J., J. Fu, R. Allen, V. Yang, I. C. Campbell, A. Ottensmeyer, C. R. Ethier, and M. Pardue. 2019. 'Menopause exacerbates visual dysfunction in experimental glaucoma', *Exp Eye Res*, 186: 107706.

Ford, M. R., W. J. Dupps, Jr., A. M. Rollins, R. A. Sinha, and Z. Hu. 2011. 'Method for optical coherence elastography of the cornea', *J Biomed Opt*, 16: 016005.

Fortune, B., B. V. Bui, J. C. Morrison, E. C. Johnson, J. Dong, W. O. Cepurna, L. Jia, S. Barber, and G. A. Cioffi. 2004. 'Selective ganglion cell functional loss in rats with experimental glaucoma', *Invest Ophthalmol Vis Sci*, 45: 1854-62.

Foster, P. J., and Y. Jiang. 2014. 'Epidemiology of myopia', *Eye (Lond)*, 28: 202-8.

Fox, Stuart Ira. 2011. *Human physiology* (McGraw-Hill: New York).

Foxton, R. H., A. Finkelstein, S. Vijay, A. Dahlmann-Noor, P. T. Khaw, J. E. Morgan, D. T. Shima, and Y. S. Ng. 2013. 'VEGF-A is necessary and sufficient for retinal neuroprotection in models of experimental glaucoma', *Am J Pathol*, 182: 1379-90.

Frankfort, B. J., A. K. Khan, D. Y. Tse, I. Chung, J. J. Pang, Z. Yang, R. L. Gross, and S. M. Wu. 2013. 'Elevated intraocular pressure causes inner retinal dysfunction before cell loss in a mouse model of experimental glaucoma', *Invest Ophthalmol Vis Sci*, 54: 762-70.

Gacheru, S. N., P. C. Trackman, M. A. Shah, C. Y. O'Gara, P. Spacciapoli, F. T. Greenaway, and H. M. Kagan. 1990. 'Structural and catalytic properties of copper in lysyl oxidase', *J Biol Chem*, 265: 19022-7.

Girard, M. J., A. Dahlmann-Noor, S. Rayapureddi, J. A. Bechara, B. M. Bertin, H. Jones, J. Albon, P. T. Khaw, and C. R. Ethier. 2011. 'Quantitative mapping of scleral fiber orientation in normal rat eyes', *Invest Ophthalmol Vis Sci*, 52: 9684-93.

Girard, M. J., N. G. Strouthidis, A. Desjardins, J. M. Mari, and C. R. Ethier. 2013. 'In vivo optic nerve head biomechanics: performance testing of a three-dimensional tracking algorithm', *J R Soc Interface*, 10: 20130459.

Glickman, R. D. 2011. 'Ultraviolet phototoxicity to the retina', *Eye Contact Lens*, 37: 196-205.

Goel, M., R. G. Picciani, R. K. Lee, and S. K. Bhattacharya. 2010. 'Aqueous humor dynamics: a review', *Open Ophthalmol J*, 4: 52-9.

Gogola, A., N. J. Jan, K. L. Lathrop, and I. A. Sigal. 2018. 'Radial and Circumferential Collagen Fibers Are a Feature of the Peripapillary Sclera of Human, Monkey, Pig, Cow, Goat, and Sheep', *Invest Ophthalmol Vis Sci*, 59: 4763-74.

Goh, Y., M. Nakajima, I. Azuma, and O. Hayaishi. 1988. 'Prostaglandin D2 reduces intraocular pressure', *Br J Ophthalmol*, 72: 461-4.

Goldich, Y., A. L. Marcovich, Y. Barkana, Y. Mandel, A. Hirsh, Y. Morad, I. Avni, and D. Zadok. 2012. 'Clinical and corneal biomechanical changes after collagen cross-linking with riboflavin and UV irradiation in patients with progressive keratoconus: results after 2 years of follow-up', *Cornea*, 31: 609-14.

Gossman, C. A., D. M. Linn, and C. Linn. 2016. 'Glaucoma-inducing Procedure in an In Vivo Rat Model and Whole-mount Retina Preparation', *J Vis Exp*.

Gough, J. E., C. A. Scotchford, and S. Downes. 2002. 'Cytotoxicity of glutaraldehyde crosslinked collagen/poly(vinyl alcohol) films is by the mechanism of apoptosis', *J Biomed Mater Res*, 61: 121-30.

Greco, A., M. I. Rizzo, A. De Virgilio, A. Gallo, M. Fusconi, and M. de Vincentiis. 2016. 'Emerging Concepts in Glaucoma and Review of the Literature', *Am J Med*, 129: 1000 e7-00 e13.

Grytz, R., and J. T. Siegwart, Jr. 2015. 'Changing material properties of the tree shrew sclera during minus lens compensation and recovery', *Invest Ophthalmol Vis Sci*, 56: 2065-78.

Guo, L., S. E. Moss, R. A. Alexander, R. R. Ali, F. W. Fitzke, and M. F. Cordeiro. 2005. 'Retinal ganglion cell apoptosis in glaucoma is related to intraocular pressure and IOP-induced effects on extracellular matrix', *Invest Ophthalmol Vis Sci*, 46: 175-82.

Gurwitz, J. H., S. M. Yeomans, R. J. Glynn, B. E. Lewis, R. Levin, and J. Avorn. 1998. 'Patient noncompliance in the managed care setting. The case of medical therapy for glaucoma', *Med Care*, 36: 357-69.

Hadidi, P., D. D. Cissell, J. C. Hu, and K. A. Athanasiou. 2017. 'Temporal development of near-native functional properties and correlations with qMRI in self-assembling fibrocartilage treated with exogenous lysyl oxidase homolog 2', *Acta Biomater*, 64: 29-40.

Hamard, P., H. Hamard, J. Dufaux, and S. Quesnot. 1994. 'Optic nerve head blood flow using a laser Doppler velocimeter and haemorheology in primary open angle glaucoma and normal pressure glaucoma', *Br J Ophthalmol*, 78: 449-53.

Hannon, B. G., S. A. Schwaner, E. M. Boazak, B. G. Gerberich, E. J. Winger, M. R. Prausnitz, and C. R. Ethier. 2019. 'Sustained scleral stiffening in rats after a single genipin treatment', *J R Soc Interface*, 16: 20190427.

Hannon, B.G., J. Fu, R.K. Kim, A.J. Feola, C.R.1 Ethier, and M.T Pardue. 2018. "Early deficits in visual and retinal function in the rat microbead model of glaucoma." In *ISER Biennial Meeting*. Belfast, Northern Ireland, UK.

Harper, A. R., and J. A. Summers. 2015. 'The dynamic sclera: extracellular matrix remodeling in normal ocular growth and myopia development', *Exp Eye Res*, 133: 100-11.

Hayreh, S. S. 1976. 'The pathogenesis of optic nerve lesions in glaucoma', *Trans Sect Ophthalmol Am Acad Ophthalmol Otolaryngol*, 81: 197-213.

———. 2004. 'Radial optic neurotomy for nonischemic central retinal vein occlusion', *Arch Ophthalmol*, 122: 1572-3.

Hayreh, S. S., H. E. Kolder, and T. A. Weingeist. 1980. 'Central retinal artery occlusion and retinal tolerance time', *Ophthalmology*, 87: 75-8.

He, Z., B. V. Bui, and A. J. Vingrys. 2006. 'The rate of functional recovery from acute IOP elevation', *Invest Ophthalmol Vis Sci*, 47: 4872-80.

He, Z., D. Zhao, A. K. van Koeverden, C. T. Nguyen, J. K. H. Lim, V. H. Y. Wong, A. J. Vingrys, and B. V. Bui. 2018. 'A Model of Glaucoma Induced by Circumlimbal Suture in Rats and Mice', *J Vis Exp*.

Heijl, A., M. C. Leske, B. Bengtsson, L. Hyman, B. Bengtsson, M. Hussein, and Group Early Manifest Glaucoma Trial. 2002. 'Reduction of intraocular pressure and glaucoma progression: results from the Early Manifest Glaucoma Trial', *Arch Ophthalmol*, 120: 1268-79.

Hennink, W. E., and C. F. van Nostrum. 2002. 'Novel crosslinking methods to design hydrogels', *Adv Drug Deliv Rev*, 54: 13-36.

Hernandez, M. R. 2000. 'The optic nerve head in glaucoma: role of astrocytes in tissue remodeling', *Prog Retin Eye Res*, 19: 297-321.

Hernandez, M. R., X. X. Luo, F. Igoe, and A. H. Neufeld. 1987. 'Extracellular matrix of the human lamina cribrosa', *Am J Ophthalmol*, 104: 567-76.

Hersh, P. S., R. D. Stulting, D. Muller, D. S. Durrie, R. K. Rajpal, and Group United States Crosslinking Study. 2017. 'United States Multicenter Clinical Trial of Corneal Collagen Crosslinking for Keratoconus Treatment', *Ophthalmology*, 124: 1259-70.

Holden, B. A., T. R. Fricke, D. A. Wilson, M. Jong, K. S. Naidoo, P. Sankaridurg, T. Y. Wong, T. J. Naduvilath, and S. Resnikoff. 2016. 'Global Prevalence of Myopia and High Myopia and Temporal Trends from 2000 through 2050', *Ophthalmology*, 123: 1036-42.

Hrabchak, C., J. Rouleau, I. Moss, K. Woodhouse, M. Akens, C. Bellingham, F. Keeley, M. Dennis, and A. Yee. 2010. 'Assessment of biocompatibility and initial evaluation of genipin cross-linked elastin-like polypeptides in the treatment of an osteochondral knee defect in rabbits', *Acta Biomater*, 6: 2108-15.

Hu, J. Y., B. C. H. Ang, and L. W. Yip. 2020. 'Efficacy of the XEN gel stent on intraocular pressure lowering in East Asian eyes', *Int Ophthalmol*.

Huang, L. L., H. W. Sung, C. C. Tsai, and D. M. Huang. 1998. 'Biocompatibility study of a biological tissue fixed with a naturally occurring crosslinking reagent', *J Biomed Mater Res*, 42: 568-76.

Huang, W., F. Hu, M. Wang, F. Gao, P. Xu, C. Xing, X. Sun, S. Zhang, and J. Wu. 2018. 'Comparative analysis of retinal ganglion cell damage in three glaucomatous rat models', *Exp Eye Res*, 172: 112-22.

Hwang, Y. J., J. Larsen, T. B. Krasieva, and J. G. Lyubovitsky. 2011. 'Effect of genipin crosslinking on the optical spectral properties and structures of collagen hydrogels', *ACS Appl Mater Interfaces*, 3: 2579-84.

Hwang, Yu Jer, Joseph Granelli, Manasa Tirumalasetty, and Julia Lyubovitsky. 2013. "Microscopic imaging of glyceraldehyde-induced tissue glycation with intrinsic second harmonic generation and two-photon fluorescence contrasts." In *Imaging, Manipulation, and Analysis of Biomolecules, Cells, and Tissues*, edited by Daniel L. Farkas, Dan V. Nicolau and Robert C. Leif, 858725-25-7. San Francisco, CA: Society of Photo-Optical Instrumentation Engineers (SPIE).

Inman, D. M., W. S. Lambert, D. J. Calkins, and P. J. Horner. 2013. 'alpha-Lipoic acid antioxidant treatment limits glaucoma-related retinal ganglion cell death and dysfunction', *PLoS One*, 8: e65389.

Ishikawa, M., T. Yoshitomi, C. F. Zorumski, and Y. Izumi. 2015. 'Experimentally Induced Mammalian Models of Glaucoma', *Biomed Res Int*, 2015: 281214.

Jacobi, P. C., T. S. Dietlein, and F. K. Jacobi. 2000. 'A comparative study of topical vs retrobulbar anesthesia in complicated cataract surgery', *Arch Ophthalmol*, 118: 1037-43.

Jia, L., W. O. Cepurna, E. C. Johnson, and J. C. Morrison. 2000a. 'Effect of general anesthetics on IOP in rats with experimental aqueous outflow obstruction', *Invest Ophthalmol Vis Sci*, 41: 3415-9.

———. 2000b. 'Patterns of intraocular pressure elevation after aqueous humor outflow obstruction in rats', *Invest Ophthalmol Vis Sci*, 41: 1380-5.

Johnson, E. C., L. M. Deppmeier, S. K. Wentzien, I. Hsu, and J. C. Morrison. 2000. 'Chronology of optic nerve head and retinal responses to elevated intraocular pressure', *Invest Ophthalmol Vis Sci*, 41: 431-42.

Johnson, Justin M., and Taghi M. Khoshgoftaar. 2019. 'Survey on deep learning with class imbalance', *Journal of Big Data*, 6: 27.

Johnson, T. V., and S. I. Tomarev. 2010. 'Rodent models of glaucoma', *Brain Res Bull*, 81: 349-58.

Kerrigan-Baumrind, L. A., H. A. Quigley, M. E. Pease, D. F. Kerrigan, and R. S. Mitchell. 2000. 'Number of ganglion cells in glaucoma eyes compared with threshold visual field tests in the same persons', *Invest Ophthalmol Vis Sci*, 41: 741-8.

Kerstetter, J. R., R. F. Brubaker, S. E. Wilson, and L. J. Kullerstrand. 1988. 'Prostaglandin F2 alpha-1-isopropylester lowers intraocular pressure without decreasing aqueous humor flow', *Am J Ophthalmol*, 105: 30-4.

Khan, A. K., D. Y. Tse, M. E. van der Heijden, P. Shah, D. M. Nusbaum, Z. Yang, S. M. Wu, and B. J. Frankfort. 2015. 'Prolonged elevation of intraocular pressure results in retinal ganglion cell loss and abnormal retinal function in mice', *Exp Eye Res*, 130: 29-37.

Kim, B. C., H. G. Kim, S. A. Lee, S. Lim, E. H. Park, S. J. Kim, and C. J. Lim. 2005. 'Genipin-induced apoptosis in hepatoma cells is mediated by reactive oxygen species/c-Jun NH2-terminal kinase-dependent activation of mitochondrial pathway', *Biochem Pharmacol*, 70: 1398-407.

Kim, M., A. Takaoka, Q. V. Hoang, S. L. Trokel, and D. C. Paik. 2014. 'Pharmacologic alternatives to riboflavin photochemical corneal cross-linking: a comparison study of cell toxicity thresholds', *Invest Ophthalmol Vis Sci*, 55: 3247-57.

Kimball, E. C., C. Nguyen, M. R. Steinhart, T. D. Nguyen, M. E. Pease, E. N. Oglesby, B. C. Oveson, and H. A. Quigley. 2014. 'Experimental scleral cross-linking increases glaucoma damage in a mouse model', *Exp Eye Res*, 128: 129-40.

Kingma, Diederik P., and Jimmy Ba. 2014. 'Adam: A Method for Stochastic Optimization', *ArXiv*, abs/1412.6980.

Kitahara, Y., M. Takeuchi, K. Miura, T. Mine, T. Matsui, and S. Yamagishi. 2008. 'Glyceraldehyde-derived advanced glycation end products (AGEs). A novel biomarker of postprandial hyperglycaemia in diabetic rats', *Clin Exp Med*, 8: 175-7.

Klein, B. E., R. Klein, W. E. Sponsel, T. Franke, L. B. Cantor, J. Martone, and M. J. Menage. 1992. 'Prevalence of glaucoma. The Beaver Dam Eye Study', *Ophthalmology*, 99: 1499-504.

Koo, H. J., Y. S. Song, H. J. Kim, Y. H. Lee, S. M. Hong, S. J. Kim, B. C. Kim, C. Jin, C. J. Lim, and E. H. Park. 2004. 'Antiinflammatory effects of genipin, an active principle of gardenia', *Eur J Pharmacol*, 495: 201-8.

Koriyama, Y., A. Furukawa, M. Muramatsu, J. Takino, and M. Takeuchi. 2015. 'Glyceraldehyde caused Alzheimer's disease-like alterations in diagnostic marker levels in SH-SY5Y human neuroblastoma cells', *Sci Rep*, 5: 13313.

Koschade, S. E., M. A. Koch, B. M. Braunger, and E. R. Tamm. 2019. 'Efficient determination of axon number in the optic nerve: A stereological approach', *Exp Eye Res*, 186: 107710.

Krawczyk, B. 2016. 'Learning from imbalanced data: open challenges and future directions', *Progress in Artificial Intelligence*, 5: 221-32.

Kreiter, J., A. Rupprecht, L. Zimmermann, M. Moschinger, T. I. Rokitskaya, Y. N. Antonenko, L. Gille, M. Fedorova, and E. E. Pohl. 2019. 'Molecular Mechanisms Responsible for Pharmacological Effects of Genipin on Mitochondrial Proteins', *Biophys J*, 117: 1845-57.

Kunz, Clayton, and Hanumant Singh. 2008. "Hemispherical refraction and camera calibration in underwater vision." In *OCEANS 2008*, 1-7. IEEE.

Kwon, Y. H., J. H. Fingert, M. H. Kuehn, and W. L. Alward. 2009. 'Primary open-angle glaucoma', *N Engl J Med*, 360: 1113-24.

Kwong, J. M., N. Vo, A. Quan, M. Nam, H. Kyung, F. Yu, N. Piri, and J. Caprioli. 2013. 'The dark phase intraocular pressure elevation and retinal ganglion cell degeneration in a rat model of experimental glaucoma', *Exp Eye Res*, 112: 21-8.

Lambert, W. S., L. Ruiz, S. D. Crish, L. A. Wheeler, and D. J. Calkins. 2011. 'Brimonidine prevents axonal and somatic degeneration of retinal ganglion cell neurons', *Mol Neurodegener*, 6: 4.

Land, M. 2019. 'Eye movements in man and other animals', *Vision Res*, 162: 1-7.

Lani, R., M. S. Dias, C. A. Abreu, V. G. Araujo, T. Goncalo, G. Nascimento-Dos-Santos, A. M. Dantas, S. Allodi, M. Fiorani, H. Petrs-Silva, and R. Linden. 2019. 'A subacute model of glaucoma based on limbal plexus cautery in pigmented rats', *Sci Rep*, 9: 16286.

Lari, D. R., D. S. Schultz, A. S. Wang, O. T. Lee, and J. M. Stewart. 2012. 'Scleral mechanics: comparing whole globe inflation and uniaxial testing', *Exp Eye Res*, 94: 128-35.

Larin, K. V., and D. D. Sampson. 2017. 'Optical coherence elastography - OCT at work in tissue biomechanics [Invited]', *Biomed Opt Express*, 8: 1172-202.

Lempitsky, V. , and A. Zisserman. 2010. 'Learning To Count Objects in Images', *Advances in Neural Information Processing Systems 31 (Nips 2018)*.

Levkovitch-Verbin, H., H. A. Quigley, K. R. Martin, D. Valenta, L. A. Baumrind, and M. E. Pease. 2002. 'Translimbal laser photocoagulation to the trabecular meshwork as a model of glaucoma in rats', *Invest Ophthalmol Vis Sci*, 43: 402-10.

Levy, A. M., M. A. Fazio, and R. Grytz. 2018. 'Experimental myopia increases and scleral crosslinking using genipin inhibits cyclic softening in the tree shrew sclera', *Ophthalmic Physiol Opt*, 38: 246-56.

Leys, Christophe, Christophe Ley, Olivier Klein, Philippe Bernard, and Laurent Licata. 2013. 'Detecting outliers: Do not use standard deviation around the mean, use absolute deviation around the median', *Journal of Experimental Social Psychology*, 49: 764-66.

Lima, L. H., W. Cella, C. Brue, and S. H. Tsang. 2010. 'Unilateral electronegative ERG in a presumed central retinal artery occlusion', *Clin Ophthalmol*, 4: 1311-4.

Liu, C. W., L. Chi, P. Tu, J. Xue, H. Ru, and K. Lu. 2019. 'Quantitative proteomics reveals systematic dysregulations of liver protein metabolism in sucralose-treated mice', *J Proteomics*, 196: 1-10.

Liu, H. H., B. V. Bui, C. T. Nguyen, J. M. Kezic, A. J. Vingrys, and Z. He. 2015. 'Chronic ocular hypertension induced by circumlimbal suture in rats', *Invest Ophthalmol Vis Sci*, 56: 2811-20.

Liu, H. H., Z. He, C. T. Nguyen, A. J. Vingrys, and B. V. Bui. 2017. 'Reversal of functional loss in a rat model of chronic intraocular pressure elevation', *Ophthalmic Physiol Opt*, 37: 71-81.

Liu, T. X., X. Luo, Y. W. Gu, B. Yang, and Z. Wang. 2014. 'Correlation of discoloration and biomechanical properties in porcine sclera induced by genipin', *Int J Ophthalmol*, 7: 621-5.

Liu, T. X., and Z. Wang. 2013. 'Collagen crosslinking of porcine sclera using genipin', *Acta Ophthalmol*, 91: e253-7.

———. 2017. 'Biomechanics of sclera crosslinked using genipin in rabbit', *Int J Ophthalmol*, 10: 355-60.

Liu, Y., C. M. McDowell, Z. Zhang, H. E. Tebow, R. J. Wordinger, and A. F. Clark. 2014. 'Monitoring retinal morphologic and functional changes in mice following optic nerve crush', *Invest Ophthalmol Vis Sci*, 55: 3766-74.

Mabuchi, F., M. Aihara, M. R. Mackey, J. D. Lindsey, and R. N. Weinreb. 2003. 'Optic nerve damage in experimental mouse ocular hypertension', *Invest Ophthalmol Vis Sci*, 44: 4321-30.

Mafwiri, M., R. J. Bowman, M. Wood, and J. Kabiru. 2005. 'Primary open-angle glaucoma presentation at a tertiary unit in Africa: intraocular pressure levels and visual status', *Ophthalmic Epidemiol*, 12: 299-302.

Marina, N., N. D. Bull, and K. R. Martin. 2010a. 'A semiautomated targeted sampling method to assess optic nerve axonal loss in a rat model of glaucoma', *Nat Protoc*, 5: 1642-51.

Marina, Nephtali, Natalie D. Bull, and Keith R. Martin. 2010b. 'A semiautomated targeted sampling method to assess optic nerve axonal loss in a rat model of glaucoma', *Nat. Protocols*, 5: 1642-51.

Martini, Frederic H.; Nath, Judi L. 2010. *Anatomy and Physiology, 2nd Edition* (Pearson).

Matsumoto, C. S., K. Shinoda, and K. Nakatsuka. 2011. 'High correlation of scotopic and photopic electroretinogram components with severity of central retinal artery occlusion', *Clin Ophthalmol*, 5: 115-21.

Matsumoto, Y., A. Kanamori, M. Nakamura, and A. Negi. 2014. 'Rat chronic glaucoma model induced by intracameral injection of microbeads suspended in sodium sulfate-sodium hyaluronate', *Jpn J Ophthalmol*, 58: 290-7.

Mattson, M. S., J. Huynh, M. Wiseman, M. Coassin, J. A. Kornfield, and D. M. Schwartz. 2010. 'An in vitro intact globe expansion method for evaluation of cross-linking treatments', *Invest Ophthalmol Vis Sci*, 51: 3120-8.

Mc, Lean Jm, D. M. Gordon, and H. Koteen. 1951. 'Clinical experiences with ACTH and cortisone in ocular diseases', *Trans Am Acad Ophthalmol Otolaryngol*, 55: 565-72.

Medeiros, F. A., R. Lisboa, R. N. Weinreb, J. M. Liebmann, C. Girkin, and L. M. Zangwill. 2013. 'Retinal ganglion cell count estimates associated with early development of visual field defects in glaucoma', *Ophthalmology*, 120: 736-44.

Mi, F. L., Y. C. Tan, H. C. Liang, R. N. Huang, and H. W. Sung. 2001. 'In vitro evaluation of a chitosan membrane cross-linked with genipin', *J Biomater Sci Polym Ed*, 12: 835-50.

Mikelberg, F. S., S. M. Drance, M. Schulzer, H. M. Yidegiligne, and M. M. Weis. 1989. 'The normal human optic nerve. Axon count and axon diameter distribution', *Ophthalmology*, 96: 1325-8.

Mittag, T. W., J. Danias, G. Pohorenec, H. M. Yuan, E. Burakgazi, R. Chalmers-Redman, S. M. Podos, and W. G. Tatton. 2000. 'Retinal damage after 3 to 4 months of elevated intraocular pressure in a rat glaucoma model', *Invest Ophthalmol Vis Sci*, 41: 3451-9.

Morgan, I. G., K. Ohno-Matsui, and S. M. Saw. 2012. 'Myopia', *Lancet*, 379: 1739-48.

Morgan, J. E., and J. R. Tribble. 2015. 'Microbead models in glaucoma', *Exp Eye Res*, 141: 9-14.

Mori, S., Y. Murai, K. Ueda, M. Sakamoto, T. Kurimoto, Y. Yamada-Nakanishi, and M. Nakamura. 2020. 'A comparison of the 1-year surgical outcomes of ab externo trabeculotomy and microhook ab interno trabeculotomy using propensity score analysis', *BMJ Open Ophthalmol*, 5: e000446.

Morrison, J. C. 2005. 'Elevated intraocular pressure and optic nerve injury models in the rat', *J Glaucoma*, 14: 315-7.

Morrison, J. C., W. O. Cepurna, S. Tehrani, T. E. Choe, H. Jayaram, D. C. Lozano, B. Fortune, and E. C. Johnson. 2016. 'A Period of Controlled Elevation of IOP (CEI) Produces the Specific Gene Expression Responses and Focal Injury Pattern of Experimental Rat Glaucoma', *Invest Ophthalmol Vis Sci*, 57: 6700-11.

Morrison, J. C., W. O. Cepurna Ying Guo, and E. C. Johnson. 2011. 'Pathophysiology of human glaucomatous optic nerve damage: insights from rodent models of glaucoma', *Exp Eye Res*, 93: 156-64.

Morrison, J. C., F. W. Fraunfelder, S. T. Milne, and C. G. Moore. 1995. 'Limbal microvasculature of the rat eye', *Invest Ophthalmol Vis Sci*, 36: 751-6.

Morrison, J. C., E. C. Johnson, W. Cepurna, and L. Jia. 2005. 'Understanding mechanisms of pressure-induced optic nerve damage', *Prog Retin Eye Res*, 24: 217-40.

Morrison, J. C., E. Johnson, and W. O. Cepurna. 2008. 'Rat models for glaucoma research', *Prog Brain Res*, 173: 285-301.

Morrison, J. C., C. G. Moore, L. M. Deppmeier, B. G. Gold, C. K. Meshul, and E. C. Johnson. 1997. 'A rat model of chronic pressure-induced optic nerve damage', *Exp Eye Res*, 64: 85-96.

Morrison, J. C., K. B. Nylander, A. K. Lauer, W. O. Cepurna, and E. Johnson. 1998. 'Glaucoma drops control intraocular pressure and protect optic nerves in a rat model of glaucoma', *Invest Ophthalmol Vis Sci*, 39: 526-31.

Motulsky, H. J., and R. E. Brown. 2006. 'Detecting outliers when fitting data with nonlinear regression - a new method based on robust nonlinear regression and the false discovery rate', *BMC Bioinformatics*, 7: 123.

Myers, K. M., B. Coudrillier, B. L. Boyce, and T. D. Nguyen. 2010. 'The inflation response of the posterior bovine sclera', *Acta Biomater*, 6: 4327-35.

Nagata, A., T. Higashide, S. Ohkubo, H. Takeda, and K. Sugiyama. 2009. 'In vivo quantitative evaluation of the rat retinal nerve fiber layer with optical coherence tomography', *Invest Ophthalmol Vis Sci*, 50: 2809-15.

Neyshabur, B., S. Bhojanapalli, D. McAllester, and N. Srebro. 2017. 'Exploring Generalization in Deep Learning', *Advances in Neural Information Processing Systems 30 (Nips 2017)*, 30.

Nickells, R. W. 1996. 'Retinal ganglion cell death in glaucoma: the how, the why, and the maybe', *J Glaucoma*, 5: 345-56.

Noecker, R. J. 2006. 'The management of glaucoma and intraocular hypertension: current approaches and recent advances', *Ther Clin Risk Manag*, 2: 193-206.

Olsen, T. W., S. Y. Aaberg, D. H. Geroski, and H. F. Edelhauser. 1998. 'Human sclera: thickness and surface area', *Am J Ophthalmol*, 125: 237-41.

Osborne, Jason W., and Elaine. Waters. 2002. 'Four assumptions of multiple regression that researchers should always test', *Practical Assessment, Research & Evaluation*, 8.

Patel, B. C., T. A. Burns, A. Crandall, S. T. Shomaker, N. L. Pace, A. van Eerd, and T. Clinch. 1996. 'A comparison of topical and retrobulbar anesthesia for cataract surgery', *Ophthalmology*, 103: 1196-203.

Pazos, M., H. Yang, S. K. Gardiner, W. O. Cepurna, E. C. Johnson, J. C. Morrison, and C. F. Burgoyne. 2016. 'Expansions of the neurovascular scleral canal and contained optic nerve occur early in the hypertonic saline rat experimental glaucoma model', *Exp Eye Res*, 145: 173-86.

Pena, J. D., O. Agapova, B. T. Gabelt, L. A. Levin, M. J. Lucarelli, P. L. Kaufman, and M. R. Hernandez. 2001. 'Increased elastin expression in astrocytes of the lamina cribrosa in response to elevated intraocular pressure', *Invest Ophthalmol Vis Sci*, 42: 2303-14.

Phillips, J. R., and N. A. McBrien. 2004. 'Pressure-induced changes in axial eye length of chick and tree shrew: significance of myofibroblasts in the sclera', *Invest Ophthalmol Vis Sci*, 45: 758-63.

Pijanka, J. K., B. Coudrillier, K. Ziegler, T. Sorensen, K. M. Meek, T. D. Nguyen, H. A. Quigley, and C. Boote. 2012. 'Quantitative mapping of collagen fiber orientation in non-glaucoma and glaucoma posterior human sclerae', *Invest Ophthalmol Vis Sci*, 53: 5258-70.

Porciatti, V. 2015. 'Electrophysiological assessment of retinal ganglion cell function', *Exp Eye Res*, 141: 164-70.

Porciatti, V., T. Pizzorusso, M. C. Cenni, and L. Maffei. 1996. 'The visual response of retinal ganglion cells is not altered by optic nerve transection in transgenic mice overexpressing Bcl-2', *Proc Natl Acad Sci U S A*, 93: 14955-9.

Prusky, G. T., N. M. Alam, S. Beekman, and R. M. Douglas. 2004. 'Rapid quantification of adult and developing mouse spatial vision using a virtual optomotor system', *Invest Ophthalmol Vis Sci*, 45: 4611-6.

Qu, Y., Y. He, A. Saidi, Y. Xin, Y. Zhou, J. Zhu, T. Ma, R. H. Silverman, D. S. Minckler, Q. Zhou, and Z. Chen. 2018. 'In Vivo Elasticity Mapping of Posterior Ocular Layers Using Acoustic Radiation Force Optical Coherence Elastography', *Invest Ophthalmol Vis Sci*, 59: 455-61.

Quigley, H. A., E. M. Addicks, W. R. Green, and A. E. Maumenee. 1981. 'Optic nerve damage in human glaucoma. II. The site of injury and susceptibility to damage', *Arch Ophthalmol*, 99: 635-49.

Quigley, H. A., and A. T. Broman. 2006. 'The number of people with glaucoma worldwide in 2010 and 2020', *Br J Ophthalmol*, 90: 262-7.

Quigley, H. A., and W. R. Green. 1979. 'The histology of human glaucoma cupping and optic nerve damage: clinicopathologic correlation in 21 eyes', *Ophthalmology*, 86: 1803-30.

Quigley, H. A., R. M. Hohman, R. Sanchez, and E. M. Addicks. 1985. 'Optic nerve head blood flow in chronic experimental glaucoma', *Arch Ophthalmol*, 103: 956-62.

Quigley, H. A., and A. Sommer. 1987. 'How to use nerve fiber layer examination in the management of glaucoma', *Trans Am Ophthalmol Soc*, 85: 254-72.

Quigley, H., and D. R. Anderson. 1976. 'The dynamics and location of axonal transport blockade by acute intraocular pressure elevation in primate optic nerve', *Invest Ophthalmol*, 15: 606-16.

Rada, J. A., S. Shelton, and T. T. Norton. 2006. 'The sclera and myopia', *Exp Eye Res*, 82: 185-200.

Ramsundar, Bharath, and Reza Bosagh Zadeh. 2018. *TensorFlow for deep learning : from linear regression to reinforcement learning* (O'Reilly Media: Beijing).

Read, A. T., and C. K. Govind. 1997. 'Regeneration and sex-biased transformation of the sexually dimorphic pincer claw in adult snapping shrimps', *Journal of Experimental Zoology*, 279: 356-66.

Redfern, W. S., S. Storey, K. Tse, Q. Hussain, K. P. Maung, J. P. Valentin, G. Ahmed, A. Bigley, D. Heathcote, and J. S. McKay. 2011. 'Evaluation of a convenient method of assessing rodent visual function in safety pharmacology studies: effects of sodium iodate on visual acuity and retinal morphology in albino and pigmented rats and mice', *J Pharmacol Toxicol Methods*, 63: 102-14.

Remtulla, S., and P. E. Hallett. 1985. 'A schematic eye for the mouse, and comparisons with the rat', *Vision Res*, 25: 21-31.

Reynaud, J., G. Cull, L. Wang, B. Fortune, S. Gardiner, C. F. Burgoyne, and G. A. Cioffi. 2012. 'Automated quantification of optic nerve axons in primate glaucomatous and normal eyes--method and comparison to semi-automated manual quantification', *Invest Ophthalmol Vis Sci*, 53: 2951-9.

Ripley, Brian D. 1996. *Pattern recognition and neural networks* (Cambridge University Press: Cambridge ; New York).

Ritch, Matthew D., Bailey G. Hannon, A. Thomas Read, Andrew J. Feola, Grant A. Cull, Juan Reynaud, John C. Morrison, Claude F. Burgoyne, Machelle T. Pardue, and C. Ross Ethier. 2019. "AxoNet: an AI-based tool to count retinal ganglion cell axons." In *arXiv e-prints*.

Robin, A., and D. S. Grover. 2011. 'Compliance and adherence in glaucoma management', *Indian J Ophthalmol*, 59 Suppl: S93-6.

Ronneberger, O., P. Fischer, and T. Brox. 2015. 'U-Net: Convolutional Networks for Biomedical Image Segmentation', *Medical Image Computing and Computer-Assisted Intervention, Pt Iii*, 9351: 234-41.

Rowland, C. R., D. P. Lennon, A. I. Caplan, and F. Guilak. 2013. 'The effects of crosslinking of scaffolds engineered from cartilage ECM on the chondrogenic differentiation of MSCs', *Biomaterials*, 34: 5802-12.

Samsel, P. A., L. Kisiswa, J. T. Erichsen, S. D. Cross, and J. E. Morgan. 2011. 'A novel method for the induction of experimental glaucoma using magnetic microspheres', *Invest Ophthalmol Vis Sci*, 52: 1671-5.

Samuels, B. C., J. T. Siegwart, W. Zhan, L. Hethcox, M. Chimento, R. Whitley, J. C. Downs, and C. A. Girkin. 2018. 'A Novel Tree Shrew (Tupaia belangeri) Model of Glaucoma', *Invest Ophthalmol Vis Sci*, 59: 3136-43.

Sanchez, R. M., G. R. Dunkelberger, and H. A. Quigley. 1986. 'The number and diameter distribution of axons in the monkey optic nerve', *Invest Ophthalmol Vis Sci*, 27: 1342-50.

Sapienza, A., A. L. Raveu, E. Reboussin, C. Roubeix, C. Boucher, J. Degardin, D. Godefroy, W. Rostene, A. Reaux-Le Goazigo, C. Baudouin, and S. Melik

Parsadaniantz. 2016. 'Bilateral neuroinflammatory processes in visual pathways induced by unilateral ocular hypertension in the rat', *J Neuroinflammation*, 13: 44.

Sappington, R. M., B. J. Carlson, S. D. Crish, and D. J. Calkins. 2010. 'The microbead occlusion model: a paradigm for induced ocular hypertension in rats and mice', *Invest Ophthalmol Vis Sci*, 51: 207-16.

Saw, S. M., G. Gazzard, E. C. Shih-Yen, and W. H. Chua. 2005. 'Myopia and associated pathological complications', *Ophthalmic Physiol Opt*, 25: 381-91.

Sawada, A., and A. H. Neufeld. 1999. 'Confirmation of the rat model of chronic, moderately elevated intraocular pressure', *Exp Eye Res*, 69: 525-31.

Schindelin, J., I. Arganda-Carreras, E. Frise, V. Kaynig, M. Longair, T. Pietzsch, S. Preibisch, C. Rueden, S. Saalfeld, B. Schmid, J. Y. Tinevez, D. J. White, V. Hartenstein, K. Eliceiri, P. Tomancak, and A. Cardona. 2012. 'Fiji: an open-source platform for biological-image analysis', *Nat Methods*, 9: 676-82.

Schmid, H., M. Renner, H. B. Dick, and S. C. Joachim. 2014. 'Loss of inner retinal neurons after retinal ischemia in rats', *Invest Ophthalmol Vis Sci*, 55: 2777-87.

Schneider, C. A., W. S. Rasband, and K. W. Eliceiri. 2012. 'NIH Image to ImageJ: 25 years of image analysis', *Nat Methods*, 9: 671-5.

Schultz, D. S., J. C. Lotz, S. M. Lee, M. L. Trinidad, and J. M. Stewart. 2008. 'Structural factors that mediate scleral stiffness', *Invest Ophthalmol Vis Sci*, 49: 4232-6.

Schuman, J. S., M. R. Hee, A. V. Arya, T. Pedut-Kloizman, C. A. Puliafito, J. G. Fujimoto, and E. A. Swanson. 1995. 'Optical coherence tomography: a new tool for glaucoma diagnosis', *Curr Opin Ophthalmol*, 6: 89-95.

Schuman, J. S., M. R. Hee, C. A. Puliafito, C. Wong, T. Pedut-Kloizman, C. P. Lin, E. Hertzmark, J. A. Izatt, E. A. Swanson, and J. G. Fujimoto. 1995. 'Quantification of nerve fiber layer thickness in normal and glaucomatous eyes using optical coherence tomography', *Arch Ophthalmol*, 113: 586-96.

Schwaner, S. A., B. G. Hannon, A. J. Feola, and C. R. Ethier. 2020. 'Biomechanical properties of the rat sclera obtained with inverse finite element modeling', *Biomech Model Mechanobiol*.

Scott, A. W., N. M. Bressler, S. Ffolkes, J. S. Wittenborn, and J. Jorkasky. 2016. 'Public Attitudes About Eye and Vision Health', *JAMA Ophthalmol*.

Shareef, S. R., E. Garcia-Valenzuela, A. Salierno, J. Walsh, and S. C. Sharma. 1995. 'Chronic ocular hypertension following episcleral venous occlusion in rats', *Exp Eye Res*, 61: 379-82.

Sherwood, J. M., E. Reina-Torres, J. A. Bertrand, B. Rowe, and D. R. Overby. 2016. 'Measurement of Outflow Facility Using iPerfusion', *PLoS One*, 11: e0150694.

Shinohara, K., T. Yoshida, H. Liu, S. Ichinose, T. Ishida, K. I. Nakahama, N. Nagaoka, M. Moriyama, I. Morita, and K. Ohno-Matsui. 2018. 'Establishment of novel therapy to reduce progression of myopia in rats with experimental myopia by fibroblast transplantation on sclera', *J Tissue Eng Regen Med*, 12: e451-e61.

Sigal, I. A., J. G. Flanagan, and C. R. Ethier. 2005. 'Factors influencing optic nerve head biomechanics', *Invest Ophthalmol Vis Sci*, 46: 4189-99.

Sigal, I. A., J. G. Flanagan, I. Tertinegg, and C. R. Ethier. 2004. 'Finite element modeling of optic nerve head biomechanics', *Invest Ophthalmol Vis Sci*, 45: 4378-87.

———. 2007. 'Predicted extension, compression and shearing of optic nerve head tissues', *Exp Eye Res*, 85: 312-22.

Silver, D. M., and O. Geyer. 2000. 'Pressure-volume relation for the living human eye', *Curr Eye Res*, 20: 115-20.

Singh, M., Z. Han, A. Nair, A. Schill, M. D. Twa, and K. V. Larin. 2017. 'Applanation optical coherence elastography: noncontact measurement of intraocular pressure, corneal biomechanical properties, and corneal geometry with a single instrument', *J Biomed Opt*, 22: 20502.

Smedowski, A., M. Pietrucha-Dutczak, K. Kaarniranta, and J. Lewin-Kowalik. 2014. 'A rat experimental model of glaucoma incorporating rapid-onset elevation of intraocular pressure', *Sci Rep*, 4: 5910.

Sommer, A., J. M. Tielsch, J. Katz, H. A. Quigley, J. D. Gottsch, J. Javitt, and K. Singh. 1991. 'Relationship between intraocular pressure and primary open angle glaucoma among white and black Americans. The Baltimore Eye Survey', *Arch Ophthalmol*, 109: 1090-5.

Sommer, C., C. Straehle, U. Köthe, and F. A. Hamprecht. 2011. "Ilastik: Interactive learning and segmentation toolkit." In *2011 IEEE International Symposium on Biomedical Imaging: From Nano to Macro*, 230-33.

Song, W., Y. Tang, J. Qiao, H. Li, B. Rong, S. Yang, Y. Wu, and X. Yan. 2017. 'The comparative safety of genipin versus UVA-riboflavin crosslinking of rabbit corneas', *Mol Vis*, 23: 504-13.

Spoerl, E., A. G. Boehm, and L. E. Pillunat. 2005. 'The influence of various substances on the biomechanical behavior of lamina cribrosa and peripapillary sclera', *Invest Ophthalmol Vis Sci*, 46: 1286-90.

Spoerl, E., M. Huhle, and T. Seiler. 1998. 'Induction of cross-links in corneal tissue', *Exp Eye Res*, 66: 97-103.

Stewart, J. M., D. S. Schultz, O. T. Lee, and M. L. Trinidad. 2009. 'Exogenous collagen cross-linking reduces scleral permeability: modeling the effects of age-related cross-link accumulation', *Invest Ophthalmol Vis Sci*, 50: 352-7.

Struebing, F. L., R. King, Y. Li, J. N. Cooke Bailey, Neighborhood consortium, J. L. Wiggs, and E. E. Geisert. 2018. 'Genomic loci modulating retinal ganglion cell death following elevated IOP in the mouse', *Exp Eye Res*, 169: 61-67.

Sung, H. W., C. N. Chen, R. N. Huang, J. C. Hsu, and W. H. Chang. 2000. 'In vitro surface characterization of a biological patch fixed with a naturally occurring crosslinking agent', *Biomaterials*, 21: 1353-62.

Sung, H. W., R. N. Huang, L. L. Huang, and C. C. Tsai. 1999. 'In vitro evaluation of cytotoxicity of a naturally occurring cross-linking reagent for biological tissue fixation', *J Biomater Sci Polym Ed*, 10: 63-78.

Sung, H. W., I. L. Liang, C. N. Chen, R. N. Huang, and H. F. Liang. 2001. 'Stability of a biological tissue fixed with a naturally occurring crosslinking agent (genipin)', *J Biomed Mater Res*, 55: 538-46.

Szigeti, A., E. Tatrai, A. Szamosi, P. Vargha, Z. Z. Nagy, J. Nemeth, D. C. DeBuc, and G. M. Somfai. 2014. 'A morphological study of retinal changes in unilateral amblyopia using optical coherence tomography image segmentation', *PLoS One*, 9: e88363.

Tanna, A. P., and M. Johnson. 2018. 'Rho Kinase Inhibitors as a Novel Treatment for Glaucoma and Ocular Hypertension', *Ophthalmology*, 125: 1741-56.

Templeton, J. P., F. L. Struebing, A. Lemmon, and E. E. Geisert. 2014. 'ImagePAD, a novel counting application for the Apple iPad, used to quantify axons in the mouse optic nerve', *Exp Eye Res*, 128: 102-8.

Tham, Y. C., X. Li, T. Y. Wong, H. A. Quigley, T. Aung, and C. Y. Cheng. 2014. 'Global prevalence of glaucoma and projections of glaucoma burden through 2040: a systematic review and meta-analysis', *Ophthalmology*, 121: 2081-90.

Tielsch, J. M., J. Katz, A. Sommer, H. A. Quigley, and J. C. Javitt. 1994. 'Family history and risk of primary open angle glaucoma. The Baltimore Eye Survey', *Arch Ophthalmol*, 112: 69-73.

Tonge, T. K., B. J. Murienne, B. Coudrillier, S. Alexander, W. Rothkopf, and T. D. Nguyen. 2013. 'Minimal preconditioning effects observed for inflation tests of planar tissues', *J Biomech Eng*, 135: 114502.

Tripathi, R. C. 1972. 'Aqueous outflow pathway in normal and glaucomatous eyes', *Br J Ophthalmol*, 56: 157-74.

———. 1977. 'Uveoscleral drainage of aqueous humour', *Exp Eye Res*, 25 Suppl: 305-8.

Turner, P. V., and M. A. Albassam. 2005. 'Susceptibility of rats to corneal lesions after injectable anesthesia', *Comp Med*, 55: 175-82.

Ueda, J., S. Sawaguchi, T. Hanyu, K. Yaoeda, T. Fukuchi, H. Abe, and H. Ozawa. 1998. 'Experimental glaucoma model in the rat induced by laser trabecular photocoagulation after an intracameral injection of India ink', *Jpn J Ophthalmol*, 42: 337-44.

Urcola, J. H., M. Hernandez, and E. Vecino. 2006. 'Three experimental glaucoma models in rats: comparison of the effects of intraocular pressure elevation on retinal ganglion cell size and death', *Exp Eye Res*, 83: 429-37.

Usui, T., S. Shizuuchi, H. Watanabe, and F. Hayase. 2004. 'Cytotoxicity and oxidative stress induced by the glyceraldehyde-related Maillard reaction products for HL-60 cells', *Biosci Biotechnol Biochem*, 68: 333-40.

Valloli, Varun Kannadi, and Kinal Mehta. 2019. 'W-Net: Reinforced U-Net for Density Map Estimation', *ArXiv*, abs/1903.11249.

Vasavada, D., P. Baskaran, and S. Ramakrishnan. 2017. 'Retinal Vascular Occlusion Secondary to Retrobulbar Injection: Case Report and Literature Review', *Middle East Afr J Ophthalmol*, 24: 57-60.

Viswanathan, S., L. J. Frishman, J. G. Robson, R. S. Harwerth, and E. L. Smith, 3rd. 1999. 'The photopic negative response of the macaque electroretinogram: reduction by experimental glaucoma', *Invest Ophthalmol Vis Sci*, 40: 1124-36.

Viswanathan, S., L. J. Frishman, J. G. Robson, and J. W. Walters. 2001. 'The photopic negative response of the flash electroretinogram in primary open angle glaucoma', *Invest Ophthalmol Vis Sci*, 42: 514-22.

Wang, C., T. T. Lau, W. L. Loh, K. Su, and D. A. Wang. 2011. 'Cytocompatibility study of a natural biomaterial crosslinker--Genipin with therapeutic model cells', *J Biomed Mater Res B Appl Biomater*, 97: 58-65.

Wang, L G., Weiyuan. Shao, Yao. Lu, Hao. Ye, Jian. Pu, and Yingbin. Zheng. 2018. 'Crowd Counting with Density Adaption Networks', *ArXiv*, abs/1806.10040.

Wang, M., and C. C. Corpuz. 2015. 'Effects of scleral cross-linking using genipin on the process of form-deprivation myopia in the guinea pig: a randomized controlled experimental study', *BMC Ophthalmol*, 15: 89.

Wareham, L. K., A. C. Dordea, G. Schleifer, V. Yao, A. Batten, F. Fei, J. Mertz, M. Gregory-Ksander, L. R. Pasquale, E. S. Buys, and R. M. Sappington. 2019. 'Increased bioavailability of cyclic guanylate monophosphate prevents retinal ganglion cell degeneration', *Neurobiol Dis*, 121: 65-75.

Weber, A. J., and D. Zelenak. 2001. 'Experimental glaucoma in the primate induced by latex microspheres', *J Neurosci Methods*, 111: 39-48.

Wei, X., S. P. Cai, X. Zhang, X. Li, X. Chen, and X. Liu. 2012. 'Is low dose of estrogen beneficial for prevention of glaucoma?', *Med Hypotheses*, 79: 377-80.

Weinreb, R. N., T. Aung, and F. A. Medeiros. 2014. 'The pathophysiology and treatment of glaucoma: a review', *JAMA*, 311: 1901-11.

Weinreb, R. N., and P. T. Khaw. 2004. 'Primary open-angle glaucoma', *Lancet*, 363: 1711-20.

Wessels, I. F., and J. Bowers. 1998. 'Avoiding Tenon's capsule', *Ophthalmology*, 105: 942-3.

Williams, M.N., C.A.G. Grajales, and D. Kurkiewicz. 2013. 'Assumptions of multiple regression: correcting two misconceptions', *Practical Assessment, Research & Evaluation*, 18.

Wollensak, G., and E. Iomdina. 2008a. 'Crosslinking of scleral collagen in the rabbit using glyceraldehyde', *J Cataract Refract Surg*, 34: 651-6.

———. 2008b. 'Long-term biomechanical properties after collagen crosslinking of sclera using glyceraldehyde', *Acta Ophthalmol*, 86: 887-93.

Wollensak, G., E. Iomdina, D. D. Dittert, O. Salamatina, and G. Stoltenburg. 2005. 'Cross-linking of scleral collagen in the rabbit using riboflavin and UVA', *Acta Ophthalmol Scand*, 83: 477-82.

Wollensak, G., and E. Spoerl. 2004. 'Collagen crosslinking of human and porcine sclera', *J Cataract Refract Surg*, 30: 689-95.

Wollensak, G., E. Spoerl, and T. Seiler. 2003. 'Riboflavin/ultraviolet-a-induced collagen crosslinking for the treatment of keratoconus', *Am J Ophthalmol*, 135: 620-7.

Wong, F. F., D. R. Lari, D. S. Schultz, and J. M. Stewart. 2012. 'Whole globe inflation testing of exogenously crosslinked sclera using genipin and methylglyoxal', *Exp Eye Res*, 103: 17-21.

Xu, B., M. J. Chow, and Y. Zhang. 2011. 'Experimental and modeling study of collagen scaffolds with the effects of crosslinking and fiber alignment', *Int J Biomater*, 2011: 172389.

Yang, H., J. C. Downs, and C. F. Burgoyne. 2009. 'Physiologic intereye differences in monkey optic nerve head architecture and their relation to changes in early experimental glaucoma', *Invest Ophthalmol Vis Sci*, 50: 224-34.

Yang, Q., K. S. Cho, H. Chen, D. Yu, W. H. Wang, G. Luo, I. H. Pang, W. Guo, and D. F. Chen. 2012. 'Microbead-induced ocular hypertensive mouse model for screening and testing of aqueous production suppressants for glaucoma', *Invest Ophthalmol Vis Sci*, 53: 3733-41.

Yoo, J. S., Y. J. Kim, S. H. Kim, and S. H. Choi. 2011. 'Study on genipin: a new alternative natural crosslinking agent for fixing heterograft tissue', *Korean J Thorac Cardiovasc Surg*, 44: 197-207.

Zaimi, A., M. Wabartha, V. Herman, P. L. Antonsanti, C. S. Perone, and J. Cohen-Adad. 2018. 'AxonDeepSeg: automatic axon and myelin segmentation from microscopy data using convolutional neural networks', *Sci Rep*, 8: 3816.

Zarei, K., T. E. Scheetz, M. Christopher, K. Miller, A. Hedberg-Buenz, A. Tandon, M. G. Anderson, J. H. Fingert, and M. D. Abramoff. 2016. 'Corrigendum: Automated Axon Counting in Rodent Optic Nerve Sections with AxonJ', *Sci Rep*, 6: 34124.

Zhang, N., T. L. Favazza, A. M. Baglieri, I. Y. Benador, E. R. Noonan, A. B. Fulton, R. M. Hansen, P. M. Iuvone, and J. D. Akula. 2013. 'The rat with oxygen-induced retinopathy is myopic with low retinal dopamine', *Invest Ophthalmol Vis Sci*, 54: 8275-84.

Zhao, Y., B. Yu, Y. H. Xiang, X. J. Han, Y. Xu, K. F. So, A. D. Xu, and Y. W. Ruan. 2013. 'Changes in retinal morphology, electroretinogram and visual behavior after transient global ischemia in adult rats', *PLoS One*, 8: e65555.

Zhi, Z., W. O. Cepurna, E. C. Johnson, J. C. Morrison, and R. K. Wang. 2012. 'Impact of intraocular pressure on changes of blood flow in the retina, choroid, and optic nerve head in rats investigated by optical microangiography', *Biomed Opt Express*, 3: 2220-33.